Étude expérimentale et numériques des inondations urbaines

Pascal Finaud-Guyot

UNIVERSITÉ DE MONTPELLIER

Habilitation à Diriger les Recherches

Ecole Doctorale GAIA, filière *Sciences de la Terre et de l'Eau*

présentée et soutenue publiquement le 11 Juin 2021

Pascal FINAUD-GUYOT

Etude expérimentale et numérique des inondations urbaines

Jury :

Philippe Fraunié	Professeur émerite de l'université de Toulon	Rapporteur
Vincent Guinot	Professeur de l'univerité de Montpellier	Examinateur
Gislain Lipeme Kouyi	Professeur de l'INSA de Lyon	Rapporteur
Robert Mosé	Professeur de l'université de Strasbourg	Président du jury, Examinateur
Sandra Soares-Frazao	Professeur à l'Universié Catholique de Louvain	Rapporteur

Table des matières

Première partie

Curriculum Vitae détaillé

Chapitre 1

Parcours professionnel

Pascal Finaud-Guyot

Né le 13 janvier 1982 à Rosny-Sous-Bois (93), France
Maître de conférences (CNU60) en mécanique des fluides environnementale et modélisation numérique

Université de Montpellier
pascal.finaud-guyot@umontpellier.fr
Tel : +33 (0)4 67 14 42 75

1.1 Parcours académique et professionnel

1.1.1 Activités professionnelles

Depuis 2019[1] Maître de conférences (CNU 60) de l'Université de Montpellier, Montpellier France

- Enseignement Polytech Montpellier, départements STE (Sciences et Technologies de l'Eau) et EGC (Eau et Génie Civil)
- Recherche Laboratoire HydroSciences Montpellier (UMR 5569), équipe H2U (Hydrologie et Hydraulique Urbaines)
  INRIA Sophia Antipolis - Méditerranée, équipe-projet Lemon (INRIA, Laboratoire HydroSciences Montpellier, Institut Montpellierain Alexandre Grothendieck)

2010 2019 Maître de conférences du ministère de l'agriculture (CNECA 3[2])

- Enseignement École Nationale du Génie de l'Eau et de l'Environnement de Strasbourg, Strasbourg France
- Recherche Laboratoire Icube (UMR 7357), équipe MécaFlu, Strasbourg France

2009-2010 Attaché Temporaire d'Enseignement et de Recherche (CNU 36)
Université Montpellier 2, Montpellier France

2006-2009 Ingénieur chargé d'études en hydraulique
Bureau d'études Ginger Environnement & Infrastructures, Montpellier France

2006-2008 Vacataire d'enseignement à Polytech Montpellier, Montpellier France

2008 Vacataire d'enseignement au Conservatoire National des Arts et Métiers, Montpellier France

Juillet 2003 Chargé de Valorisation du Patrimoine Fluvial, Les Pavillons-Sous-Bois France

2. Commission Nationale des Enseignants-Chercheurs relevant du ministère chargé de l'Agriculture : Mathématiques – Physique – Mécanisation – Génie rural et industriel

1.1.2 Formation académique

2009 Diplôme de doctorat de l'Université Montpellier 2. *Modélisation macroscopique des inondations fluviales et urbaines : prise en compte des écoulements directionnels et des échanges lit majeur-lit mineur*
Encadrement : V. Guinot et C. Delenne, laboratoire HydroSciences Montpellier, UMR HSM 5569
Jury : N. Rivière (président), S. Soares-Frazao (examinatrice), R. Mosé (rapporteur), P. Fraunié (rapporteur), C. Llovel (invitée)
Financement : Ginger Environnement & Infrastructures (Bourse CIFRE n°2006/838)

2008 Certification TOEIC (Score : 935)

2005 Diplôme d'ingénieur en Sciences et Technologies de l'Eau de Polytech Montpellier

2005 Master of Sciences in Water Management, Cranfield University at Silsoe (United-Kingdom)

Septembre-Décembre 2005 Ingénieur stagiaire au sein du Bureau d'études Ginger Environnement & Infrastructures, Montpellier France. *Élaboration du schéma directeur d'irrigation sur le bassin versant du Llech et de la Lentilla (66)*

Mai-Septembre 2005 Stage de Master 2 au Cemagref de Montpellier. *Développement d'un cadre d'évaluation des méthodes de gestion participative.*

Juillet-Août 2004 Ingénieur stagiaire au Syndicat Intercommunal à Vocation Multiple de l'Étang de l'Or, Mauguio France. *Rédaction du Cahier des Charges préalable à l'établissement du Schéma Directeur d'Alimentation en Eau Potable*

2002 DEUG Sciences de la Vie de l'Université Paris VI, Paris France

2000-2002 Classe Préparatoire aux Grandes Écoles (BCPST), lycée A. Schweitzer, Le Raincy France

1.2 Responsabilités administratives et collectives

1.2.1 Responsabilités administratives

2020-... Membre du groupe de travail *Développement Durable* du laboratoire HydroSciences Montpellier

2019-... Membre du groupe de travail *Développement Durable et Responsabilité Sociétale* de Polytech Montpellier

2018-2019 Membre du groupe de travail *Mise en place du télétravail* de l'ENGEES

2018-2019 Représentant élu au CHSCT de l'ENGEES

2017-2019 Représentant élu au Comité Technique de l'ENGEES

2015-2016 Représentant élu au Comité Scientifique de l'ENGEES

2015 Membre du jury de recrutement de maître de conférences ENGEES

2012-2014 Représentant élu au Conseil des Enseignements et au Conseil des Études et de la Vie Étudiante

1.2.2 Responsabilités d'enseignement

Depuis le début de ma carrière, je suis responsable de plusieurs unités d'enseignement (voir tableau 1.1). Mon rôle consiste à articuler chaque UE avec les UE précédentes et suivantes (tant par le contenu enseigné que dans l'emploi du temps), à choisir les intervenants, à définir les évolutions de contenu et des méthodes pédagogiques employées ainsi que de vérifier les moyens techniques pour les enseignements (notamment la compatibilité des versions logicielles) mais également à organiser le contrôle des connaissances. Ces responsabilités ont cessées sur l'année 2019-2020 du fait de mon détachement au sein de l'université de Montpellier. Suite à mon intégration définitive au 1er septembre 2020, j'ai pris en charge l'organisation de 2 UE au sein de Polytech Montpellier.

TABLE 1.1 – Liste détaillée des unités d'enseignement dont j'ai été responsable.

Période	Unité d'Enseignement	Intitulé de la formation	Établissement
2020-	Informatique appliquée	EGC3	Polytech
2020-	Hydraulique à surface libre	EGC3	Polytech
2015-2019	Hydraulique à surface libre	Mastère EPA	ENGEES
2015-2019	Hydraulique générale et en charge	Mastère EPA	ENGEES
2014-2019	Projet aménagement de rivières	FI 1A	ENGEES
2012-2019	Modélisation avancée des inondations	FI et FIPA 3A	ENGEES
2015-2016	Projet Pluridisciplinaire	FI et FIPA 2A	ENGEES
2014-2017	Hydraulique générale, en charge et à surface libre	FOAD	ENGEES
2012-2016	Water supply networks	Master WEO	USTH
2010-2015	Modélisation des cours d'eau	FIPA 2A	ENGEES
2010-2015	Partial Differential Equations & modeling	Master MNI	UdS
2010-2014	Project M1S1	Master MNI	UdS

EGC : Formation par apprentissage *Eau et Génie Civil*
FI : Formation initiale
FIPA : Formation par apprentissage
FOAD : Formation ouverte à distance
Mastère EPA : Mastère spécialisé Eau Potable et Assainissement (formation niveau bac +6)
Master MNI : Master Modélisation Numérique en Ingénierie
Master WEO : Master Water Environment Oceanography
UdS : Université de Strasbourg
USTH : University of Sciences and Technologies of Hanoï

1.2.3 Responsabilités de recherche

Au sein du laboratoire Icube, j'ai été le responsable scientifique de l'axe de recherche sur les inondations urbaines qui regroupe 3 maîtres de conférences. Cette responsabilité a inclut la gestion du pilote Icube d'étude des inondations urbaines (voir section 6.1). J'ai également initié, au sein du laboratoire Icube, la thématique de recherche sur le transport solide en cours d'eau dans le cadre d'une collaboration avec le laboratoire Live (UMR 7362).

Par ailleurs, j'ai été responsable de 5 projets de recherche (en tant que porteur ou coordinateur de WorkPackage).

Enfin, je suis régulièrement rapporteur pour des revues scientifiques (2 à 3 par an) : Journal of Hydroinformatics, Advances in Water Resources, Environmental Modelling and Software, Journal of Hydrology.

Chapitre 2

Synthèse de mes activités d'enseignement

Résumé

- Volume annuel moyen : 315h eq. TD (18% CM, 29% TD et 53% TP/Projet) auprès de formations variées (48% niveau L3, 19% M1, 9% M2, 17% Mastère et 7% formations continues)
- Rédaction de 82 supports de cours (polycopiés, supports multimédia et présentations orales) - voir annexe A
- Responsable de 12 unités d'enseignement depuis 2010 (voir tableau 1.1)
- Encadrement de 7 apprentis-ingénieurs pendant leur cursus à l'ENGEES ou à Polytech et tutorat de 40 élèves-ingénieurs pendant leurs stages en entreprise
- Champs thématique : le cycle de l'eau (naturel et anthropique) et la modélisation

Depuis ma thèse, j'exerce des activités d'enseignements en parallèle de mes recherches. J'ai réalisé mes enseignements au sein de plusieurs établissements : l'université de Montpellier (Vacations de thèse, ATER et McF depuis 2019) et l'ENGEES (entre 2010 et 2019). La liste de mes enseignements, répartis par établissement et par champs disciplinaire, est disponible en annexe B.

2.1 Description de mes activités d'enseignement

Mes enseignements portent sur :

le cycle de l'eau (naturel et anthropique) en allant de la mécanique des fluides aux connaissances générales en sciences de l'eau (hydraulique en charge et à surface libre, hydrogéologie, hydrologie) jusqu'aux enseignements pratiques pour l'ingénieur (transport solide et dynamique fluviale, aménagement de cours d'eau et conception d'ouvrages de lutte contre les inondations, réalisation de Plan de Prévention du Risque Inondation, diagnostic et dimensionnement de réseaux d'eau potable, détermination de pluies et de débits de projet).

la modélisation avec les bases théoriques (analyse de fonctions, résolution d'équations différentielles : méthodes aux différences finies, aux volumes finis, aux éléments finis et spectrales, ...), leur application à la résolution de problèmes d'hydrologie et d'hydraulique (écrêtement d'hydrogramme, résolution de lignes d'eau en canal à surface libre, calcul des écoulements dans un réseau de conduite en charge) et l'utilisation de logiciels d'ingénierie pour la modélisation des cours d'eau en 1D et 2D (HECRas 1D et 2D), des aquifères (ASM Win, HPP Win), des réseaux d'eau potable (Porteau) et le calcul de débit à l'exutoire de bassin versant (GR4J).

Enseignements présentiels

Mes enseignements sont répartis de la Licence 1 au Mastère, incluant également des formations ouvertes à distance et des formations continues. Mes activités pédagogiques incluent des cours magistraux, des travaux

dirigés et pratiques ainsi que l'encadrement de projet (voir figure 2.1). Depuis 2010, le volume total de mes enseignements se porte en moyenne à 315h eq. TD avec une diminution à 200-250h sur les dernières années. Par ailleurs, mes enseignements ont fortement évolué ; en effet, je suis en charge d'une dizaine de cours actuellement et j'enseigne un cours pendant 3 à 4 ans en moyenne.

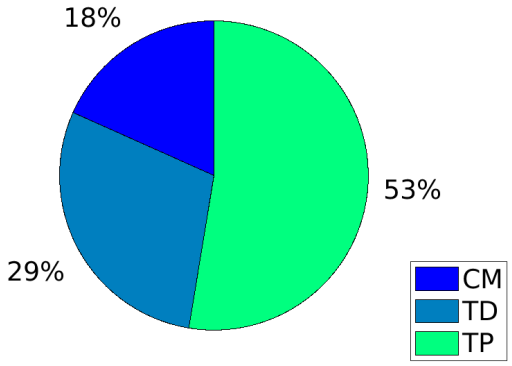

(a)

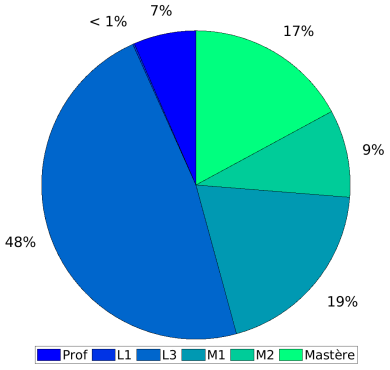

(b)

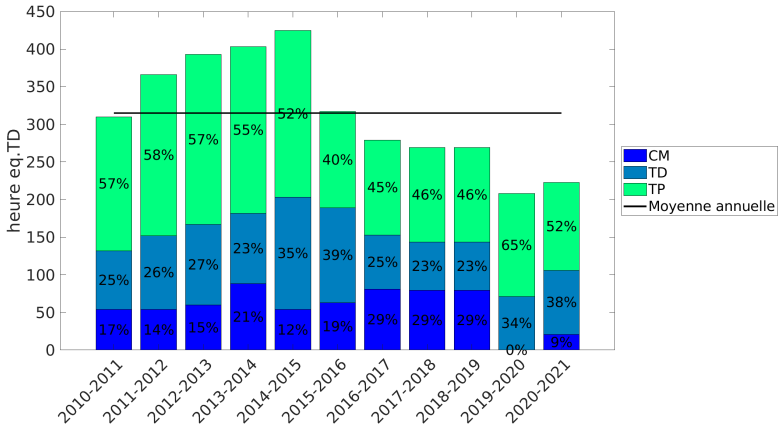

(c) L'absence de CM pour l'année 2019-2020 est liée à mon détachement au sein de l'université de Montpellier en septembre 2019.

FIGURE 2.1 – Répartition de mes enseignements depuis 2010. (a) Répartition entre CM, TD et TP/Projet (moyenne depuis 2010) ; (b) Répartition en fonction du niveau académique (moyenne depuis 2010) ; (c) Évolution de mon volume d'enseignement.

Autres activités pédagogiques

J'ai également en charge du suivi d'étudiants en stage (environ 40 tutorats depuis 2010) et de sept apprentis-ingénieurs (en moyenne 1 nouvel apprenti tous les deux ans). Ce suivi se fait sur l'ensemble de la scolarité à l'école (3 ans d'encadrement par apprenti). Il consiste en un accompagnement pour faire le lien entre l'école et l'entreprise et pour aider à la définition des sujets pour les projets et stages de l'apprenti.

2.2 Démarche pédagogique

Aujourd'hui, toutes mes activités d'enseignement sont réalisées au sein de Polytech Montpellier (départements Sciences et Technologies de l'Eau et Eau et Génie Civil ainsi que dans la formation de prépa intégrée Peip). Avant 2019, mes principales activités d'enseignement étaient réalisées au sein des formations de l'ENGEES mais j'intervenais également dans des formations d'autres établissements (Université de Strasbourg, École Nationale Supérieure d'Architecture de Strasbourg, INSA de Strasbourg, Université des Sciences et des Technologies de Hanoï, ...) pour me confronter à une diversité d'approches, d'objectifs et de parcours de formation. Cette expérience m'a été particulièrement utile pour me construire une démarche pédagogique propre.

L'ensemble des enseignements que je dispense est dans des formations à caractère professionnalisant. L'accent est donc mis sur les besoins du monde professionnel, soit par le choix d'exemples réels, soit par une mise en situation lors de projet, soit avec l'intervention de professionnels. Mon expérience de 4 ans au sein du bureau d'études Ginger Environnement & Infrastructures, les interactions que j'entretiens avec le monde professionnel (VNF, Ubertone, Saint-Gobain, Conseil Départemental 68, Artelia, Berest, ...) ainsi que les formations continues que je dispense (dont le public est principalement composé de professionnels en exercice) me permettent d'identifier clairement les situations auxquelles pourront être confrontés les futurs ingénieurs.

Autant que possible, j'essaye que mes enseignements forment un continuum entre bases théoriques, connaissances techniques et mise en situation professionnelle comme par exemple avec mes enseignements à l'ENGEES portant sur l'hydraulique, la modélisation et l'aménagement des cours d'eau et sur les réseaux d'eau potable. Cela me permet ainsi de garantir la cohérence entre tous les enseignements tout en introduisant une diversité d'approches pédagogiques à travers les différents intervenants en TD et/ou en projet.

Avec le temps, j'ai convergé vers un unique polycopié d'hydraulique pour toutes mes formations [1]. Pour cela, un effort de conceptualisation a du être mené afin qu'il soit accessible à tous les étudiants (du niveau L2 au Mastère et en formation continue). Dans chaque cursus, les objectifs de formation sont clairement présentés pour éviter toute ambiguïté sur les connaissances attendues et sur le niveau de précision requis. L'unicité du document me permet d'être plus efficace dans sa mise à jour et laisse l'opportunité aux apprenants de compléter leur formation en parallèle du cours ou même lors de leur vie professionnelle.

Ma participation active aux formations ouvertes à distance (Formation en hydraulique générale et Diplôme d'établissement "GEomatique et Métier de l'Eau") m'a permis de découvrir ce type de formation et de prendre conscience des différences essentielles dans la construction des activités pédagogiques par rapport aux approches d'enseignement en présentiel. En effet, le découpage de l'enseignement en grains élémentaires et la proposition d'activités de natures variées (présentation enregistrée, vidéo d'illustration, QCM d'autoévaluation, TD et corrections détaillées, ...) sont particulièrement nécessaires. Par ailleurs, ce type d'approche enrichit les enseignements en présentiel car cela permet de fournir des ressources d'autoformation pour compléter le cours.

2.3 Supports pédagogiques

En appui de mes enseignements, j'ai produit différents supports sous forme de polycopiés, d'activités multimédia (vidéo, QCM ou exercice) et de présentations orales (voir annexe A et synthèse dans le tableau 2.1). Ces supports sont conçus comme des éléments que les ingénieurs pourront conserver au long de leur

1. https://team.inria.fr/lemon/files/2019/11/Poly_Hydraulique_20192020_light.pdf

carrière afin de revoir ou d'approfondir certaines notions ou méthodologies. Certains éléments sont ainsi publiés en ligne[2].

TABLE 2.1 – Synthèse de mes publications d'enseignement

	Total
Polycopié	22
Activité multimédia	60

2. https://team.inria.fr/lemon/pfg_enseignement/

Chapitre 3

Synthèse de mes activités de recherche

Résumé

- Valorisation scientifique (voir section 3.1) :
  - 14 publications de rang A, 23 conférences avec actes et 7 articles de presse ou reportages publiés
  - 1 publication de rang A et 7 conférences avec actes soumises
  - 4 publications en cours de rédaction, dont 2 en premier auteur
- Principal concepteur et développeur de Flood1D2D (https://sourcesup.renater.fr/projects/flood1d2d/) ; co-développeur du code SW2D (https://sw2d.inria.fr/)
- Responsable scientifique de l'axe de recherche sur les inondations urbaines au laboratoire Icube
- Responsable de 5 projets de recherche (porteur ou coordinateur de WorkPackage), participation à 11 projets de recherche (voir section 3.2)
- Encadrement de 2 ingénieurs de recherche contractuels (voir section 3.3.3), 4 doctorants (voir section 3.3.1) et 13 stagiaires de Master (voir section 3.3.4)
- Participation à 3 jurys de doctorat (voir section 3.3.2)
- Membre du GIS Hydraulique pour l'Environnement et le Développement Durable (https://www.shf-hydro.org/8-presentation_du_gis_hed-100.html)
- Reviewer (2 à 3 par an) : Journal of Hydroinformatics, Advances in Water Resources, Environmental Modelling and Software, Journal of Hydrology.
- 8 collaborations (attestées par des communications scientifiques) : équipes du laboratoire Icube, monde industriel, collectivités territoriales et laboratoires locaux, nationaux et internationaux.

J'ai réalisé mes activités de recherche au sein de plusieurs établissements : le laboratoire HydroSciences Montpellier (UMR 5569, IRD UM CNRS) pour la préparation de mon doctorat et mon poste d'ATER ainsi que depuis 2019 et le laboratoire Icube (UMR 7357, CNRS ENGEES INSA UdS) entre 2010 et 2019. J'ai également intégré depuis octobre 2019 l'équipe-projet Lemon de l'INRIA Sophia Antipolis - Méditerranée (https://team.inria.fr/lemon/).

Ce chapitre présente mes activités de recherche de manière factuelle :

section 3.1 l'ensemble de mes publications,

section 3.2 les projets de recherche avec financement auxquels j'ai contribué,

section 3.3 l'encadrement de stagiaires et de doctorants

section 3.4 les collaborations productives

3.1 Communications scientifiques

Les résultats de mes recherches sont présentés dans 14 publications de rang A, 23 conférences avec actes et 7 articles de presse ou reportages (voir tableau 3.1). Actuellement, 11 autres communications à comité de

lecture sont en préparation : 1 ACL et 7 C-ACT soumis, ainsi que 4 publications en cours de rédaction (dont 2 que je porte en premier auteur).

TABLE 3.1 – Synthèse des communications scientifiques

Type de publication	Nombre
ACL - Articles avec comité de lecture (publiés ou acceptées)	14
C-ACT - Communications avec actes dans un congrès	23
Communications avec comité de lecture (soumis ou en préparation)	12
PV - Article de presse / reportage	7

3.1.1 Articles publiés ou acceptés dans des revues à comité de lecture (rang A)

Entre parenthèse sont indiqués les facteurs d'impact à 5ans des différents journaux.

ACL1. P. Finaud-Guyot, P.-A. Garambois, G. Dellinger, F. Lawniczak and P. François. *Experimental characterization of various scale hydraulic signatures in a flooded branched street network.* Urban Water Journal, 16(9) : 609-624, 2020. https://dx.doi.org/10.1080/1573062X.2020.1713173 (IF = 2.17)

ACL2. L. Pujol, P.-A. Garambois, P. Finaud-Guyot, J. Monnier, K. Larnier, R. Mosé, S. Biancamaria, H. Yesou, D. Moreira, A. Paris and S. Calmant. *Estimation of Multiple Inflows and Effective Channel by Assimilation of Multi-satellite Hydraulic Signatures : The Ungauged Anabranching Negro River.* Journal of Hydrology, 2020. https://doi.org/10.1016/j.jhydrol.2020.125331 (IF = 3.83)

ACL3. P.-A. Garambois, K. Larnier, J. Monnier, P. Finaud-Guyot, J. Verley, A.-S. Montazem and S. Calmant. *Variational estimation of effective channel and ungauged anabranching river discharge from multi-satellite water heights of different spatial sparsity.* Journal of Hydrology 581 : 124409, 2020. https://dx.doi.org/10.1016/j.jhydrol.2019.124409 (IF = 3.83)

ACL4. X. Li, S. Erpicum, M. Bruwier, E. Mignot, P. Finaud-Guyot, P. Archambeau, M. Pirotton, et B. Dewals. *Laboratory Modelling of Urban Flooding : Strengths and Challenges of Distorted Scale Models.* Hydrology and Earth System Sciences, 23 : 1567-1580, 2019. https://dx.doi.org/10.5194/hess-23-1567-2019 (IF = 5.46)

ACL5. A.-S. Montazem, P.-A. Garambois, S. Calmant, P. Finaud-Guyot, J. Monnier, D. M. Moreira, J. Minear and S. Biancamaria. *Wavelet-Based River Segmentation Using Hydraulic Control-Preserving Water Surface Elevation Profile Properties.* Geophysical Research Letters, 46(12) : 6534-6543, 2019. https://dx.doi.org/10.1029/2019GL082986 (IF = 5.10)

ACL6. P. Finaud-Guyot, P.-A. Garambois, Q. Araud, F. Lawniczak, P. François, J. Vazquez, and R. Mosé. *Experimental insight for flood flow repartition in urban areas.* Urban Water Journal, 15(3) :242–250, March 2018. https://dx.doi.org/10.1080/1573062X.2018.1433861 (IF = 2.17)

ACL7. Chen, P.-A. Garambois, P. Finaud-Guyot, G. Dellinger, R. Mosé, A. Terfous, and A. Ghenaim. *Variance based sensitivity analysis of 1D and 2D hydraulic models : An experimental urban flood case.* Environmental Modelling & Software, 109 :167–181, November 2018. https://dx.doi.org/10.1016/j.envsoft.2018.08.008 (IF = 5.32)

ACL8. P.-A. Garambois, S. Calmant, H. Roux, A. Paris, J. Monnier, P. Finaud-Guyot, A. S. Montazem, and J. Santos da Silva. *Hydraulic visibility : Using satellite altimetry to parameterize a hydraulic model of an ungauged reach of a braided river.* Hydrological Processes, 31(4) :756–767, February 2017. https://dx.doi.org/10.1002/hyp.11033 (IF = 3.08)

ACL9. A. Arrault, P. Finaud-Guyot, P. Archambeau, M. Bruwier, S. Erpicum, M. Pirotton, and B. Dewals. *Hydrodynamics of long-duration urban floods : experiments and numerical modelling.* Natural Hazards and Earth System Sciences Discussions, 16(6) :1–29, February 2016. https://dx.doi.org/10.5194/nhess-16-1413-2016 (IF = 3.28)

ACL10. Q. Araud, P. Finaud-Guyot, V. Guinot, R. Mosé, and J. Vazquez. *An eigenvector-based linear reconstruction approach for time stepping in discontinuous Galerkin scheme used to solve shallow water equations.* International Journal for Numerical Methods in Fluids, 70(12) :1590–1604, December 2012. https://dx.doi.org/10.1002/fld.3645 (IF = 1.64)

ACL11. P. Finaud-Guyot, C. Delenne, V. Guinot, and C. Llovel. *1d-2d coupling for river flow modeling.* Comptes Rendus Mécanique, 339(4) :226–234, 2011. https://dx.doi.org/10.1016/j.crme.2011.02.00 (IF = 1.44)

ACL12. P. Finaud-Guyot, C. Delenne, and V. Guinot. *Coupling of 1d and 2d models for river flow modelling.* La Houille Blanche, (3) :23–28, 2011. https://dx.doi.org/10.1051/lhb/2011028 (IF = 0.21)

ACL13. C. Delenne, P. Finaud-Guyot, V. Guinot, and B. Cappelaere. *Sensitivity of the 1d shallow water equations with source terms : Solution method for discontinuous flows.* International Journal for Numerical Methods in Fluids, 67(8) :981–1003, 2010. https://dx.doi.org/10.1002/fld.2398 (IF = 1.64)

ACL14. P. Finaud-Guyot, C. Delenne, J. Lhomme, V. Guinot, and C. Llovel. *An approximate-state Riemann solver for the two-dimensional shallow water equations with porosity.* International Journal for Numerical Methods in Fluids, 62(12) :1299-1331, 2010. https://dx.doi.org/10.1002/fld.2066 (IF = 1.64)

3.1.2 Conférences internationales et nationales avec actes

C-ACT1. M. Koehl, G. Piasny, V. Thomine, P.-A. Garambois, P. Finaud-Guyot, S. Guillemin and L. Schmitt. *4D GIS for monitoring river bank erosion at meander bend scale : case of Moselle River.* In International Archives of the Photogrammetry, Remote Sensing and Spatial Information Sciences - ISPRS Archives, Vol 44, pages 63–70, 2020. https://doi.org/10.5194/isprs-archives-XLIV-4-W1-2020-63-2020

C-ACT2. V. Ayoub, C. Delenne, P. Matgen, P. Finaud-Guyot and R. Hostache. *Towards fast large-scale flood simulations using 2D Shallow water modelling with depth-dependant porosity.* RiverFlow 2020, Delft, Netherlands, 2020.

C-ACT3. X. Li, S. Erpicum, E. Mignot, M. Bruwier, P. Finaud-Guyot, P. Archambeau, M. Pirotton and B. Dewals. *Uncertainties in laboratory modelling of urban flooding.* EGU general assembly, april 2019, Austria.

C-ACT4. P.-A. Garambois, K. Larnier, L. Pujol, P. Finaud-Guyot, A. S. Montazem, J. Monnier, S. Biancamaria and S. Calmant. *Inference of complex and spatially distributed braided river channels parameters and inflows discharges by assimilation of historical altimetric time series and forthcoming SWOT data.* EGU general assembly, april 2019, Austria.

C-ACT5. A. Ghenaim, P. Finaud-Guyot, P.-A. Garambois, A. Terfous, J. Vazquez and R. Mosé. *Experimental characterization of hydraulic signature of an urban geometry during floods.* 4th International Conference on Water Resources (ICWR-2018), November 2018, Malaisie.

C-ACT6. P. Finaud-Guyot, P.-A. Garambois, S. Chen, G. Dellinger, A. Ghenaim, and A. Terfous. *1d/2d porosity model for urban flood modeling : case of a dense street networks.* In A. Paquier and N. Rivière, editors, E3S Web of Conferences, volume 40, page 06010, Lyon, France, 2018. https://doi.org/10.1051/e3sconf/20184006010

C-ACT7. A. S. Montazem, P.-A. Garambois, P. Finaud-Guyot, K. Larnier, J. Monnier, and S. Calmant. *Hydraulic visibility and decomposition of river flow state variables from remote sensing in various hydro-geomorphological contexts.* Remote Sensing and Hydrology Symposium (ICRS-IAHS), May 2018, Cordoba, Spain.

C-ACT8. P.-A. Garambois, K. Larnier, L. Pujol, J. Verley, P. Finaud-Guyot, A. Montazem, J. Monnier, S. Biancamaria and S. Calmant. *Inference of complex river channels parameters and distributed discharges from historical altimetric time series and forthcoming SWOT data.* AGU fall meeting, 2018, Washington DC.

C-ACT9. F. Saleh, S. Biancamaria, P.-A. Garambois, V. Ramaswamy, and P. Finaud-Guyot. *Combining satellite measurements and numerical flood prediction models to save life and properties from flooding.* AGU fall meeting, New-Orleans, 2017.

C-ACT10. S. Chen, P.-A. Garambois, P. Finaud-Guyot, G. Dellinger, A. Terfous, and A. Ghenaim. *Sensitivity analysis of urban flood flows to hydraulic controls.* In EGU General Assembly Conference Abstracts, volume 19, page 1711, 2017.

C-ACT11. P. Archambeau, M. Bruwier, P. Finaud-Guyot, S. Erpicum, M. Pirotton, and B. Dewals. *Lessons learned from combined experimental and numerical modelling of urban floods.* In EGU General Assembly Conference Abstracts, volume 19, page 8664, 2017.

C-ACT12. D. Eschbach, F. Longchampt, L. Schmitt, M. Tremolieres, J.-N. Beisel, P. Finaud-Guyot, S. Payraudeau, S. Weill, G. Imfeld, P. Grussenmeyer, M. Koehl, and S. Guillemin. *Restauration fonctionnelle de l'hydrosystème de la Réserve Naturelle de l'île du Rohrschollen (Rhin supérieur, Bas-Rhin – LIFE08 NAT/F/00471).* Strasbourg, France, March 2015.

C-ACT13. D. Eschbach, L. Schmitt, M. Tremolieres, C. Grac, P. Finaud-Guyot, J.-N. Beisel, S. Weill, S. Payraudeau, G. Imfeld, and P. Grussenmeyer. *Functional restoration of a Rhine anastomosing channel : temporal trajectory, initial state, post-restoration monitoring, modelling (Upper Rhine, France, Rohrschollen island).* Lyon, France, 2015. GRAIE.

C-ACT14. D. Eschbach, L. Schmitt, M. Tremolieres, J.-N. Beisel, C. Grac, P. Finaud-Guyot, S. Payraudeau, S. Weill, G. Imfeld, and P. Grussenmeyer. *Functional hydromorphological restoration of a Rhine anastomosing channel (Upper Rhine, France) : implications of the temporal trajectory and inter-disciplinary monitoring for evaluating pre-restoration state.* Paris - La défense, France, December 2014.

C-ACT15. D. Eschbach, F. Longchampt, L. Schmitt, M. Tremolieres, C. Grac, J.-N. Beisel, and P. Finaud-Guyot. *Restauration fonctionnelle d'une annexe hydraulique rhénane : le Bauerngrundwasser sur l'île du Rohrschollen (LIFE08 NAT/F/000471).* 2014.

C-ACT16. Q. Araud, P. Finaud-Guyot, F. Lawniczak, P. François, J. Vazquez, and R. Mosé. *Modeling flood in an urban area : Validation of numerical tools against experimental data.* In Advances in Hydroinformatics, pages 207–220. Springer, 2014.

C-ACT17. J. Laurent, P. Finaud-Guyot, A. Wanko Ngnien, and R. Mosé. *Hydrodynamic of artificial wetlands at the outlet of urban catchment : complementarity of the systemic approach and computational fluid dynamics tools.* Lyon, France, October 2013. SFGP.

C-ACT18. D. Eschbach, L. Schmitt, A. Zimmermann, Q. Lejeune, and P. Finaud-Guyot. *Evaluating a functional hydromorphological restoration of a lateral channel of the Upper Rhine (France) : first results and implications of the temporal trajectory to restoration sustainability.* In 8th IAG-International Conference on Geomorphology" Geomorphology and sustainability", 2013.

C-ACT19. J. Laurent, N. Duclos, P. Finaud-Guyot, A. Wanko Ngnien, and R. Mosé. *Multi-traçage pour l'évaluation du fonctionnement hydrodynamique de zones humides artificielles à l'exutoire d'un bassin versant urbain.* Aix en Provence, France, October 2012.

C-ACT20. Q. Araud, P. Finaud-Guyot, V. Guinot, R. Mosé, and J. Vazquez. *Exploration of different methods to calculate the flux at the interface of a discontinuous galerkin scheme to solve the shallow water equations.* Hamburg, Germany, June 2012.

C-ACT21. Q. Araud, P. Finaud-Guyot, R. Mose, J. Vazquez, S. Isel, and V. Guinot. *Simplified Discontinuous Galerkin Schemes for Shallow Water Simulations.* In Proceedings of the 34th World Congress of the International Association for Hydro-Environment Research and Engineering : 33rd Hydrology and Water Resources Symposium and 10th Conference on Hydraulics in Water Engineering, page 4008. Engineers Australia, 2011.

C-ACT22. P. Finaud-Guyot, C. Delenne, and V. Guinot. *Coupling of 1d and 2d models for river flow modeling.* In Proceedings of simHydro 2010 - hydraulic modeling and uncertainties, 2010.

C-ACT23. C. Delenne, P. Finaud-Guyot, V. Guinot, and B. Cappelaere. *Empirical versus Direct sensitivity computations : application to the shallow water equations.* In Proceedings of simHydro 2010 - hydraulic modeling and uncertainties, 2010.

3.1.3 Articles soumis / en préparation

ACLprep1. L. Mimeau, Y. Tramblay, L. Brocca, C. Massari, S. Camici and P. Finaud-Guyot. *Sensitivity analysis of soil moisture to precipitation and temperature variability in the Mediterranean region.* Hydrology and Earth System Sciences, in review, 2020. https://doi.org/10.5194/hess-2020-302

ACLprep2. V. Guinot and P. Finaud-Guyot. *Local downscaling of shallow water simulations.* Submitted to Simhydro 2021 - 6th International Conference, Sophia Antipolis, France.

ACLprep3. C. Choley, P. Finaud-Guyot, G. Dellinger and R.Mosé. *Towards a discharge law to characterize street-building exchanges during urban floods.* Submitted to Simhydro 2021 - 6th International Conference, Sophia Antipolis, France.

ACLprep4. C. Choley, P. Finaud-Guyot, P.-A. Garambois and R.Mosé. *An effective urban flood model accounting for street-building exchanges.* Submitted to Simhydro 2021 - 6th International Conference, Sophia Antipolis, France.

ACLprep5. V. Montoya, C. Delenne, P. Finaud-Guyot, R. Hostache. *How to optimally represent riverbed geometry with a simplified cross-section shape in shallow water models ?* Submitted to Simhydro 2021 - 6th International Conference, Sophia Antipolis, France.

ACLprep6. V. Ayoub, C. Delenne, R. Hostache and P. Finaud-Guyot. *Contribution of a depth-dependent porosity model for the rapid simulation of flood inundations.* Submitted to Simhydro 2021 - 6th International Conference, Sophia Antipolis, France.

ACLprep7. J. G. Caldas Steinstraesser, C. Delenne, P. Finaud-Guyot, V. Guinot, J. L. Kahn Casapia, A. Rousseau. *SW2D-LEMON : a new software for upscaled shallow water modeling.* Submitted to Simhydro 2021 - 6th International Conference, Sophia Antipolis, France.

ACLprep8. L. Pujol, P.-A. Garambois, J. Monnier, P. Finaud-Guyot, K. Larnier and R. Mosé. *Integrated hydraulic-hydrological assimilation chain : towards multisource data fusion from river network to headwaters.* Submitted to Simhydro 2021 - 6th International Conference, Sophia Antipolis, France.

ACLprep9. P. Finaud-Guyot, Garambois P.-A. and Chen S. *1D/2D porosity-like model for urban flood modeling.* In preparation.

ACLprep10. P. Finaud-Guyot and V. Guinot. *Local downscaling of shallow water simulations.* In preparation.

ACLprep11. V. Ayoub, C. Delenne, R. Hostache and P. Finaud-Guyot. *Potential of porosity-based model for 2D large scale flood modeling.* In preparation.

ACLprep12. C. Choley, P. Finaud-Guyot, P.-A. Garambois and R.Mosé. *Characterization of the various scale effect of the street-building exchange on urban flood.* In preparation.

3.1.4 Vulgarisation scientifique

PV1. Les inondations en milieu urbain - Interview de R. Mosé. Emission Télématin Sciences sur France 2 - 05/06/2018. https://www.france.tv/france-2/telematin/528895-sciences-les-inondations-en-milieu-urbain.html

PV2. Demey, J. Le logiciel qui aide à prévenir les inondations - Interview de P. Finaud-Guyot. Le Journal du Dimanche - 28/01/2018. https://www.lejdd.fr/societe/le-logiciel-qui-aide-a-prevenir-les-inondations-3558503

PV3. Interview télévisée de G. Piasny et L. Schmitt. Journal du soir sur France 3 Lorraine 23/01/2018. https://france3-regions.francetvinfo.fr/grand-est/emissions/jt-1920-lorraine

PV4. Inondations en Lorraine : quand la science se sert des crues - Interview de G. Piasny et L. Schmitt. Emission télévisée de Mirabelle TV - 23/01/2018 https://www.mirabelle.tv/inondations-en-moselle-quand-la-science-se-sert-des-crues/

PV5. Les innovations anti-inondations - Interview de R. Mosé. Emission FuturMag sur Arté - 01/05/2016. https://davidpaturel.wordpress.com/2016/05/01/arte-futuremag-les-innovations-anti-innondations-realisation/

PV6. Diguet, A. 2015. Une maquette géante pour comprendre les inondations. Le Journal du CNRS - 24/11/2015. https://lejournal.cnrs.fr/diaporamas/une-maquette-geante-pour-comprendre-les-inondations

PV7. L'étude des crues en milieu urbain - Interview télévisée de R. Mosé et P. Finaud-Guyot. Emission Lab20 sur Alsace20 - 06/12/2013.

3.2 Liste des projets de recherche financés

3.2.1 Projets que je porte

2019-2022 Projet ANR DEUFI - Étude numérique et expérimentale des inondations urbaines : influence des échanges avec le bâti (ANR-18-CE01-0020)
porteur : A. Paquier, IRSTEA Lyon
financement Icube : 178k€
partenaires : IRSTEA Lyon, laboratoire Icube, LMFA, GRED, Cerema, Artelia, G-Eau, Université de Liège HECE, Korea Institute of Civil Engineering and Building Technology

2017-2021 Projet *Moselle sauvage - Étude hydromorphologique de la Moselle sauvage, modélisation de tendances évolutives futures et proposition de scénarios de gestion*
Porteurs : L. Schmitt (laboratoire LIVE), P. Finaud-Guyot (laboratoire Icube), P.-A. Garambois (laboratoire Icube)
financement Agence de l'eau Rhin Meuse (315k€) et 1/2 bourse doctorale région Grand Est (50k€)

2017-2018 Projet Interne Icube - *Développement d'un outil de Simulation des Inondations Réelles : apport de la parallélisation et des techniques de maillage adaptatif*
porteur : P. Finaud-Guyot (laboratoire Icube)
financement : 8k€

2015 Projet du Conseil Scientifique de l'ENGEES - *Investigation expérimentale des inondations urbaines*
porteur : P. Finaud-Guyot (laboratoire Icube)
financement : 5k€

2014-2015 Projet IDEX CNRS - MODELROH - MODELisation interdisciplinaire d'une restauration fonctionnelle d'un hydrosystème fluvial ; bénéfices et risques (l'île du ROHrschollen, Strasbourg)
porteur : L. Schmitt (laboratoire LIVE)
financement Icube : 7k€
partenaires : Laboratoires LIVE, LHYGES et Icube

3.2.2 Autres projets auxquels je participe

2021-2022 Projet KimWaters Phase 2 - *ActNAO - Les normes hydrologiques face aux non-stationnarités en Afrique de l'Ouest*
porteur : V. Borrell, A. Ogilvie et J.E. Paturel

2018-2021 Projet Luxembourg FNR CASCADE - *Combining earth observation with a large scale model cascade for assessing flood hazard at high spatial resolution*
porteur : R. Hostache (LIST)

2018-2019 Projet TOSCA du CNES - *Estimation des débits de cours d'eau avec le satellite SWOT (Surface water and Ocean topography, CNES/NASA)*
porteur : J.F. Crétaux (LEGOS)
financement Icube : 20k€
partenaires : IMFT, Laboratoire Icube, IMT, LEGOS LNHE, IRSTEA

2017-2019 Projet *Thomas Jefferson Fund - Combining Satellite Measurements and Numerical Flood Prediction Models to Save Lives and Property from Flooding : The New York Metropolitan Area Test Bed*

porteurs : F. Saleh (Stevens Institute NYC) et P.-A. Garambois (laboratoire Icube)
financement Icube : 10k€
partenaires : laboratoire Icube, Stevens Institute NYC

2017-2018 Projet Interne Icube - Caractérisation Expérimentale et Numérique des Inondations Urbaines en régime stationnaire et transitoire
porteur : G. Dellinger (laboratoire Icube)
financement Icube : 8k€

2011-2012 Projet EC2CO - *Risque associé au transfert de polluants lors d'une inondation urbaine : une approche expérimentale et numérique*
porteur : E. Mignot (LMFA)
financement Icube : 41k€
partenaires : LMFA (UMR 5509), LGCIE (Equipe d'accueil 4126), IMFS (UMR 7507)

3.3 Encadrement de la recherche

3.3.1 Encadrement de thèses - 3 soutenues

2019-... C. Choley. Etude expérimentale et numérique des échanges rue-bâti lors d'inondations urbaines. Université de Strasbourg.
Directeur : R. Mosé (PR, ENGEES - Icube) à 10%
Encadrant : P. Finaud-Guyot (90%)
Financement ANR DEUFI
Communications scientifiques associées (voir section 3.1) : ACLprep12, ACLprep4, ACLprep3.

2019-... L. Pujol. *Synergie optimale de données télédétectées et multicapteurs et pour la modélisation cartographique d'hydrosystèmes complexes.* Université de Strasbourg.
Directeurs : J. Monnier (PR, INSA - IMT) (20%) et R. Mosé (PR, ENGEES - Icube) (10%)
Encadrants : P.-A. Garambois (Mcf, INSA - Icube) (70%)
Participation à l'encadrement
Financement CNES - Icube
Communications scientifiques associées (voir section 3.1) : C-ACT4, C-ACT8, ACL2, ACLprep8.

2018-... G. Piasny. *Étude hydromorphologique de la Moselle sauvage, modélisation de tendances évolutives futures et proposition de scénarios de gestion* Université de Strasbourg.
Directeur : L. Schmitt (PR, Université de Strasbourg - LIVE) (33%)
Encadrants : P.-A. Garambois (Mcf, INSA - Icube) (33%) et P. Finaud-Guyot (33%)
Financement : Agence de l'eau Rhin Meuse et région Grand Est
Communications scientifiques associées (voir section 3.1) : PV3, PV4, C-ACT1.

2017-2019 A. Montazem. *Représentation et segmentation hydraulique effective de rivières à l'échelle globale pour le calcul de débit par altimétrie SWOT.* Université Paul Sabatier (Toulouse).
Directeur : S. Calmant (DR, IRD - LEGOS)
Encadrant : P.-A. Garambois (Mcf, INSA - Icube)
Participation à l'encadrement
Financement : bourse CNES-Université Paul Sabatier (Toulouse)
Devenir post-thèse : Post-doc au Laboratoire d'Etudes en Géophysique et Océanographie Spatiales (UMR 5566)
Communications scientifiques associées (voir section 3.1) : ACL5, ACL8, C-ACT4, C-ACT7, C-ACT8.

2014-2018 S. Chen. *Effective shallow water models for complex flood flow patterns in urban areas - Modèle effectif par une approche de Saint-Venant pour les écoulements complexes lors d'inondations urbaines.* Université de Strasbourg.

Directeurs : A. Ghenaïm (PR, INSA - Icube) (10%), A. Terfous (MCf INSA - Icube) (10%)
Encadrants : P.-A. Garambois (Mcf, INSA - Icube) (40%) et P. Finaud-Guyot (40%)
Financement : Chinese Scholarship Council
Devenir post-thèse : Post-doc au College of Civil Engineering and Architecture, Zhejiang University (China)
Communications scientifiques associées (voir section 3.1) : ACL7, C-ACT6, C-ACT10, ACLprep9.

2010-2012 Q. Araud. *Simulations des écoulements en milieu urbain lors d'un événement pluvieux extrême.* Université de Strasbourg.
Directeurs : R. Mosé (PR, ENGEES - Icube) (33%), J. Vazquez (PR, ENGEES - Icube) (33%)
Encadrant : P. Finaud-Guyot (33%)
Devenir post-thèse : Ingénieur chargé d'étude à Hydratec Strasbourg
Communications scientifiques associées (voir section 3.1) : ACL6, ACL10, C-ACT16, C-ACT20, C-ACT21.

3.3.2 Participation à des jurys de thèses

2018 S. Chen. *Effective shallow water models for complex flood flow patterns in urban areas - Modèle effectif par une approche de Saint-Venant pour les écoulements complexes lors d'inondations urbaines.* Université de Strasbourg.
Encadrant de thèse

2017 M. Xiao. *Experimental and Numerical Study of Open Channel Intersections.* École centrale de Lyon.
Examinateur

2012 Q. Araud. *Simulations des écoulements en milieu urbain lors d'un événement pluvieux extrême.* Université de Strasbourg.
Encadrant de thèse

3.3.3 Encadrement de contractuels de recherche

2017-2018 L. Pujol - ingénieur de recherche au laboratoire Icube
Financement : Tosca CNES
Travaux de tests d'algorithmes d'inversions de débits à partir de données satellitaires sur le bassin de l'Amazone ; analyse des jeux de données hydrauliques
Co-encadrement (50%) avec P.-A. Garambois (Mcf, INSA - Icube)

2017-2018 G. Piasny - ingénieur de recherche aux laboratoires Icube et LIVE
Financement : Région Agence de l'Eau Rhin Meuse
Modélisation (1D, 2D) du transport solide et de l'évolution morphologique du Rohrschollen (Rhin Strasbourg), acquisition de données géomorphologiques sur la Moselle sauvage (Bayon).
Co-encadrement (33%) avec P.-A. Garambois (Mcf, INSA - Icube) et L. Schmitt (PR, UdS - LIVE)

3.3.4 Liste des stages encadrés

3.3.4.1 Stage de M2

1. Montoya V., 2020. *Apport des approches à porosité pour la modélisation rapide de grandes zones d'inondation.* Travail de Fin d'Études. Polytech Montpellier. Co-encadrement à 50%. Communication scientifique associée (voir section 3.1) : ACLprep5.
2. Dahik C., 2018. *Procédure de remaillage adaptatif pour la simulation d'écoulements.* Master 2 Calcul scientifique et mathématiques de l'information. Université de Strasbourg. Co-encadrement à 50%. Actuellement en thèse de doctorat au sein de l'institut FEMTO-ST (UMR 6174).

3. Payet T., 2018. *Étude numérique et expérimentale des inondations urbaines en régime permanent et transitoire*. Travail de Fin d'Études. ENGEES. Co-encadrement à 33%. Actuellement Ingénieur
4. Velten J. 2018. *Étude expérimentale du transport solide au droit d'ouvrages dans des écoulements à forte pente*. Travail de Fin d'Études. ENGEES. Participation à l'encadrement. Stage réalisé en collaboration avec l'ONF - Restauration des Terrains de Montagne. Actuellement Ingénieur de projet à Safege Consulting
5. Piasny G. 2016. *Modélisation hydrosédimentaire de l'hydrosystème fluvial de l'île du Rohrschollen*. Master 2 Sciences de l'Eau et de l'Environnement. Université François Rabelais de Tours. Co-encadrement à 50%. Actuellement en thèse de doctorat au laboratoire Live de Strabourg.
6. Bessard T., 2014. *Suivi scientifique d'un projet de restauration d'un bras du Rhin par la ville de Strasbourg - Modélisation hydrosédimentaire du BauernGrundWasser*. Travail de Fin d'Études. ENGEES. Encadrement à 100%. Actuellement Ingénieur programmeur chez Sopra Steria.
7. Hemmerlé N., 2011. *Comparaison des logiciels Mike 11 et SW2D pour la modélisation du pilote inondation de l'IMFS*. Master 2 Ingénierie et Sciences pour l'Environnement. Université de Strasbourg. Co-encadrement à 70%.
8. Jest J., 2011. *Comparaison des logiciels HECRas et Telemac pour la modélisation du pilote inondation de l'IMFS*. Master 2 Mécanique Numériques en Ingénierie. Université de Strasbourg. Co-encadrement à 70%. Actuellement Ingenieur chez Gaggenau Industrie.
9. Poglio J., 2011. *Protection du pont-rail "Millepattes" à Mulhouse (68) sur le canal de décharge de l'Ill contre d'accumulation des embâcles*. Travail de Fin d'Études. ENGEES. Co-encadrement à 50%. Actuellement Responsable MOE chez SNCF Réseau.

3.3.4.2 Stage de M1

1. Bloch H., 2017. *Développement d'une procédure de remaillage pour la modélisation des inondations*. Master 1 en Calcul Haute Performance. Université de Lille. Co-encadrement à 50%.
2. Jimenez Huidobro C., 2016. *Développement d'une méthodologie de calibration pour la simulation d'inondations urbaines*. Stage Pratique de l'Ingénierie. ENGEES. Encadrement à 100%.
3. Suzuki R., 2015. *Implémentation d'un modèle de turbulence pour la simulations d'inondations urbaines*. Master 1. Hokkaido University (Japon). Encadrement à 100%.
4. Granzotto R., 2009. *Développement d'une interface graphique pour une chaîne logicielle de calcul*. Stage d'ingénieur IG. Polytech Montpellier. Co-encadrement à 50%.

3.3.4.3 Autre

1. Bastide Y., 2019. *Modèles à porosité pour la simulation du ruissellement en milieu agricole*. Projet de Fin d'Etude STE. Polytech Montpellier. Encadrement à 50%.
2. Dominguez R., 2016. *Changement d'échelle pour la modélisation des inondations urbaines*. Projet de Fin d'Etude STE. Polytech Montpellier. Encadrement à 50%.
3. Poletti C., 2019. *Analyse de sensibilité d'un modèle 2D à porosité variable pour la modélisation des inondations à large échelle*. Projet Industriel de Fin d'Etude STE. Polytech Montpellier. Encadrement à 50%.
4. Camus V., 2016. *Conception d'un algorithme de reconstitution de la géométrie du pilote Icube*. Stage de L2. IUT Louis Paster - Strasbourg. Co-encadrement à 50%.
5. Macler L., 2012. *Conception d'un algorithme de déplacement optimisé pour le pilote inondation Icube*. Stage de L3. IUT Louis Pasteur - Strasbourg. Co-encadrement à 50%.
6. Benoist S. et Miquel F., 2010. *Réalisation d'une interface graphique pour le logiciel de modélisation hydrodynamique SW2D*. Projet de Fin d'Étude IG. Polytech Montpellier. Co-encadrement à 50%.

7. Bernard E., 2009. *Modélisation hydraulique à surface libre : calage et validation du code de calcul SW12D*. Projet de Fin d'Etude STE. Polytech Montpellier. Encadrement à 100%.

Les projets de fin d'étude sont des projets de longues durées (2 mois) effectués en dernière année d'école d'ingénieur (équivalent M2). Les étudiants mènent un projet industriel ou de recherche.

3.4 Collaborations

Mes activités de recherche ont permis de renforcer ou de créer plusieurs collaborations locales à internationales mais également avec le monde industriel. Par soucis de concision, seules les collaborations attestées par une communication scientifique sont présentées ici (voir tableau 3.2).

TABLE 3.2 – Synthèse des collaborations productives

Collaboration	Projet associé (voir section 3.2)	Communications
Icube, LIVE	Moselle Sauvage	C-ACT1
Icube, LIVE et LHYGES	IDEX CNRS - MODELROH	C-ACT12, C-ACT13, C-ACT14, C-ACT15, C-ACT18
Icube, IMFT, IMT, LEGOS LNHE, IRSTEA	Tosca CNES	ACL2,ACL3, ACL5, ACL8,C-ACT4, C-ACT7
Icube, Stevens Institute of technology (USA)	Thomas Jefferson Fund	C-ACT9
HydroSciences Montpellier, Luxembourg Institute of Science and Technology (Luxembourg)	Cascade	C-ACT2,ACLprep11
HydroSciences Montpellier, Research institute for geo-hydrological protection (Italy)		ACLprep1
Icube, Hydraulics in environmental and civil engineering - University of Liège (Belgium)	ANR DEUFI	ACL4, ACL9, C-ACT3, C-ACT11.
Icube, HydroSciences Montpellier		ACL10, C-ACT20, C-ACT21, ACLprep12, ACLprep4, ACLprep3

Chapitre 4

Activités d'expertise

Depuis ma thèse financée par une bourse CIFRE, j'ai réalisé différentes études d'ingénierie en tant que salarié du bureau d'études Ginger Environnement & Infrastructures. En parallèle de mes activités d'enseignement et de recherche, j'ai maintenu mes relations avec le monde industriel à travers des activités d'expertise. Les fonds dégagés par ces études ont permis de financer des actions de recherche : maintenance du pilote Icube d'étude des inondations, achat de matériel expérimental, recrutement de stagiaires et participation à des colloques.

2018 Expertise auprès du tribunal administratif de Chalons en Champagne

2016-2017 Contrat d'expertise R&D Ubertone (2.2k€)
- Étalonnage de sondes Doppler en veine hydraulique

2011-2013 Contrat d'expertise R&D Saint-Gobain, Pont-A-Mousson (25k€)
- Développement d'un logiciel de modélisation d'organes de coulée pour la réalisation de tuyaux en fonte

Pendant le doctorat (2007-2009) Études d'ingénierie réalisée pour la société Ginger Environnement & Infrastructures
- Étude d'impact de la modification d'une digue sur la commune de Thuir (66) : *Modélisation bidimensionnelle (SW2D) des écoulements de l'Adou en période de crue ; Étude d'impact de la reprise d'une digue*
- Modélisation de l'impact de la construction d'un remblai en lit majeur du Rhône à Port-Saint-Louis-du-Rhône (06) : *Modélisation bidimensionnelle (SW2D) des écoulements du Rhône pour une crue centennale au niveau de l'embouchure ; Étude d'impact de la mise en place d'un remblai dans le champ d'expansion de crue*
- Modélisation de la zone inondable du secteur aval du ruisseau des Aygalades de Marseille, propositions d'aménagements complémentaires et étude du ruissellement urbain : *Modélisation bidimensionnelle (SW2D) des inondations pour la crue centennale du ruisseau des Aygalades et du ruisseau de Plombières dans un contexte urbain ; Analyse de l'impact de plusieurs projets d'aménagement ; Modélisation bidimensionnelle (SW2D) du ruissellement urbain ; Proposition d'aménagements complémentaires en vue de la réduction du risque inondation et pluvial*

Deuxième partie

Activités de recherche : étude expérimentale et numérique des inondations urbaines

Chapitre 5

Introduction

La croissance démographique mondiale induit une urbanisation toujours plus importante, notamment à proximité des cours d'eau [50]. La vulnérabilité des populations et des biens aux inondations est ainsi accrue. Par ailleurs, l'urbanisation modifie les paysages et les sols et impacte ainsi le cycle hydrologique et l'aléa inondation. La connaissance des inondations et de leurs impacts est aujourd'hui un élément prépondérant d'aide à la décision vis à vis des politiques d'aménagement du territoire. Les cartes d'aléas sont ainsi fréquemment produite à travers la modélisation numérique des écoulements.

Les modèles mathématiques permettant de décrire les principaux processus intervenant lors d'inondations sont connus depuis le XIXe siècle avec les équations de Navier-Stokes. Dans des configurations simples et/ou idéalisées, les différents termes de ce modèle sont relativement bien connus et les équations peuvent être résolues simplement. Pour reproduire des inondations urbaines réelles, la paramétrisation de la variabilité des phénomènes nécessiterait d'appréhender les lois physiques (description de la turbulence, représentation de la vitesse en proche paroi, ...) avec un nombre déraisonnable de paramètres et/ou d'accéder à des données in-situ à forte résolution spatio-temporelle. A l'aide d'hypothèses simplificatrices, un nombre important de modèles mathématiques ont été proposés à partir du modèle de Navier-Stokes en vue d'applications spécifiques ou pour être en cohérence avec les moyens de l'époque (disponibilité des données et puissances de calcul). Ce nombre est encore accru lorsque l'on confond le modèle mathématique décrivant la physique du problème considéré et la méthode numérique (voire l'outil numérique) employée.

La démocratisation de l'accès à des puissances de calcul grandissantes, l'importance du nombre d'outils de modélisation (combinaison d'un/de modèle(s) mathématique(s) et de l'approche numérique de résolution) et la demande grandissante pour une description précise des aléas conduisent à ignorer les limitations spécifiques à chaque outil (par méconnaissance des hypothèses mathématiques et numériques et/ou de la complexité physique du problème modélisé). L'hydrologie urbaine n'échappe pas à cette constatation. En effet, les outils de modélisation disponibles n'ont généralement pas été développés pour de telles configurations et les données nécessaires, ne serait-ce que pour représenter précisément la topographie, sont souvent inaccessibles ou inexistantes.

Ainsi, la modélisation des inondations urbaines est souvent une tautologie dans le sens où on présuppose que les phénomènes physiques modélisés sont correctement décrits par un modèle mathématique (sans que cela ai toutefois pu être démontré) et le fait que les résultats de cette modélisation correspondent au modèle mathématique employé suffit pour le valider comme étant un bon descripteur de la réalité physique. On oublie ainsi que plusieurs modèles mathématiques (a fortiori numérique) sont parfois capable de produire les mêmes résultats sans que l'on ne puisse déterminer lequel est le plus réaliste en particulier avec peu de données in-situ de validation. Une meilleure caractérisation de l'hydrodynamique des inondations urbaines apparaît donc comme essentielle pour déterminer plus précisément les configurations d'écoulement rencontrées. Ces données doivent permettre de déterminer l'ordre d'importance des phénomènes physiques (stationnarité des phénomènes, turbulence, caractère hydrostatique du profil de pression, uniformité du profil de vitesse, ...). C'est à cette condition que l'on peut envisager produire des outils de modélisation plus fiable.

Mes activités de recherche se sont concentrées principalement sur l'étude des inondations urbaines. Une

approche expérimentale a été employée pour caractériser les phénomènes physiques en jeu lors d'inondations urbaines. Je me suis également intéressé à la modélisation numérique de ces inondations à différentes échelles.

Chapitre 6

Études expérimentales

La bibliographie montre qu'il existe peu de jeu de données physiques décrivant finement les inondations, notamment en milieu urbain. La richesse des données recueillies par les collectivités territoriales lors d'évènements passés, telles que les repères Plus Hautes Eaux Connues [1], est souvent illusoire. En effet, ces données correspondent à des niveaux d'eau instantanés et sont souvent considérées comme caractérisant le débit maximal de la crue ignorant les phénomènes d'hystérésis décorrélant les instants pour lesquels les maximums de hauteur d'eau et de débit apparaissent [17]. L'acquisition de données lors d'inondations urbaines avec une grande résolution spatio-temporelle est particulièrement complexe voire impossible (notamment pour des périodes de retour importantes) [31, 38]. Face à ces difficultés, des travaux proposent d'exploiter les réseaux de caméras pour mesurer des hauteurs d'eau [36] et/ou des données issues des réseaux sociaux [5].

La modélisation physique, à travers des expériences de laboratoire, est une approche permettant d'étudier les caractéristiques des écoulements dans des géométries complexes et également de produire des données permettant la validation de modèles numériques. Les expériences d'étude des inondations urbaines ont principalement considéré deux échelles différentes : locale (correspondant à l'échelle du carrefour) et globale (correspondant à l'échelle de la ville entière ou du quartier) [39].

Les travaux à échelle locale étudient principalement l'hydrodynamique à proximité d'un endroit d'intérêt : l'écoulement à proximité d'une digue rompue [56, 29, 62], les écoulements vers le réseau de métro [28] ou d'assainissement [12, 37, 52] ou la répartition des débits dans les jonctions et bifurcations [60, 4, 26, 25, 33, 8] (parmi d'autres) ou dans les carrefours [38, 33, 41, 43, 51]. Les hypothèses employées pour les expériences (par exemple : déconnexion des écoulements dans les intersections matérialisée par un champ de vitesses injecté uniforme) ne sont pas nécessairement valides et la sensibilité des résultats à ces hypothèses est rarement vérifiée. Par ailleurs, les gammes de paramètres testés (largeur de canal, pente, ...) sont souvent partielles. La multiplicité des expériences ne permet pas toujours de palier ce problème car les configurations testées diffèrent souvent trop pour pouvoir agréger les données. En pratique, il est compliqué de proposer une formulation exploitable sur une large gamme de paramètres pour un usage dans des outils numériques.

Les expériences à échelle globale s'intéresse principalement à l'effet d'un quartier ou d'une ville (souvent idéalisée) sur une inondation [30, 58, 61, 59, 64, 23]. Peu de mesures sont réalisées sur les écoulements à l'intérieur du quartier et les mécanismes de répartition de l'eau dans le réseau de rues ne sont pas étudiés. Ainsi, ces expériences permettent d'obtenir des données de comparaison pour des modélisations numériques mais ne permettent pas de déterminer la physique des écoulements et les mécanismes de répartition de l'eau.

Ma contribution à l'étude expérimentale des inondations urbaines s'est donc consacrée au développement d'un pilote visant à produire des données pour valider des codes de calculs (voir section 7.1), mieux comprendre la physique des inondations urbaines. La première section est consacrée à la présentation de ce pilote, de ses équipements de mesure et à son analyse dimensionnelle. La seconde section compare les distributions de débit amont et aval. Les sections trois et quatre s'intéressent à la répartition de l'écoulement dans le réseau de rues en terme de hauteurs d'eau (voir section 6.3) et de distributions des débits (voir section 6.4).

1. dont la mise en place est imposée par l'article L563-3 du code de l'environnement

Les travaux que j'ai mené sur l'étude expérimentale des inondations urbaines ont été conduits dans le cadre des thèses de doctorat de Quentin Araud et Cécile Choley (voir section 3.3.1). Ces travaux ont notamment été publiés dans ACL9, ACL6, ACL4 et ACL1.

6.1 Le pilote Icube d'étude des inondations urbaines

Cet axe de recherche a été initié par José Vazquez et Robert Mosé avant mon arrivée au laboratoire Icube, notamment avec la recherche de financement et la conception du pilote expérimental. J'ai rapidement été en charge de cette thématique, notamment pour la définition des campagnes expérimentales mais également pour l'exploitation et la valorisation des données. Fabrice Lawniczak et Pierre François ont activement contribué à la conception de la métrologie du pilote, à la réalisation des expériences et à leur analyse.

Le pilote Icube d'étude des inondations urbaines vise à répondre à deux principaux objectifs : la production de jeu de validation pour les codes de modélisation des inondations urbaines et l'étude de phénomènes de propagation des inondations dans un réseau de rue.

6.1.1 Présentation du dispositif expérimental

Le dimensionnement de ce pilote a été réalisé sur la base d'un réseau de rues proposé dans le cadre du projet ANR *Rives* [46] afin de reproduire les rues d'un quartier européen moyen (au sens statistique) mesurant 1km × 1km [35]. Ce quartier est composé de 7 rues orientées globalement dans la direction Nord-Sud intersectant 7 rues orientées Ouest-Est (cf figure 6.1). Ces rues, séparées par 64 blocs considérés comme imperméables, produisent des carrefours à 3 et 4 branches avec différents angles d'intersection et différentes largeurs de rues (12, 5cm pour les rues les plus larges - 4, C et F et 4, 5cm pour les plus étroites). La pente globale du pilote peut être réglée entre 0 et 2% dans chaque direction (Nord-Sud et Ouest-Est).

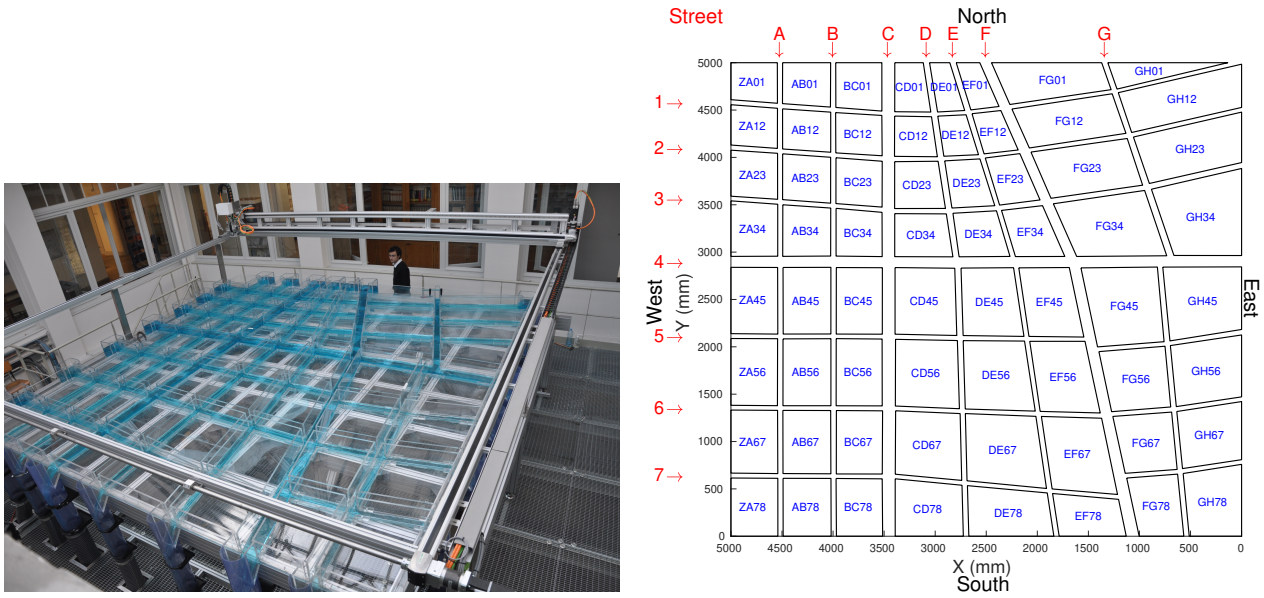

(a) (b)

FIGURE 6.1 – Description du pilote Icube d'étude des inondations urbaines. (a) photographie du dispositif ; (b) Plan du réseau de rues.

L'eau est injectée à l'amont de chaque rue (face Nord ou Ouest) avec une pompe volumétrique contrôlant un débit amont avec une précision (constructeur) de 1%. Les pompes ont une capacité d'injection entre 0, 5

et 15m^3/h (respectivement 1 et 30m^3/h) pour les petites (respectivement grandes) rues. Le débit total injecté par l'ensemble des pompes est toutefois limité à 100m^3/h en raison des dimensions du réseau de rues et des dimensions du réservoir d'alimentation. A l'aval de chaque rue (face Sud ou Est), un seuil rectangulaire peut être installé pour créer un contrôle aval dans le réseau de rue. Le débit à l'aval de chaque rue est déterminé à partir d'une mesure de niveau d'eau sur un seuil calibré avec une précision inférieure à 3% [2].

En complément des mesures de débits en entrée et sortie de chaque rue, les hauteurs d'eau peuvent être mesurées sur l'ensemble du pilote. Deux dispositifs successifs ont été employés : une sonde optique détectant le changement de phase air/eau couplée à un robot de déplacement vertical puis une caméra filmant l'eau par le coté des rues permettant une mesure du niveau d'eau par traitement d'image (voir figure 6.2). Pour ces deux dispositifs, la précision de l'appareil de mesure est de l'ordre de 1mm en vertical tandis que les fluctuations temporelles observées en un point (avec expériences conduites en régime permanent) sont comprises entre 2mm et 12mm (en fonction de l'endroit et de la configuration testée). Par ailleurs, les deux dispositifs mesurent des hauteurs d'eau supérieures à 3cm.

Enfin, un capteur ultrason permet de mesurer le profil instantané de vitesse sur la verticale. Chaque profil est ensuite moyenné sur la durée de mesure afin de produire un profil moyen non affecté par la turbulence. En réalisant plusieurs profils sur une section transversale de l'écoulement, le débit dans chaque tronçon (entre deux carrefours successifs) est calculé par intégration numérique. L'intégration est réalisée en supposant un profil polynomial sur la verticale pour déterminer le débit unitaire sur chaque transect vertical de mesure puis en supposant un profil horizontal de débit unitaire décrit également par une fonction polynomiale. La vitesse à la paroi (murs et fond) est supposée non-nulle correspondant à une sous-couche laminaire d'épaisseur négligeable. La comparaison des débits ainsi mesuré dans les tronçons amont et aval de chaque rue montre que les méthodes d'estimation des débits diffèrent de moins de 2%.

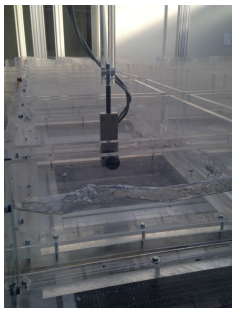

(a) Caméra de mesure sur le coté d'une rue

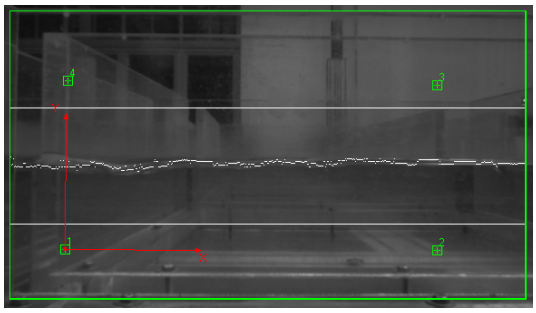

(b) Profil instantanté de hauteur d'eau extrait automatiquement des images prise par caméra

FIGURE 6.2 – Illustration du dispositif de mesure de hauteur d'eau par caméra

6.1.2 Analyse dimensionnelle

Le réseau de rues du pilote Icube d'étude des inondations urbaines a été conçu sur une plateforme de 5m$\times$5m avec une échelle horizontale $\lambda_L = L_{exp}/L_{reel} = 1/200$; où L fait référence à la dimension horizontale (longueur et largeur des rues) et les indices $_{exp}$ et $_{reel}$ font respectivement référence aux variables dans le pilote et en configuration réelle. Reproduire une inondation urbaine sans distorsion des échelles horizontale et verticale impliquerai qu'une hauteur d'eau réelle de 1m (déjà conséquente dans un réseau de rues) soit reproduite expérimentalement avec une hauteur de seulement 5mm. Dans une telle configuration, une mesure de hauteur d'eau avec une précision de 1mm produirait donc une erreur relative de 20%. En choisissant un facteur de distorsion de 10, définit comme le ratio entre l'échelle verticale et l'échelle horizontale, l'erreur relative pour une hauteur d'eau réelle de 1m est réduite à 2%. L'échelle verticale vaut donc $\lambda_h = h_{exp}/h_{reel} = 1/20$. Une étude sur les effets de cette distorsion a été présentée dans [34] à partir des données expérimentales de ce pilote. Elle a notamment montré que dans les configurations testées, l'influence de la distorsion sur la répartition des débits et sur les hauteurs d'eau était d'environ 10%.

Les écoulements observés, lors d'inondations urbaines réelles mais également dans les configurations expérimentales sont caractérisés par des nombres de Froude proche de l'unité : $\mathrm{Fr}_{exp} = {}^{v_{exp}}/\sqrt{gh_{exp}} \simeq 1$ et $\mathrm{Fr}_{reel} = {}^{v_{reel}}/\sqrt{gh_{reel}} \simeq 1$. On peut ainsi estimer le facteur d'échelle sur les vitesses $\lambda_v = {}^{v_{exp}}/_{v_{reel}} \simeq \sqrt{\lambda_h} = 2,2.10^{-1}$ et sur les débits $\lambda_Q = \lambda_L\lambda_h\lambda_v = 5,6.10^{-5}$. L'analyse de la crue historique de Nîmes en 1988 montre des débits estimés à $20\mathrm{m}^3/\mathrm{s}$ dans les rues étroites et $50\mathrm{m}^3/\mathrm{s}$ dans les grandes rues [40] pour une période de retour estimée comprise entre 150 et 250 ans [11]. Une crue équivalente reproduite expérimentalement (donc avec 11 petites rues et 3 larges) aurait un débit de $75\mathrm{m}^3/\mathrm{h} = \lambda_Q\left(11 \times 20\mathrm{m}^3/\mathrm{s} + 3 \times 50\mathrm{m}^3/\mathrm{s}\right)$, compris dans la gamme des débits possibles expérimentalement $\left[10;\ 100\mathrm{m}^3/\mathrm{h}\right]$ qui correspond donc à des périodes de retour importante à extrême.

Le nombre de Froude est un paramètre adimensionnel essentiel pour la caractérisation des écoulements à surface libre. Le facteur d'échelle pour ce paramètre est définit comme $\lambda_{\mathrm{Fr}} = \mathrm{Fr}_{exp}/\mathrm{Fr}_{reel}$. En introduisant la définition du nombre de Froude pour un canal rectangulaire, on trouve : $\lambda_{\mathrm{Fr}} = {}^{\lambda_v}/\sqrt{\lambda_h} \simeq 1$. Les nombres de Froude observés expérimentalement sont donc très similaires à ceux apparaissant lors de crues réelles.

Le nombre de Reynolds ($\mathrm{Re} = {}^{vL_c}/_{\nu}$ avec ν la viscosité cinématique du fluide), caractérise la turbulence et les phénomènes de dissipation d'énergie d'un écoulement. Le facteur d'échelle pour le nombre de Reynolds vaut $\lambda_{\mathrm{Re}} = \lambda_v\lambda_{L_c}$ (on suppose les fluides sont identiques dans le pilote et dans la réalité). Pour un écoulement à surface libre, Abbaspour et Kia proposent de définir la longueur caractéristique L_c comme 4 fois le rayon hydraulique [1]. En intégrant la définition du rayon hydraulique en canal rectangulaire, on a :

$$\lambda_{L_c} = \frac{L_{exp}h_{exp}}{L_{exp} + 2h_{exp}} \frac{L_{reel} + 2h_{reel}}{L_{reel}h_{reel}} = \lambda_L\lambda_h \frac{L_{reel} + 2h_{reel}}{\lambda_L L_{reel} + 2\lambda_h h_{reel}} \tag{6.1}$$

En considérant des gammes plausibles de la hauteur d'eau h_{reel} et de la largeur L_{reel} lors d'inondation urbaines : $0,1\mathrm{m} \leq h_{reel} \leq 10\mathrm{m}$ et $0,5\mathrm{m} \leq L_{reel} \leq 50\mathrm{m}$, on obtient $5.10^{-3} \leq \lambda_{L_c} \leq 4,8.10^{-2}$ et donc $1,1.10^{-3} \leq \lambda_{\mathrm{Re}} \leq 1,1.10^{-2}$. Il y a ainsi clairement une distorsion en terme de nombre de Reynolds.

La crue historique de Nîmes en 1988 est caractérisée par des hauteurs d'eau et des vitesses d'environ 1m et 1m/s pour des largeurs de rue d'environ 10m ; le nombre de Reynolds est donc d'environ $\mathrm{Re} = 3.10^6$. En considérant cette crue comme représentative, une turbulence pleinement établie caractérise les inondations urbaines. En prenant en compte la distorsion en terme de nombre de Reynolds, l'écoulement expérimental correspondant est faiblement turbulent voire dans la zone de transition entre régimes laminaire et turbulent. L'influence liée à cet écart de nombre de Reynolds sur l'écoulement est difficilement caractérisable. En effet, la rugosité des matériaux réels (béton, bitume et brique) diffère de celle du plexiglas employé pour le pilote Icube. Par ailleurs, on peut s'interroger sur la grandeur essentielle à reproduire dans l'expérience entre nombre de Reynolds réel et coefficient linéaire de perte de charge (éventuellement en prenant en compte la distorsion entre échelle horizontale et verticale).

6.2 Distribution des débits à travers un réseau de rues

6.2.1 Présentation des expériences réalisées

La distribution d'un débit à travers un réseau de rue a été étudiée expérimentalement, en régime permanent et avec une pente du fond horizontale. L'influence de plusieurs paramètres a été étudiée : le débit total injecté Q_{tot}, la distribution du débit entre les différentes rues amont et la distribution des seuils.

6.2.2 Influence du débit total injecté

L'analyse de l'influence du débit total Q_{tot} a été conduite en régime permanent, avec un écoulement torrentiel à l'aval des rues permettant ainsi que les résultats ne soient pas influencés par la condition limite aval. Les observations sur les hauteurs d'eau montrent que la transition entre les régimes fluvial et torrentiel apparaît à l'aval du dernier carrefour de chaque rue. Le débit total injecté est équiréparti entre les faces Nord et Ouest et le débit dans une face est réparti entre les rues proportionnellement à leur largeur.

Le tableau 6.1 présente le débit total injecté pour chaque configuration ainsi que la proportion du débit total sortant par la face Est (Q_E/Q_{tot}). Quel que soit le débit total injecté, environ 40% est évacué par la

face Est. La multiplication du débit injecté par 10 ne produit qu'une variation de 1% de la répartition du débit entre les faces aval. La géométrie du réseau de rues est un facteur explicatif important. En effet, la face Sud, qui draine la plus grosse part du débit, représente 54% de la largeur cumulée des rues aval.

TABLE 6.1 – Influence du débit total injecté sur la répartition des débits à l'aval

Config	Q_{tot} $(\mathrm{m}^3/\mathrm{h})$	Q_E/Q_{tot} (%)
Q010	10	41,1
Q020	20	40,7
Q060	60	40,3
Q070	70	40,4
Q080	80	40,3
Q100	100	40,5

La figure 6.3 représente l'évolution des ratios $Q_{up,k}/Q_{tot}$ et $Q_{down,k}/Q_{tot}$ pour chaque configuration expérimentale. Q_{up} et Q_{down} représentent respectivement les débits injectés et sortant de chaque rue ; l'indice k représente le nom de la rue. Pour une gamme importante de débits totaux injectés (entre 10 et $100\mathrm{m}^3/\mathrm{h}$), on observe que la variation de la proportion du débit total sortant par chaque rue reste inférieure à 2%. Pour chaque rue, le débit sortant normalisé en fonction du débit total injecté semble tendre vers un comportement asymptotique quand le débit total augmente. La répartition du débit entre les différentes rues dépend *a priori* de la largeur de la rue et de sa débitance mais également des caractéristiques géométriques des carrefours rencontrés et de l'hydrodynamique au long de l'écoulement. Il est intéressant de constater que les 3 grandes rues (F, 4 et C) drainent respectivement 10, 15 et 20% du débit total malgré le fait qu'elles ont la même largeur. Malgré des débits injectés identiques dans les rues 4 et C et une largeur cumulée des rues intersectées plus grande pour la rue 4 que pour la rue C, le débit sortant de la rue C est 5% plus grand que celui de la rue 4. Une analyse similaire est valide en comparant les rue C et F ou 4 et F. Chaque petite rue draine entre 3 et 10% du débit total injecté malgré des variations de largeur faible. Ces observations suggèrent des dynamiques complexes d'échange de masse au niveau des carrefours. Le comportement asymptotique de l'évolution du débit sortant normalisé en fonction du débit total injecté promeut que le rôle de chaque rue n'évolue pas avec le débit total et que les mécanismes de répartition de débit à travers le réseau de rues restent constants.

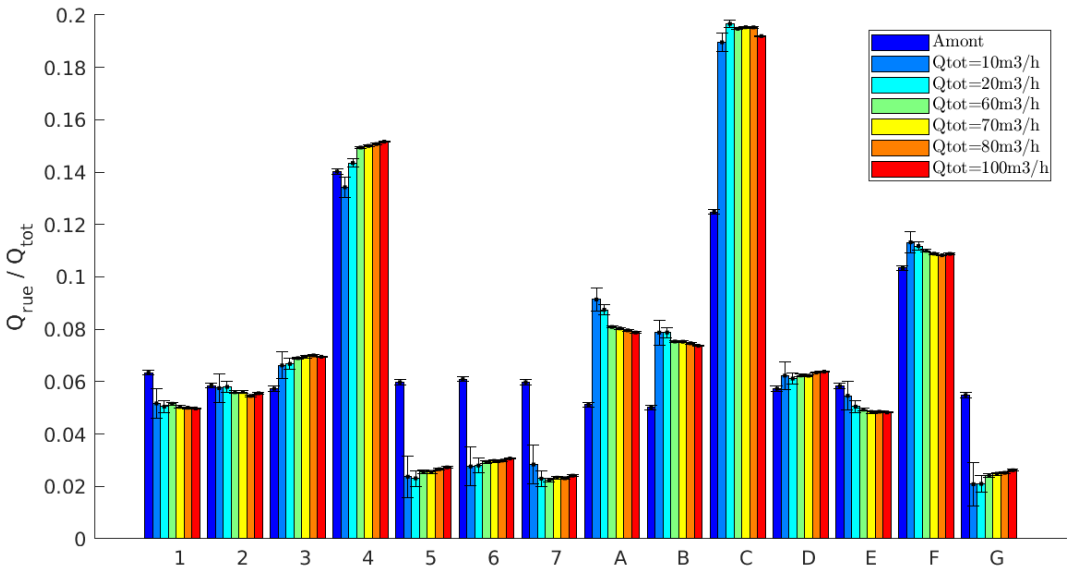

FIGURE 6.3 – Évolution des ratios $Q_{up,k}/Q_{tot}$ et $Q_{down,k}/Q_{tot}$ entre l'amont et l'aval de chaque rue. Les barres d'erreur représentant l'incertitude de mesure.

6.2.3 Influence de la distribution des débits amont

L'influence de la distribution du débit total à l'amont a été évaluée. Trois répartitions ont été employées :

Config 1 Le débit dans une face est réparti au prorata de la largeur des rues et le débit d'une face amont est définit comme une proportion du débit total $Q_{ouest} = \phi_{ouest} Q_{tot}$ avec $\phi_{ouest} \in [0, 1]$ et $Q_{nord} = Q_{tot} - Q_{ouest}$.

Config 2 Le débit total Q_{tot} est réparti équitablement entre les rues larges (4, C et F).

Config 3 Le débit total Q_{tot} est réparti entre les rues larges (4, C et F) tel que $Q_4 = 50\% Q_{tot}$ et $Q_C = Q_F = 25\% Q_{tot}$. Cette configuration revient à une équirépartition du débit total entre les faces Nord et Ouest.

6.2.3.1 Influence de ϕ_{ouest}

Cette analyse se base uniquement sur la configuration 1 pour des débits totaux $Q_{tot} \in \{60, 70, 80\}$ m^3/h et ϕ_{ouest} allant de 0 à 1 par pas de $0,1$. Ici encore, la pente du fond est nulle et aucun seuil n'est installé à l'aval des rues pour éviter toute influence de la condition limite aval.

La figure 6.4 montre l'évolution de $\phi_{est} = Q_{est}/Q_{tot}$ (la proportion du débit total sortant par la face Est) en fonction du paramètre ϕ_{ouest}. On constate que les courbes sont quasi confondues ce qui indique que la modification du débit total injecté n'influence pas significativement la répartition du débit entre les faces aval. Les courbes augmentent avec l'augmentation de ϕ_{ouest}, traduisant que l'augmentation du débit injecté par la face Ouest se traduit logiquement par une augmentation du débit sortant par la face Est. On observe également l'effet filtrant du réseau de rues qui tend à uniformiser la répartition des débits. En effet, une variation de ϕ_{ouest} entre 0 et 1 se traduit uniquement par une variation de ϕ_{est} de $0,1$ (entre $0,37$ et $0,47$).

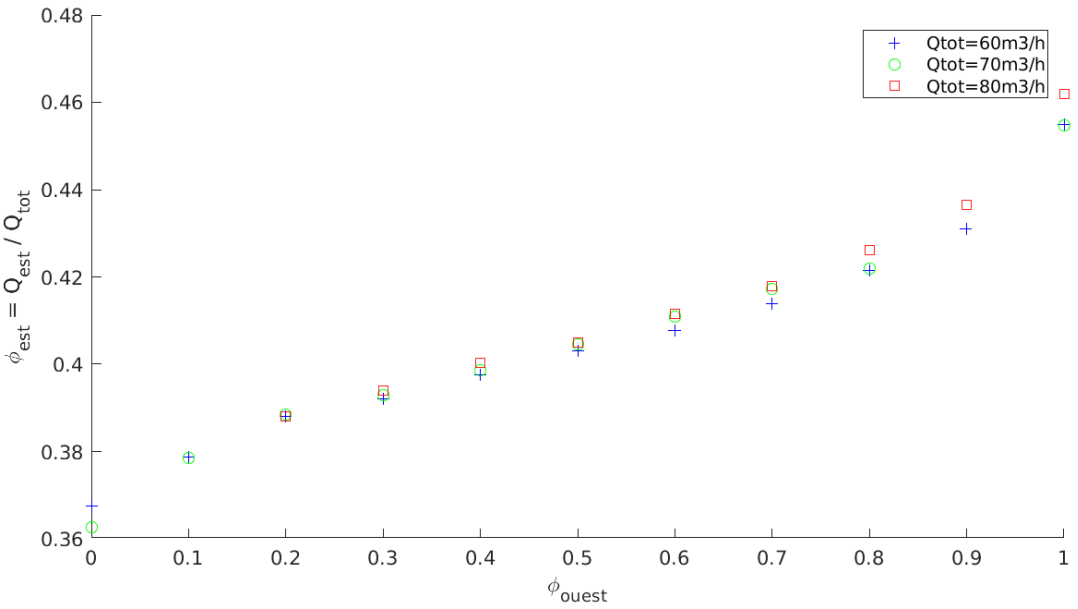

FIGURE 6.4 – Influence du paramètre ϕ_{ouest} sur la répartition du débit entre les face aval (Est et Sud).

La figure 6.5 présente, pour chaque rue, l'évolution du ratio $\delta_{50}Q_{rue}\left(\phi_{ouest}\right)$ définit comme :

$$\delta_{50}Q_{rue}\left(\phi_{ouest}\right) = \frac{Q_{rue}\left(\phi_{ouest}\right) - Q_{rue}\left(\phi_{ouest} = 0,5\right)}{Q_{rue}\left(\phi_{ouest} = 0,5\right)}$$

Ce ratio représente la variation entre le débit sortant par une rue dans une configuration donnée (une valeur de ϕ_{ouest}) et le débit sortant de cette même rue pour $\phi_{ouest} = 0,5$ normalisée par le débit sortant de cette même rue pour $\phi_{ouest} = 0,5$. En cohérence avec l'analyse de la figure 6.4, on observe que l'augmentation de ϕ_{ouest} se traduit par une augmentation de $\delta_{50}Q_{rue}$ pour les rues 1 à 7 (face Est) et une diminution pour les rues A à G (face Sud). On observe également que le débit sortant par une rue peut être modifié de manière significative (jusqu'à environ $40\% \simeq 30\% - (-10\%)$ pour la rue 1). Cette gamme de variation ne semble pas être corrélée à la largeur des rues puisque les variations les plus grandes sont observées pour la rue étroite 1 et les rues larges 4 et C mais pas pour la rue large F. L'évolution de $\delta_{50}Q_{rue}$ avec ϕ_{ouest} est monotone pour les rues 2 à 4, C, et E et F. La non-monotonicité de cette variation pour les autres rues illustre la complexité des mécanismes de répartition des débits dans le réseau de rues.

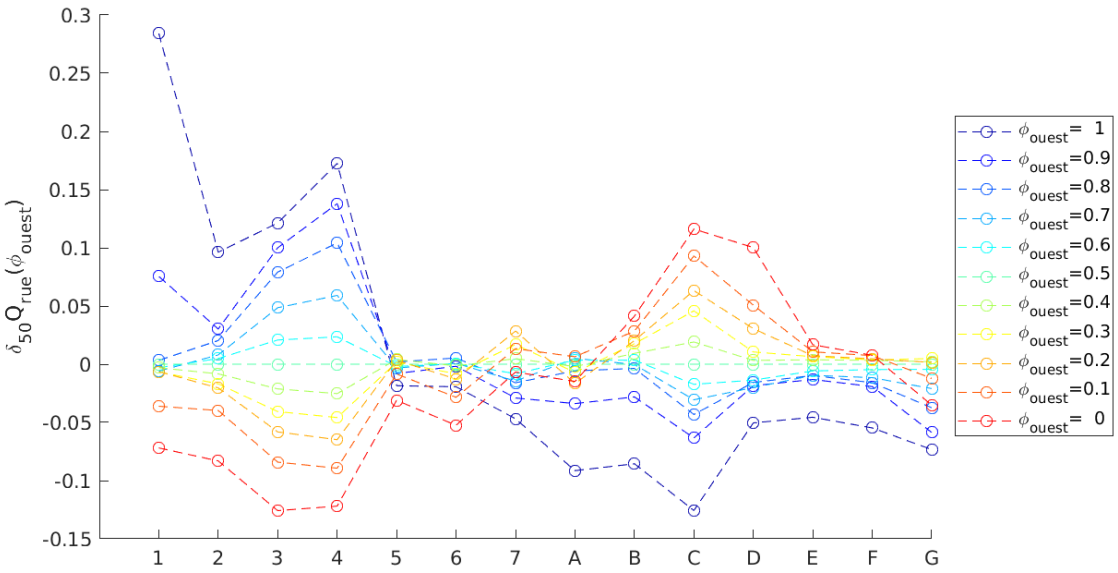

FIGURE 6.5 – Évolution de la variation du débit sortant par chaque rue normalisée en fonction de la répartition du débit total entre les faces amont (Ouest et Nord).

6.2.3.2 Etude de la répartition des débits

Cette analyse compare l'effet de plusieurs distributions du débit total Q_{tot} entre les rues amont :

Config 1 Le débit total est équiréparti entre les faces Nord et Ouest et le débit dans une face distribué proportionnellement à la largeur des rues.

Config 2 Le débit total est réparti équitablement entre les rues larges (4, C et F).

Config 3 Le débit total est réparti entre les rues larges (4, C et F) tel que $Q_4 = 50\%Q_{tot}$ et $Q_C = Q_F = 25\%Q_{tot}$. Cette configuration revient à une équirépartition du débit total entre les faces Nord et Ouest.

La figure 6.6 montre l'évolution des ratios $Q_{up,k}/Q_{tot}$ et $Q_{down,k}/Q_{tot}$ pour chaque configuration expérimentale. Pour chaque rue, la diminution de la variabilité entre les débits entrants et sortants illustre l'effet filtrant du réseau de rues sur la distribution des débits. Par ailleurs, le débit de sortie de chaque rue semble converger vers le comportement asymptotique mis en évidence précédemment (voir section 6.2.2). C'est particulièrement notable pour les rues larges qui drainent environ 20%, 15% et 10% du débit total pour les rues C, 4 et F.

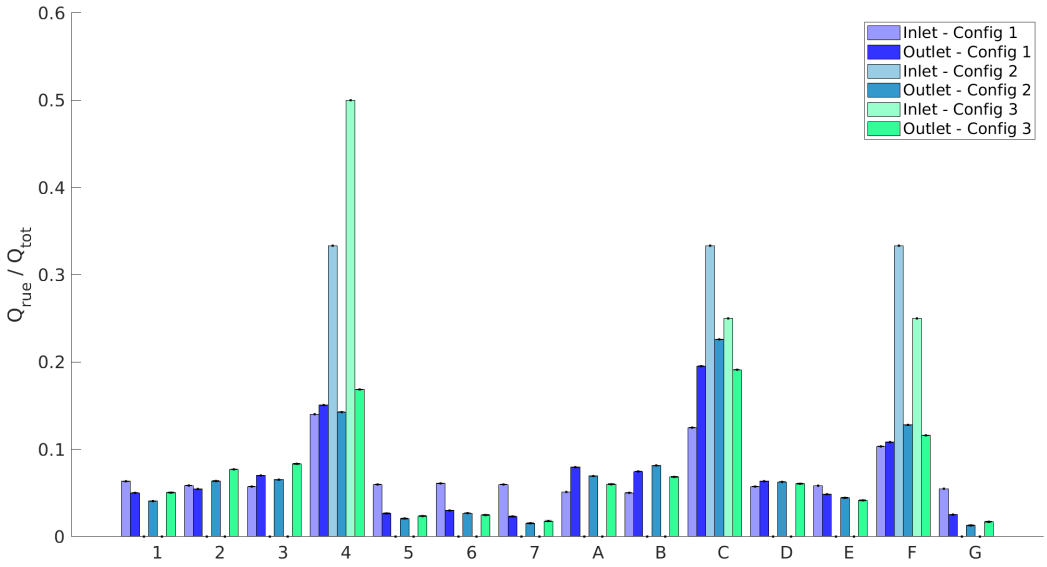

FIGURE 6.6 – Évolution de la répartition des débits à l'aval du réseau de rues pour différentes répartitions à l'amont. Config 1 : Le débit total est équiréparti entre les faces Nord et Ouest et le débit dans une face distribué proportionnellement à la largeur des rues ; Config 2 : Le débit total est réparti équitablement entre les rues larges (4, C et F) ; Config 3 : Le débit total est réparti entre les rues larges (4, C et F) tel que $Q_4 = 50\%Q_{tot}$ et $Q_C = Q_F = 25\%Q_{tot}$.

6.2.4 Influence de la condition limite aval

L'influence des conditions limite aval sur la répartition des débits a été évaluée en installant des seuils de différentes hauteurs à l'aval des rues. La figure 6.7 compare les débits à l'amont et à l'aval des rues pour différentes distributions des seuils sur les faces aval. Les courbes verte (*Est=0cm - Sud=3cm*) et jaune (*Est=3cm - Sud=0cm*) montrent la répartition des débits quand les seuil sont installés sur une unique face. Lorsque les seuils sont uniquement sur la face sud (courbe verte), on observe pour les rues A à G (de la face Sud), un débit qui diminue par rapport aux configurations sans seuil (*Est=0cm - Sud=0cm* et *Est=3cm - Sud=0cm*). De la même manière, les seuils sur la face Est (courbe jaune) produisent une diminution du débit pour les rues de cette face (1 à 7).

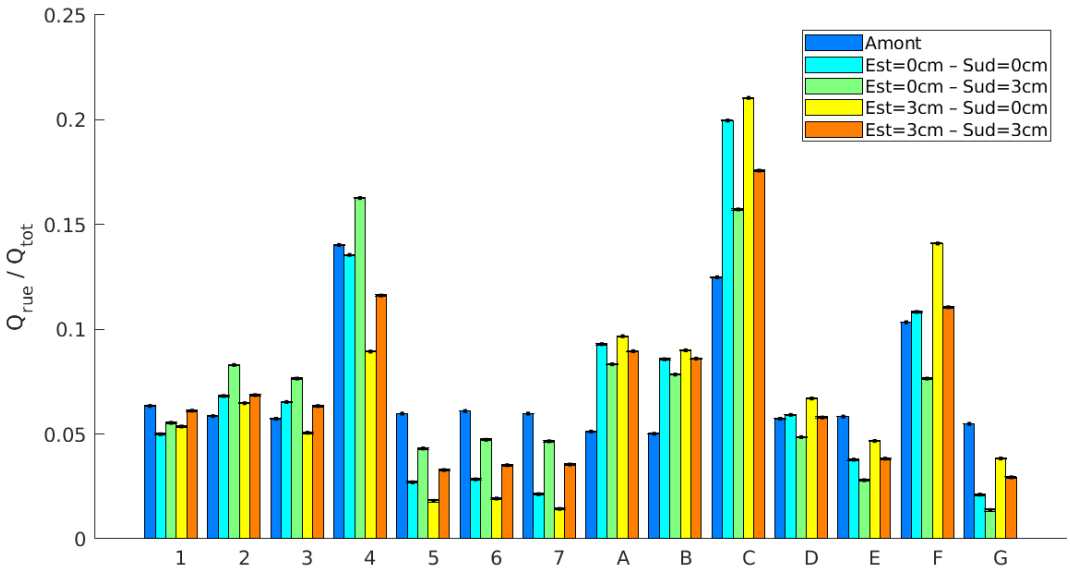

FIGURE 6.7 – Évolution de la répartition des débits à l'aval du réseau de rues pour différentes répartitions à l'amont.

La figure 6.8 compare le débit à l'aval de chaque rue du fait de l'installation des seuils par rapport à la configuration sans seuil. La mise en place de seuils modifie significativement la répartition des débits de sortie avec les débits multipliés par un facteur $0,7$ à $2,3$. Pour les configurations avec des seuils uniquement sur une face (*Est=0cm* - *Sud=3cm* et *Est=3cm* - *Sud=0cm*), la modification du débit (par rapport à la configuration sans seuil est plus marquée pour les rues les plus éloignées de l'amont (principalement F, G et 5, 6, 7). Pour la configuration avec des seuils sur toutes les rues, on observe une modification du débit de chaque rue plus marquée pour la face Est que pour la face Sud. Ces variations différentes pour chaque rue suggèrent que les mécanismes de répartition des débits sont modifiées à l'intérieur du réseau de rues. Le théorème d'Euler appliqué sur un carrefour relie sa géométrie et l'hydrodynamique dans les rues (faisant intervenir un terme inertiel et un terme de pression). La répartition du débit entre les rues est donc, au moins en partie, liée à l'importance relative des termes inertiels et de pression. L'ajout des seuils remonte le niveau d'eau dans l'ensemble du réseau et diminue donc les vitesses d'écoulement. On peut donc supposer que cette réduction de la vitesse modifie l'importance relative des termes inertiels et de pression et peut donc modifier la répartition des débits.

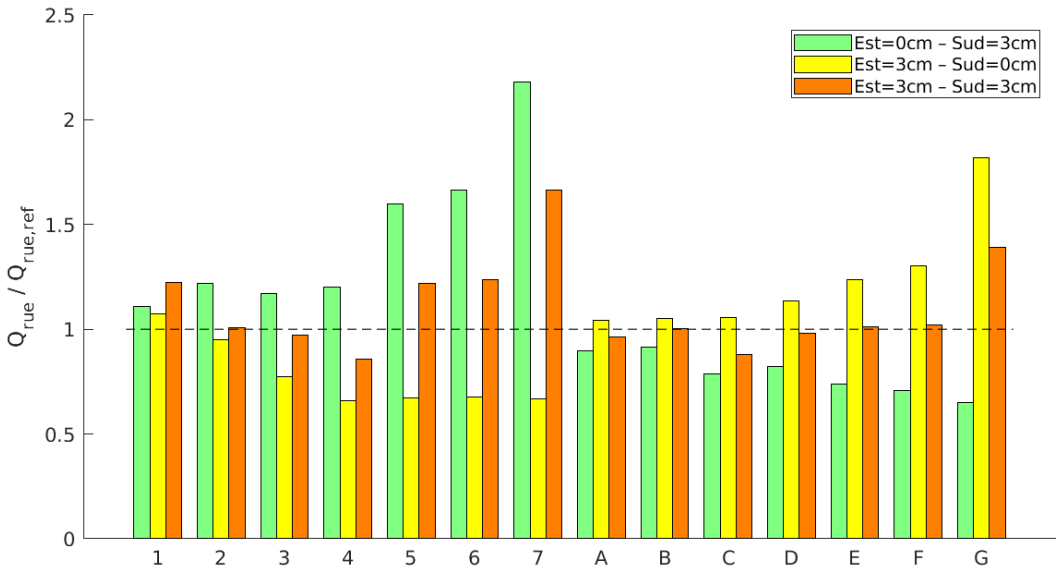

FIGURE 6.8 – Effet des seuils sur le débit sortant de chaque rue. Pour chaque rue, le débit de référence $Q_{rue,ref}$ est le débit sortant de cette rue dans la configuration sans seuil.

6.3 Analyse de la distribution des hauteurs d'eau

Malgré l'automatisation de la mesure de hauteur d'eau, cette mesure sur l'ensemble du pilote demande plusieurs jours pour chaque configuration. Les mesures ont donc été réalisées pour différents débits totaux injectés et pour une équirépartition de Q_{tot} entre les faces amont (Ouest et Nord). Pour un débit $Q_{tot} = 80\text{m}^3/\text{h}$, les hauteurs d'eau ont été cartographiées avec et sans seuil à l'aval (voir figures 6.9a et 6.9b).

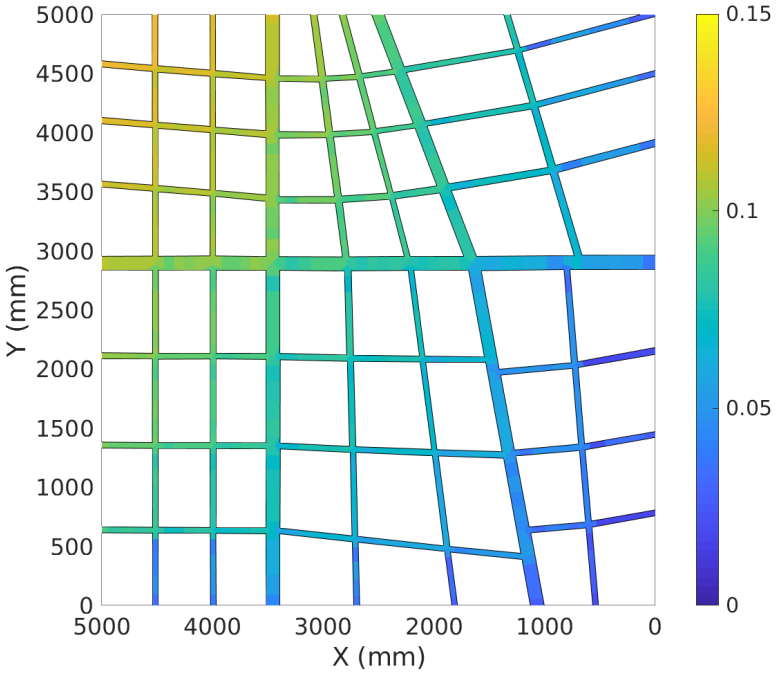

(a) Pas de seuil aval

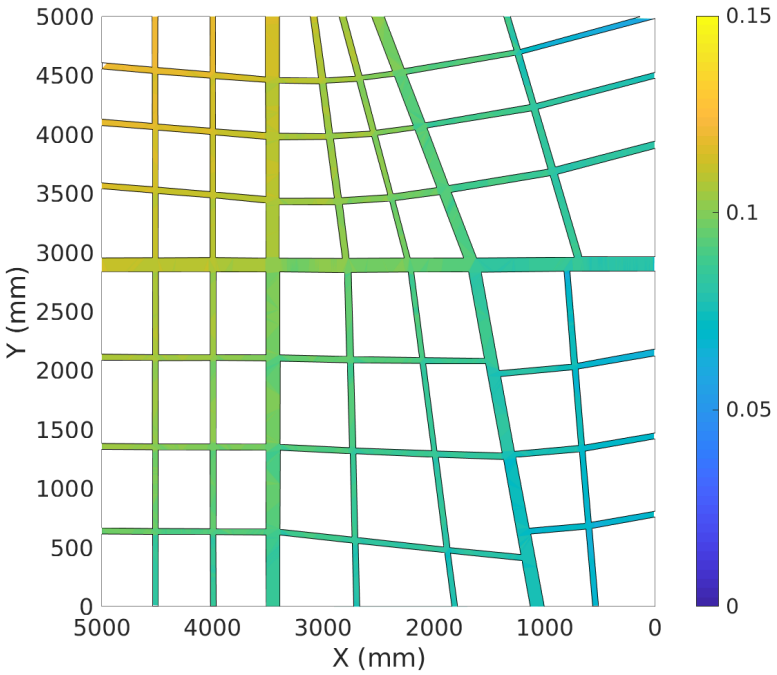

(b) Seuil de 3cm à l'aval de toutes les rues

FIGURE 6.9 – Cartographie des hauteurs d'eau pour $Q_{tot} = 80\text{m}^3/\text{h}$ équiréparti entre les faces d'injection (Nord et Ouest)

Dans les deux cas (mais également pour les autres configurations mesurées - non présentées ici), on observe que le gradient de hauteur d'eau est orienté depuis le coin Nord-Ouest vers le coin Sud-Est. L'ajout des seuils à l'aval des rues augmente les niveaux d'eau sur l'ensemble du quartier. Cette augmentation est toutefois réduite à quelques millimètres à l'amont du réseau de rues.

Afin de comparer les hauteurs d'eau mesurées pour différents débits totaux, des profils adimensionnels ont été produits. Pour chaque rue, la hauteur d'eau est normalisée par la différence entre la hauteur d'eau à l'amont et à l'aval de la rue : $h^* = (h - h_{aval}) / (h_{amont} - h_{aval})$. La figure 6.10 présente les profils en long de hauteur normalisée pour deux rues et pour différents débits totaux. On constante que pour les deux rues (mais également pour les autres - non présentées ici), les profils de hauteur normalisée se superposent. Le débit total injecté semble n'influencer que l'amplitude de variation des hauteurs d'eau et pas la distribution à l'intérieur du réseau de rues. Par ailleurs, le profil de hauteur d'eau (normalisée) montre une diminution rapide au niveau de chaque carrefour. Entre les carrefours, la diminution du niveau d'eau est plus lente avec toutefois un "creux" immédiatement à l'aval du carrefour. Ce creux correspond aux zones de recirculations apparaissant à l'aval d'un carrefour qui réduisent la largeur effective de l'écoulement et provoque un effet Venturi avec une accélération et une chute localisée de la ligne d'eau.

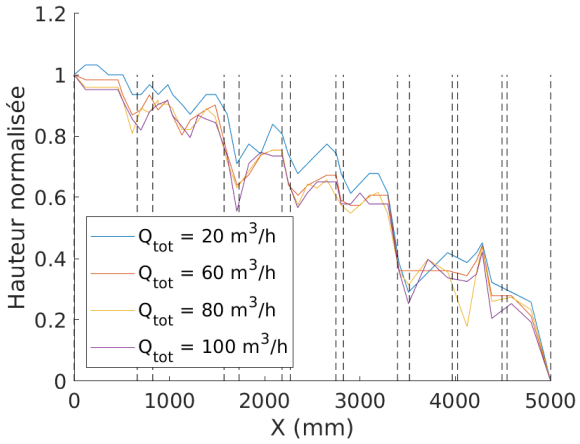

(a) Rue 4

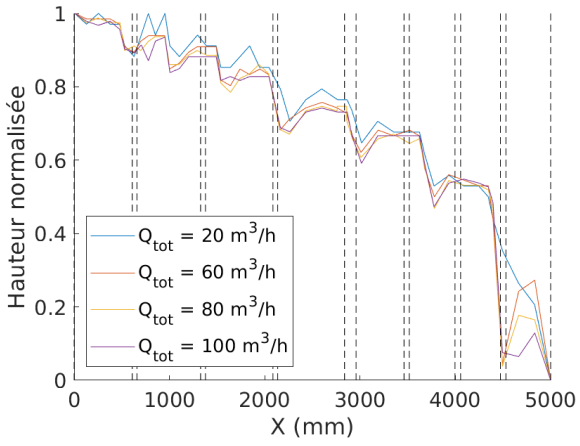

(b) Rue B

FIGURE 6.10 – Évolution de la hauteur d'eau normalisée pour $Q_{tot} = \{20, 100\}\,\mathrm{m}^3/\mathrm{h}$ équiréparti entre les faces d'injection (Nord et Ouest). Les barres verticales pointillées matérialisent la position des carrefours.

6.4 Caractérisation de l'écoulement dans le réseau de rues

Afin de mieux comprendre les mécanismes de répartition des débits à l'échelle du quartier, une cartographie des flux dans les rues a été réalisée à partir des mesures de vitesses dans les rues (voir section 6.1.1). Un débit total de 80m^3/h est équiréparti entre les faces amont (Nord et Ouest) et le débit de chaque face est distribué proportionnellement à la largeur des rues. L'écoulement se fait sur fond plat et avec des seuils de 3cm à l'aval des rues pour permettre une mesure des vitesses dans les rues.

6.4.1 Analyse des mesures de vitesse

Des profils verticaux de vitesse sont mesurés (voir section 6.1.1) 7cm à l'amont de chaque carrefour avec 3 (respectivement 5) mesures sur la largeur des rues étroites (respectivement larges). Les niveaux de couleur de la figure 6.11 cartographient la vitesse moyenne sur chaque tronçon et les flèches montrent la vitesse moyenne sur la verticale. Dans tous les tronçons, l'écoulement est orienté de l'Ouest vers l'Est ou du Nord vers le Sud, dans le sens du gradient de hauteur d'eau (voir section 6.3).

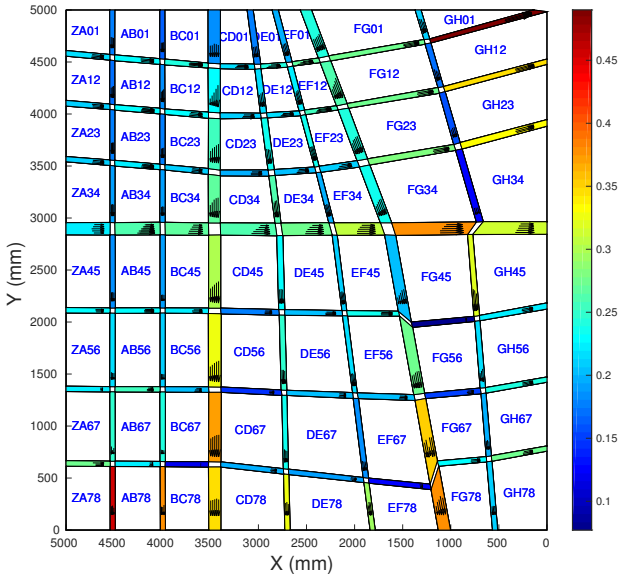

FIGURE 6.11 – Carte des vitesses mesurées dans le réseau de rues

Les profils transversaux de vitesses sont quasi-uniformes pour les rues étroites et dissymétriques pour les rues larges. Cette différence de comportement peut-être corrélée au ratio L/B de la longueur du tronçon sur sa largeur. En effet, la distance nécessaire pour qu'un écoulement à surface libre retrouve un profil de vitesse non perturbé est estimée par $L = \kappa B$ avec $\kappa \in [10; 50]$. Considérant les grandeurs géométriques des rues, les rues étroites ont un ratio moyen $\overline{L/B}$ de l'ordre de 10 contre 5 pour les rues larges. L'échelle horizontale du pilote expérimentale étant la même pour L et B, cette constatation a priori est transposable aux inondations réelles. Ainsi, l'hypothèse courante (tant sur les approches expérimentales que de modélisation) consistant à considérer que les carrefours sont hydrodynamiquement déconnectés semble erronée. Cette observation devra être confirmée ou infirmée dans d'autres configurations expérimentales.

6.4.2 Analyse de la distribution des débits

L'intégration des profils de vitesse permet, moyennant des hypothèses pour extrapoler la forme du profil de vitesse, d'accéder au débit dans chaque tronçon (voir section 6.1.1). La comparaison de ces débits avec ceux imposés par les pompes ou mesurés dans les tronçons aval permet de valider les hypothèses d'intégration.

La figure 6.12 présente la carte des débits dans chaque tronçon. Les débits les plus importants sont véhiculés par les rues larges qui drainent 42% du débit total. La largeur cumulée des rues larges sur la largeur totale représente environ 38%. Cela suggère que la répartition du débit entre les rues larges et étroites est contrôlée par la largeur des rues. A échelle plus fine, cette constatation n'est plus vraie avec des rues de largeurs comparables ayant des débits aval relativement différents (par exemple, les rues larges 4, C et F ou les rues étroites A, B, D et E).

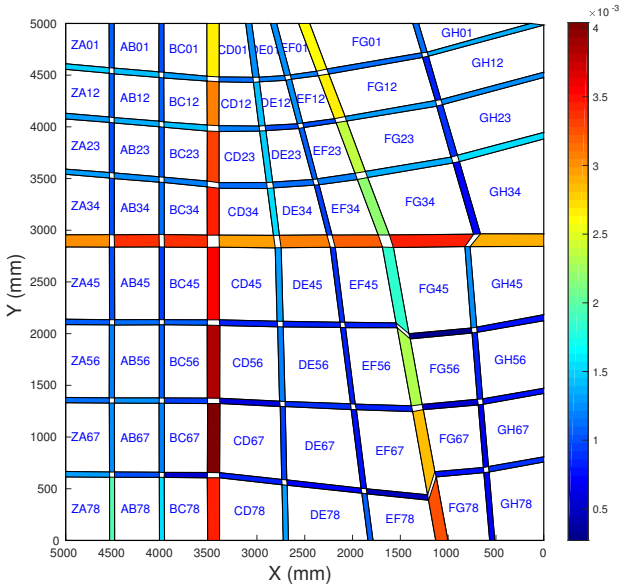

FIGURE 6.12 – Carte des débits calculés dans le réseau de rues

La figure 6.13 présente le débit unitaire $q = Q/B$ dans chaque tronçon. La comparaison des débits unitaires dans les rues étroites et larges ne permet pas de mettre en évidence des différences significatives (les différences entre rues sont inférieures à la variabilité longitudinale observée dans certaines rues). Ainsi il semble erroné de vouloir négliger le rôle des rues étroites dans la répartition des débits devant celui des rues larges, notamment lorsque la largeur cumulée des rues étroites n'est pas négligeable devant celle des rues larges. La forte variabilité spatiale des débits (et des débits unitaires) le long de chaque rue suggère des mécanismes complexes de répartition des débits à petite échelle.

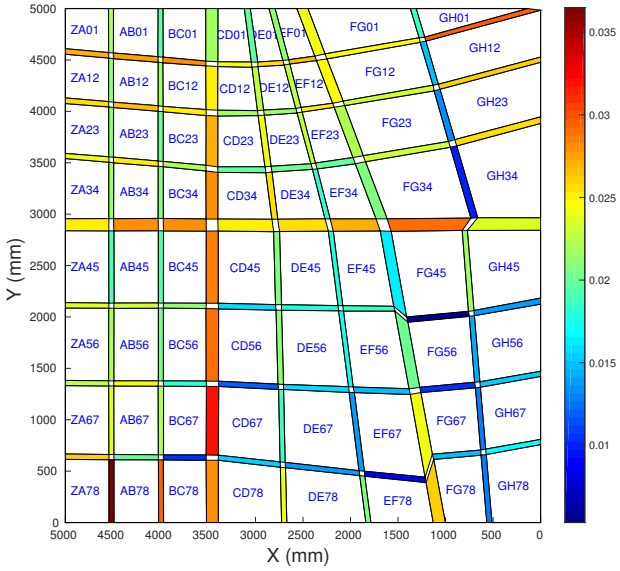

FIGURE 6.13 – Carte des débits unitaires calculés dans le réseau de rues

6.4.3 Répartition des débits à échelle fine

La connaissance des débits dans chaque tronçon permet de caractériser la répartition des flux à l'échelle des sous-quartiers. Un sous-quartier est définit comme un réseau de petites rues encadré par des grandes rues.

Le tableau 6.2 présente la répartition des débits à l'échelle des sous-quartiers. Sur l'ensemble des sous-quartiers, le paramètre ϕ_{est} varie dans la gamme $\phi_{est} \in [0,43;\ 0,72]$ et est supérieur à $0,42$, la valeur obtenue à l'échelle du quartier. Cette différence est liée aux grandes rues qui véhiculent environ 40% du débit total et dont 2 sur 3 débouchent sur la face Sud.

Par ailleurs, on constate que les valeurs de ϕ_{est} pour les trois sous-quartiers Nord (AB123, DE123 et G123) sont très proches du ratio du nombre de rue de la face Est sur le nombre de rues total pour les faces Est et Sud ; par exemple pour AB123, $\phi_{est} = 0,63$ et 3 rues / 5 rues$= 0,60$. Cela suggère que la largeur des rues contrôle au premier ordre la répartition des débits dans ces sous-quartiers. Le paramètre ψ_{est}, pour les sous-quartiers AB123, DE123 et G123, est proche de 1. Cela confirme que le débit entrant dans ces sous-quartiers est distribué à l'aval proportionnellement à la largeur des rues de sorties. Par comparaison, les sous-quartiers AB567, DE567 et G567 (plus proche de la sortie Sud du réseau de rues) ont une valeurs de ψ_{est} inférieure à 1 ce qui indique que le débit est dévié vers le Sud et drainé par les sorties Sud.

Afin d'étudier la corrélation entre les répartitions amont et aval des débits à l'échelle du sous-quartier, le tableau 6.2 présente l'évolution du ratio ϕ_{ouest}/ϕ_{est} en fonction du sous-quartier. Un ratio $\phi_{ouest}/\phi_{est} = 1$ indique un sous-quartier "transparent" qui ne modifie pas la répartition des débits entre les faces amont et aval ; $\phi_{ouest}/\phi_{est} < 1$ correspond à un sous-quartier déviant le débit vers la face Est. Il apparaît ainsi que les sous-quartiers AB123, DE123, G123 sont transparents. De manière remarquable, le sous-quartier DE567 est transparent ($\phi_{ouest}/\phi_{est} = 0,93$) bien que la répartition des débits aval ne correspondent pas à la distribution des largeurs de rues ($\psi_{est} = 0,81$). Cette observation et la forte variabilité des vitesses et des débits unitaires dans ce sous-quartier suggèrent que les effets inertiels ont un rôle non négligeable sur la répartition du débit dans ces carrefours.

TABLE 6.2 – Comparaison de la répartition aval des débits par rapport à l'amont à l'échelle des sous-quartiers. ϕ_{est} (respectivement ϕ_{ouest}) représente le débit sortant par les rues de la face Est (respectivement Ouest) du sous-quartier dimensionnalité par le débit total entrant dans le sous-quartier (par les rues Nord et Ouest). ψ_{est} est définit comme $\psi_{est} = \phi_{est} B_{tot}/B_{est}$ et représente le ratio de $q_{est} = Q_{est}/B_{est}$ sur $q_{tot} = Q_{tot}/B_{tot}$. $\psi_{est} = 1$ indique que la répartition des débits à l'aval du sous-quartier correspond à la distribution des largeurs.

Sous-quartier	ϕ_{ouest}	ϕ_{est}	ψ_{est}	ϕ_{ouest}/ϕ_{est}
AB123	0,66	0,63	1,05	0,97
DE123	0,58	0,56	1,00	0,98
G123	0,79	0,72	1,03	0,91
AB567	0,64	0,46	0,77	0,72
DE567	0,51	0,48	0,81	0,93
G567	0,66	0,43	0,59	0,66

Chapitre 7

Modélisation numérique des inondations

Les travaux que j'ai mené sur la modélisation numérique des inondations ont été conduit dans le cadre ma propre thèse de doctorat et celles de Q. Araud et S. Chen (voir section 3.3.1). Ces travaux ont notamment été publiés dans ACL14, ACL13, ACL10 et ACL7.

Les équations d'état décrivant un système modélisé, les méthodes numériques employées pour les résoudre et la disponibilité des données pour les paramétriser sont autant de facteurs qui conditionnent la qualité des résultats produits, notamment lorsque le modèle est employé pour extrapoler des configurations (plus grande période de retour, état projet, ...). L'amélioration de la modélisation des inondations peut ainsi être envisagée à travers trois approches : améliorer l'adéquation modèle numérique - données disponibles pour faciliter le calage, employer des équations d'état décrivant au mieux l'hydrodynamique des phénomènes considérés, améliorer/employer les schémas numériques les plus pertinent. L'intérêt de ces améliorations peut être significativement mis en défaut par les contraintes opérationnelles qui incluent les coûts de modélisation (pré et post processing de la modélisation mais également le coût numérique en terme de temps de calcul/machine de calcul).

Ma recherche, consacrée aux approches numériques pour la modélisation des inondations, est structurée en deux axes :

— la caractérisation de modèles existants,

— le développement de nouvelles approches de modélisation.

7.1 Caractérisation de modèles existants pour la modélisation des inondations urbaines

7.1.1 Comparaison d'approches 2D et 3D

La modélisation des inondations emploie généralement des approches de complexité variée allant d'une représentation 1D des écoulements couplée à un modèle d'échange de masse (et parfois de quantité de mouvement) aux carrefours à une modélisation 3D basée sur les équations de Navier-Stokes.

L'approche 1D suppose une uniformité des vitesses sur la section d'écoulement ce qui est remis en cause par de nombreuses données expérimentales [4, 24, 43, 42]. Les effets de la non-uniformité de la vitesse peuvent être numériquement pris en compte (notamment à travers une paramétrisation supplémentaire des équations de Saint-Venant 1D avec un coefficient de Boussinesq) mais ce coefficient est fortement variable dans l'espace et dans le temps ce qui complexifie fortement l'emploi d'une telle approche pour de la modélisation prédictive.

L'approche 3D n'impose généralement pas (ou peu) d'hypothèse sur l'hydrodynamique de l'écoulement modélisée. En revanche, elle demande une paramétrisation complexe, notamment pour des configurations réelles avec une variabilité spatiale de l'intensité des phénomènes physiques (on peut par exemple penser à la variabilité des lois de paroi du fait de la variabilité des matériaux et phénomènes rencontrés), et des coûts importants en termes de pré et post-processing mais également en termes de calcul. Cette approche est donc

trop coûteuse pour des applications opérationnelles. Par ailleurs, le monde opérationnel s'intéressant aux inondations (ingénieurs chargés d'étude et maîtres d'ouvrage) est dans l'ensemble peu formé sur l'usage, les potentialités et les limites de ce type d'approche.

L'approche 2D constitue un intermédiaire entre les approches 1D et 3D car elle est basée sur des hypothèses moins contraignantes que l'approche 1D et elle est moins coûteuse en termes de calcul, de pré et de post-processing. Les données expérimentales acquises sur le pilote Icube d'étude des inondations urbaines (voir section 6.1) ont donc été confrontées aux codes :

Neptune2D développé dans le cadre de la thèse de Q. Araud (voir section 3.3.1), qui résout les équations de Saint-Venant 2D par une approche aux éléments finis avec un schéma de Galerkin discontinu ;

Ansys-Fluent qui résout les équations RANS (Reynolds Averaged Navier-Stokes) sur un maillage tridimensionnel. Pour les graphiques présentés par la suite, un modèle $k - \epsilon$ est utilisé.

Seule la comparaison des résultats est présentée ci-après, la construction du modèle et l'analyse de sensibilité au maillage et aux différents paramètres (modèle de turbulence, coefficient de Strickler, ...) sont décrites par [2].

La figure 7.1 compare la répartition des débits expérimentaux et modélisés pour différentes configurations. La première colonne compare les débits expérimentaux et modélisés sortant de chaque rue. Pour l'ensemble des configurations, la distribution expérimentale des débits à l'aval du réseau de rue est reproduite par les modélisations 2D et 3D. La seconde (respectivement troisième) colonne de la figure 7.1 représente, pour chaque rue, l'écart entre les débits simulés et mesurés adimensionnalisé par le débit total injecté (respectivement par le débit de la rue). La modélisation 3D reproduit généralement les débits expérimentaux avec moins d'erreurs que la modélisation 2D. On observe toutefois que les erreurs maximales n'apparaissent pas pour les mêmes rues et configuration quand on compare approches 2D et 3D (l'erreur maximale est observée pour la rue 5 de la configuration $Q_{tot} = 20\text{m}^3/\text{h}$ pour l'approche 3D et la rue G de la configuration $Q_{tot} = 80\text{m}^3/\text{h}$ pour l'approche 2D). Le tableau 7.1 fait la synthèse les écarts maximum et moyen obtenus pour les différentes configurations entre les débits expérimentaux et simulés. L'erreur de la modélisation sur le débit à l'aval de chaque rue représente moins de 1% du débit total en moyenne (avec un maximum à $2,3\%$). Des erreurs significatives (10% en moyenne allant jusqu'à 35%) sur le débit d'une rue peuvent toutefois être observées.

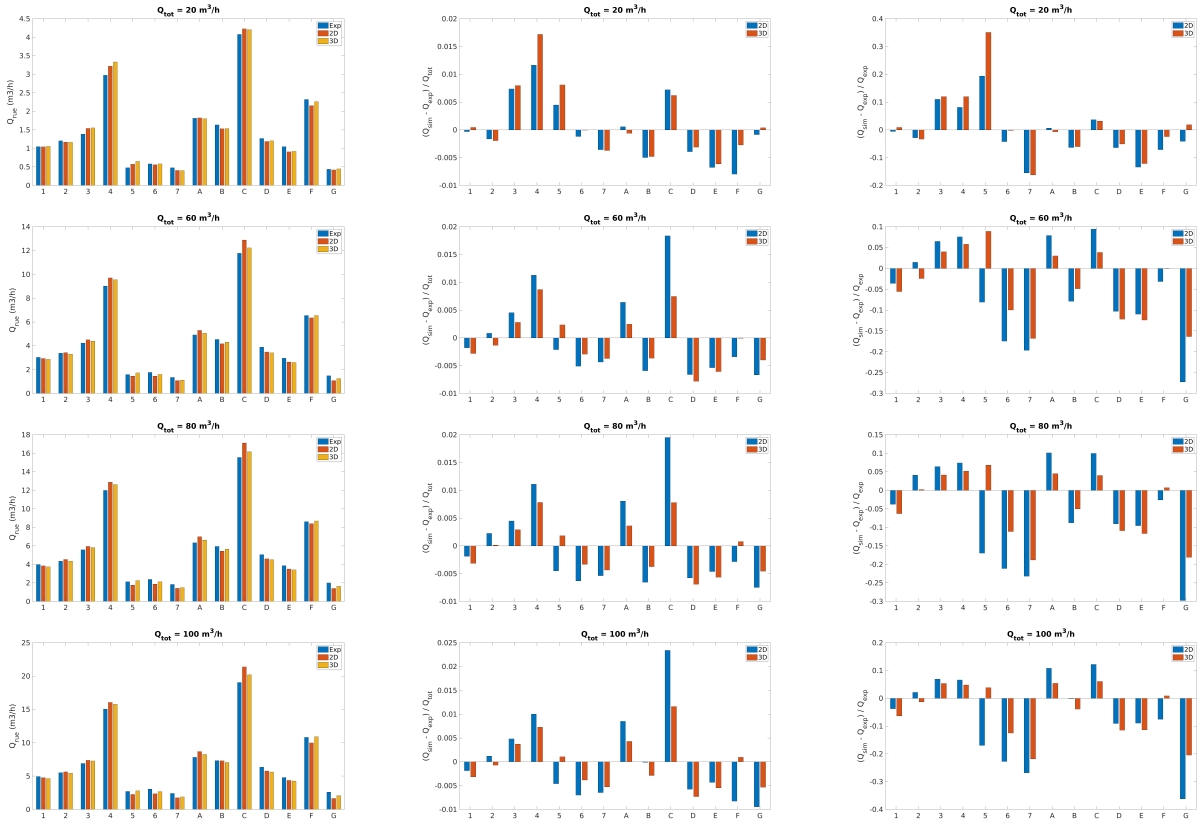

FIGURE 7.1 – Comparaison des débits mesurés et simulés à l'aval des rues. Pour chaque rue, Q_{sim} représente le débit sortant simulé (par une approche 2D ou 3D), Q_{exp} le débit expérimental sortant et Q_{tot} le débit total sortant du réseau de rues.

TABLE 7.1 – Caractérisation des erreurs moyennes et maximales obtenues en comparant les débits simulés et mesurés

		2D	3D
Qtot	Erreur max	$2,3\%$	$1,7\%$
	Erreur moyenne	$0,7\%$	$0,5\%$
Qrue	Erreur max	$36,2\%$	$35,1\%$
	Erreur moyenne	$12,2\%$	$8,2\%$

La figure 7.2 compare les hauteurs d'eau mesurées et simulées pour la configuration avec un débit total $Q_{tot} = 100\text{m}^3/\text{h}$ équiréparti entre les faces d'injection Nord et Ouest ($\phi_{ouest} = 50\%$). Les résultats issus des deux modèles montrent, en accord avec les mesures expérimentales, un gradient de hauteur d'eau orienté depuis le coin Nord-Ouest vers le coin Sud-Est. La modélisation 2D tend toutefois à surestimer la hauteur d'eau pour les points les plus éloignés des conditions limites aval (coin Nord-Ouest du réseau de rues) (voir figure 7.2 bas gauche). La carte des écarts relatifs sur les hauteurs d'eau modélisées montrent que la précision des modèles 2D et 3D est environ de 10% avec toutefois des écarts significatifs en termes de hauteurs avec des écarts pouvant atteindre 50% localement. Dans le cas du modèle 2D, les écarts sont plus marqués immédiatement à l'aval des carrefours. Ces zones correspondent aux endroits où les résultats 3D

montrent que l'hypothèse d'un profil de pression hydrostatique (employée par la modélisation 2D) n'est pas vérifiée.

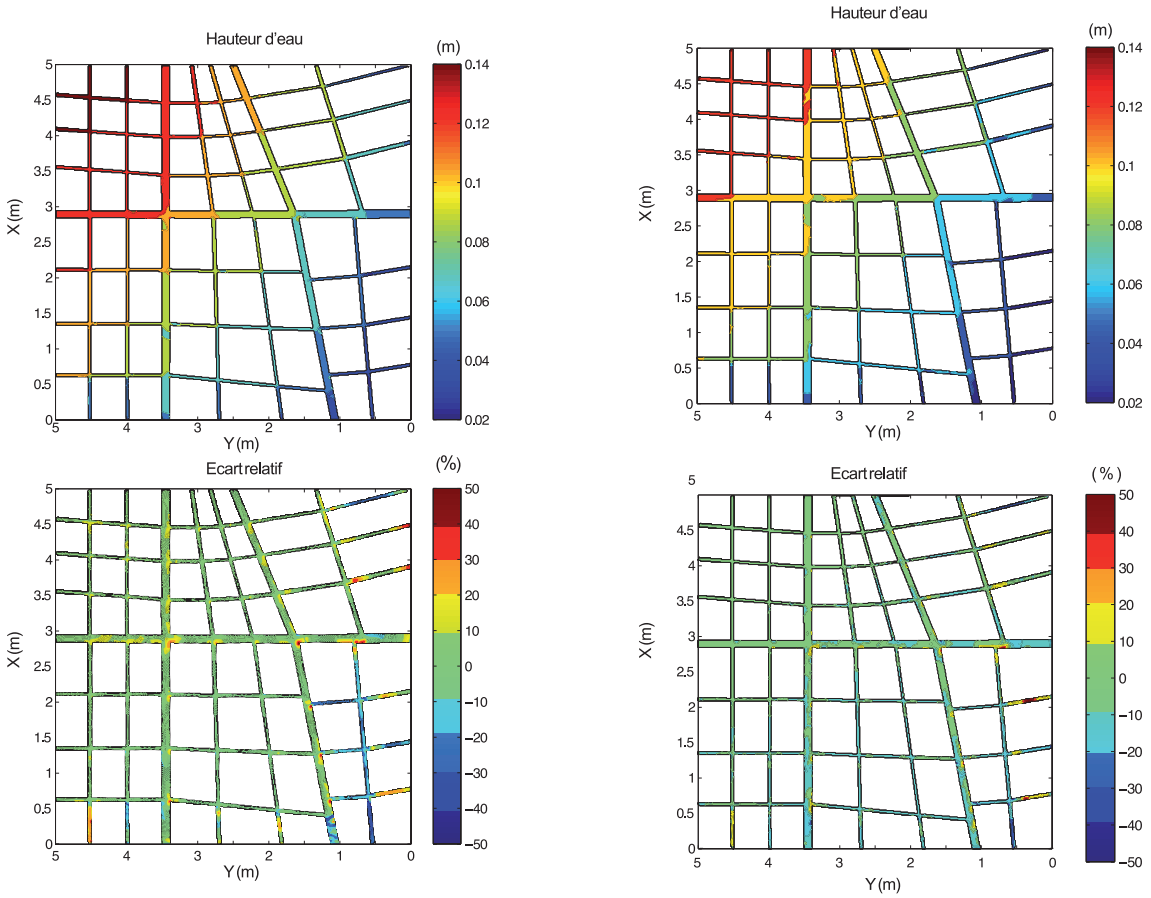

FIGURE 7.2 – Comparaison des hauteurs d'eau mesurées expérimentalement et simulées. Haut : cartes des hauteurs d'eau modélisées ; Bas : carte des écarts relatifs ; Gauche : avec Neptune2D ; Droite : avec Ansys-Fluent.

L'importance des phénomènes tridimensionnels dans le pilote expérimental peut a priori expliquer les difficultés rencontrées par l'approche 2D pour reproduire les données expérimentales. Actuellement, aucune donnée sur les champs de vitesses verticaux dans le pilote ne permet de confirmer ou d'infirmer cette hypothèse. Toutefois, des vitesses verticales significatives impliquent que le profil de pression n'est hydrostatique. La figure 7.3 présente les écarts entre la pression modélisée au fond du pilote par l'approche 3D et la pression hydrostatique normalisés par la pression hydrostatique. Au niveau de nombreux carrefours, l'écart entre la pression réelle et la pression hydrostatique est significatif (environ 10%). Ces écarts peuvent induire un mauvais bilan des forces s'exerçant sur le fluide au niveau des carrefours et ainsi modifier la répartition des débits. Il est ainsi probable que les écarts de répartition de débits entre les deux modélisations soient expliqués par l'incapacité de l'approche 2D à prendre en compte l'effet des pressions non-hydrostatique.

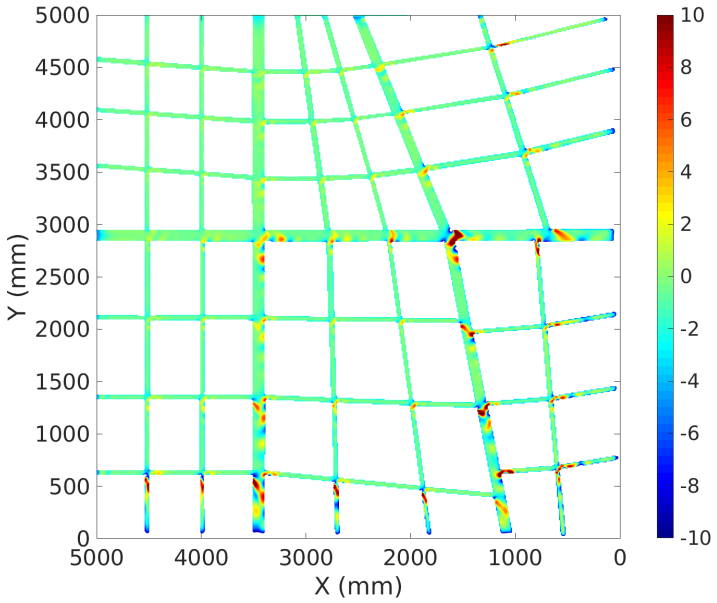

FIGURE 7.3 – Écart relatif entre la pression modélisée au fond du pilote par l'approche 3D et la pression hydrostatique

La confrontation de modèles numériques 2D et 3D aux données expérimentales montre que la modélisation 3D permet de reproduire plus finement la physique observée. Cette légère amélioration peut toutefois être contrebalancée par les coûts du 3D (à la fois en préparation du modèle et en simulation). L'intercomparaison des résultats issus des deux modèles montrent que les écarts peuvent s'expliquer en partie par l'invalidité de l'hypothèse d'un profil de pression hydrostatique employée dans les approches 2D. Cette observation devrait être investiguée plus avant expérimentalement et in-situ pour être confirmée ou infirmée. Le cas échéant, les approches de modélisation *nouvelle génération* devraient ainsi s'affranchir de cette hypothèse.

7.1.2 Analyse de sensibilité dans un réseau de rues

La modélisation d'inondations dans un réseau de rues implique un nombre conséquent de conditions limites par rapport à une modélisation en cours d'eau ; par exemple : 28 conditions limites (1 par rue) pour le pilote Icube contre seulement 2 (Amont et Aval) pour un cours d'eau. L'augmentation du nombre de paramètres et la difficulté opérationnelle pour estimer chaque condition à la limite dans un réseau de rues peut se traduire par une incertitude de modélisation conséquente. Dans le cadre opérationnel, l'estimation de cette incertitude passe souvent par l'emploi d'une méthode OAT (One At a Time). Cette approche consiste à étudier la variation de résultats d'une simulation en perturbant chaque paramètre indépendamment des autres. La limite d'une telle approche réside essentiellement dans l'impossibilité de détecter les interactions entre paramètres d'entrée (qui peuvent être importante pour des systèmes d'équations non-linéaires comme les équations de Saint-Venant). Une méthode globale de décomposition de la variance est ainsi privilégiée [49, 54, 53] pour caractériser la sensibilité des résultats du modèle à ses paramètres. L'inconvénient d'une telle méthode reste le nombre important de simulations à réaliser pour décrire correctement l'espace des paramètres.

Une modélisation de la configuration expérimentale avec un débit total injecté $Q_{tot} = 80\text{m}^3/\text{h}$ équiréparti entre les faces amont a été réalisée avec Telemac2D. Une analyse de convergence au maillage et une calibration du coefficient de Strickler K ont été réalisées. La sensibilité des résultats à quatre paramètres est évaluée : Q_{Ouest} et Q_{Nord} les débits d'entrée sur les faces Ouest et Nord, la hauteur d'eau en sortie h_{out} et un coefficient de frottement uniforme K. Les gammes de variations des paramètres sont déterminées à partir

des incertitudes expérimentales ($Q^{cal}_{north} \pm 5\%$, $Q^{cal}_{west} \pm 5\%$; $h^{cal}_{out} \pm 10\%$ et $K^{cal} \pm 50\%$). $N_s = 2000$ jeux de paramètres permettent une bonne estimation a des indices de Sobol d'ordre 1 dans cette configuration avec la méthode de [49].

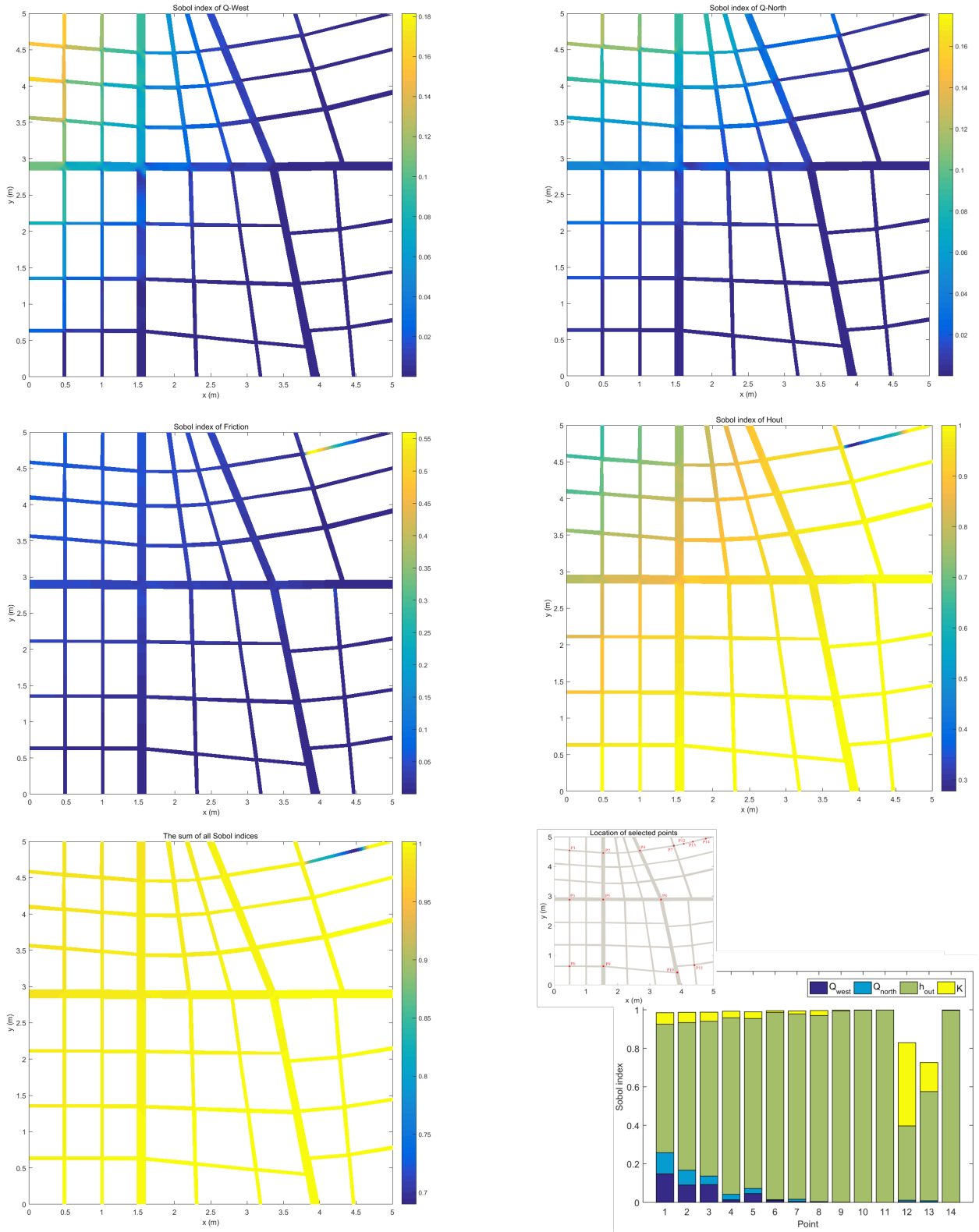

FIGURE 7.4 – Sensibilité des résultats de simulation pour un débit entrant total de $80\text{m}^3/\text{h}$ équiréparti entre faces Nord et Ouest. Les cartes représentent le pourcentage de la variance de la hauteur d'eau locale expliquée par chaque paramètre ; Haut Gauche : Q_{Ouest} ; Haut Droite : Q_{Nord} ; Milieu Gauche : K ; Milieu Droite : h_{out} ; Bas Gauche : Somme des indices de Sobol d'ordre 1 ; Bas Droite : Décomposition des sensibilités locales des hauteurs d'eau.

La figure 7.4 présente les cartes des indices de Sobol d'ordre 1 pour la hauteur d'eau. Ces indices correspondent au pourcentage de la variance de la hauteur d'eau locale expliquée par chaque paramètre. La somme de ces indices (figure 7.4, bas gauche) est partout inférieure ou égale à 1 indiquant que le nombre de simulations ($N = 2000$) est suffisant au vue de l'espace des paramètres testés. Il est intéressant de noter que cette somme diminue significativement à l'aval de la rue 1, endroit dans lequel l'écoulement est torrentiel juste à l'aval du carrefour G1 et présente un ressaut hydraulique avant l'exutoire aval de cette rue. La présence de cette structure induit une forte variabilité des hauteurs d'eau et une potentielle équifinalité entre les paramètres (coefficient de Strickler, débit dans la rue et hauteur d'eau) qui peut expliquer l'importance des coefficients de Sobol d'ordre supérieur à 1. Il faudrait également vérifier la validité de la méthode d'estimation des indices de Sobol dans de telles configurations hydrauliques.

La hauteur d'eau à la condition limite aval h_{out} et le coefficient de Strickler K sont les paramètres expliquant principalement la variance de la hauteur d'eau (entre 30 et 100% pour h_{out} et jusqu'à 55% pour le coefficient de Strickler contre au plus 18% pour les débits Q_{Ouest} et Q_{Nord}. La sensibilité à K et h_{out} évolue globalement dans la direction Nord-Ouest vers Sud-Est avec une décroissance (respectivement croissance) suivant cette direction de la sensibilité à K (respectivement h_{out}). Le gradient de sensibilité aux débits amonts (Q_{Ouest} et Q_{Nord}) suivent cette même direction et l'effet de conditions limites amont diminue pour être quasiment nulle à l'aval. Cette analyse montre ainsi l'importance des conditions limites (en particulier aval) sur la détermination du champs de hauteur d'eau dans le réseau de rues. La définition de l'étendue des modèles opérationnels est donc particulièrement critique pour garantir la meilleure fiabilité des résultats.

7.2 Développement de nouvelles approches pour la modélisation des inondations

Une partie conséquente de ma recherche est consacrée au développement de nouvelles approches pour la modélisation des inondations, en particulier en milieu urbain. Ces travaux ont été réalisés dans le cadre de plusieurs thèses de doctorat (voir section 3.3.1) et ont été publiés dans plusieurs articles et actes de conférences (voir section 3.1). J'ai également développé (ou contribué à développer) quatre logiciels de modélisation des inondations. Le tableau 7.2 organise ces travaux selon l'objectif visé : le développement de nouveaux modèles ou la mise au point de méthodes numériques. Par soucis de concision, seule une partie de ces travaux sont présentés ici afin d'illustrer mes différentes actions de développement et notamment celles que je souhaite poursuivre prochainement.

TABLE 7.2 – Tableau de synthèse

Développement de modèles	Thèse	Publication	Code
Modèle 1D/2D pour les inondations en rivière	P. Finaud-Guyot [13]	ACL12, ACL11	SW12D
Modèle Discontinuous Galerkin	Q. Araud [2]		Neptune2D
Modèle d'échange rue-bâti	C. Choley	ACLprep4, ACLprep12	SW2D Lemon
Modèle 1D/2D pour les inondations urbaines	S. Chen [6]	C-ACT6	Flood1D2D

Mise au point de méthodes numériques	Thèse	Publication
Solveur de Riemann PorAS	P. Finaud-Guyot [13]	ACL14
Schéma EVR-DG	Q. Araud [2]	ACL10
Calcul de la sensibilité directe	-	ACL13

7.2.1 Solveur de Riemann PorAS pour la résolution des équations à porosité

La modélisation macroscopique des inondations urbaines considère la zone urbaine comme un milieu poreux. L'effet du bâti sur l'écoulement n'est plus pris en compte en représentant les murs dans la simulation mais plutôt en représentant leurs effets à travers une porosité définissant l'espace disponible pour l'écoulement. Il existe aujourd'hui plusieurs systèmes, basés sur les équations shallow water et paramétrisés par une ou

plusieurs porosités. Les équations shallow water 1D [1] à porosité uniforme s'écrivent de manière générique :

$$\frac{\partial \mathbf{U}}{\partial t} + \frac{\partial \mathbf{F}}{\partial x} = \mathbf{S} \tag{7.1}$$

où $\mathbf{U}$ est le vecteur des variables conservées, $\mathbf{F}$ est le vecteur flux et $\mathbf{S}$ le vecteur des termes sources :

$$\mathbf{U} = \begin{bmatrix} \phi h \\ \phi q \end{bmatrix} \quad \mathbf{F} = \begin{bmatrix} \phi q \\ \phi \dfrac{q^2}{h} + \dfrac{1}{2} g h^2 \end{bmatrix} \quad \mathbf{S} = \begin{bmatrix} 0 \\ g\phi h \left(S_0 - S_f\right) + g h^2 \dfrac{\partial \phi}{\partial x} \end{bmatrix} \tag{7.2}$$

où g représente l'accélération de la pesanteur, ϕ est la porosité *i.e.* le ratio entre la surface de la maille disponible pour l'écoulement et la surface totale de la maille, h est la hauteur d'eau et q le débit unitaire. $S_0 = -\partial z_b / \partial x$ est la pente du fond (avec z_b la cote du fond) et $S_f = \left[u / \left(K h^{2/3}\right)\right]^2$ la pente de la ligne des frottements. Dans la suite, on considère $S_f = 0$ pour ne pas prendre en compte l'effet des frottements pour le calcul des flux à travers l'interface entre deux mailles. Numériquement, ce terme est pris en compte de manière séparée avec un algorithme de type *time-splitting*.

La résolution de ces équations par une approche aux volumes finis permet d'estimer la valeur du vecteur $\mathbf{U}_i^{n+1}$ dans la maille i au temps t^{n+1} à partir des valeurs au temps t^n et des flux traversant les interfaces de la maille i :

$$\mathbf{U}_i^{n+1} = \mathbf{U}_i^n - \frac{\Delta t}{\phi_i \Omega_i} \left[\sum_{j \in N(i)} L_j \mathbf{F}_j \cdot \mathbf{n}_j + \mathbf{S}\left(\mathbf{U}_i^n\right) \right] \tag{7.3}$$

où Δt représente le pas de temps de calcul, $N(i)$ la liste des interfaces délimitant la maille i, L_j la longueur de l'interface j, $\mathbf{n}_j$ le vecteur unitaire normal à l'interface j et orienté vers l'extérieur de la maille i. Pour garantir la stabilité du schéma numérique, Δt doit vérifier la condition CFL : $\Delta t \leq \Delta x / \max_j(\lambda_j)$ avec Δx la distance entre deux mailles et λ_j la célérité d'onde à travers l'interface j. $\mathbf{F}_j$ représente le vecteur des flux traversant l'interface j entre les dates t^n et t^{n+1}. Ce flux peut être déterminé en résolvant un problème de Riemann à travers l'interface j avec $\mathbf{U}_L$ et $\mathbf{U}_R$ les états gauche et droit du problème de Riemann.

Le système d'équations shallow water à porosité (7.1) est un système hyperbolique caractérisé par 2 équations. Il a donc existence de la matrice Jacobienne $\mathbf{A} = \partial \mathbf{F} / \partial \mathbf{U}$ qui admet deux valeurs propres : $\lambda_1 = u - c$ et $\lambda_2 = u + c$ avec $c = \sqrt{gh}$ la célérité des ondes de pression. En multipliant (7.1) à gauche par $\mathbf{A}$, il vient :

$$\begin{aligned} \mathbf{A}\frac{\partial \mathbf{U}}{\partial t} + \mathbf{A}\frac{\partial \mathbf{F}}{\partial x} &= \mathbf{A}\mathbf{S} \\ \frac{\partial \mathbf{F}}{\partial \mathbf{U}}\frac{\partial \mathbf{U}}{\partial t} + \mathbf{A}\frac{\partial \mathbf{F}}{\partial x} &= \mathbf{A}\mathbf{S} \\ \frac{\partial \mathbf{F}}{\partial t} + \mathbf{A}\frac{\partial \mathbf{F}}{\partial x} &= \mathbf{A}\mathbf{S} \end{aligned} \tag{7.4}$$

Ce système d'équations est lui aussi hyperbolique et en introduisant $\mathbf{K}$, $\mathbf{K}^{-1}$ et $\mathbf{\Lambda}$ les matrices des vecteurs propres de $\mathbf{A}$ et son inverse ainsi que la matrice des valeurs propres de $\mathbf{A}$, on obtient :

$$\begin{aligned} \frac{\partial \mathbf{F}}{\partial t} + \mathbf{A}\frac{\partial \mathbf{F}}{\partial x} &= \mathbf{A}\mathbf{S} \\ \mathbf{K}^{-1}\frac{\partial \mathbf{F}}{\partial t} + \mathbf{K}^{-1}\mathbf{A}\frac{\partial \mathbf{F}}{\partial x} &= \mathbf{K}^{-1}\mathbf{A}\mathbf{S} \\ \mathbf{K}^{-1}\frac{\partial \mathbf{F}}{\partial t} + \mathbf{K}^{-1}\mathbf{A}\mathbf{K}\mathbf{K}^{-1}\frac{\partial \mathbf{F}}{\partial x} &= \mathbf{K}^{-1}\mathbf{A}\mathbf{K}\mathbf{K}^{-1}\mathbf{S} \\ \mathbf{K}^{-1}\frac{\partial \mathbf{F}}{\partial t} + \mathbf{\Lambda}\mathbf{K}^{-1}\frac{\partial \mathbf{F}}{\partial x} &= \mathbf{\Lambda}\mathbf{K}^{-1}\mathbf{S} \\ \frac{\partial \mathbf{W}}{\partial t} + \mathbf{\Lambda}\frac{\partial \mathbf{W}}{\partial x} &= \mathbf{\Lambda}\mathbf{S}' \end{aligned} \tag{7.5}$$

1. Dans les configurations 2D, il est possible de se ramener à un problème 1D en projetant les équations dans le référentiel associé à l'interface entre deux mailles de calcul.

avec $\mathrm{d}\mathbf{W} = \mathbf{K}^{-1}\mathrm{d}\mathbf{F}$ et $\mathbf{S}' = \mathbf{K}^{-1}\mathbf{S}$:

$$\mathrm{d}\mathbf{W} = \frac{1}{2c}\begin{bmatrix} \lambda_2 dF1 - dF2 \\ -\lambda_1 dF1 + dF2 \end{bmatrix}, \quad \mathbf{S}' = \frac{1}{2c}\begin{bmatrix} -g\phi h S_0 - gh^2\dfrac{\partial \phi}{\partial x} \\ g\phi h S_0 + gh^2\dfrac{\partial \phi}{\partial x} \end{bmatrix} = \frac{1}{2c}\begin{bmatrix} -S \\ +S \end{bmatrix} \tag{7.6}$$

L'équation (7.5) est équivalente au système d'équations :

$$\frac{\mathrm{d}W_k}{\mathrm{d}t} = \lambda_k S'_k \text{ suivant } \frac{\mathrm{d}x}{\mathrm{d}t} = \lambda_k, \quad k = \{1,2\} \tag{7.7}$$

où W_k est l'invariant de Riemann suivant la caractéristique k et où $\mathrm{d}W_k = \sum_{l=1}^{2} K^{-1}_{l,k}\mathrm{d}F_l$ avec $K^{-1}_{l,k}$ la valeur de la ligne k et de la colonne l de la matrice $\mathbf{K}^{-1}$. Sous l'hypothèse que λ_k est constante sur le pas de temps de calcul (ce qui est justifié au vue de la finesse de la discrétisation temporelle imposée par la condition *CFL*), (7.7) peut être intégrée entre $A_k\left(x_k, t^n\right)$ le pied de la caractéristique λ_k au temps t^n et $M\left(x_{i+1/2}, t^{n+1/2}\right)$ l'interface au temps $t^{n+1/2}$:

$$\begin{aligned} \int_{A_k(x_k,t^n)}^{M\left(x_{i+1/2},t^{n+1/2}\right)} \mathrm{d}W_k &= \int_{t^n}^{t^{n+1/2}} \lambda_k \overline{S'_k}\mathrm{d}t, \quad k = \{1,2\} \\ \int_{A_k(x_k,t^n)}^{M\left(x_{i+1/2},t^{n+1/2}\right)} \sum_{l=1}^{2} K^{-1}_{l,k}\mathrm{d}F_l &= \int_{t^n}^{t^{n+1/2}} \lambda_k \overline{S'_k}\mathrm{d}t, \quad k = \{1,2\} \end{aligned} \tag{7.8}$$

où $\overline{S'_k}$ est la moyenne de S'_k le long du chemin d'intégration et où :

$$K^{-1}_{l,k} = \begin{cases} K^{-1}_{l,k}\left(\mathbf{U}_L\right) & \text{si } \lambda_k < 0 \\ K^{-1}_{l,k}\left(\mathbf{U}_R\right) & \text{si } \lambda_k > 0 \end{cases} \tag{7.9}$$

Sur le chemin d'intégration, λ_k et $K^{-1}_{l,k}$ sont constants et (7.8) peut donc s'écrire :

$$\begin{aligned} \sum_{l=1}^{2} K^{-1}_{l,k} \int_{A(x_k,t^n)}^{M\left(x_{i+1/2},t^{n+1/2}\right)} \mathrm{d}F_l &= \int_{t^n}^{t^{n+1/2}} \lambda_k \overline{S'_k}\mathrm{d}t, \quad k = \{1,2\} \\ \sum_{l=1}^{2} K^{-1}_{l,k}\left(F_{l,M} - F_{l,A_k}\right) &= \int_{t^n}^{t^{n+1/2}} \lambda_k \overline{S'_k}\mathrm{d}t, \quad k = \{1,2\} \end{aligned} \tag{7.10}$$

avec A_k à gauche de l'interface pour $\lambda_k > 0$, à droite sinon. En supposant que les deux ondes λ_1 et λ_2 caractérisent deux ondes de raréfaction, on a $\lambda_1 < 0$ et $\lambda_2 > 0$:

$$\begin{cases} \sum_{l=1}^{2} K^{-1}_{l,R}\left(F_{l,M} - F_{l,R}\right) = \int_{t^n}^{t^{n+1/2}} \lambda_1 \overline{S'_1}\mathrm{d}t \\ \sum_{l=1}^{2} K^{-1}_{l,L}\left(F_{l,M} - F_{l,L}\right) = \int_{t^n}^{t^{n+1/2}} \lambda_2 \overline{S'_2}\mathrm{d}t \end{cases}$$
$$\begin{cases} \lambda_2\left(F_{1,M} - F_{1,R}\right) - \left(F_{2,M} - F_{2,R}\right) = \frac{\Delta t}{2}\lambda_1 \overline{S'} = -\lambda_1 S_1 \\ -\lambda_1\left(F_{1,M} - F_{1,L}\right) + \left(F_{2,M} - F_{2,L}\right) = \frac{\Delta t}{2}\lambda_2 \overline{S'} = \lambda_2 S_2 \end{cases} \tag{7.11}$$

En supposant $S_1 = S_2$, la résolution du système (7.11) permet d'estimer les flux à l'interface :

$$\begin{cases} F_{1,M} = \frac{1}{\lambda_2 - \lambda_1}\left[F_{2,L} - F_{2,R} + \lambda_2 F_{1,R} - \lambda_1 F_{1,L} + S^{(1)}\right] \\ F_{2,M} = \frac{1}{\lambda_2 - \lambda_1}\left[\lambda_2 F_{2,L} - \lambda_1 F_{2,R} + \lambda_2\lambda_1\left(F_{1,R} - F_{1,L}\right) + \left(\lambda_2 + \lambda_1\right) S^{(2)}\right] \end{cases} \tag{7.12}$$

$S^{(1)}$ et $S^{(2)}$ sont les termes source "topographiques" correspondant aux effets des variations de topographie et de porosité à l'interface :

$$
\begin{aligned}
S^{(1)} &= \frac{1}{2} g \left(h_{LR}^{(1)}\right)^2 (\phi_R - \phi_L) - (\phi h)_{LR}^{(1)} (z_{b,R} - z_{b,L}) \\
S^{(2)} &= \frac{1}{2} g \left(h_{LR}^{(2)}\right)^2 (\phi_R - \phi_L) - (\phi h)_{LR}^{(2)} (z_{b,R} - z_{b,L})
\end{aligned}
\tag{7.13}
$$

Ces expressions font intervenir les termes $(\phi h)_{LR}^{(1)}$, $(\phi h)_{LR}^{(2)}$, $\left(h_{LR}^{(1)}\right)^2$ et $\left(h_{LR}^{(2)}\right)^2$ qui doivent être estimés à l'interface. La réalisation de bilans de masse et de quantité de mouvement permettent de déterminer des valeurs de ces termes afin de préserver les conditions d'équilibre statique (voir [14]) :

$$
\begin{aligned}
(\phi h)_{LR}^{(1)} &= \min(\phi_L; \phi_R) \left(z_{LR} - \frac{z_{b,L} + z_{b,R}}{2}\right) \\
\left(h_{LR}^{(1)}\right)^2 &= \begin{cases} h_L & \text{si } \phi_L > \phi_R \\ h_R & \text{si } \phi_L < \phi_R \end{cases} \\
z_{LR} &= \begin{cases} z_L & \text{si } z_{b,L} > z_{b,R} \\ z_R & \text{si } z_{b,L} < z_{b,R} \end{cases} \\
(\phi h)_{LR}^{(2)} &= 0 \\
\left(h_{LR}^{(2)}\right)^2 &= 0
\end{aligned}
\tag{7.14}
$$

Ce nouveau solveur de Riemann PorAS a été validé sur plusieurs cas tests. La figure 7.5 présente une comparaison des résultats simulés avec les solveurs PorAS et HLLC avec la solution semi-analytique pour un écoulement permanent au-dessus d'une surélévation du fond. Les deux solveurs reproduisent fidèlement la hauteur d'eau sur la bosse. En revanche, seul le solveur PorAS arrive à produire un profil de débit unitaire correct. L'incapacité du solveur HLLC a produire un profil de débit unitaire constant est lié au fait que le solveur HLLC n'est plus well-balanced pour des équations à porosité [22, 32]. La figure 7.6 compare la solution semi-analytique avec celles des solveurs PorAS et HLLC pour un écoulement permanent dans un rétrécissement. Les deux solveurs reproduisent fidèlement la hauteur d'eau dans le rétrécissement, même en configuration transcritique. Le solveur PorAS est également validé sur des cas tests transitoires avec et sans porosité [14]. Il permet ainsi de résoudre les équations shallow water à porosité isotrope.

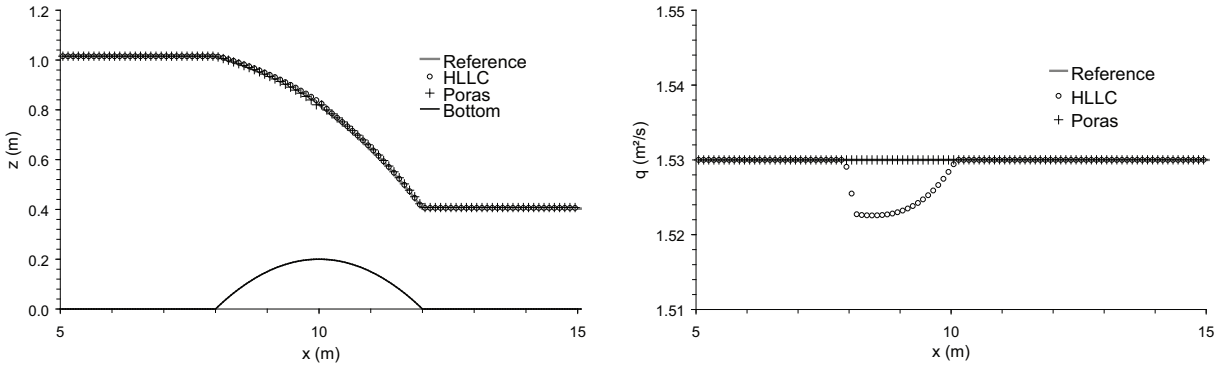

(a) profil de hauteur d'eau

(b) débit unitaire

FIGURE 7.5 – Écoulement permanent sur une surélévation du fond.

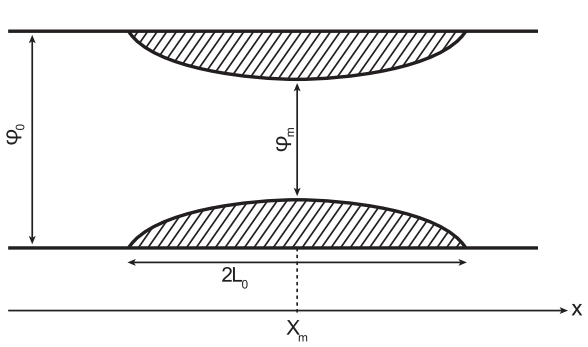

(a) distribution de la porosité : $X_m = 50\text{m}$, $L_0 = 25\text{m}$, $\phi_0 = 1$ et $\phi_m = 0,5$

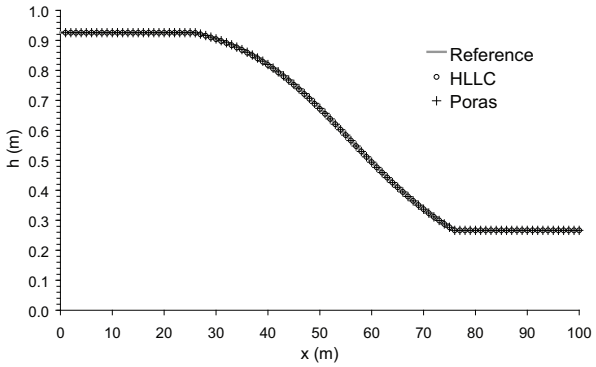

(b) profil de hauteur d'eau

FIGURE 7.6 – Écoulement permanent dans un rétrécissement.

7.2.2 Modèle *1D/2D* opérationnel pour la modélisation des inondations urbaines

Les écoulements dans les intersections de rues décrits dans la littérature et observés dans le pilote Icube d'étude des inondations urbaines montrent la présence de zone de recirculation dans les rues aval des carrefours. Ces contractions d'écoulement, induisent localement des accélérations, pouvant produire un changement de régime avec un passage de fluvial à l'amont du carrefour à torrentiel à l'aval (comportement observé qualitativement dans tous les derniers tronçons de rue des expériences sans seuil ; voir section 6).

D'un point de vue opérationnel, la connaissance des champs de hauteur et de vitesse 1D dans chaque rue est généralement suffisante. La modélisation 1D des rues semblent donc suffisante toutefois, la physique des écoulements dans les carrefours impose une approche 2D dans la mesure où les modèles de répartition de débit au carrefour restent trop spécifiques à certaines configurations (3 branches, permanent, sections identiques, absence de changement de régime, ...).

Ces deux constations suggèrent la mise au point d'un modèle pour la reproduire des inondations urbaines, 2D dans les carrefours et 1D dans les rues sans direction supposée pour l'écoulement. Le couplage 1D-2D est réalisé à l'aide d'une approche *cut-cell*. Afin de faciliter les calculs numériques au droit du couplage mais également pour permettre aux zones 1D de reproduire les pertes de charge liées aux changement de direction (ce que ne peut faire un modèle 1D classique), l'hydrodynamique de toutes les mailles est représentée par un modèle shallow water 2D :

$$\frac{\partial}{\partial t}\begin{bmatrix} h \\ q \\ r \end{bmatrix} + \frac{\partial}{\partial x}\begin{bmatrix} q \\ \frac{q^2}{h} + \frac{1}{2}gh^2 \\ \frac{qr}{h} \end{bmatrix} + \frac{\partial}{\partial y}\begin{bmatrix} r \\ \frac{qr}{h} \\ \frac{r^2}{h} + \frac{1}{2}gh^2 \end{bmatrix} = \begin{bmatrix} 0 \\ gh\left(S_{0,x} - S_{f,x}\right) \\ gh\left(S_{0,y} - S_{f,y}\right) \end{bmatrix} \tag{7.15}$$

avec t (respectivement x et y) la coordonnée de temps (respectivement les coordonnées d'espace), g l'accélération gravitationnelle, h représente la hauteur d'eau, q (respectivement r) le débit unitaire dans la direction x (respectivement y). $S_{0,x}$ (respectivement $S_{0,y}$) est la pente du fond dans la direction x (respectivement y) et $S_{f,x}$ (respectivement $S_{f,y}$) la pente de la ligne des frottements dans la direction x (respectivement y) exprimée à partir de la formule de Strickler :

$$S_{0,x} = -\frac{\partial z_b}{\partial x} \quad S_{0,y} = -\frac{\partial z_b}{\partial y} \quad S_{f,x} = \frac{(u^2+v^2)^{1/2}}{K^2 h^{4/3}}u \quad S_{f,y} = \frac{(u^2+v^2)^{1/2}}{K^2 h^{4/3}}v \tag{7.16}$$

où z_b est la cote du fond, K le coefficient de Strickler et $u = q/h$ (respectivement $v = r/h$) la vitesse dans la direction x (respectivement y).

Dans les rues modélisées avec une unique maille sur la largeur (approche 1D), ce modèle est incapable de prendre en compte l'effet des zones de recirculations présentes à l'aval des carrefours. Une approche effective est donc employée considérant que les mailles 1D représentent la totalité de la largeur de la rue et peuvent contenir deux domaines différents (voir figure 7.7) :

Ω_u la zone d'écoulement ineffectif du fait de la recirculation et pour laquelle le vecteur vitesse modélisé est supposé nul ;

Ω_v la zone d'écoulement contracté par la recirculation.

La contraction est représentée par $\phi = L_v/L$ avec $L = L_u + L_v$ où L représente la largeur totale de la maille 1D (et donc de la rue) et L_u (respectivement L_v) est la largeur de la recirculation (respectivement de l'écoulement contracté). Cette définition de ϕ, correspondant à une largeur effective d'écoulement, est analogue à une porosité telle que définie par [31].

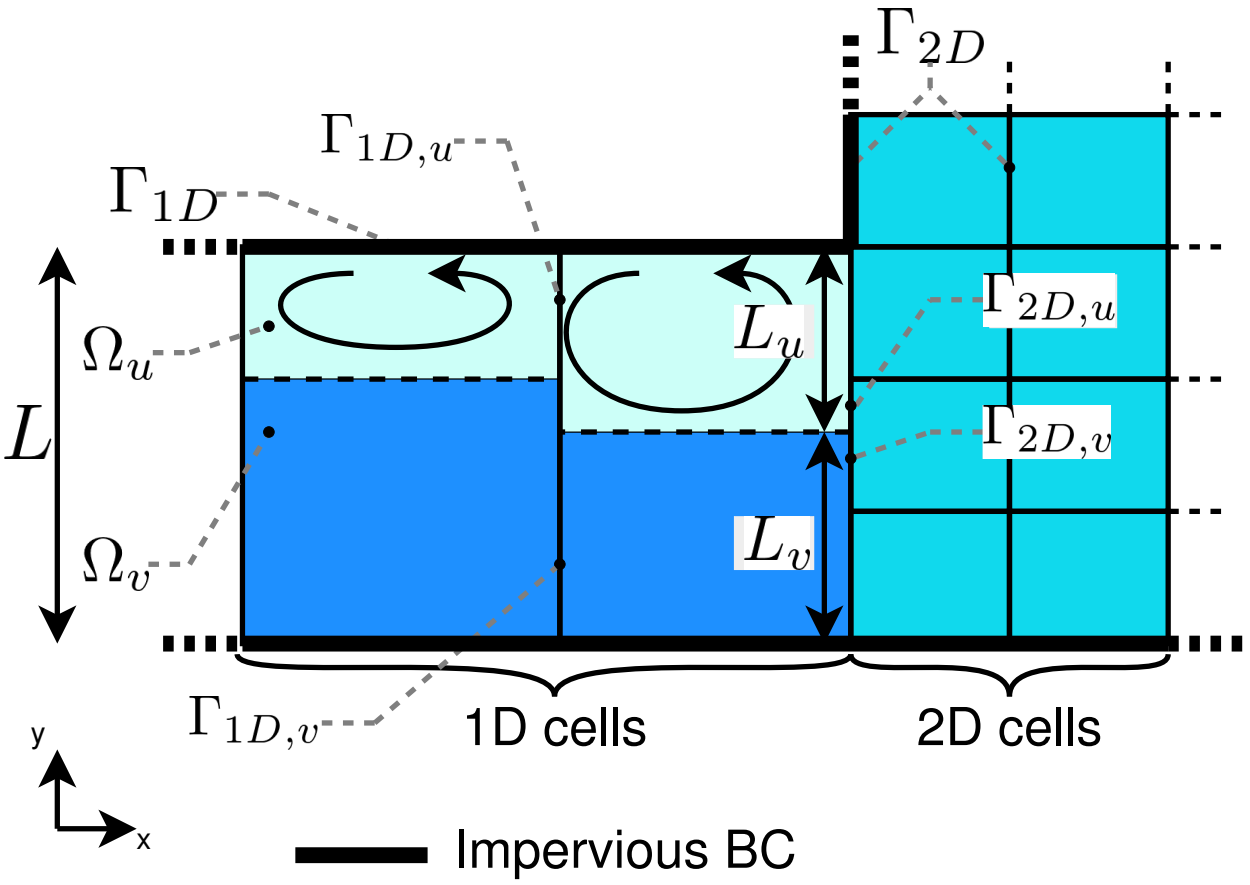

FIGURE 7.7 – Schéma d'une configuration classique avec un couplage 1D/2D "frontal" à proximité d'un carrefour

Les équations shallow water 2D sont discrétisées avec une approche aux volumes finis :

$$\mathbf{U}_i^{n+1} = \mathbf{U}_i^n - \Delta t \left[\frac{1}{A_i} \sum_{j \in N(i)} \mathbf{P}_{i,j} L_j \mathbf{F}_j^n + \mathbf{S}(\mathbf{U}_i^n) \right] \tag{7.17}$$

où $\mathbf{U}_i = [h\ q\ r]^T$ est le vecteur des variables modélisées, $\mathbf{F}_j^n$ représente les flux de Riemann à travers l'interface j, $\mathbf{S}(\mathbf{U}_i^n)$ est le vecteur des termes source qui s'appliquent sur la maille i, L_j est la longueur de l'interface j

et $\mathbf{P}_{i,j}$ est la matrice de passage entre le système de coordonnées global et celui attaché à l'interface j de la maille i et $N(i)$ représente l'ensemble des interfaces entourant la maille i.

Du fait de la topologie du maille considéré, l'ensemble des interfaces entourant la maille i, $N(i)$ peut être décomposé $N(i) = N_{1D,w} \cup N_{1D,BC} \cup N_{1D1D} \cup N_{2D,BC} \cup N_{2D2D} \cup N_{1D2D}$ en différents ensembles d'interfaces en fonction de la nature des éléments à gauche et à droite de l'interface :

$N_{1D,W}$	est l'ensemble des interfaces d'une maille 1D correspondant à un mur
$N_{1D,BC}$	est l'ensemble des interfaces d'une maille 1D correspondant à une condition limite du modèle
$N_{2D,BC}$	est l'ensemble des interfaces d'une maille 2D correspondant à une condition limite du modèle
N_{1D1D}	est l'ensemble des interfaces entre deux mailles 1D
N_{2D2D}	est l'ensemble des interfaces entre deux mailles 2D
N_{1D2D}	est l'ensemble des interfaces entre une maille 1D et une maille 2D

Les ensembles $N_{1D,w}$, N_{1D1D} et N_{1D2D} regroupent des interfaces pouvant être en contact avec les deux domaines d'écoulement Ω_u et Ω_v définis à l'échelle sous-maille. Ces ensembles sont donc redivisés : $N_{1D,W} \cup N_{1D1D} \cup N_{1D2D} = (N_{1D,Wu} \cup N_{1D,Wv}) \cup (N_{1D1D,u} \cup N_{1D1D,v}) \cup (N_{1D2D,u} \cup N_{1D2D,v})$.

L'équation (7.17) devient ainsi :

$$\begin{aligned}
\mathbf{U}_i^{n+1} = \mathbf{U}_i^n & \\
& - \frac{\Delta t}{A_i} \sum_{j \in N_{1D,BC} \cup N_{2D,BC}} \mathbf{P}_{i,j} L_j \mathbf{F}_j^n \\
& - \frac{\Delta t}{A_i} \sum_{j \in N_{2D2D}} \mathbf{P}_{i,j} L_j \mathbf{F}_j^n \\
& - \frac{\Delta t}{A_i} \sum_{j \in N_{1D,Wu} \cup N_{1D1D,u} \cup N_{1D2D,u}} \mathbf{P}_{i,j} L_{u,j} \mathbf{F}_{u,j}^n \\
& - \frac{\Delta t}{A_i} \sum_{j \in N_{1D,v} \cup N_{1D1D,v} \cup N_{1D2D,v}} \mathbf{P}_{i,j} L_{v,j} \mathbf{F}_{v,j}^n \\
& - \Delta t \mathbf{S}(\mathbf{U}_i^n)
\end{aligned} \tag{7.18}$$

où la longueur $L_{u,j}$ (respectivement $L_{v,j}$) représente la largeur de la recirculation (respectivement de l'écoulement contracté) le long de l'interface j. $L_{u,j}$ est estimée comme la moyenne des largeurs de recirculation de part et d'autre : $L_{u,j} = (L_{u,L} + L_{u,R})/2$ où l'indice $_L$ (respectivement $_R$) fait référence à la maille du coté gauche (respectivement droit) de l'interface. En prenant en compte la définition de ϕ, il vient $L_u = (1 - \phi) \times L_j$ et donc :

$$\begin{aligned}
L_{u,j} = \frac{(L_{u,L} + L_{u,R})}{2} = \left[1 - \frac{\phi_L + \phi_R}{2}\right] \times L_j \\
L_{v,j} = \frac{\phi_L + \phi_R}{2} \times L_j
\end{aligned} \tag{7.19}$$

Les flux ($\mathbf{F}_j^n$, $\mathbf{F}_{u,j}^n$ et $\mathbf{F}_{v,j}^n$), à travers chaque type d'interface, sont calculés à l'aide du solveur de Riemann PorAS (voir section 7.2.1) paramétrisé en fonction des états gauche et droit de chaque interface. Le tableau 7.3 explicite comme le solveur de Riemann est paramétrisé pour prendre en compte les spécificité des états gauche et droit de chaque interface.

TABLE 7.3 – Description du calcul des flux de Riemann. $\mathbf{F}_1$ est le flux de masse à travers l'interface, $\mathbf{F}_2$ (respectivement $\mathbf{F}_3$) est le flux de quantité de mouvement dans la direction normale (respectivement tangentielle) à l'interface. L'exposant ^{r} indique les flux calculés par le solveur de Riemann PorAS (voir section 7.2.1).

Ensemble	Domaine		$\mathbf{U}_L$	$\mathbf{U}_R$	ϕ_k	Flux		
	Gauche où 1D	Droite où 2D				$\mathbf{F}_1$	$\mathbf{F}_2$	$\mathbf{F}_3$
$N_{1D1D,u}$	$\Omega_{1D,u}$	$\Omega_{1D,u}$	$\begin{bmatrix} h & 0 & 0 \end{bmatrix}$	$\begin{bmatrix} h & 0 & 0 \end{bmatrix}$	$\frac{\phi_L+\phi_R}{2}$	0	$\mathbf{F}_2^r$	$\mathbf{F}_3^r$
$N_{1D1D,v}$	$\Omega_{1D,v}$	$\Omega_{1D,v}$	$\begin{bmatrix} h & \frac{q}{\phi} & \frac{r}{\phi} \end{bmatrix}$	$\begin{bmatrix} h & \frac{q}{\phi} & \frac{r}{\phi} \end{bmatrix}$	$\frac{\phi_L+\phi_R}{2}$	$\mathbf{F}_1^r$	$\mathbf{F}_2^r$	$\mathbf{F}_3^r$
$N_{1D,Wu}$	$\Omega_{1D,u}$	Mur	$\begin{bmatrix} h & 0 & 0 \end{bmatrix}$	BC	1	0	$\mathbf{F}_2^r$	$\mathbf{F}_3^r$
$N_{1D,Wv}$	$\Omega_{1D,v}$	Mur	$\begin{bmatrix} h & \frac{q}{\phi} & \frac{r}{\phi} \end{bmatrix}$	BC	1	0	$\mathbf{F}_2^r$	$\mathbf{F}_3^r$
$N_{1D2D,u}$	$\Omega_{1D,u}$	Ω_{2D}	$\begin{bmatrix} h & 0 & 0 \end{bmatrix}$	$\begin{bmatrix} h & q & r \end{bmatrix}$	ϕ_{1D}	0	$\mathbf{F}_2^r$	$\mathbf{F}_3^r$
$N_{1D2D,v}$	$\Omega_{1D,v}$	Ω_{2D}	$\begin{bmatrix} h & \frac{q}{\phi} & \frac{r}{\phi} \end{bmatrix}$	$\begin{bmatrix} h & q & r \end{bmatrix}$	ϕ_{1D}	$\mathbf{F}_1^r$	$\mathbf{F}_2^r$	$\mathbf{F}_3^r$

Ce nouveau modèle a été implanté dans le code de calcul Flood1D2D [2]. L'intérêt de cette nouvelle paramétrisation des équations shallow water pour modéliser les inondations urbaines est montré sur deux cas tests. Le premier cas test vise à modéliser l'écoulement dans un carrefour (voir section 7.2.2.1) et le second dans un réseau de rues (voir section 7.2.2.2).

7.2.2.1 Modélisation d'un carrefour isolé

Le nouveau modèle est validé pour la modélisation d'un carrefour isolé sur la configuration expérimentale étudiée par [43]. Les rues sont modélisées avec une maille sur toute la largeur et l'intersection est maillée finement (environ 15 mailles sur la largeur d'une rue) (voir figure 7.8a). Des conditions limites symétriques sont employées afin de garantir une équirépartition des débits dans les branches aval : $Q_{Nord} = Q_{Ouest} = 0,075\text{m}^3/\text{s}$ et des courbes de tarage identiques à l'aval des rues Est et Sud. La simulation est menée en régime permanent et confrontée à une simulation avec le logiciel Telemac 2D qui sert de référence.

La porosité dans les rues aval est paramétrisée avec la relation : $\phi(s) = as^2 + bs + c$ où ϕ est le ratio B/B_s avec B_s la largeur totale de la rue et B la largeur de la recirculation, s est l'abscisse le long de la rue aval ($s = 0$ est positionné arbitrairement à l'amont de la rue et orienté dans le sens de l'écoulement). a, b et c sont trois coefficients calculés tels que $\phi(0) = \phi(L_s) = 1$ et $\phi(L_s/2) = 0,3$ avec $L_s = 3,3\text{m}$ la longueur de la recirculation (déterminée à partir de la simulation de référence). Les modélisations réalisées avec Flood1D2D utilisent un coefficient de Strickler uniforme $K = 100\text{m}^{1/3}.\text{s}^{-1}$.

La figure 7.8b compare les lignes d'eau modélisées avec Telemac2D (Courbe Référence), avec Flood1D2D paramétrisé sans porosité (Courbe 1D2D - K) et avec Flood1D2D paramétrisé avec porosité (Courbe 1D2D - ϕ). Les profils de hauteur d'eau à l'amont du carrefour sont comparables avec la référence (avec une différence d'environ 5mm pour une hauteur d'eau moyenne de $0,11\text{m}$. A l'aval du carrefour, du fait de la zone de recirculation, l'écoulement est accéléré et la surface libre de la solution de référence présente une inflexion pour $x \in [3,5; 8,5]\,\text{m}$. Cette forme est reproduite par Flood1D2D lorsqu'il est paramétrisé par une porosité mais pas lorsqu'il est paramétrisé seulement par un coefficient de Strickler. Même avec un coefficient de Strickler variant spatialement, ce type de profil contracté ne peut être reproduit par une approche 1D classique car le coefficient de frottement intervient seulement dans le terme source S_f de l'équation de Saint-Venant (voir (7.16)). En effet, ce terme est de signe strictement opposé à celui de la vitesse et donc de signe constant dans chaque rue aval. Le profil de hauteur d'eau modélisé par une telle approche ne peut donc varier que de manière monotone.

Le nouveau modèle propose donc une approche 1D effective capable de prendre en compte l'effet des recirculations sur les niveaux d'eau. Une calibration du profil de porosité et du coefficient de frottement doit

2. https://sourcesup.renater.fr/projects/flood1d2d/

permettre de mieux reproduire la référence. La problématique de l'équifinalité entre les termes K et ϕ doit toutefois être investiguée.

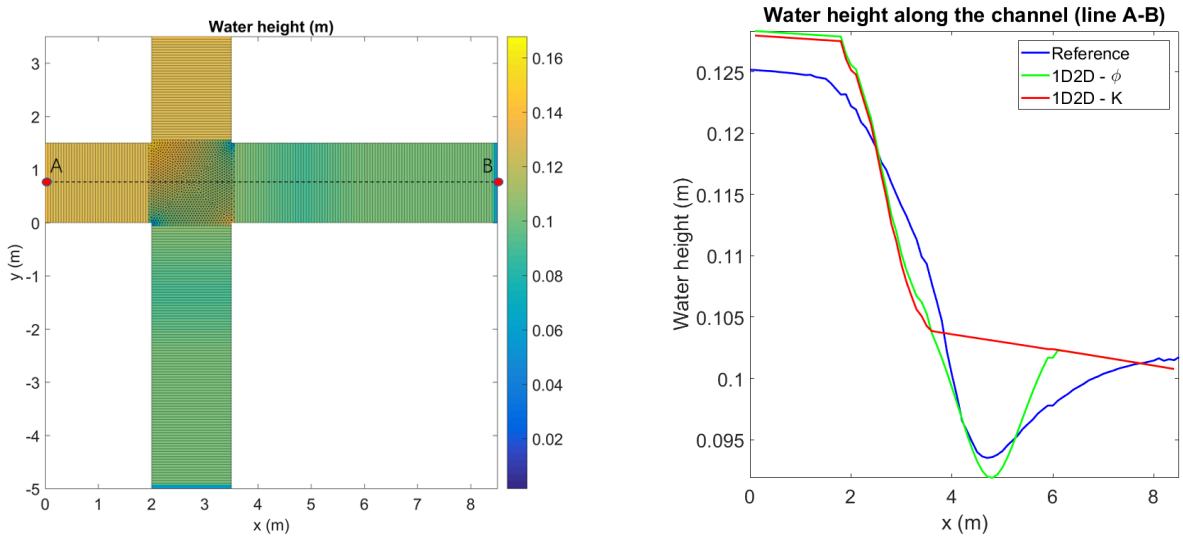

(a) (b)

FIGURE 7.8 – Modélisation d'un carrefour à 4 branches. (a) Carte des hauteurs d'eau produite par Flood1D2D paramétrisé avec K et ϕ, pour un débit amont $Q = 0,15\text{m}^3/\text{s}$ équiréparti entre les branches Nord et Ouest et avec une courbe de tarage à l'aval des branches Sud et Est ; (b) profils de hauteur d'eau obtenus avec les différentes approches.

7.2.2.2 Modélisation d'un réseau de carrefours

Cette section montre les effets d'une distribution de porosité sur l'écoulement modélisé à l'échelle de plusieurs carrefours. La réponse du nouveau modèle est étudiée sur une sous partie du pilote Icube d'étude des inondations urbaines afin d'utiliser toute la complexité d'un jeu de données expérimental tout en limitant les coûts de calcul et le nombre de paramètres. La sous partie choisie comprend 4 carrefours connectés par des rues de largeurs et orientations variables, au centre du dispositif expérimental (voir figure 7.9a). La largeur des rues larges (F et 4) est de 12.5cm et 5cm pour les plus petites. Un carrefour est identifié par le nom des deux rues le formant (ex. 'E3'). Une sous partie d'une rue est nommée en utilisant les noms des carrefours amont et aval (ex. 'E3E4').

Les données expérimentales en régime permanent ([2, 15, 16]) permettent de connaître le débit et les hauteurs d'eau dans chaque rue, ces dernières étant mesurées de chaque côté de la rue. Le réseau est modélisé en utilisant un modèle 1D2D sur un maillage non structuré avec un pas d'espace $\triangle x = 0.025\text{m}$ (voir figure 7.9b). Les rues sont modélisées avec des mailles 1D et les carrefours en 2D. Les conditions aux limites consistent en des débits amonts pour les rues E, F, 3 et 4 (correspondant aux valeurs expérimentales) et des courbes de tarage expérimentales pour chaque condition limite aval. Le solveur de Riemann PorAS est utilisé pour le calcul des flux (voir section 7.2.1). Dans chaque configuration, une simulation de 1000s permet d'atteindre un régime permanent sur tout le domaine. Cette configuration est utilisée pour tester la réponse du nouveau modèle avec deux paramétrisations différentes :

Config 1 Pas de porosité ($\phi = 1$ partout) et des valeurs du coefficient de Strickler différentes dans les rues K_{street} et les carrefours K_{cross} ;

Config 2 Un coefficient de Strickler uniforme sur tout le domaine et une distribution de porosité dans chaque rue.

Config 1 : Surface de réponse à K_{street} et K_{cross} Le modèle est paramétrisé avec deux coefficients de Strickler uniformes : K_{street} dans les rues et K_{cross} dans les carrefours. Chaque paramètre est pris parmi les valeurs $\{25,\ 50,\ 75,\ 100,\ 125,\ 150\}\ \mathrm{m}^{1/3}.\mathrm{s}^{-1}$ et toutes les combinaisons sont testées.

La figure 7.9c compare les débits simulés dans les rues de sorties avec les valeurs expérimentales ; pour chaque rue, la première barre correspond à la mesure expérimentale. Pour tous les jeux de paramètres testés, les débits simulés pour les rues E et F (respectivement 3 et 4) sous- (respectivement sur-)estime les valeurs mesurées. Le paramètre K_{street} semble contrôler le valeur du débit moyen dans la rue (voir par exemple la variation de débit pour la rue 4 quand K_{street} varie de 25 à 50). K_{cross} a un impact plus limité sur la répartition des débits avec une influence toujours similaires autour de la valeur imposée par K_{street}.

Il apparaît donc que le modèle 1D2D paramétrisé uniquement avec un coefficient de Strickler (même variable en espace) soit incapable de reproduire la répartition expérimentale des débits.

Config 2 : Surface de réponse à K_{unif}, ϕ_L et ϕ_N Dans la mesure où la sensibilité du modèle aux paramètres K_{street} et K_{cross} est faible, un coefficient uniforme $K_{unif} = 75\mathrm{m}^{1/3}.\mathrm{s}^{-1}$ est employé. Dans chaque rue à l'aval d'un carrefour, la porosité est définie comme avec une fonction parabolique de la position :

$$\phi(s) = \begin{cases} as^2 + bs + c \text{ pour } 0 \leq s \leq 0.5 & \text{avec } \phi(0) = \phi\,(1/2) = 1 \text{ et } \phi(1/4) = \phi_r \\ 1 & \text{ailleurs} \end{cases} \tag{7.20}$$

où s est l'abscisse curviligne adimensionnalisée (0 (respectivement 1) à l'amont (respectivement aval) de chaque rue. Le modèle est paramétrisé en ajustant les valeurs de a, b et c, avec ϕ_L dans les rues larges (F et 4) et ϕ_N dans les rues étroites (E et 3). La surface de réponse du modèle est déterminée pour toutes les combinaisons de ϕ_L et ϕ_N dans $\{0.25,\ 0.50,\ 0.75,\ 1.00\}$.

La figure 7.9d compare les débits simulés avec les valeurs expérimentales ; pour chaque rue, la première barre correspond à la mesure expérimentale. Pour toutes les rues, la gamme de paramètres permet d'obtenir des simulations sous- et sur-estimant la valeur expérimentale (contrairement aux résultats de la configuration 1). En raison du coût de chaque simulation, l'échantillonnage de l'espace des paramètres est grossier. Toutefois, la surface de réponse est pratiquement centrée autour de la valeur expérimentale ce qui suggère l'existence d'au moins un jeu de paramètres ϕ_L et ϕ_N permettant de retrouver les valeurs expérimentales.

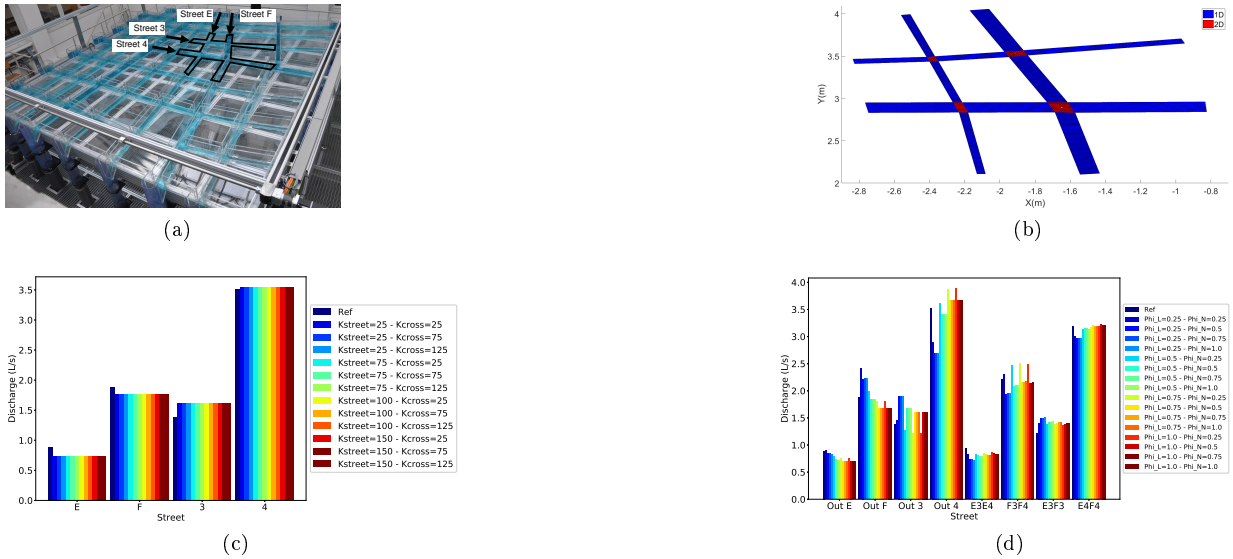

(a) (b) (c) (d)

FIGURE 7.9 – Analyse de sensibilité dans un réseau de carrefours. (a) pilote Icube et zone modélisée ; (b) maillage 1D2D employé ; (c) sensibilité du débit de sortie à une paramétrisation avec K_{street} et K_{cross} ; (d) sensibilité du débit de sortie et dans les rues à une paramétrisation avec ϕ_L et ϕ_N.

Chapitre 8

Conclusion

Le changement climatique accroît les préoccupations liées aux inondations. En effet, la population concernée par ce risque naturel majeur est importante à échelle française et planétaire et devrait augmenter dans les années à venir. La modélisation reste aujourd'hui l'outil principal pour produire des cartes d'aléas aidant le décideur pour l'aménagement durable du territoire.

Ma recherche contribue donc, depuis le début de mon doctorat, à la mise au point d'outils numériques opérationnels pour la modélisation des inondations. Deux approches complémentaires ont été employées : des campagnes expérimentales visant à mieux comprendre la dynamique des inondations urbaines et une étude numérique proposant de nouveaux modèles ou schémas numériques pour la modélisation des inondations, notamment en zone urbaine.

J'ai développé le programme expérimental du pilote Icube d'étude des inondations urbaines. Sur ce pilote, la distorsion géométrique (échelle horizontale $\lambda_L = 1/200$ et échelle verticale $\lambda_h = 1/20$), nécessaire pour permettre de mesurer la distribution des hauteurs et des vitesses, autorise probablement des effets tridimensionnels expérimentaux exagérés par rapport aux effets présents dans la réalité (qui restent inconnus par manque de données in-situ). Plusieurs campagnes expérimentales ont toutefois été réalisées en régime permanent afin de caractériser les écoulements à différentes échelles.

A l'échelle du quartier, la répartition des débits entre les différentes rues aval a été caractérisée pour différentes répartitions des débits amont et distribution de seuils à l'aval. Un effet de filtrage de la géométrie sur la répartition des débits aval a été mis en évidence. Au cours des expériences menées, il n'a pas été possible de perturber significativement cette répartition. La réalisation de mesures en régime torrentiel (obtenu en imposant une pente dans les rues) ou la réalisation d'expériences transitoires pourraient permettre de modifier plus significativement cette répartition et ainsi comprendre les paramètres déterminant dans la répartition des masses d'eau entre quartiers inondés.

La caractérisation des hauteurs et vitesses dans le réseau de rues a permit d'explorer la répartition des débits à échelle plus fine. La distribution des hauteurs d'eau adimensionnalisées par la différence amont-aval est indépendante des débits totaux injectés dans le pilote, suggérant ainsi que l'hydrodynamique n'est pas modifiées significativement entre les différentes expériences. L'analyse des profils de vitesse sur la largeur des rues montrent que l'hypothèse courante que les carrefours n'exercent pas d'influence les uns sur les autres n'est pas vérifiée dans toutes les configurations. Par ailleurs, l'étude de la déviation du débit par les sous-quartiers montrent des comportements très différents rendant le downscaling des grandeurs moyennes à l'échelle du quartier non trivial.

Enfin, les expériences fournissent des jeux de données conséquents et inédits pour la validation de codes de calculs des inondations urbaines. En effet, la modélisation des configurations expérimentales a permis de montrer que les apports de la modélisation 3D par rapport à la modélisation 2D restent modérés (notamment en prenant en compte les coups de calcul dans l'évaluation) hormis à l'échelle locale notamment dans les zones où les profils de pression ne sont pas hydrostatiques. La comparaison de différents schémas numériques a montré que les méthodes aux éléments finis testées (schéma RKDG, EVRDG) apportent, par rapport aux méthodes aux volumes finis (schéma de Godunov), une précision (à finesse de discrétisation équivalente) très

inférieure à la sensibilité du modèle aux incertitudes sur les paramètres et pour des temps de calcul supérieurs.

Un modèle couplé 1D/2D pour la modélisation des inondations urbaines est implanté dans le code de calcul Flood1D2D. Ce modèle propose de modéliser les carrefours avec une approche 2D classique et les rues avec une approche effective pseudo-1D. Les équations de Saint-Venant employées sont paramétrisées dans les rues avec une porosité pour prendre en compte l'effet des recirculations qui jouent un rôle déterminant dans la répartition de débit dans un réseau de rues. Ce nouveau modèle est validé sur un cas test de rupture de barrage dans un canal coudé et sur un écoulement en carrefour en régime permanent. L'ajout du terme de porosité permet de reproduire les déformations de la surface libre calculée par un modèle 2D fin classique là où un modèle 1D/2D sans porosité échoue. Par ailleurs, ce nouveau modèle permet de reproduire de manière réaliste la distribution des débits observés expérimentalement sur le pilote Icube d'étude des inondations. La potentielle équifinalité entre les paramètres porosité ϕ et Strickler K doit encore être investiguée de même que la question du profil de porosité $\phi(s)$ dans une rue.

La qualité des résultats produits par un modèle physique est directement influencée par le schéma numérique employé pour sa résolution. Le schéma aux EFd (éléments finis discontinus - Discontinuous Galerkin) avec une discrétisation temporelle par la méthode EVR constitue ainsi un bon intermédiaire entre un schéma VF (aux volumes finis) et un schéma EFd avec schéma de Runge Kutta 2. Par ailleurs, tous ces schémas sont basés sur une description conservative de la masse et de la quantité de mouvement nécessitant la résolution d'un problème de Riemann à l'interface entre deux mailles de calcul. Le solveur PorAS permet de mieux estimer ces flux pour des équations de Saint-Venant avec et sans porosité en comparaison avec un solveur HLLC classique.

Troisième partie

Projet de recherche

Ma thèse de doctorat m'a notamment appris que la recherche n'avait pas de fin car la réponse à une question amène généralement d'autres interrogations. Ma recherche n'échappe pas à cette règle et les travaux que j'ai mené depuis le début de ma thèse et jusqu'à présent sont les bases pour mon projet de recherche futur. Ce projet est structuré autour de trois axes de recherche : la modélisation opérationnelle des inondations urbaines, la mise au point de méthodes multi-échelles pour les inondaitons et le développement d'approches stochastiques.

Pour pouvoir explorer ces thématiques, je poursuivrai ma recherche active de financement à la fois pour pouvoir obtenir des jeux de données (expérimentales ou in-situ) alimentant mes travaux mais également pour financer des stages de Master et des thèses de doctorat. Les collaborations existantes devront probablement être élargies pour enrichir mes travaux des idées et méthodes d'autres collègues. Enfin, j'adapterai mes thématiques pour faire le lien avec les directions privilégiées par mes deux équipes de recherche de rattachement : Hydrologie et Hydraulique Urbaines du laboratoire HydroSciences Montpellier [1] et Lemon de l'INRIA Sophia Antipolis - Méditerranée [2].

1. http://www.hydrosciences.org/
2. https://team.inria.fr/lemon/

Chapitre 9

Modélisation opérationnelle des inondations urbaines

Les inondations urbaines sont caractérisées par une importante variété de phénomènes : écoulements dans les rues d'origine variée (débordement de cours d'eau, ruisselement pluvial, submersion marine et tsunamis, ...), création d'embâcles (liés au transport de voiture ou de flottants), échanges entre les écoulements dans la rue et les réseaux souterrains (assainissement, métro, ...) ou l'intérieur des bâtiments. A l'heure d'aujourd'hui, il existe peu de modèles prédictifs pour ces phénomènes et ils sont très rarement implantés dans des outils numériques.

En contexte opérationnel, l'absence d'outils mais également le manque de temps et de données conduit souvent à considérer que ces phénomènes ont une influence très modérée ou négligeable sur la dynamique d'une inondation. Toutefois, les observations pendant et après une inondation suggèrent que ces effets peuvent jouer un rôle essentiel, au moins à échelle locale.

Cet axe de recherche propose donc de caractériser les différents phénomènes intervenant lors d'inondations urbaines et de proposer des approches de modélisation pour les effets principaux.

9.1 Caractérisation in-situ des inondations urbaines

Pour mettre au point des outils de modélisation des inondations urbaines fiables, il faut être à même d'identifier les modèles pertinents pour reproduire la physique observée. Il est donc nécessaire de déterminer les paramètres et la gamme de variabilité des paramètres (et des variables d'écoulement) lors des inondations urbaines. Les observatoires du Verdanson (à Montpellier), de la Zone Atelier Environnement Urbain (à Strasbourg) et de l'Yzeron (à Oullins), dans lesquels je suis (ou j'ai été) impliqué et avec qui je collabore, constituent de bonnes opportunités pour caractériser les inondations générées par différents phénomènes (respectivement : crue éclair et ruissellement urbain, remontée de nappe et crue lente).

A partir des données in-situ lors d'inondations urbaines, il est notamment nécessaire de déterminer (sans que cette liste soit exhaustive) :

- le gradient temporel des variables (débit, hauteur) pour déterminer dans quelle mesure une inondation urbaine peut être considérée comme une succession de régimes permanents ;
- l'importance des effets tridimensionnels et la validité de l'hypothèse d'un profil de pression hydrostatique ;
- les valeurs du nombre de Froude pour déterminer le caractère fluvial ou torrentiel de l'écoulement et ainsi déterminer les points de contrôle principaux ;
- les valeurs du nombre de Reynolds pour déterminer l'importance de la turbulence dans l'écoulement ;
- l'importance des phénomènes "complémentaires".

Ces données doivent notamment permettre *(i)* de mieux connaître la validité des conclusions établies en configuration expérimentale, *(ii)* d'identifier des configurations expérimentales pertinentes pour exploiter les

pilotes existants ou en construire de nouveaux et *(iii)* de définir les termes prépondérant à prendre en compte dans les modèles mathématiques pour les inondations urbaines.

Dans la mesure où la réglementation française impose de caractériser des évènements de période de retour au moins centennale, il convient de caractériser des évènements rares. Comme en témoigne la faible quantité de données réelles disponible, l'observation de tels évènements est particulièrement complexe. L'augmentation du nombre de caméras en ville et les drones constituent de réelles opportunités pour caractériser les niveaux d'eau (et potentiellement des vitesses de surface). Les travaux menés sur l'acquisition de données in-situ pourront bénéficier de la méthodologie que j'ai développé pour la mesure de hauteur d'eau par caméra sur le pilote Icube d'étude des inondations urbaines. Par ailleurs, de nouvelles collaborations peuvent émerger avec des équipes de recherche en métrologie (par exemple l'équipe Télédétection, Radiométrie et Imagerie Optique du laboratoire Icube), des collectivités territoriales et/ou des entreprises spécialisées dans la mesure par drone.

Il semble illusoire de vouloir accéder à toutes les données physiques de l'écoulement (hauteur, débit, profil de vitesse, ...) avec une grande résolution spatio-temporelle notamment lors d'évènements extrêmes. L'utilisation de techniques d'analyse de sensibilité, telles que celle que j'ai contribué à développer [10] ou que j'ai employées [7], peut permettre d'identifier les endroits où positionner des capteurs afin qu'ils soient les plus informatifs pour des modélisations à même d'interpoler temporellement et spatialement les grandeurs mesurées in-situ.

9.2 Modélisation effective des inondations urbaines

La mise au point d'un outil opérationnel pour les inondations urbaines impose d'identifier les modéles les plus adaptés pour la physique à reproduire tout en garantissant la cohérence entre la paramétrisation nécessaire et les données disponibles. La mise au point de modèles effectifs pour les différents phénomènes à prendre en compte et leur implantation dans un code de calcul hydrodynamique peut permettre d'identifier pour quelles combinaisons de forçages hydrologiques et de topographie/géométrie leurs effets sont réellement négligeables.

La caractérisation des échanges rue-bâti est en cours dans le cadre de l'ANR DEUFI[1] (voir section 3.2) notamment avec la thèse de C. Choley (voir section 3.3.1). Un modèle préliminaire a été proposé prenant le parti-pris que le bâti peut être assimilé à un réservoir et qu'une loi de vanne $Q = C_d S\sqrt{2g}\sqrt{h_{up} - h_{down}}$[2] permet d'estimer les débits d'échange à travers chaque ouverture (fenêtre, porte, ...). La simulation d'un hydrogramme dans un canal bordé de bâtiments (voir figure 9.1) ou dans un réseau de rues (voir figure 9.2) montre que les échanges rue-bâti peuvent modifier significativement la dynamique d'une inondation urbaine. Les hypothèses du modèle et les lois d'échange employées doivent encore être validées notamment sur des expériences. Par la suite, la modélisation de différentes configurations urbaines soumises à des phénomènes variés permettra de déterminer l'influence réelle de ces échanges.

Une approche similaire pourra être employée sur les autres phénomènes pouvant impacter la dynamique d'une inondation urbaine.

1. ANR-18-CE01-0020
2. C_d est le coefficient de débit, S la section de l'ouverture et $h_{up} - h_{down}$ la différence de hauteur d'eau entre l'amont et l'aval de l'ouverture.

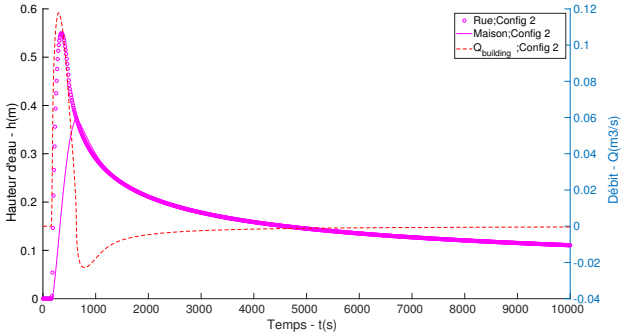

(a) Comparaison des niveaux d'eaux dans la rue et dans un bâtiment

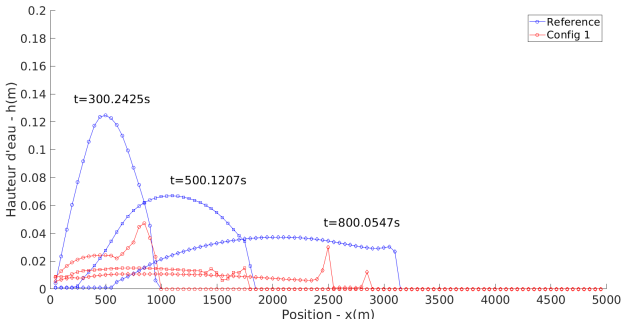

(b) Comparaison des hauteurs d'eau dans la rue à différents instants en prenant en compte ou en négligeant les échanges avec le bâti.

FIGURE 9.1 – Modélisation des échanges rues-bâti dans une rue bordée de bâtiments

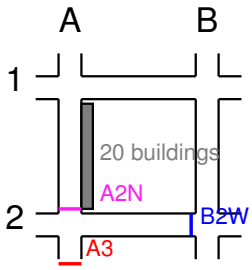

(a) Représentation schématique de la configuration étudiée

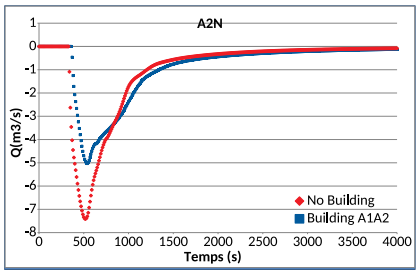

(b) Comparaison des hydrogrammes au point A2N avec et sans bâtiment modélisés

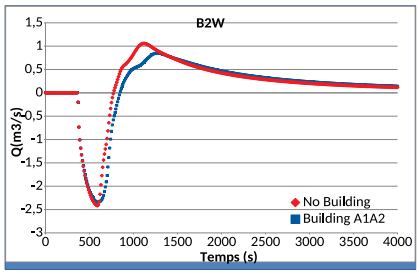

(c) Comparaison des hydrogrammes au point B2W avec et sans bâtiment modélisés

FIGURE 9.2 – Modélisation des échanges rues-bâti dans un réseau de rues

Chapitre 10

Approche multi-échelle pour les inondations

La protection contre le risque inondation nécessite de le caractériser à différentes échelles. Généralement, la protection des bâtiments sensibles impose une approche locale et l'aménagement de territoire nécessite une approche globale. En contexte opérationnel, les échelles pour laquelle les données sont disponibles et celle de l'étude sont rarement cohérentes. Il convient donc de metre en place des modèles adaptés à chaque échelle et des approches pour passer de l'une à l'autre.

10.1 Modélisation macroscopique

Au cours des 10 dernières années, un nombre important d'approches pour la modélisation macroscopique des inondations urbaines a été développé. En effet, plusieurs modèles à porosité ont été proposés (voir [19] pour une intercomparaison : modèle à porosité simple [9, 3, 27, 22], modèle à porosité intégrale[55, 57, 21], modèle à porosités multiples[18], modèle à porosité variable sur la verticale [44, 45, 20]. Ces modèles permettent de calculer rapidement l'inondation dans des zones urbaines étendues. Afin de démocratiser ces méthodes, je contribue à la mise au point et à la diffusion du code de calcul SW2D [1] avec les éléments nécessaires pour une prise en main par des industriels et pour permettre à d'autres équipes de recherche de contribuer à ce logiciel.

Le solveur de Riemann PorAS a permis d'améliorer l'estimation des flux à travers les interfaces pour les équations du modèle à porosité isotrope (voir section 7.2.1). La méthodologie employée pourrait être généralisée pour d'autres modèles à porosité avec potentiellement une amélioration de l'estimation des flux aux interfaces.

Le ruissellement pluvial est à l'origine d'inondations urbaines significatives, notamment lors d'orages dans la région méditerranéenne. Le ruissellement est caractérisé par de faibles hauteurs d'eau et est mal reproduit par les modèles de Saint-Venant classiques ou au prix d'une discrétisation spatiale très fine (et prohibitive en terme de coût de calcul) pour prendre en compte la micro-topographie. Le modèle à porosité variable sur la verticale constitue une réelle opportunité pour reproduire ces phénomènes. Toutefois, la prise en compte de la micro topographie sur les écoulements en lame mince pose la question des échelles spatiales des définitions de la porosité (voir section 10.1) et de l'axe suivant lequel la calculer (vertical, perpendiculaire à la surface libre ou à la pente moyenne du fond)(voir section 10.2).

1. https://sw2d.inria.fr/

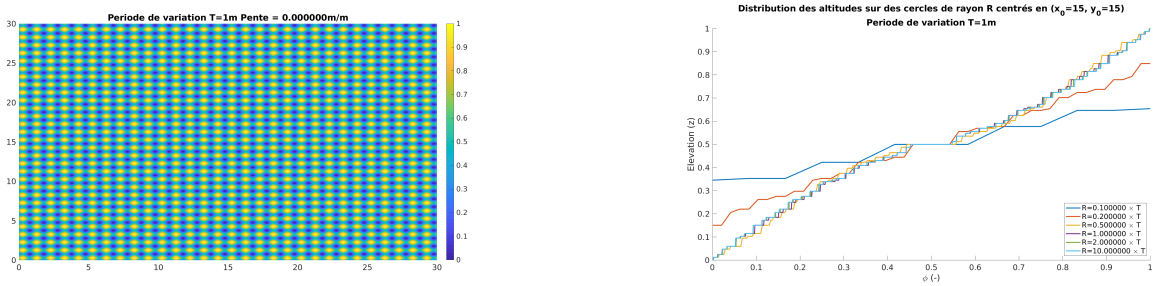

FIGURE 10.1 – Gauche : topographie synthétique générée. Droite : Sensibilité de la loi de porosité en fonction de la zone de prise de statistiques sur la topographie.

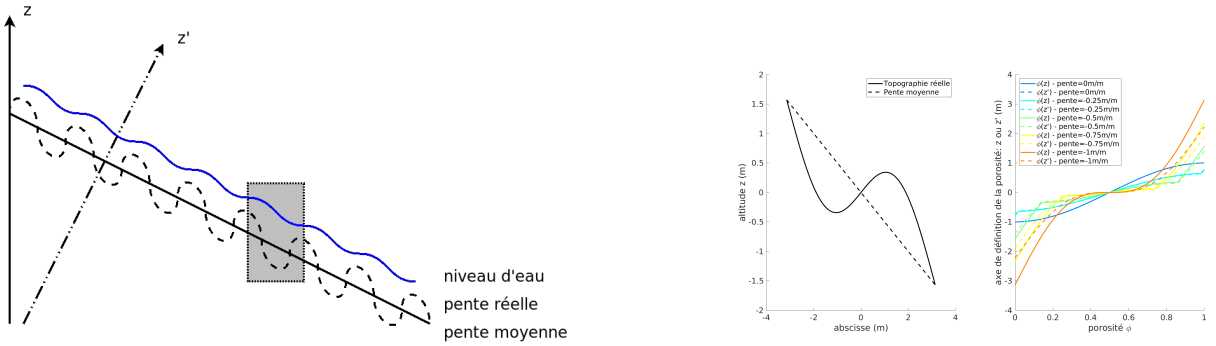

FIGURE 10.2 – Sensibilité de la loi de porosité en fonction de l'axe considéré (z ou z'). L'axe z' est définit perpendiculairement à la pente moyenne du fond. Le graphique de droite illustre que le choix de l'axe induit des distributions de porosité significativement différentes et que cet écart diminue avec la pente moyenne du fond.

Pour permettre l'utilisation de ces modèles à porosité dans un contexte opérationnel, il convient de définir une méthodologie de détermination des paramètres du modèle (distributions de porosité, coefficients de perte de charge) à partir des données topographiques et d'occupation du sol. La réalisation de comparaisons, sur des configurations urbaines réelles, entre des modélisations fines et macroscopiques peut permettre de proposer une méthodologie optimale pour définir les paramètres. Toutefois la collecte de données suffisantes est potentiellement problématique. Pour palier cela, l'emploi d'algorithmes pour la génération automatique de topographies et de plans d'organisation du bâti [48, 63] peut permettre de créer des configurations suffisamment variées.

L'emploi de l'assimilation de données peut permettre de faciliter la mise au point de cartes optimales de porosité pour reproduire les résultats des modélisations fines. Par la suite, l'apprentissage supervisé peut permettre de faire le lien entre données physiques (occupation du sol, plan des rues et du bâti, ...) et cartes de paramètres assimilés. Pour faciliter l'utilisation de ces modèles dans un contexte opérationnel, la mise au point d'algorithmes mettant en œuvre les liens identifiés doit être envisagée. La collaboration établie avec P. A. Garambois et J. Monnier permet d'envisager la mise au point d'algorithmes d'assimilation de données pour des modèles à porosité.

10.2 Downscaling dans les modèles d'inondation urbaine

La connaissance de l'hydrodynamique à échelle fine est essentielle pour caractériser l'aléa lors d'inondation urbaines (échelle est en cours de définition dans le cadre de l'ANR DEUFI[2]). Toutefois, la modélisation d'un

2. ANR-18-CE01-0020

quartier ou d'une ville avec une précision suffisante (de l'ordre de la dizaine de mailles sur la largeur de la rue) nécessite des coups de calcul prohibitifs. Les modèles macroscopiques à porosité sont quant à eux adaptés à la modélisation des inondations urbaines à l'échelle de la ville mais ne permettent pas de décrire l'hydrodynamique à une échelle suffisamment fine pour la définition du risque dans la ville.

La combinaison de ces deux types de modèles pourrait potentiellement palier cela réalisant un downscaling depuis la simulation macroscopique vers l'échelle fine. Toutefois, les expériences menées sur le pilote inondation Icube ont montré la non-trivialité du downscaling depuis les observations à échelle du quartier vers l'hydrodynamique à l'échelle des sous-quartiers et des carrefours [15, 16]. Pour décrire l'hydrodynamique à échelle fine, deux stratégies peuvent être utilisées à partir des résultats d'une simulation à porosité : *(i)* utiliser les données de la simulation pour déterminer les conditions limites d'une modélisation classique à échelle locale ou *(ii)* utiliser des fonctions de downscaling permettant de déduire les grandeurs hydrodynamiques à échelle sous-maille.

La détermination des conditions limite du modèle fin pose la question de la cohérence entre les échelles. Pour la réalisation d'un couplage faible entre les deux modèles (macroscopique et fin), cela suppose qu'au cours de simulation fine, l'hydrodynamique modélisée ne soit pas incohérente avec celle modélisée par le modèle macroscopique. Par exemple, le modèle fin ne doit pas calculer un flux sortant du domaine quand le modèle macroscopique impose un flux entrant. De telles incohérences pourraient indiquer la nécessité d'un couplage fort. Une méthodologie pour ce couplage doit être mise en place tout en garantissant que le modèle couplé reste plus rapide que le modèle fin.

L'utilisation de fonctions de downscaling permettant de déterminer la distribution des grandeurs hydrodynamiques à une échelle sous-maille du modèle macroscopique peut permettre de s'affranchir d'une seconde modélisation classique à échelle fine qui pourrait être fortement demandeuse en temps de calcul. Ces fonctions pourraient être déterminées en utilisant les résultats de la recherche visant à mettre au point une méthodologie pour la détermination des cartes de porosité. En effet, les simulations réalisées (avec les approches macroscopique et classique) sur différentes géométries permettent d'obtenir un jeu de données suffisant pour réaliser de l'apprentissage supervisé pour déterminer ces fonctions de downscaling. Ces travaux débutent actuellement au sein de l'équipe-projet Lemon (INRIA Sophia Antipolis - Méditerranée) dans le cadre d'un projet avec l'IRT St-Exupery.

Chapitre 11

Modélisation stochastique des inondations

Les travaux que j'ai conduit montrent que plusieurs problématiques sont décrites par des modèles non détermistes. L'emploi de méthodes stochastiques permet de s'intéresser à de telles problématiques et m'apparaît donc comme une direction de recherche naturelle. Bien que nouvelle pour moi, cette thématique pourra être développée au sein de l'équipe-projet Lemon de l'INRIA, notamment avec l'appui de Gwladys Toulemonde (statisticienne et membre de l'équipe).

11.1 Modélisation stochastique de la pluie

Les inondations par ruissellement urbain dépendent directement de la pluie tombant sur ou à proximité de la zone d'étude. Toutefois, la résolution des pixels radar ($1km^2$) est insuffisante. En effet, la simulation d'inondations urbaines par ruissellement lors d'orages cévenols sur des bassins versants montpelliérains montre que la spatialisation de la pluie à une échelle inférieure au pixel radar est déterminante pour les résultats.

Depuis 2019, l'observatoire du Verdanson porté par le laboratoire HydroSciences Montpellier inclut un réseau dense de pluviographes (voir figure 11.1) permettant de décrire la pluie à une échelle infra pixel radar. Ces données doivent permettre d'étudier le lien entre spatialisation de la pluie d'une part, et d'autre part occupation du sol et forçage météo (notamment l'orientation et la direction du vent). L'objectif est de pouvoir déterminer des fonctions de downscaling des mesures de pluie radar et connaître la probabilité de distribution spatiale de la pluie.

Ces fonctions et probabilités associées permettront d'estimer des cartes de forçages probables pour un modèle hydraulique et d'en déduire l'inondation associée. L'analyse statistique des résultats de simulation permettra de déterminer des probabilités d'observation des niveaux d'eau et des vitesses.

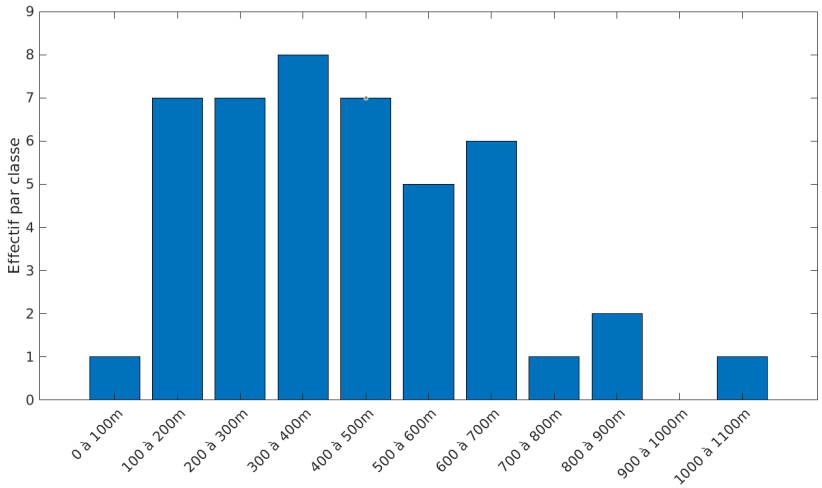

FIGURE 11.1 – Distribution des distances entre pluviomètres de l'observatoire du Verdanson

11.2 Modélisation stochastique des embâcles de véhicules

Les observations d'inondations urbaines mettent en évidence le phénomène de déplacement de véhicules et leur accumulation qui constitue un obstacle aux écoulements. L'effet de telles obstructions sur l'hydrodynamique dans un réseau de rues peut être significatif [7] et leur prise en compte doit donc être envisagée dans des modélisations prédictives. Des études expérimentales ont déterminé les conditions de mise en mouvement de véhicules lors d'inondation et ont exploré la formation d'embâcles. La modélisation du transport des véhicules par l'écoulement a également été investigué en employant un couplage faible [47].

L'effet des embâcles de véhicule peut toutefois être pris en compte au cours de la simulation à travers une modification de la cote du fond des mailles de calcul, par l'ajout de termes de perte de charge et/ou par la réduction d'une porosité. Ces travaux sur le transport de véhicules pourraient être la continuité des travaux conduits actuellement au sein de l'équipe-projet Lemon (INRIA Sophia Antipolis - Méditerranée) sur le transport de scalaire passif. Une approche stochastique sera mise en place pour palier la difficulté de fixer la distribution spatiale des véhicules avant la crue. Le blocage et le déblocage d'un ou plusieurs véhicules en un point devront également être modélisés par des fonctions de probabilité prenant en compte des covariables comme le nombre de véhicules dans le voisinage du point, les caractéristiques de la géométrie et potentiellement l'hydrodynamique locale.

11.3 Modélisation stochastique des échanges rue-bâti

Une piste de recherche est envisagée si les travaux en cours sur les échanges rue-bâti montrent que ce phénomène influe significativement sur la dynamique des inondations urbaines. En effet, les différentes ouvertures peuvent être enfoncées au cours de l'inondation. Dans la mesure où les propriétés de l'ouverture (porte verrouillée ou non, volets fermés ou non, résistance à la pression) ainsi que le transport de flottants par l'écoulement ne peuvent être déterminés, une approche stochastique similaire à celle employée pour les embâcles de véhicules peut permettre de déterminer les probabilités d'observation des niveaux d'eau et des vitesses.

Bibliographie

[1] A. Abbaspour and S. H. Kia. Numerical investigation of turbulent open channel flow with semi-cylindrical rough beds. *KSCE Journal of Civil Engineering*, 18(7) :2252–2260, November 2014.

[2] Q. Araud. *Simulations des écoulements en milieu urbain lors d'un évènement pluvieux extrême*. Thèse de doctorat, Université de Strasbourg, 2012.

[3] P. D. Bates. Development and testing of a subgrid-scale model for moving-boundary hydrodynamic problems in shallow water. *Hydrological Processes*, 14(11-12) :2073–2088, 2000.

[4] J. L. Best and I. Reid. Separation Zone at Open-Channel Junctions. *Journal of Hydraulic Engineering*, 110(11) :1588–1594, 1984.

[5] P. Chaudhary, S. D'Aronco, M. Moy de Vitry, J. P. Leitão, and J. D. Wegner. Flood-Water level estimation from social media images. In *ISPRS Annals of Photogrammetry, Remote Sensing and Spatial Information Sciences*, volume IV-2-W5, pages 5–12. Copernicus GmbH, May 2019.

[6] S. Chen. *Effective Shallow Water Models for Complex Flood Flow Patterns in Urban Areas*. Thèse de doctorat, Université de Strasbourg, 2018.

[7] S. Chen, P.-A. Garambois, P. Finaud-Guyot, G. Dellinger, R. Mosé, A. Terfous, and A. Ghenaim. Variance based sensitivity analysis of 1D and 2D hydraulic models : An experimental urban flood case. *Environmental Modelling & Software*, 109 :167–181, November 2018.

[8] M. M. L. P. Coelho. Experimental determination of free surface levels at open-channel junctions. *Journal of Hydraulic Research*, 53(3) :394–399, May 2015.

[9] A. Defina, L. D'Alpaos, and B. Mattichio. A new set of equations for very shallow water and partially dry areas suitable to 2D numerical domains. In *Proceedings Specialty Conference "Modelling of Flood Propagation over Initially Dry Areas"*, Milano (Italy), July 1994.

[10] C. Delenne, P. Finaud-Guyot, V. Guinot, and B. Cappelaere. Sensitivity of the 1D shallow water equations with source terms : Solution method for discontinuous flows. *International Journal for Numerical Methods in Fluids*, 67(8) :981–1003, 2011.

[11] M. Desbordes, P. Durepaire, J.C. Gilly, and J.M.Y. Masson Maurin. *3 Octobre 1988 : Inondations sur Nîmes et sa région : Manifestations, Causes et conséquences*. C. lacour edition, 1989.

[12] Slobodan Djordjević, Adrian J. Saul, Gavin R. Tabor, John Blanksby, Istvan Galambos, Nuridah Sabtu, and Gavin Sailor. Experimental and numerical investigation of interactions between above and below ground drainage systems. *Water Science and Technology : A Journal of the International Association on Water Pollution Research*, 67(3) :535–542, 2013.

[13] P. Finaud-Guyot. *Modélisation macroscopique des inondations fluviales et urbaines - Prise en compte des écoulements directionnels et des échanges lit majeur - lit mineur*. Thèse de doctorat, Université Montpellier II - Sciences et Techniques du Languedoc, 2009.

[14] P. Finaud-Guyot, C. Delenne, J. Lhomme, V. Guinot, and C. Llovel. An approximate-state Riemann solver for the two-dimensional shallow water equations with porosity. *International Journal for Numerical Methods in Fluids*, 62(12) :1299–1331, 2010.

[15] P. Finaud-Guyot, P.-A. Garambois, Q. Araud, F. Lawniczak, P. François, J. Vazquez, and R. Mosé. Experimental insight for flood flow repartition in urban areas. *Urban Water Journal*, 15(3) :242–250, 2018.

[16] P. Finaud-Guyot, P.-A. Garambois, G. Dellinger, F. Lawniczak, and P. François. Experimental characterization of various scale hydraulic signatures in a flooded branched street network. *Urban Water Journal*, 16(9) :609–624, 2020.

[17] W. H. Graf and M. S. Altinakar. *Hydrodynamique*. Eyrolles, 1991.

[18] V. Guinot. Multiple porosity shallow water models for macroscopic modelling of urban floods. *Advances in Water Resources*, 37 :40–72, March 2012.

[19] V. Guinot. A critical assessment of flux and source term closures in shallow water models with porosity for urban flood simulations. *Advances in Water Resources*, 109 :133–157, November 2017.

[20] V. Guinot, C. Delenne, A. Rousseau, and O. Boutron. Flux closures and source term models for shallow water models with depth-dependent integral porosity. *Advances in Water Resources*, 122 :1–26, December 2018.

[21] V. Guinot, B. F. Sanders, and J. E. Schubert. Dual integral porosity shallow water model for urban flood modelling. *Advances in Water Resources*, 103 :16–31, May 2017.

[22] V. Guinot and S. Soares-Frazao. Flux and source term discretization in two-dimensional shallow water models with porosity on unstructured grids. *International Journal for Numerical Methods in Fluids*, 50 :309–345, 2006.

[23] M. S. Güney, G. Tayfur, G. Bombar, and S. Elci. Distorted Physical Model to Study Sudden Partial Dam Break Flows in an Urban Area. *Journal of Hydraulic Engineering*, 140(11) :05014006, November 2014.

[24] S. K. Gurram. *A study of subcritical and transitional combining flow in open channel junctions*. PhD thesis, Banaras Hindu University, Varanasi, India, 1994.

[25] S. K. Gurram and K. S. Karki. Discussion of "Subcritical Open-Channel Junction Flow" by Chung-Chieh Hsu, Wen-Jung Lee, and Cheng-Hsi Chang. *Journal of Hydraulic Engineering*, 126(1) :87–89, January 2000.

[26] S. K. Gurram, K. S. Karki, and W. H. Hager. Subcritical Junction Flow. *Journal of Hydraulic Engineering*, 123(5) :447–455, May 1997.

[27] J. M. Hervouet, H. Samie, and B. Moreau. Modelling urban areas in dam-break flood-wave numerical simulations. In *Proceedings of the International Seminar and Workshop on Rescue Actions Based on Dambreak Flow Analysis*, Seinâjoki (Finland), October 2000.

[28] T. Ishigaki, K. Toda, and K. Inoue. Hydraulic model tests of inundation in urban area with underground space. In *Proceedings 30th IAHR Congress, Thessaloniki, Greece*, pages 487–493, 2003.

[29] Y. Jia, T. Zhu, C. Riahi-Nezhad, and Y. Zhang. Numerical Modeling of Flow through a Breached Levee and during Levee Closure. In *World Environmental and Water Resources Congress 2010*, pages 1304–1316. American Society of Civil Engineers, 2010.

[30] L. A. LaRocque, M. Elkholy, M. Hanif Chaudhry, and J. Imran. Experiments on Urban Flooding Caused by a Levee Breach. *Journal of Hydraulic Engineering*, 139(9) :960–973, September 2013.

[31] J. Lhomme. *Modélisation des inondations en milieu urbain : Approches unidimensionnelle, bidimensionnelle et macroscopique*. PhD thesis, Université Montpellier 2, 2006.

[32] J. Lhomme and V. Guinot. A general approximate-state Riemann solver for hyperbolic systems of conservation laws with source terms. *International Journal for Numerical Methods in Fluids*, 53 :1509–1540, 2007.

[33] C. W. Li and C. Zeng. Flow division at a channel crossing with subcritical or supercritical flow. *International Journal for Numerical Methods in Fluids*, 62(1) :56–73, January 2010.

[34] X. Li, S. Erpicum, M. Bruwier, E. Mignot, P. Finaud-Guyot, P. Archambeau, M. Pirotton, and B. Dewals. Technical note : Laboratory modelling of urban flooding : strengths and challenges of distorted scale models. *Hydrology and Earth System Sciences*, 23(3) :1567–1580, March 2019.

[35] G. Lipeme Kouyi, D. Fraisse, N. Rivière, V. Guinot, and B. Chocat. One-dimensional modelling of the interactions between heavy rainfall-runoff in an urban area and flooding flows from sewer networks and rivers. *Water science and technology : a journal of the International Association on Water Pollution Research*, 60(4) :927–34, 2009.

[36] S.-W. Lo, J.-H. Wu, F.-P. Lin, and C.-H. Hsu. Cyber Surveillance for Flood Disasters. *Sensors (Basel)*, 15(2) :2369–2387, January 2015.

[37] P. Lopes, J. Leandro, R. F. Carvalho, P. Páscoa, and R. Martins. Numerical and experimental investigation of a gully under surcharge conditions. *Urban Water Journal*, 12(6) :468–476, August 2015.

[38] E. Mignot. *Etude expérimentale et numérique de l'inondation d'une zone urbanisée : cas des écoulements dans les carrefours en croix*. PhD thesis, Ecole Centrale de Lyon, 2005.

[39] E. Mignot, X. Li, and B. Dewals. Experimental modelling of urban flooding : A review. *Journal of Hydrology*, 568 :334–342, January 2019.

[40] E. Mignot, A. Paquier, and S. Haider. Modeling floods in a dense urban area using 2D shallow water equations. *Journal of Hydrology*, 327(1-2) :186–199, July 2006.

[41] E. Mignot, A. Paquier, and N. Rivière. Experimental and numerical modeling of symmetrical four-branch supercritical. *Journal of Hydraulic Research*, 46(6) :723–738, November 2008.

[42] L. S. Nanía, M. Gómez, J. Dolz, P. Comas, and J. Pomares. Experimental Study of Subcritical Dividing Flow in an Equal-Width, Four-Branch Junction. *Journal of Hydraulic Engineering*, 137(10) :1298–1305, October 2011.

[43] Leonardo S. Nanía, Manuel Gómez, and José Dolz. Experimental study of the dividing flow in steep street crossings. *Journal of Hydraulic Research*, 42(4) :406–412, January 2004.

[44] I. Özgen, D. Liang, and R. Hinkelmann. Shallow water equations with depth-dependent anisotropic porosity for subgrid-scale topography. *Applied Mathematical Modelling*, 40(17) :7447–7473, September 2016.

[45] I. Özgen, J. Zhao, D. Liang, and R. Hinkelmann. Urban flood modeling using shallow water equations with depth-dependent anisotropic porosity. *Journal of Hydrology*, 541 :1165–1184, October 2016.

[46] A. Paquier. Rapport final du projet RIVES Risque d'inondation en ville et évaluation de scénarios. Synthèse. Technical report, Cemagref, 2009.

[47] A. Paquier. Rapport Scientifique Final du projet RIVES "Risques d'inondation en ville et étude de scénarios. Technical report, Cemagref, 2009.

[48] Y. I. H. Parish and P. Müller. Procedural Modeling of Cities. In *Proceedings of the 28th Annual Conference on Computer Graphics and Interactive Technique*, pages 301–308, 2001.

[49] M. Ratto, A. Pagano, and P. Young. State Dependent Parameter metamodelling and sensitivity analysis. *Computer Physics Communications*, 177(11) :863–876, December 2007.

[50] M. Reghezza. *Réflexions autour de la vulnérabilité métropolitaine : la métropole parisienne face au risque de crue centennale*. PhD thesis, Université de Nanterre - Paris X, December 2006.

[51] N. Rivière, R. J. Perkins, B. Chocat, and A. Lecus. Flooding flows in city crossroads : experiments and 1-D modelling. *Water Science & Technology*, 54(6-7) :75, October 2006.

[52] M. Rubinato, R. Martins, G. Kesserwani, J. E. T. Leandro, S. Djordjević, and J. Shucksmith. Experimental calibration and validation of sewer/surface flow exchange equations in steady and unsteady flow conditions. *Journal of Hydrology*, 552 :421–432, September 2017.

[53] A. Saltelli, P. Annoni, I. Azzini, F. Campolongo, M. Ratto, and S. Tarantola. Variance based sensitivity analysis of model output. Design and estimator for the total sensitivity index. *Computer Physics Communications*, 181(2) :259–270, February 2010.

[54] A. Saltelli, M. Ratto, T. Andres, F. Campolongo, J. Cariboni, D. Gatelli, M. Saisana, and S. Tarantola. *Global Sensitivity Analysis. The Primer*. John Wiley & Sons, Ltd, Chichester, UK, December 2007.

[55] B. F. Sanders, J. E. Schubert, and H. A. Gallegos. Integral formulation of shallow-water equations with anisotropic porosity for urban flood modeling. *Journal of Hydrology*, 362(1) :19–38, November 2008.

[56] A. Sattar, A. Kassem, and M. Chaudhry. Case Study : 17th Street Canal Breach Closure Procedures. *Journal of Hydraulic Engineering*, 134(11) :1547–1558, 2008.

[57] J. E. Schubert and B. F. Sanders. Building treatments for urban flood inundation models and implications for predictive skill and modeling efficiency. *Advances in Water Resources*, 41 :49–64, June 2012.

[58] G. P. Smith, P. F. Rahman, and C. Wasko. A comprehensive urban floodplain dataset for model benchmarking. *International Journal of River Basin Management*, 14(3) :345–356, July 2016.

[59] S. Soares-Frazao and Yves Zech. Dam-break flow through an idealised city. *Journal of Hydraulic Research*, 46(5) :648–658, September 2008.

[60] Edward H. Taylor. Flow Characteristics at Rectangular Open-Channel Junctions. *Transactions of the American Society of Civil Engineers*, 109(1) :893–902, January 1944.

[61] G. Testa, D. Zuccala, F. Alcrudo, J. Mulet, and S. Soares-Frazao. Flash flood flow experiment in a simplified urban district. *Journal of Hydraulic Research*, 45 - Extra issue :37–44, 2007.

[62] S. Van Emelen, S. Soares-Frazao, C. K. Riahi-Nezhad, M. Chaudhry, J. Imran, and Y. Zech. Simulations of the New Orleans 17th Street Canal breach flood. *Journal of Hydraulic Research*, 50(1) :70–81, February 2012.

[63] C. A. Vanegas, D. G. Aliaga, B. Beneř, and P. A. Waddell. Interactive Design of Urban Spaces using Geometrical and Behavioral Modeling. *ACM Transactions on Graphics*, 28(111) :10, 2009.

[64] M. Velickovic, Y. Zech, and S. Soares-Frazão. Steady-flow experiments in urban areas and anisotropic porosity model. *Journal of Hydraulic Research*, 55(1) :85–100, January 2017.

Quatrième partie

Annexes

Annexe A

Liste des supports d'enseignements produits

A.1 Publications de transfert (publications d'enseignement rédigées, polycopiés)

1. P. Finaud-Guyot. 2020. Correction du cahier de TD *Hydrologie de bassin*, 40 pages, Polytech Montpellier.
2. P. Finaud-Guyot. 2019. Correction du cahier de TD *Méthodes Mathématiques pour l'Ingénieur*, 23 pages, Polytech Montpellier.
3. P. Finaud-Guyot et P.-A. Garambois. 2017 (remis à jour en 2020). Polycopié de Mécanique des fluides, d'hydraulique en charge et à surface libre, 212 pages, Polytech Montpellier. [1]
4. P. Finaud-Guyot. 2018 (remis à jour en 2019). Cahier de TD hydraulique à surface libre, 193 pages, ENGEES.
5. P. Finaud-Guyot. 2017 (remis à jour en 2019). Cahier de TD hydraulique en charge, 92 pages, ENGEES.
6. Finaud-Guyot P., 2013. Modélisation avancée des cours d'eau – Utilisation de HECRas 2D. 50 pages, ENGEES.
7. P. Finaud-Guyot et P.-A. Garambois. 2016 (remis à jour en 2017). Cartographie des résultats de simulation HECRas, 16 pages, ENGEES.
8. P. Finaud-Guyot et P.-A. Garambois. 2016. Construction d'un modèle HECRas avec RiverGIS, 21 pages, ENGEES.
9. P. Finaud-Guyot et P.-A. Garambois. 2016 (remis à jour en 2017). Guide de modélisation hydraulique - Du MNT au modèle hydraulique : règles de digitalisation, 9 pages, ENGEES.
10. Finaud-Guyot P. et al. 2014. Protocole de TP d'hydraulique, 50 pages, ENGEES.
11. Finaud-Guyot P., 2014. TD d'hydraulique à surface libre - Correction détaillée des exercices, 46 pages, ENGEES, Formation Initiale.
12. Finaud-Guyot P., 2014. TD d'hydraulique en charge avancée - Correction détaillée des exercices, 6 pages, ENGEES, Formation Initiale.
13. Finaud-Guyot P., 2014. TD d'hydraulique à surface libre avancée - Correction détaillée des exercices, 8 pages, ENGEES, Formation Initiale.
14. Finaud-Guyot P., 2014. Modélisation avancée des cours d'eau – Manuel de maillage sous SMS. 17 pages, ENGEES, Formation initiale.

1. https://team.inria.fr/lemon/files/2019/11/Poly_Hydraulique_20192020_light.pdf

15. Finaud-Guyot P., 2013. Polycopié d'hydraulique générale, en charge et à surface libre - Support de cours, 78 pages, ENGEES, Formation continue.
16. Finaud-Guyot P., 2013. Polycopié d'hydraulique générale, en charge et à surface libre - Cahier d'exercices corrigés, 78 pages, ENGEES, Formation continue.
17. Finaud-Guyot P., 2013. Modélisation avancée des cours d'eau – Manuel de maillage sous BlueKenue. 4 pages, ENGEES, Formation initiale.
18. Finaud-Guyot P., 2013. TD d'hydraulique en charge - Correction détaillée des exercices, 27 pages, ENGEES, Formation Initiale.
19. Finaud-Guyot P., 2012. TD d'hydrogéologie - Correction détaillée des exercices, 8 pages, ENGEES, Formation Initiale.
20. Finaud-Guyot P., 2012. Partial Differential Equations and modeling. Polycopié de cours, 60 pages, Master MNI 1 ère année. (En anglais)
21. Finaud-Guyot P., 2011. TD de mécanique des fluides - Correction détaillée des exercices, 50 pages, ENGEES, Formation Initiale.
22. Finaud-Guyot P., 2010 (remis à jour en 2013). Hydrodynamique souterraine. Polycopié de cours, 32 pages, Master STEE, UM2.

A.2 Supports audio-visuels et multimédia

1. P. Finaud-Guyot, 2020. Hydrologie de bassin - Vidéos de présentation (4 vidéos), Polytech Montpellier.
2. P. Finaud-Guyot, 2019. TD d'hydraulique en charge transitoire, ENGEES. 1 code de calcul.
3. P. Finaud-Guyot, 2016. Modélisation couplée HECRas-Qgis - TD de modélisation de cours d'eau, ENGEES, DE GEME. 5 activités + 1 projet.
4. P. Finaud-Guyot, 2014. TD d'hydraulique en charge avancée, ENGEES, 1 outil de calcul.
5. P. Finaud-Guyot, 2016. Phénomènes en mécanique des fluides et hydraulique - Vidéos d'illustration, (30 vidéos, temps cumulé 6h21), ENGEES, Formation continue.
6. P. Finaud-Guyot, 2013. Hydraulique en charge et à surface libre, ENGEES, Outils de calcul - 9 feuilles de calcul Excel.
7. P. Finaud-Guyot, 2012. Modélisation sous HECRas - TD informatique, ENGEES, 8 activités.

A.3 Principales présentations orales

1. P. Finaud-Guyot, 2020. Modélisation hydrologique - les modèles GR. 7 diapositives, Polytech Montpellier.
2. P. Finaud-Guyot, 2016 (Mise à jour en 2019). Hydraulique à surface libre. 119 diapositives, ENGEES.
3. P. Finaud-Guyot, 2015 (Mise à jour en 2019). Hydraulique à surface libre pour l'assainissement. 203 diapositives, ENGEES.
4. P. Finaud-Guyot, 2015 (Mise à jour en 2019). Hydraulique générale et en charge. 131 diapositives, ENGEES.
5. Finaud-Guyot P., 2014. Inondation et aménagement du territoire, 47 diapositives, ENGEES, Conférence ENSAS.
6. Finaud-Guyot P., 2012 (Mise à jour en 2018). Modélisation des cours d'eau – Formation au logiciel HECRas, 151 diapositives, ENGEES.
7. Finaud-Guyot P., 2012 (Mise à jour en 2018). Les différentes approches de modélisation des inondations, 71 diapositives, ENGEES.
8. Finaud-Guyot P., 2012. Modélisation 2D – Formation au logiciel SW2D, 10 diapositives, ENGEES, Formation initiale.

Annexe B

Liste des enseignements dispensés

B.1 Vacations pendant mon doctorat (2006-2008)

2007-2008 Hydraulique (3h TD, 30h TP), Sciences et Technologies de l'Eau 1ère année, Polytech Montpellier

2007-2008 Hydraulique (60h TP), Sciences et Technologies de l'Eau 2ème année, Polytech Montpellier

2006-2007 Hydraulique (3h TD, 30h TP), Sciences et Technologies de l'Eau 1ère année, Polytech Montpellier

2006-2007 Projet mathématique (8h TP), Formation ITCBTP, Conservatoire National des Arts et Métiers

B.2 Enseignements en tant qu'ATER (2009-2010)

2009-2010 Hydrodynamique souterraine (9h CM, 12h TD, 16h TP et 3x9h Terrain), Master 1 Sciences de la Terre de l'Eau et de l'Environnement, Université Montpellier 2

2009-2010 Hydraulique générale (32h TD), Licence 2 Géosciences, Prévention et Traitement des Pollutions et Licence 3 Sciences de la Terre et de l'Environnement, Université Montpellier 2

B.3 Enseignements à l'ENGEES (2010-2019)

B.3.1 Hydraulique et bases théoriques

2014-2016 Hydraulique à surface libre (12h TD), Formation Initiale 1A, ENGEES.

2012-2016 Dynamique fluviale (4h TD), Formation Initiale 1A, ENGEES.

2011-2015 Hydrogéologie (8h TD), Formation Initiale 1A, ENGEES.

2010-2016 Hydraulique en charge (12h TD), Formation Initiale 1A, ENGEES.

2010-2016 Mécanique des fluides (16h TD), Formation Initiale 1A, ENGEES.

2010-2016 Hydraulique générale (24h TP), Formation Initiale 1A, ENGEES.

2010-2015 Hydraulique générale (24h TP), Formation par Apprentissage 1A, ENGEES.

2012-2013 Water supply networks (24h Projet), Master 2 in Water Environment Oceanography (WEO), University of Sciences and Technologies of Hanoï. Cours en anglais.

B.3.2 Mise en situation de l'ingénieur

2015-2016 Projet Pluridisciplinaire (5h CM, 12h TD, 8h Terrain), Formation Initiale et par Apprentissage 2A, ENGEES.

2013-2015 Inondations et aménagement du territoire (4h CM, 20h Projet), Master 2, ENS d'Architecture de Strasbourg.

2010-2015 Modélisation des cours d'eau - HECRas 1D (16h TD), Formation par Apprentissage 2A, ENGEES.

2010-2012 SIG (6h CM, 9h TD), Master 1 Ingénierie et Sciences pour l'Environnement, Université de Strasbourg.

2010-2012 SIG (24h Projet), Master 2 Ingénierie et Sciences pour l'Environnement, Université de Strasbourg.

2010-2012 Aménagement et environnement (2h CM), M2, INSA de Strasbourg.

B.3.3 Modélisation numérique

2015-2018 Hydraulique numérique (6h TD), Mastère Eau Potable et Assainissement, ENGEES.

2014-2016 Hydraulique numérique (24h TD), Formation Initiale 1A, ENGEES.

2014-2015 Calcul scientifique (12h TD), Formation Initiale 1A, ENGEES.

2014-2016 Outils informatiques pour le calcul scientifique (8h TD), Formation Initiale 1A ENGEES.

2010-2015 Partial Differential Equations & modeling (14h CM, 10h TD), Master 1 Modélisation numérique en ingénierie, Université de Strasbourg. Cours en anglais.

2010-2015 Modeling Project M1S1 (5h TD, 50h Projet), Master 1 Modélisation numérique en ingénierie, Université de Strasbourg. Cours en anglais.

2010-2013 Applied computational engineering for heat and mass transfer (12h CM), Master 2 Modélisation numérique en ingénierie, Université de Strasbourg. Cours en anglais.

B.3.4 Enseignements en formation continue

2013 Modélisation des cours d'eau - HECRas 1D (35h CM), Formation en entreprise - Bureaux d'études GeoImpact et Infratech.

B.3.5 Enseignements à distance

2014-2017 Hydraulique générale, en charge et à surface libre (15h CM), Formation ouverte à distance, ENGEES.

B.4 Enseignements à l'Université de Montpellier - Polytech (Depuis 2019)

Depuis 2019 TP de Mécanique des fluides, Formation STE 3, Polytech' Montpellier

Depuis 2019 TP d'Hydraulique, Formation STE 3, Polytech' Montpellier

Depuis 2019 TP de Métrologie, Formation STE 3, Polytech' Montpellier

Depuis 2019 TD d'Hydrologie de bassin, Formation STE 3, Polytech' Montpellier

Depuis 2019 Projet d'Ingéniérie Mathématique et Scientifique, Formation STE 3, Polytech' Montpellier

Depuis 2019 TD de Méthodes mathématiques pour l'ingénieur, Formation STE 4, Polytech' Montpellier

Depuis 2019 TP d'Hydraulique, Formation STE 4, Polytech' Montpellier

Depuis 2019 TD d'hydrologie urbaine, Formation STE 4, Polytech' Montpellier

Depuis 2019 TD de Modélisation hydrologique, Formation STE 4, Polytech' Montpellier

Depuis 2020 CM, TD, TP d'Hydraulique a Surface Libre, Formation EGC 3 Polytech' Montpellier

Depuis 2019 TD d'Informatique appliquée, Formation EGC 3 Polytech' Montpellier

Depuis 2019 Projet EGC, Formation EGC 3 Polytech' Montpellier

Depuis 2019 TP de Métrologie, Formation EGC 3, Polytech' Montpellier

Depuis 2019 TP Découverte des inondations, Formation Peip, Polytech' Montpellier

Annexe C

Tirés à part des principaux travaux scientifiques

Cette partie présente 5 publications significatives représentatives qui illustre la diversité des travaux que j'ai conduit et qui pourront servir de base au projet de recherche proposé.

ACL1 P. Finaud-Guyot, P.-A. Garambois, G. Dellinger, F. Lawniczak and P. François. *Experimental characterization of various scale hydraulic signatures in a flooded branched street network.* Urban Water Journal, 16(9) : 609-624, 2020. https://dx.doi.org/10.1080/1573062X.2020.1713173

ACL2 L. Pujol, P.-A. Garambois, P. Finaud-Guyot, J. Monnier, K. Larnier, R. Mosé, S. Biancamaria, H. Yesou, D. Moreira, A. Paris and S. Calmant. *Estimation of Multiple Inflows and Effective Channel by Assimilation of Multi-satellite Hydraulic Signatures : The Ungauged Anabranching Negro River.* Journal of Hydrology, 2020. https://doi.org/10.1016/j.jhydrol.2020.125331

C-ACT6 P. Finaud-Guyot, P.-A. Garambois, S. Chen, G. Dellinger, A. Ghenaim, and A. Terfous. *1d/2d porosity model for urban flood modeling : case of a dense street networks.* In A. Paquier and N. Rivière, editors, E3S Web of Conferences, volume 40, page 06010, Lyon, France, 2018. https://doi.org/10.1051/e3sconf/20184006010

ACL13 C. Delenne, P. Finaud-Guyot, V. Guinot, and B. Cappelaere. *Sensitivity of the 1d shallow water equations with source terms : Solution method for discontinuous flows.* International Journal for Numerical Methods in Fluids, 67(8) :981–1003, 2010. https://dx.doi.org/10.1002/fld.2398

ACL14 P. Finaud-Guyot, C. Delenne, J. Lhomme, V. Guinot, and C. Llovel. *An approximate-state Riemann solver for the two-dimensional shallow water equations with porosity.* International Journal for Numerical Methods in Fluids, 62(12) :1299-1331, 2010. https://dx.doi.org/10.1002/fld.2066

Urban Water Journal

ISSN: 1573-062X (Print) 1744-9006 (Online) Journal homepage: https://www.tandfonline.com/loi/nurw20

Experimental characterization of various scale hydraulic signatures in a flooded branched street network

P. Finaud-Guyot, P.-A. Garambois, G. Dellinger, F. Lawniczak & P. François

To cite this article: P. Finaud-Guyot, P.-A. Garambois, G. Dellinger, F. Lawniczak & P. François (2019) Experimental characterization of various scale hydraulic signatures in a flooded branched street network, Urban Water Journal, 16:9, 609-624, DOI: 10.1080/1573062X.2020.1713173

To link to this article: https://doi.org/10.1080/1573062X.2020.1713173

URBAN WATER JOURNAL
2019, VOL. 16, NO. 9, 609–624
https://doi.org/10.1080/1573062X.2020.1713173

Taylor & Francis
Taylor & Francis Group

RESEARCH ARTICLE

Experimental characterization of various scale hydraulic signatures in a flooded branched street network

P. Finaud-Guyot [a,b,c], P.-A. Garambois [d,e], G. Dellinger [c], F. Lawniczak [f] and P. François [f]

[a]HSM, University Montpellier, CNRS, IRD, Montpellier, France; [b]LEMON, Inria, Montpellier, France; [c]ICube Laboratory (UMR 7357), Fluid Mechanics Team, ENGEES, Strasbourg, France; [d]ICube Laboratory (UMR 7357), Fluid Mechanics Team, INSA, Strasbourg, France; [e]INRAE, Aix Marseille Univ, RECOVER, Aix-en-Provence, France; [f]ICube Laboratory (UMR 7357), Fluid Mechanics Team, IUT Robert Schuman, Strasbourg, France

ABSTRACT

Understanding urban flood flow repartition mechanisms within street network remains challenging. This paper presents an experimental dataset of water depth and velocity profiles in the Icube experimental rig. The spatial variability of discharge along a street is highlighted. Comparing the water depth gradient orientation and the flow repartition promotes for complex repartition mechanisms at small scales. Comparable unit-discharge values are observed in both large and narrow streets. Interestingly, the intensity of the discharge deviation at the crossroad scale is related with the asymmetry of the velocity profile entering a crossroad. Moreover, discharges at the crossroad and the subdistrict scales show that downscaling of the flow repartition relationship is difficult. At real scale, results show that inflow velocity profile asymmetry may persist on a distance of several street widths downstream of a crossroad. Such distances are insufficient to consider disconnected crossroads as done in the literature to establish discharge repartition relationships.

ARTICLE HISTORY
Received 7 March 2019
Accepted 5 January 2020

KEYWORDS
Urban flooding; Icube experimental rig; hydraulic characterization; discharge repartition

1. Introduction

In the context of climate change, the increase of floodplain urbanization might lead to an increase in the vulnerability to floods. In such context, numerical models appear to be an interesting tool to forecast the impact of floods with various return periods and to assess mitigation and country planning policy (Costabile and Macchione 2015).

The classical modeling approaches are based on the (1D and/or 2D) shallow water equations (SWE) with (Finaud-Guyot et al. 2010; Guinot, Sanders, and Schubert 2017; Chen 2018) or without macroscopic porosity approach (Hervouet, Samie, and Moreau 2000; Finaud-Guyot et al. 2011; Arrault et al., 2016; Chen et al. 2018; Bruwier et al. 2017) or on the 3D Reynolds Average Navier-Stokes equations (RANS) (Araud 2012; Horna Munoz and Constantinescu 2018). The predictive capacity of such modeling approaches is highly dependent on the adequation between the real physics and the mathematical equations (either continuous or discrete) solved. To our best knowledge, there is currently in the bibliography no general framework enabling to determine *a priori* which modeling approach should be used to reproduce an urban flood complexity. The laboratory scale experiments are thus a reliable tool to investigate the flood propagation mechanism in complex urban geometries.

The existing experimental rigs designed to investigate urban floods consider different flow scales (Mignot, Li, and Dewals 2019). At the local scale, the hydrodynamic interactions between sewers and flooded streets are studied experimentally and numerically. Among others, Lopes et al. (2015) and Rubinato et al. (2017) focus on the sewer-surface flow exchange to study the classical weir/orifice relationship validity, determine headloss coefficients for the gully and the jet characterization over the manhole in surcharge flow configurations. Discharges and momentum exchanges are also studied in three branch junctions (Best 1987; Gurram, Karki, and Hager 1997), bifurcations (Mignot et al. 2013, 2014; Momplot et al. 2015) and four branch intersections (Mignot 2005; Mignot, Paquier, and Rivière 2008; Mignot et al. 2008; Nanía et al. 2011; Rivière, Travin, and Perkins 2011, 2014). Various flow regimes and configurations are investigated in those studies but the experimental rigs include only one hydraulic intersection and do not represent both the effect of non-uniform upstream velocity profiles and the downstream control effects for fluvial regimes.

At a larger scale, various experimental rigs exist to study flood hydrodynamics in real-world scaled configurations. Ishigaki, Toda, and Inoue (2003) present the experimental model of Kyoto city to study the importance of flows through the subway network during the city flooding. The water depths are measured at some precise locations and the discharges at some street inlets and at the junction of the street with the subway. Over the tested range, the water volume entering the subway network can represent up to 50% of the total flood volume. This study mainly focuses on the surface and subsurface exchanges but provides flow velocity measurements around $2 m.s^{-1}$ at few locations. Sattar, Kassem, and Chaudhry (2008) propose an experimental reproduction of the 17th Street levee breach in New Orleans during the Katrina storm with water depth monitoring over the whole device and some velocity measurements close to the breach. Different breach closure procedures are investigated experimentally or numerically (Jia et al. 2010). Van Emelen et al. (2012) compare the same experimental dataset with a finite volume depth-averaged shallow water model and highlight the non-negligible 3D effect close to

CONTACT P. Finaud-Guyot pascal.finaud-guyot@umontpellier.fr

the breach. Smith, Rahman, and Wasko (2016) study experimentally and numerically the 2007 flood in Newcastle (Australia). The model extent covers several houses along the existing river but few crossroads. Various hydrodynamic informations are experimentally gathered in steady state and different modeling approaches tested to account for the buildings in 2D numerical models are investigated.

To cope with the difficulty to generalize the above-mentioned results due to the site dependent approach, some more general rigs have been designed at the district scale. Soares-Frazao and Zech (2008) and Testa et al. (2007) investigate the effect of an idealized urban area (made of aligned or staggered blocks) on a dam-break flood either in a canal with a flat or a variable topography. The water depth timeseries $h(t)$ is monitored at various locations. The water depth evolution is shown to be related to the local block pattern in very transient configurations. Lipeme Kouyi et al. (2009) and Paquier (2009) assess the influence of a modification of an urban geometry (add of a roundabout, a place, or a tram line) on the flow distribution using an experimental setup based on a real-like district geometry during the Rives and Hyville projects. The experiments are carried out for steady state configuration with flow oriented from a district face to the opposite one. The same geometry is used in the Icube urban flood experimental rig presented in (Araud 2012) that compares the steady state experimental water depth and inlet/outlet discharge with various numerical software. Finaud-Guyot et al. (2018) focus on the hydraulic signature of the district by comparing the inlet/outlet discharge without investigating the flow pathway. Those existing experimental studies do not investigate the urban flood flow repartition within a street network and especially velocity profiles.

The present contribution aims to fill this gap and presents an experimental dataset composed of water depth and velocity profiles with a high spatial resolution for flood flows in a real-like branched street network. The flow repartition within the district is studied along with the upscaling effect from the flow pattern at the subdistrict scale to the global scale. This article is structured as follows: the second section presents the experimental rig and the measurement devices. The third section is devoted to the analysis of the experimental dataset (water depth, velocity profile and street discharge) from the district to the crossroad scale. The last section proposes concluding remarks and perspectives.

2. Materials and methods

2.1. The Icube urban flood experimental rig

The Icube urban flood experimental rig is built to study the hydrodynamics of flood propagation in urban configuration. The street network corresponds to the district geometry proposed during the Rives and Hyville projects (Lipeme Kouyi et al. 2009) that is assumed to be representative of typical urban geometries. The district is composed of a network of streets of different widths with various crossroad angles with 64 impermeable blocks built on a 5m $\times$ 5m plan (see Figure A1(a,b)) corresponding to a real district of 1km $\times$ 1km. The street network is composed of seven streets in the North-South direction crossed by seven streets in the West-East direction. The larger streets are 12.5cm wide and the narrower ones are 4.5cm wide.

The scaling of this experimental rig is detailed in (Finaud-Guyot et al. 2018; Araud 2012). The horizontal (resp. vertical) scaling is 1200 (resp. $^1/_{20}$) leading to a distortion factor (being the vertical to the horizontal scaling ratio) of 10; the flow respects the Froude similarity. This leads to a discharge ratio $\lambda_Q = Q_{exp}/Q_{real} = \lambda_v\lambda_h\lambda_l \approx 5.6 \times 10^{-5}$, and the inlet discharge range tested (10 to 100m^3.h^{-1}) corresponds to significant to extreme floods of more than 150 years return period. Concerning the hydrodynamic turbulence, the Reynolds ratio falls in the range $1.1 \times 10^{-3} \leq \lambda_{\mathrm{Re}} = \mathrm{Re}_{exp}/\mathrm{Re}_{real} \leq 1.1 \times 10^{-2}$ (see (Finaud-Guyot et al. 2018) for detailed calculations). Distortion factor is known to potentially induce modifications of the hydrodynamic flow structures (Li et al. 2019).

2.2. Metrology

The Icube urban flood experimental rig has been built such that water flows in a closed-circuit with a precise measurement of the street discharge at both the inlet (1% precision) and the outlet (relative accuracy lower than 3%).

An automatically moving camera can be placed on each side of a street to film the free surface through the transparent walls (see Figure 1 – Top Left). The gathered images are processed to extract the water depth profile (see Figure 1 – Top Right) and then averaged over the recording time. Figure 1 – Bottom Left presents a measured water depth profile along both sides of a street. The error bars represent the range of the measured value at each location $\left(\left[\min_{t\in T}(h(x,t))\ \max_{t\in T}(h(x,t))\right]\right)$ where T represents the recording duration). Comparing the average water depth profile (even considering the standard deviation range around the mean value – blue and red dashed line on Figure 1 – Bottom Left) highlights that the water depth on the left side of the street is slightly higher than on the right side. This can also be observed on the water depth profiles of the other streets (not presented in the present paper). The water depth recirculation that occurs downstream of crossroads inside of the flow bend is responsible for such water depth profiles across the streets (Chen 2018).

An ultrasonic sensor is placed at the free surface to measure the velocity profile at the measuring points. The instantaneous velocity profiles are acquired during 120s with a frequency of 9Hz and a vertical spacing of 1.5mm. More than 1000 profiles are thereafter averaged in order to access the mean velocity profile unaffected by turbulence. In order to measure the street discharge, all the measurement points are located 7cm upstream of each crossroad where the velocity profile is assumed to be horizontal and barely unperturbed by the upstream crossroad. Repeating the measurements over the street width (3 (resp. 5) points for the narrow (resp. large) streets) enables for the velocity integration by polynomial fitting over the cross-section to access the experimental street discharge. Velocity integration is based on the assumption that the laminar boundary layer is of negligible thickness in comparison with the

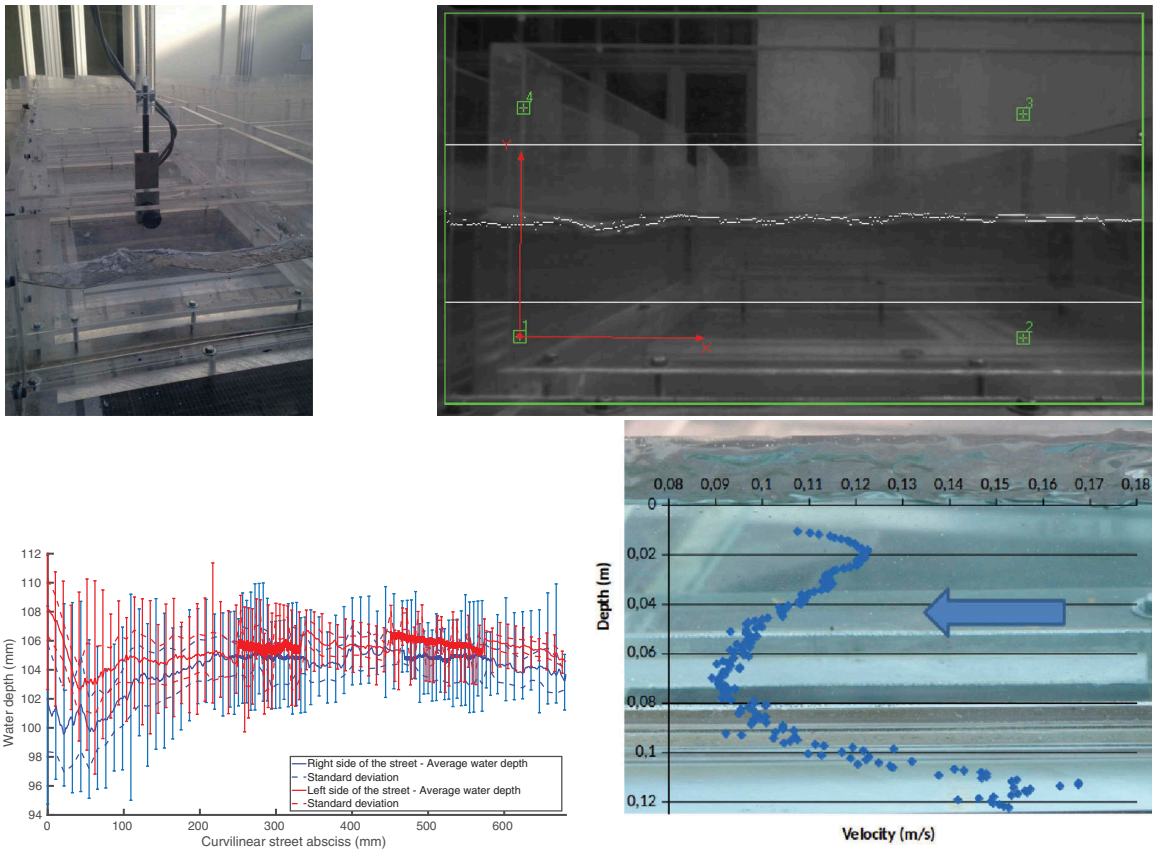

Figure 1. Experimental metrology. Top Left: Camera on the side of street B4B5. Top Right: Instantaneous water depth profile extracted from the side view of the street. Bottom Left: Comparison of the water depth profile along both sides of street B4B5. Bottom Right: Typical velocity profile along the water depth.

street dimensions. Those experimental discharges are also in agreement (difference of less than 2%) with the inlet and outlet discharges either measured by the volumetric pump characteristics or by the downstream end weir relationship.

3. Results: experimental study of the flow distribution at various scales

Thanks to spatially distributed water depth and velocity measurements, this section investigates the flow repartition mechanisms from the district to the crossroad scale. First, the experimental configuration and experimental dataset are presented; next, the flow repartition is analyzed from the large (district) scale to the crossroad scales. For the sake of clarity, the notations and definitions used are recalled in Appendix B.

3.1. Studied flow configuration

The choice is made to perform the investigations with a null bottom slope (0mm) and 3cm high rectangular weirs at the downstream end of all streets (South and East faces). Using those downstream weirs ensure subcritical flows everywhere (see Figure 2(e) and Table D1(b)) and a reduction of the relative importance of uncertainties on depth measurement and flow perturbation due to the US sensor.

A total discharge $Q_{tot}^{dis} = 80\text{m}^3.\text{h}^{-1}$ is inflowed on the upstream faces of the district (^{dis}). The total discharge is equally injected between the North and the West faces ($Q_{tot}^{dis} = Q_N^{dis} + Q_W^{dis}$ and $Q_N^{dis} = Q_W^{dis}$); the same unit discharge is injected in each street of a face such that: $Q_{up,k} = Q_{\{N,W\}}^{dis}.B_{up,k}/B_{\{N,W\}}^{dis}$ with $Q_{\{N,W\}}^{dis}$ the discharge injected on one face (North or West), $B_{up,k}$ the width of the street k in the normal direction to the street axis and $B_{\{N,W\}}^{dis}$ the cumulated street widths on a face.

3.2. Experimental hydrodynamic measurements

This section describes the experimental dataset: the water depth and the velocity profiles over the whole district.

3.2.1. Water elevation measurements

The water depth measured using the camera is plotted in Figure 1. It decreases at the district scale from the North-West to the South-East corner in the range [6cm; 12cm]. Following (Araud 2012), the water depth gradient is computed in Table D1(a) assuming that the water depth can be described by a plan equation $\hat{h}(x,y) = \alpha + \beta x + \gamma y$ at both the district and the subdistrict scale. At the district scale, $\beta/\gamma = 2.22$ highlights that the water surface slope is about 2 times larger in the x

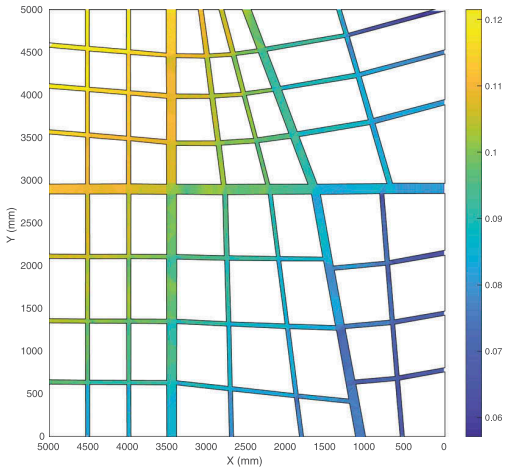

(a) Measured water depth (m). Note that the lines across the streets (especially 4, C and F) are plotting artifacts.

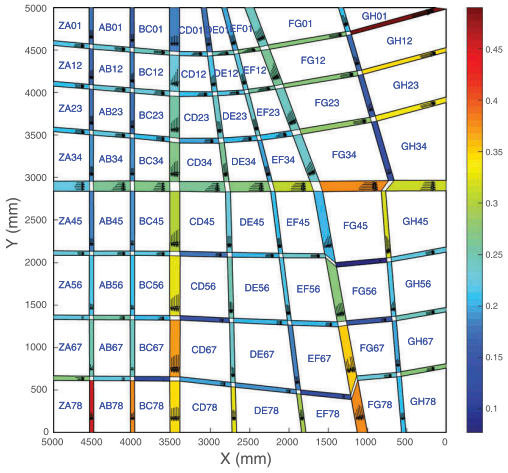

(b) Velocity in the streets ($m.s^{-1}$). The arrows represent the velocity measured 7cm upstream each crossroad.

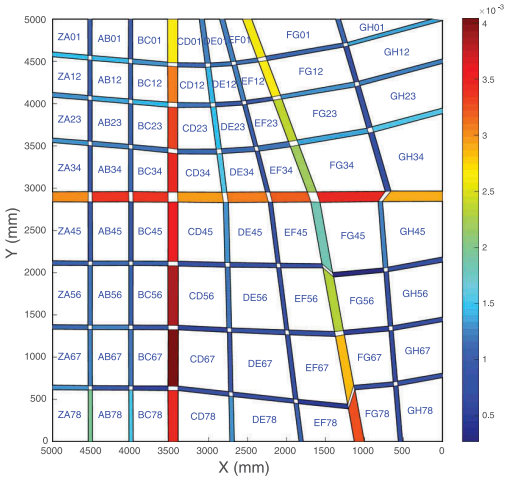

(c) Discharge ($m^3.s^{-1}$)

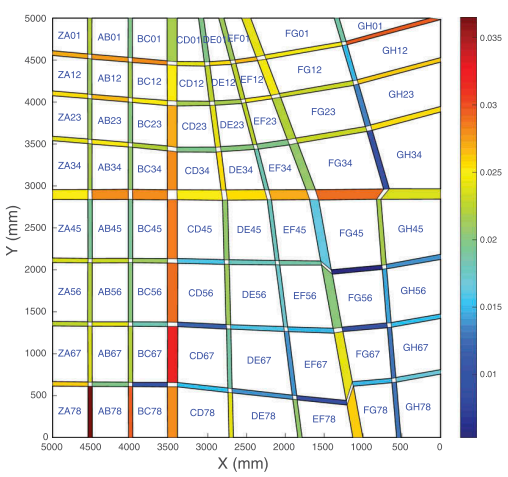

(d) Unit discharge ($m^2.s^{-1}$)

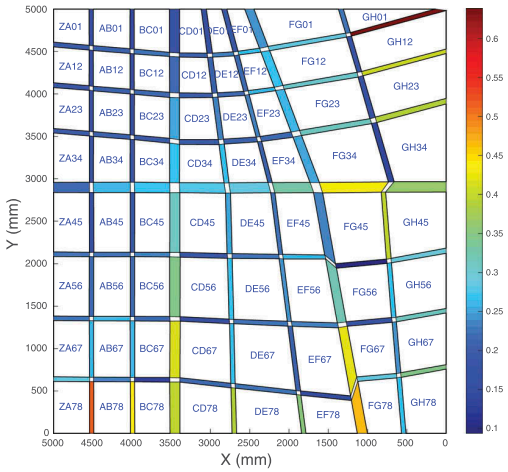

(e) Froude number

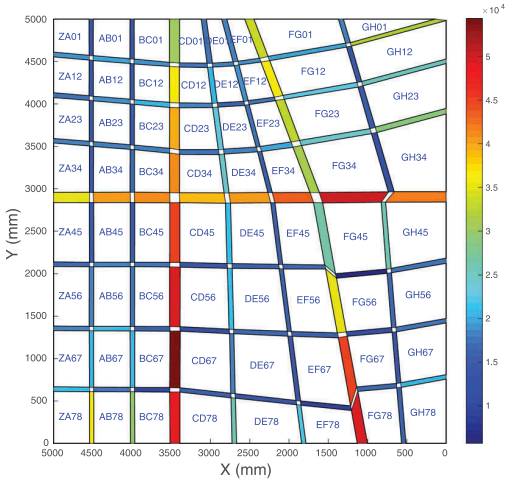

(f) Reynolds number

Figure 2. Experimental data measured within each street.

direction than in the y direction. This might indicate that the flow is mainly oriented towards the East face. However, as in the configuration without weir (see Figure 4), the discharge flowing out the district by the East face ϕ_E^{dis} represents about 40% of the total injected discharge. Therefore, the water depth potential does not characterize the flow distribution at first order. The correlation between the direction of the water depth gradient and the discharge repartition is investigated at the subdistrict scale in Section 3.4.

3.2.2. Velocity profiles

The velocity is averaged on the water depth for the different locations in Figure 2(b) and the evolution of the horizontal (depth averaged) velocity profiles along each street is shown in Figure E1. For all streets, the water flows from West to East (or North to South) direction. For the narrow streets, the velocity profiles just 7cm upstream of all crossroads are barely flat. For the large streets (4, C and F), the profiles remain unsymmetrical with a larger velocity on the right (resp. left) side of street 4 (resp C and F). Those larger velocities are located on the outer side of the street highlighting the flow throat effect due to the recirculation area occurring downstream of crossroads (see Figure C1). Assuming that $L_c = \kappa B$ is the distance along a free surface flow necessary to recover an unperturbed velocity profile downstream of a singularity, with B the water surface width and κ classically ranging in $[10; 50]$. The average width of the narrow (resp. large) streets being $\overline{B_{narrow}} = 5.3$cm ($\overline{B_{large}} = 11.8$cm) (see Table A1), the corresponding velocity control length is in the range $53\text{cm} < L_{c,narrow} < 265\text{cm}$ which is below all narrow street lengths (resp. $118\text{cm} < L_{c,large} < 590\text{cm}$ which is above all large street lengths). Therefore, the fact that the measured velocity profiles are symmetrical in the narrow streets but not in the large ones must be related to their respective L/B ratio that is important enough in the narrow street to recover an unperturbed velocity profile between two crossroads. Moreover, given that the horizontal scaling of the experimental rig is the same for the lengths and the widths of the streets, this conclusion about the perturbation of the hydrodynamics by the upstream crossroad for large streets remains valid in real-world configurations. In other words, those four branch crossroads considered in a branched network are not *hydrodynamically disconnected*.

3.3. Analysis of flow repartition

Local velocity and discharge values are of prior interest in the context of (urban) flood forecasting and are also essential to gain insight on flow repartition mechanisms in a complex branched network composed of multiple four branch crossroads. The spatial statistics on the measured/estimated flow variables and dimensionless numbers are presented in Table D1(b) and analyzed in the following sections.

3.3.1. Spatially distributed discharge map

The discharge in each street is classically obtained by integrating the velocity over the flow cross-section (see Figure 2(c)). Unsurprisingly most of the inflow discharge is flowing in large streets (4, C and F) while non-uniform discharge variations appear along streets; see for instance the discharge in street F decreasing from crossroads F0 to F5 and then increasing from F5 to F8. The outlet discharge of the large streets (4, C and F) represents $Q_{large}^{dis}/Q_{tot}^{dis} = 42\%$ of the total discharge. The cumulative width of the large streets normalized by the total street outlet width $B_{large}^{dis}/B_{tot}^{dis}$ represents 38%. The fact that $Q_{large}^{dis}/Q_{tot}^{dis} \approx B_{large}^{dis}/B_{tot}^{dis}$ suggests that the outlet flow partition between the large and the narrow streets is driven by the street

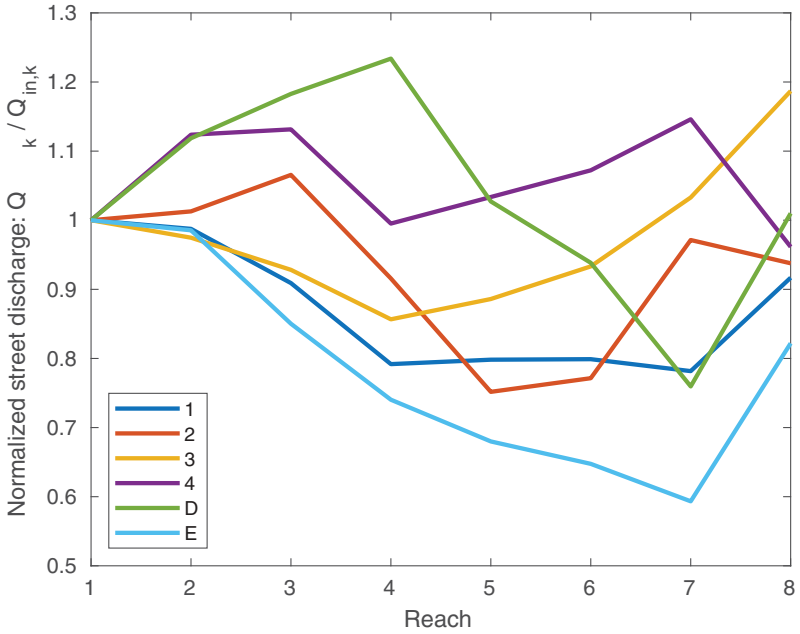

Figure 3. Evolution of the discharge along streets normalized by the street inlet discharge.

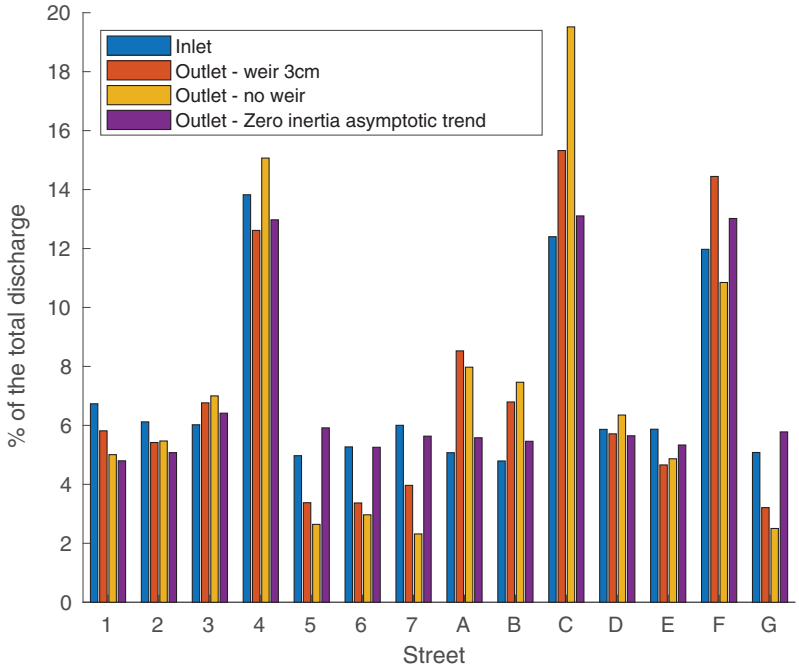

Figure 4. Evolution of the discharge ratios $(Q_{up,k}/Q_{tot}^{dis}$ (blue) and $Q_{down,k}/Q_{tot}^{dis}$ (orange, yellow) between the inlet and the outlet of each street at the district scale. The 'Zero inertia asymptotic trend' series represents $Q_{down,k}/Q_{tot}^{dis}$ for each street k computed as $\frac{Q_{down,k}}{Q_{tot}^{dis}} = \frac{B_{down,k}}{\sum_j B_{down,j}}$. The outlet discharge of the East face represents $\phi_E^{dis} = 41.7\%$ (respectively $\phi_E^{dis} = 40.5\%$) of the total discharge Q_{tot}^{dis} for the configuration with weir (respectively no weir). The variability of the 'zero inertia asymptotic trend configuration' is due to different street widths existing at the downstream end (see Table A1).

width. Remark, on the outlet faces, the discharge/unit-discharge variability between the outlet streets (for instance narrow: A, B, D, E and G or large: 4, C and F on Figures 1 and 1). Consequently, within the large (resp. small) streets the discharge partition is not correlated to the street width.

The question was raised in (Finaud-Guyot et al. 2018) between *'a discharge conservation along the street or an equilibrium between inflow and losses along the street*'. Figures 2(c) and 3 highlight the variations of the normalized discharge along the streets 1 to 4 and D to E (for which the inlet and outlet discharges differ from less than 1.2% of the total discharge Q_{tot}). The discharge along a street shows oscillations around the inlet discharge value. Consequently, along those streets there is an equilibrium between the sources and the losses in the tested configurations.

In order to enable the comparison of narrow and large streets, the unit-discharge $q = Q/B$ in the streets is plotted in Figure 2(d) and the statistics are presented in Table D1(b). Note that the unit discharge estimated in the first streets after the inlets is slightly different from the prescribed inflow discharges with a constant unit discharge in the streets of an inlet face (West or North, see protocol in Section 3.1). This stems from measurement uncertainties and small spatial variations of street width between injection and measurement locations.

The unit discharges obtained fall in the range $[0.005; 0.036]\mathrm{m}^2.\mathrm{s}^{-1}$ with an average value of $0.020\mathrm{m}^2.\mathrm{s}^{-1}$ (resp. $0.025\mathrm{m}^2.\mathrm{s}^{-1}$), a standard deviation of $0.005\mathrm{m}^2.\mathrm{s}^{-1}$ (resp. $0.003\mathrm{m}^2.\mathrm{s}^{-1}$) for the large (resp. narrow) streets (see Table D1(b)). Similar unit discharges are observed both in narrow or large streets highlighting the non-negligible role of narrow streets compared to large ones in draining water. Moreover, as shown in Figure 2(d), the spatial variability of q between reaches of a street is significant, which promotes complex flow repartition mechanisms at smaller scales.

3.3.2. Hydraulic signature at the district scale

The evolutions of the relative discharge from the inlet $Q_{up,k}/Q_{tot}^{dis}$ to the outlet $Q_{down,k}/Q_{tot}^{dis}$ for each street are presented in Figure 4, with $Q_{up,k}$ and $Q_{down,k}$ respectively the upstream and downstream discharges of street k. The blue bars correspond to the ratio at the street inlet, the orange ones to the ratio at the outlet for the studied configuration with a 3cm high weir, the third one to the outlet without any weir. For streets 1, 2, 3, 4, D and E, the normalized outflow discharges differ from the inflow discharges from less than 1.2%. Streets A, B, C and F have a discharge that significantly increases between inlet and outlet. Conversely, the streets 5 to 7 and G lose a significant part of their inlet discharge.

Interestingly, except for streets 4, 7, C and F, the relative discharge at the street outlet is modified by less than 1% of the total discharge Q_{tot}^{dis} between the configuration with and without weir. This would claim for a very limited role of the downstream control on the discharge repartition, which is coherent with the supercritical flow observed at the downstream end of the streets in the configuration without weir. This counterintuitive observation for the present subcritical configuration (see Table D1(b) and Figure 2(e)) might be explained because the experiments are in steady state and thus the inlet and outlet discharges are equal. In such

a configuration, if a weir reduces the discharge in a given street, the mass balance imposes that *(i)* the discharge has to increase in the same proportion in (an)other street(s) despite the presence of a weir and *(ii)* the flow pattern is different within the district between the configuration with and without weir. In the present case, the equilibrium is much more complicated as it applies to 14 interconnected streets. The significant evolution of the outlet discharge for streets 4, C, F and 7 claims for a modification of the flow pattern within the district.

The last bar *Zero inertia asymptotic trend* in Figure 4 represents the outlet discharge proportional to each outlet street width. This configuration represents the asymptotic discharge repartition for equally high weirs. Indeed, in such a case huge water levels imposed downstream would considerably reduce the flow velocity and hence lead to a barely flat water surface over the whole district with very small inertial effect. Since the weirs are similar, the outlet discharge of each street would become proportional to the street width. Consequently, at a street outlet, a discharge that differs from its zero inertia asymptotic trend is at least partially influenced by inertial effects upstream occurring along the streaklines. For the configuration with downstream weirs, the streets 2 to 4 and D to E have normalized outflow discharges that differ of less than 1% from the asymptotic outflow discharges. This corresponds to the streets with a barely constant discharge from the inlet to the outlet (presented in Table 1, Section 3.4).

3.4. Characterization of the flow repartition at the subdistrict and crossroad scales

This section investigates the hydrodynamic signatures at the subdistrict scale. For the sake of clarity, the definition of the subdistrict introduced in (Finaud-Guyot et al. 2018) is used: a subdistrict is the set of narrow streets surrounded by the large streets (4, C and F) or the rig frontiers (see Figure B1). This scale is first shown to be relevant since the hydraulic signature is similar within a subdistrict. A comparison of the discharge deviation at the subdistrict scale regarding various geometric properties of the experimental rig is then presented. An insight is then proposed on the upscaling from the crossroad to the (sub)district scale.

3.4.1. Is the subdistrict scale relevant?

Thanks to the discharge data in each reach, Table 1 compares the street inlet and outlet discharges at the district scale. The *Trend* line characterizes the street water balance at the district scale and shows that all streets separated by large ones either gain or lose water from the inlet to the outlet. This claims for a 'splitting' of the district hydraulic signature highlighted in Section 3.3.2 by the large streets.

Table 1 thus depicts such trends at the subdistrict scales (see lines $\Delta Q_{k,ZC}$, $\Delta Q_{k,CF}$, $\Delta Q_{k,FH}$, $\Delta Q_{k,04}$ and $\Delta Q_{k,48}$ in Table 1). For each street, the discharge variation through a subdistrict normalized by the total discharge Q_{tot}^{dis} is not monotonous along the street (except for street G) – see for instance the discharge variation for street 1: $\Delta Q_{k,ZC}$ that is negative between inlet (crossroad Z1) and the crossroad C1, almost nil between C1 and F1 $\Delta Q_{k,CF}$ and positive between F1 and the outlet (crossroad H1) $\Delta Q_{k,FH}$. This confirms that the street hydraulic signature is different for each subdistrict.

Table 1. Street discharge variation normalized by the total discharge Q_{tot}. Note that the streets Z, H, 0 and 8 are the virtual streets surrounding the studied district. $\Delta Q_{k,CF}$ (resp. $\Delta Q_{k,48}$) represents the normalized discharge variation of the street k between the crossroads *Ck* and *Fk* (resp. *k*4 and *k*8). The arrows compare the street outlet and inlet discharges: → barely constant; ↗ increasing; ↘ decreasing with a threshold corresponding to ± 1.2% of the total discharge Q_{tot}^{dis}.

		Street						
Face		1	2	3	**4**	5	6	7
East	$\Delta Q_{k,ZC}$	−0.61	0.40	−0.43		−0.10	−1.00	−3.51
	$\Delta Q_{k,CF}$	0.05	−0.88	0.46		0.19	0.89	−1.84
	$\Delta Q_{k,FH}$	0.91	−0.21	0.93		2.29	0.97	0.58
	$\Delta Q_{k,tot}$	−0.83	−0.62	0.85	−1.01	−1.54	−1.85	−1.98
	Trend	→	→	→	→	↘	↘	↘
		Street						
		A	B	**C**	D	E	**F**	G
South	$\Delta Q_{k,04}$	−0.31	0.44		1.37	−1.52		−1.83
	$\Delta Q_{k,48}$	4.21	2.57		−0.10	0.83		−2.5
	$\Delta Q_{k,tot}$	3.59	2.11	3.16	−0.06	1.14	2.70	−1.82
	Trend	↗	↗	↗	→	→	↗	↘

Figure F1 plots the inlet and outlet normalized discharges (by the total discharge Q_{tot}^{dis}) of each street of a subdistrict. It confirms that each subdistrict has its own hydraulic signature and that the large streets (4, C and F) '*act as global separators of the flow pattern*' as suggested numerically in (Chen et al. 2018) on comparable cases. The subdistrict scale thus appears to be a coherent scale for studying the discharge deviation during a flood in an urban street network and for the modeling of such phenomenon.

3.4.2. On discharge deviation at the subdistrict scale

The distributed measurements enable us to study the geometrical/hydrodynamic features and their impact on the flow deviation for each subdistrict.

3.4.2.1. Subdistrict outlet flow repartition. At the scale of the subdistrict, let us introduce the portion of the total discharge flowing out the East face $\phi_E^{sub} = Q_E^{sub}/Q_{tot}^{sub}$ where Q_E^{sub} (respectively Q_{tot}^{sub}) is the discharge leaving the subdistrict (^{sub}) by the East face (respectively entering the subdistrict); see textbox on Figure 4.

It appears that for all the subdistricts $\phi_E^{sub} > \phi_E^{dis} = 41.7\%$ (see legend of Figure 4). This flow imbalance is compensated at the district scale thanks to the significant flow deviation to the South due to large streets. As found at the district scale (see Figure 3), the flow repartition for the three northern subdistricts (AB123, DE123 and G123) between their two outlet faces is barely proportional to the number of streets per outlet face; for instance $\phi_E^{G123} = 72.2\%$ and $\frac{3\,\text{east streets}}{4\,\text{outlet streets}} = 75\%$.

3.4.2.2. Effect of the street width on the flow repartition. Since it appears to be logical that the flow is more important through a face with either a lot of streets or equivalently with an important cumulative width, Figure 4 presents the unit-discharge ratio $\psi_E^{sub} = \phi_E^{sub} B_{tot}^{sub}/B_E^{sub}$ that is the ratio of $q_E^{sub} =$

Q_E^{sub}/B_E^{sub} (the unit-discharge flowing out the subdistrict by the East face) to $q_{tot}^{sub} = Q_{tot}^{sub}/B_{tot}^{sub}$ (the subdistrict outlet unit discharge).

For the northern subdistricts (AB123, DE123 and G123) ψ_E^{sub} is barely equal to 100% implying that the discharge repartition through those subdistricts is driven by the cumulative width of the outlet face. Conversely, the southern subdistricts have a unit-discharge ratio ψ_E^{sub} smaller than 100% highlighting that the flow is deviated to the South face compared to the width outlet ratio. For the subdistrict AB567 and DE567, this might be explained by their proximity of the street outlets on the South face. Despite the vicinity of the downstream end of subdistrict G123 streets on the East face, this does not seem to 'over attract' the flow eastward. Interestingly, the flow is the most deviated to the South in the subdistrict G567 and neither the proximity with the boundary condition nor the number of streets on the South face does not seem to explain this deviation.

3.4.2.3. Effect of the inlet flow repartition of the outlet flow repartition.

It remains that the subdistrict outlet flow repartition might be related to the inlet repartition. Recalling that $\phi_W^{sub} = Q_W^{sub}/Q_{tot}^{sub}$, Figure 4 presents the ratio $\phi_E^{sub}/\phi_W^{sub}$. A $\phi_E^{sub}/\phi_W^{sub} = 100\%$ corresponds to a *transparent* subdistrict for which the discharge repartition at the inlet and the outlet is the same. All the subdistricts tend to deviate the discharge to the South ($\phi_E^{sub}/\phi_W^{sub} < 100\%$). The deviation for the northern subdistricts (AB123, DE123 and G123) is quite small which seems to be correlated to the fact that the geometry drives the flow repartition as $\psi_E^{sub} \approx 100\%$. Concerning the subdistrict DE567, the deviation is as small as for the northern subdistricts. Interestingly, the discharge flows in this subdistrict such as $\phi_W^{sub} = 51.5\%$ (corresponding barely to the equipartition between the two upstream faces). The subdistrict AB567 and G567 strongly deviates the flow to the South ($\phi_E^{sub}/\phi_W^{sub} < 72\%$) although the flow mainly enters through the West face ($\phi_W^{AB567} = 64\%$ and $\phi_W^{G567} = 66\%$).

The discharge deviation at the subdistrict scale can be analyzed in the light of the water depth gradients presented in Table D1(a). This shows that the water depth gradient is oriented towards the East face for subdistrict DE123 and G567, towards the South face for AB123, AB567 and DE567 and to the North for G123. For the outlet subdistricts AB567 and DE567, the direction of the water depth gradient is coherent with one of the flow deviations. The incoherence between water depth gradient and flow direction might be explained (*i*) by the deviation of the West-East streets to the North for G123 et G567; (*ii*) the weir at the outlet of street 1 that is not perpendicular to the street direction (the weir being aligned with the North face) and (*iii*) by the asymmetrical velocity profile in the street G4G5 entering the subdistrict G567 that is more important on the right (inner) street side.

3.4.3. On discharge deviation at the crossroad scale

Eventually, the discharge repartition and deviation occur at the crossroads composing this branched street network. The flow deviation highlighted in Figure 4 is an upscaled combination of several crossroads effect.

Figure 5(c) presents the relative discharge deviation ratio at each crossroad: $\alpha^{cross} = \left(Q_E^{cross} - Q_W^{cross}\right)/Q_{tot}^{cross}$ where $Q_{tot}^{cross} = Q_N^{cross} + Q_W^{cross}$ is the discharge that enters the crossroad through the North and West streets. When this deviation ratio is nil ($\alpha^{cross} = 0$), $Q_E^{cross} = Q_W^{cross}$ and $Q_N^{cross} = Q_S^{cross}$ characterizing a 'transparent' crossroad behavior without influence on the flow repartition; $\alpha^{cross} < 0$ (resp. $\alpha^{cross} > 0$) characterizes a flow deviation to the South (resp. East). Various crossroad behaviors can be identified from no discharge deviation (crossroad E1 and E5) to up to 30% of the discharge entering the crossroad (crossroads B7 to the East or G5 to the South).

The flow deviation at a crossroad is likely to be influenced by the local downstream water depth, the shape of the upstream velocity profile and/or to some extent to the geometry of the crossroad. Indeed, the crossroads of the AB567 subdistrict have barely the same geometry but the flow is alternatively deviated to the East or to the South. The sign of the relative discharge deviation ratio α for each crossroad is varying within a subdistrict. This promotes potential complex interactions between all crossroads which is highlighted by asymmetrical velocity profiles (see Section 3.2.2). The latest prevents to downscale the discharge deviation from the subdistrict to the crossroad scale and as shown above (see Section 3.4.2) from the district to the subdistrict scale.

4. Concluding remarks and perspectives

This contribution presents an unprecedented experimental dataset for flood flows of significant return period in a real-like branched street network. The analysis is based on accurate measurements of spatially distributed water depth and velocity profiles.

The comparison between the direction of the water depth gradient and the flow repartition, both at the district and the subdistrict scales, promotes for complex flow repartition at smaller scales. This is underlined by the observed variety of velocity profile shapes and especially the very asymmetrical ones. This asymmetry is most likely due to the recirculation effect and flow throat that occur downstream of a crossroad (see for instance Chen 2018; Nanía et al. 2011; Mignot 2005). This experiment led on the Icube urban flood experimental rig clearly highlights that all the velocity profiles in large streets are asymmetrical, which represents complex inlet flow conditions for four branch crossroads. Under the assumption that such hydrodynamic features are not artefacts due to the distorted experimental scaling, the transposition to the real-world scale ($\times$ 200) shows that such asymmetry may persist on a distance of 120m downstream of a crossroad. Such distances are insufficient to consider disconnected crossroads which is, to our best knowledge, the common framework used to establish the crossroad discharge repartition relationship in the literature.

The discharge estimation in every reach between two crossroads is enabled by those velocity profile measurements. Along a street, a significant discharge variability exists due to a spatial variability of the sign and magnitude of lateral fluxes. Comparable unit-discharge values are observed in both large and narrow streets. Significant flow deviations are observed for some subdistricts which promotes the recent macroscopic modeling approaches based on the shallow water equations coupled

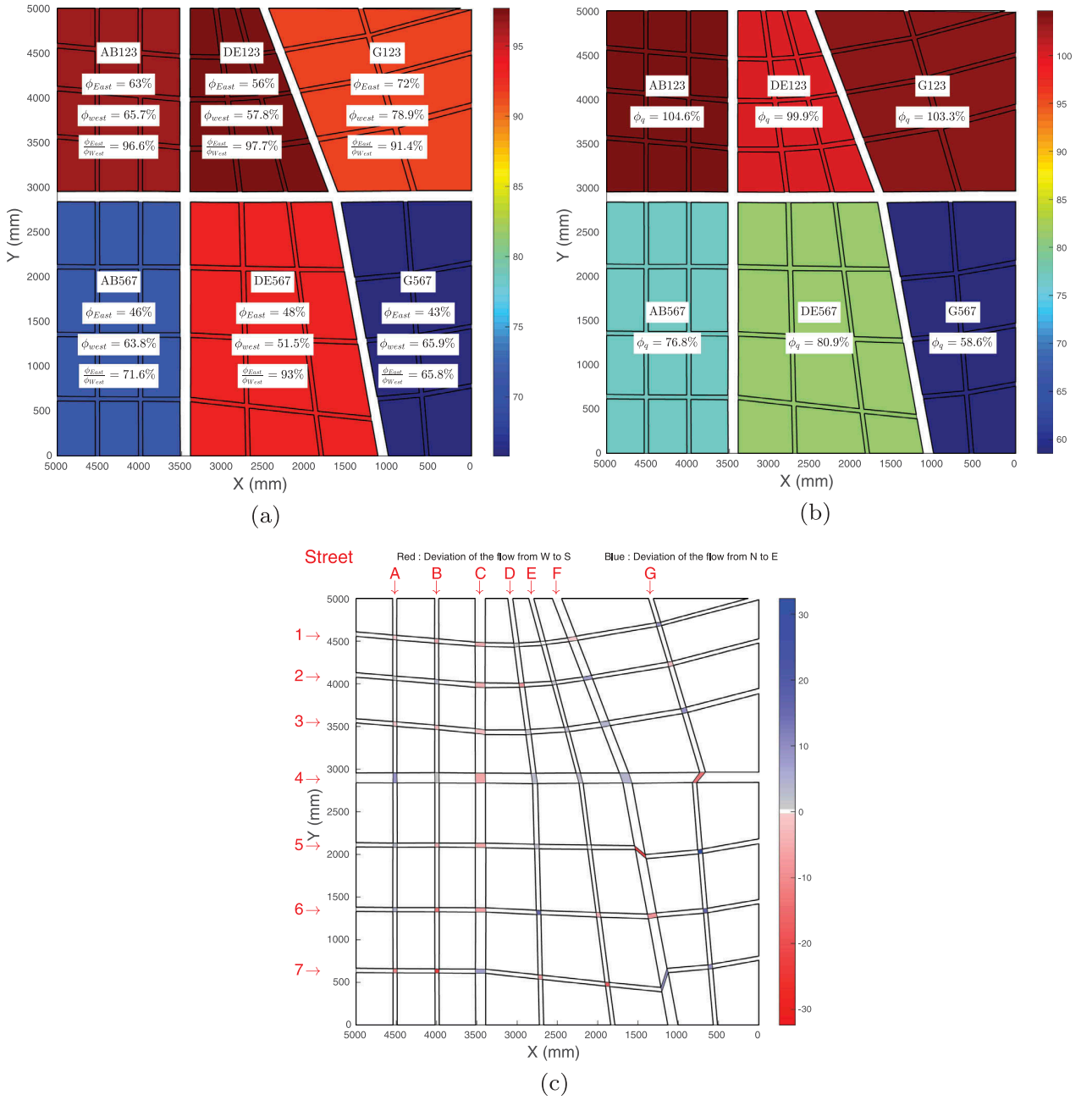

Figure 5. Flow deviation in the Icube urban flood experimental rig. (a) $\phi_E^{sub}/\phi_W^{sub}$ comparing the outlet to the inlet flow repartition; (b) unit-discharge ratio ψ_E^{sub} comparing the outlet flow repartition to the geometrical orientation; (c) relative discharge deviation α^{cross}.

with an anisotropic porosity-like parametrization (see for instance (Guinot 2017)). Interestingly, the intensity of the discharge deviation at the crossroad scale is related with the asymmetry of the velocity profile entering a crossroad. Moreover, flow repartition at both the crossroad and the subdistrict scale show that downscaling of the flow repartition relationship is difficult.

The present work paves the way for further investigations of the hydrodynamic mechanisms controlling the flow distribution at the crossroad scale with a particular insight on the non-linear upstream-downstream interaction between crossroads. Especially, the effect of the experimental rig distorsion on the 3D hydrodynamic should further be studied in order to clarify the transposability of the experimental observations to other geometrical configuration.

Acknowledgements

The authors wish to thank the Alsatian network REALISE for funding and J. Vazquez to initiate that experimental research project.

Disclosure statement

No potential conflict of interest was reported by the author(s).

ORCID

P. Finaud-Guyot http://orcid.org/0000-0002-4627-7182
P.-A. Garambois http://orcid.org/0000-0001-8350-6741
G. Dellinger http://orcid.org/0000-0002-5537-8225

References

Araud, Q. 2012. "Simulations des écoulements en milieu urbain lors d'un évènement pluvieux extrême." Thèse de doctorat, Université de Strasbourg. https://tel.archives-ouvertes.fr/tel-00814408.

Arrault, A., P. Finaud-Guyot, P. Archambeau, M. Bruwier, S. Erpicum, M. Pirotton, and B. Dewals. 2016. "Hydrodynamics of Long-duration Urban Floods: Experiments and Numerical Modelling." *Natural Hazards and Earth System Sciences Discussions* 16 (6): 1–29. February.

Best, J. L. 1987. Flow Dynamics at River Channel Confluences: Implications for Sediment Transport and Bed Morphology. *Recent developments in fluvial sedimentology* 39: 27–35

Bruwier, M., P. Archambeau, S. Erpicum, M. Pirotton, and B. Dewals. 2017. "Shallow-water Models with Anisotropic Porosity and Merging for Flood Modelling on Cartesian Grids." *Journal of Hydrology* 554: 693–709. November. doi:10.1016/j.jhydrol.2017.09.051.

Chen, S. 2018. "Effective Shallow Water Models for Complex Flood Flow Patterns in Urban Areas." Thèse de doctorat, Université de Strasbourg.

Chen, S., P.-A. Garambois, P. Finaud-Guyot, G. Dellinger, R. Mosé, A. Terfous, and A. Ghenaim. 2018. "Variance Based Sensitivity Analysis of 1d and 2d Hydraulic Models: An Experimental Urban Flood Case." *Environmental Modelling & Software* 109: 167–181. November. doi:10.1016/j.envsoft.2018.08.008.

Costabile, P., and F. Macchione. 2015. "Enhancing River Model Set-up for 2-D Dynamic Flood Modelling." *Environmental Modelling & Software* 67: 89–107. doi:10.1016/j.envsoft.2015.01.009.

Finaud-Guyot, P., C. Delenne, V. Guinot, and C. Llovel. 2011. "1d-2d Coupling for River Flow Modeling." *Comptes Rendus Mécanique* 339 (4): 226–234. doi:10.1016/j.crme.2011.02.001.

Finaud-Guyot, P., C. Delenne, J. Lhomme, V. Guinot, and C. Llovel. 2010. "An Approximate-state Riemann Solver for the Two-dimensional Shallow Water Equations with Porosity." *International Journal for Numerical Methods in Fluids* 62 (12): 1299–1331.

Finaud-Guyot, P., P.-A. Garambois, Q. Araud, F. Lawniczak, P. Fran¸cois, J. Vazquez, and R. Mosé. 2018. "Experimental Insight for Flood Flow Repartition in Urban Areas." *Urban Water Journal* 15 (3): 242–250. doi:10.1080/1573062X.2018.1433861.

Guinot, V. 2017. "A Critical Assessment of Flux and Source Term Closures in Shallow Water Models with Porosity for Urban Flood Simulations." *Advances in Water Resources* 109: 133–157. November. doi:10.1016/j.advwatres.2017.09.002.

Guinot, V., B. F. Sanders, and J. E. Schubert. 2017. "Dual Integral Porosity Shallow Water Model for Urban Flood Modelling." *Advances in Water Resources* 103: 16–31. May. doi:10.1016/j.advwatres.2017.02.009.

Gurram, S. K., K. S. Karki, and W. H. Hager. 1997. "Subcritical Junction Flow." *Journal of Hydraulic Engineering* 123 (5): 447–455. May. doi:10.1061/(ASCE)0733-9429(1997)123:5(447).

Hervouet, J. M., H. Samie, and B. Moreau. 2000. "Modelling Urban Areas in Dam-break Flood-wave Numerical Simulations." Proceedings of the International Seminar and Workshop on Rescue Actions Based on Dambreak Flow Analysis, Seinâjoki, Finland, October.

Horna Munoz, D., and G. Constantinescu. 2018. "Application of a 3-D CFD Model to Investigate Flood-related Engineering Problems." E3S Web of Conferences, Vol. 40. Lyon: A. Paquier and N. Rivière. September.

Ishigaki, T., K. Toda, and K. Inoue. 2003. "Hydraulic Model Tests of Inundation in Urban Area with Underground Space." Proceedings 30th IAHR Congress, 487–493. Thessaloniki, Greece

Jia, Y., T. Zhu, C. Riahi-Nezhad, and Y. Zhang. 2010. "Numerical Modeling of Flow through a Breached Levee and during Levee Closure." World Environmental and Water Resources Congress 2010, rovidence, Rhode Island, United States, 1304–1316. American Society of Civil Engineers. https://ascelibrary.org/doi/pdf/10.1061/41114%28371%29140

Li, X., S. Erpicum, M. Bruwier, E. Mignot, P. FinaudGuyot, P. Archambeau, M. Pirotton, and B. Dewals. 2019. "Technical Note: Laboratory Modelling of Urban Flooding: Strengths and Challenges of Distorted Scale Models." *Hydrology and Earth System Sciences* 23 (3): 1567–1580. March. doi:10.5194/hess-23-1567-2019.

Lipeme Kouyi, G., D. Fraisse, N. Rivière, V. Guinot, and B. Chocat. 2009. "One-dimensional Modelling of the Interactions between Heavy Rainfall-runoff in an Urban Area and Flooding Flows from Sewer Networks and Rivers." *Water Science and Technology: A Journal of the International Association on Water Pollution Research* 60 (4): 927–934. doi:10.2166/wst.2009.431.

Lopes, P., J. Leandro, R. F. Carvalho, P. Páscoa, and R. Martins. 2015. "Numerical and Experimental Investigation of a Gully under Surcharge Conditions." *Urban Water Journal* 12 (6): 468–476. August. doi:10.1080/1573062X.2013.831916.

Mignot, E. 2005. "Etude expérimentale et numérique de l'inondation d'une zone urbanisée: Cas des écoulements dans les carrefours en croix." PhD thesis, Ecole Centrale de Lyon.

Mignot, E., D. Doppler, N. Rivière, I. Vinkovic, J.-N. Gence, and S. Simoëns. 2014. "Analysis of Flow Separation Using a Local Frame-axis: Application to the Open-channel Bifurcation." *Journal of Hydraulic Engineering* 140: 280–290. doi:10.1061/(ASCE)HY.1943-7900.0000828.

Mignot, E., X. Li, and B. Dewals. 2019. "Experimental Modelling of Urban Flooding: A Review." *Journal of Hydrology* 568: 334–342. January. doi:10.1016/j.jhydrol.2018.11.001.

Mignot, E., A. Paquier, and N. Rivière. 2008. "Experimental and Numerical Modeling of Symmetrical Four-branch Supercritical." *Journal of Hydraulic Research* 46 (6): 723–738. November.

Mignot, E., N. Rivière, R. J. Perkins, and A. Paquier. 2008. "Flow Patterns in a Four-Branch Junction with Supercritical Flow." *Journal of Hydraulic Engineering* 134 (6): 701–713. doi:10.1061/(ASCE)0733-9429(2008)134:6(701).

Mignot, E., C. Zeng, G. Dominguez, C. W. Li, N. Rivière, and P. H. Bazin. 2013. "Impact of Topographic Obstacles on the Discharge Distribution in Open-channel Bifurcations." *Journal of Hydrology* 494: 10–19. doi:10.1016/j.jhydrol.2013.04.023.

Momplot, A., G. Lipeme Kouyi, E. Mignot, N. Rivière, and J.-L. Bertrand-Krajewski. 2015. "Une nouvelle structure d'écoulement en bifurcation à surface libre." *La Houille Blanche* 5: 78–83. October. doi:10.1051/lhb/20150058.

Nanía, L. S., M. Gómez, J. Dolz, P. Comas, and J. Pomares. 2011. "Experimental Study of Subcritical Dividing Flow in an Equal-Width, Four-Branch Junction." *Journal of Hydraulic Engineering* 137 (10): 1298–1305. October. doi:10.1061/(ASCE)HY.1943-7900.0000423.

Paquier, A. 2009. Projet RIVES : Risques d'inondation en ville et évaluation de scénarios. Rapport scientifique final, p. 145. ANR Cemagref Publications.

Rivière, N., G. Travin, and R. J. Perkins. 2011. "Subcritical Open Channel Flows in Four Branch Intersections." *Water Resources Research* 47 (10): W10517. October. doi:10.1029/2011WR010504.

Rivière, N., G. Travin, and R. J. Perkins. 2014. "Transcritical Flows in Three and Four Branch Open-Channel Intersections." *Journal of Hydraulic Engineering* 140 (4): 04014003. doi:10.1061/(ASCE)HY.1943-7900.0000835.

Rubinato, M., R. Martins, G. Kesserwani, J. E. T. Leandro, S. Djordjevié, and J. Shucksmith. 2017. "Experimental Calibration and Validation of Sewer/surface Flow Exchange Equations in Steady and Unsteady Flow Conditions." *Journal of Hydrology* 552: 421–432. September. doi:10.1016/j.jhydrol.2017.06.024.

Sattar, A., A. Kassem, and M. Chaudhry. 2008. "Case Study: 17th Street Canal Breach Closure Procedures." *Journal of Hydraulic Engineering* 134 (11): 1547–1558. doi:10.1061/(ASCE)0733-9429(2008)134:11(1547).

Smith, G. P., P. F. Rahman, and C. Wasko. 2016. "A Comprehensive Urban Floodplain Dataset for Model Benchmarking." *International Journal of River Basin Management* 14 (3): 345–356. July. doi:10.1080/15715124.2016.1193510.

Soares-Frazao, S., and Y. Zech. 2008. "Dam-break Flow through an Idealised City." *Journal of Hydraulic Research* 46 (5): 648–658. September. doi:10.3826/jhr.2008.3164.

Testa, G., D. Zuccala, F. Alcrudo, J. Mulet, and S. SoaresFrazao. 2007. "Flash Flood Flow Experiment in a Simplified Urban District." *Journal of Hydraulic Research* 45: 37–44. doi:10.1080/00221686.2007.9521831.

Van Emelen, S., S. Soares-Frazao, C. K. Riahi-Nezhad, M. Chaudhry, J. Imran, and Y. Zech. 2012. "Simulations of the New Orleans 17th Street Canal Breach Flood." *Journal of Hydraulic Research* 50 (1): 70–81. February. doi:10.1080/00221686.2011.642578.

Appendix A. Geometrical dimension of the Icube urban flood experimental rig

Table A1. Statistics about street dimensions.

	Width			Length		
	min	mean	max	min	mean	max
	B_{min}	B_{mean}	B_{max}	L_{min}	L_{mean}	L_{max}
Narrow	4.2cm	5.3cm	6.8cm	27.2cm	57.1cm	118.2cm
Large	10.6cm	11.8cm	13cm	42.6cm	57.7cm	81.5cm

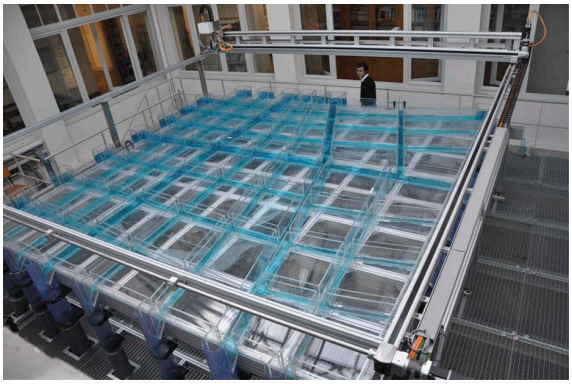

(a) Photography

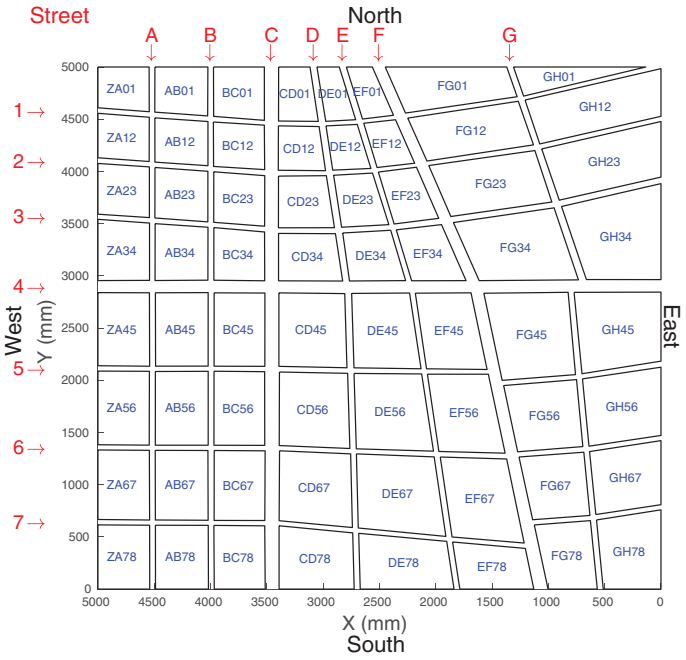

(b) Plan view

Figure A1. Icube urban flood experimental rig.

Appendix B. Definition

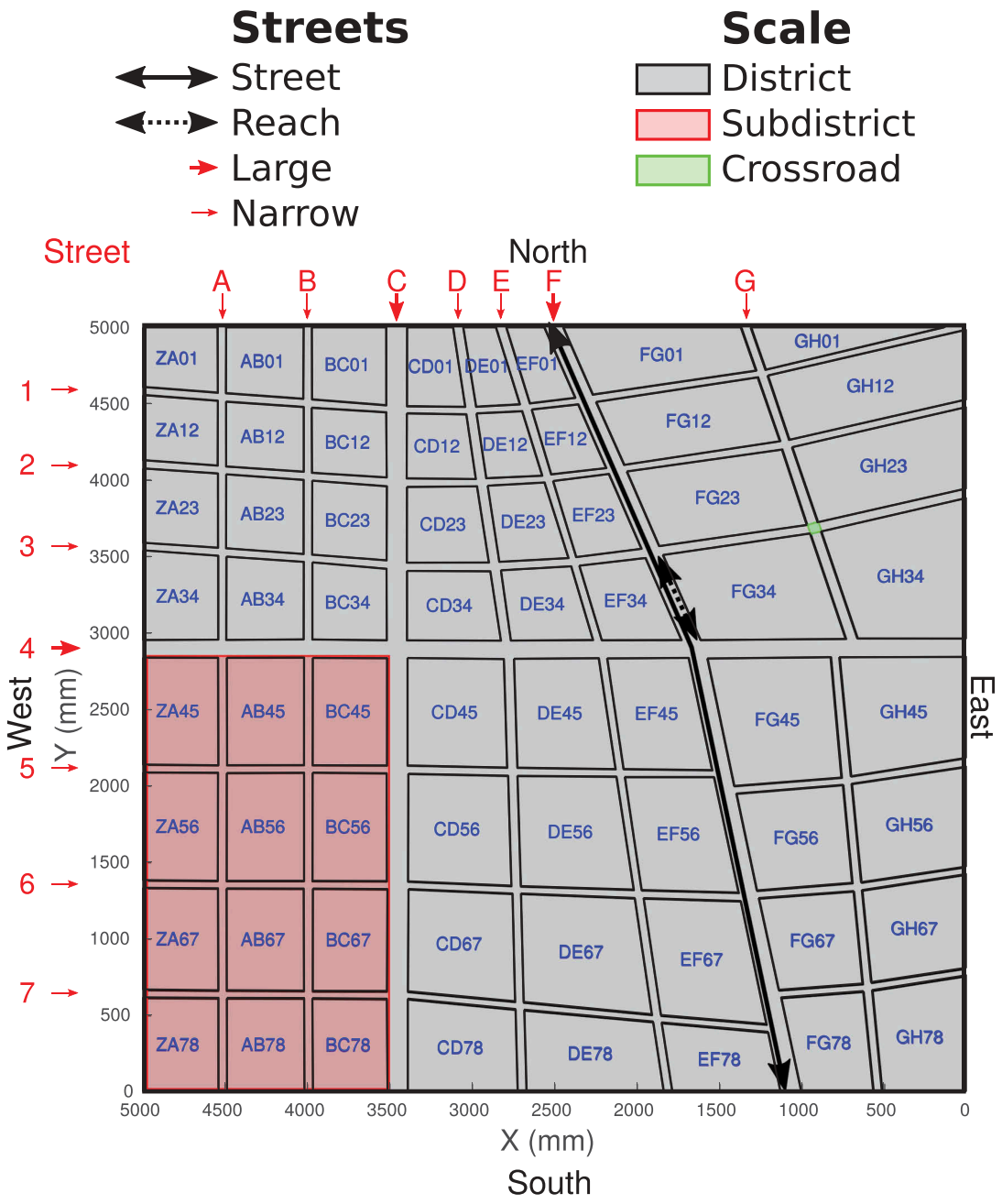

Figure B1. Definition of the different scales.

For the sake of clarity, the following notations and definitions are used:

- The whole device is denoted as the district whereas the subdistrict corresponds to the narrow street networks bounded by the district limit and the large network (see Figure B2). A reach is a rectilinear part of the experimental rig between two successive crossroads. A street includes the eight reaches between the inlet and the outlet.
- Each crossroad is identified by the letter and the digit of the corresponding crossing streets. A street extent is denoted by the corresponding upstream and downstream crossroads. A subdistrict is identified using all the street names crossing within the subdistrict; the existing subdistricts are thus *AB*123, *DE*123, *G*123, *AB*567, *DE*567 and *G*567.
- For all the considered variables, the superscript $^{\{dis,sub,cross\}}$ indicates that they are defined for the whole district (^{dis}), a subdistrict (^{sub}) or a specific crossroad (^{cross}). For the sake of clarity, the superscripts ^{sub} and ^{cross} can be replaced by the explicit names of the subdistrict or the crossroad.

- $Q_{tot}^{\{dis,sub,cross\}}$ is the total discharge injected in the district, the subdistrict and the crossroad.
- Q_N and Q_W: the upstream discharge injected by the North (respectively West) face. Q_E and Q_S: the downstream discharge flowing out the East (respectively South) face. $q_{\{N,W,S,E\}}$ is the unit-discharge of a face. Q_N, Q_W, Q_E, Q_S and $q_{\{N,W,S,E\}}$ are defined at the district, the subdistrict or the crossroad scale (the superscript $^{\{dis,sub,cross\}}$ is used to avoid confusion). Similar notations are used for the street width: $B_{\{N,W\}}^{dis}$ is the cumulative street width on the North (West) face of the district; $B_{tot}^{sub} = B_E^{sub} + B_S^{sub}$ is the cumulative street width at the outlet of a subdistrict (with a sum on the East and South faces).
- The subscripts $_{up,k}$ and $_{down,k}$ applied to $\mathcal{F}$ indicate that $\mathcal{F}$ is considered at the inlet (respectively outlet) of street k. $\mathcal{F}$ is the width B or the discharge. $B_{down,k}$ is thus the width at the downstream end of street k and $Q_{up,k}$ and $Q_{down,k}$ are the discharge injected in (respectively that flows out) the street k (where k corresponds either to A, B, C, D, E, F, G, 1, 2, 3, 4, 5, 6, 7).
- The subscripts $_{large}$ and $_{narrow}$ applied to $\mathcal{F}$ indicate that $\mathcal{F}$ is summed on the large (respectively narrow) streets. $\mathcal{F}$ is the width B or the discharge Q: $B_{narrow} = \sum_{k\in\{1,2,3,5,6,7,A,B,D,E,G\}} B_{down,k}$ and $B_{large} = \sum_{k\in\{4,C,F\}} B_{down,k}$.
- $\phi_{\{E,W\}}^{\{dis,sub\}} = Q_{\{E,W\}}^{\{dis,sub\}} / Q_{tot}^{\{dis,sub\}}$ represents the discharge entering by the West (respectively leaving by the East) face normalized by the total discharge either at the district ^{dis} or the subdistrict scale ^{sub}.
- $\psi_E^{sub} = q_E^{sub} / q_{tot}^{sub}$ represents the East unit-discharge q_E^{sub} normalized by the total leaving unit-discharge q_{tot}^{sub}.
- $\psi_E^{sub} = \left(Q_E^{sub} / B_E^{sub}\right) / \left(Q_{tot}^{sub} / B_{tot}^{sub}\right) = \phi_E^{sub} \cdot \frac{B_{tot}^{sub}}{B_E^{sub}}$.
- $\alpha^{cross} = \left(Q_E^{cross} - Q_W^{cross}\right) / Q_{tot}^{cross}$ is the relative discharge deviation by the crossroad ^{cross}.

Appendix C. Crossroad hydrodynamic

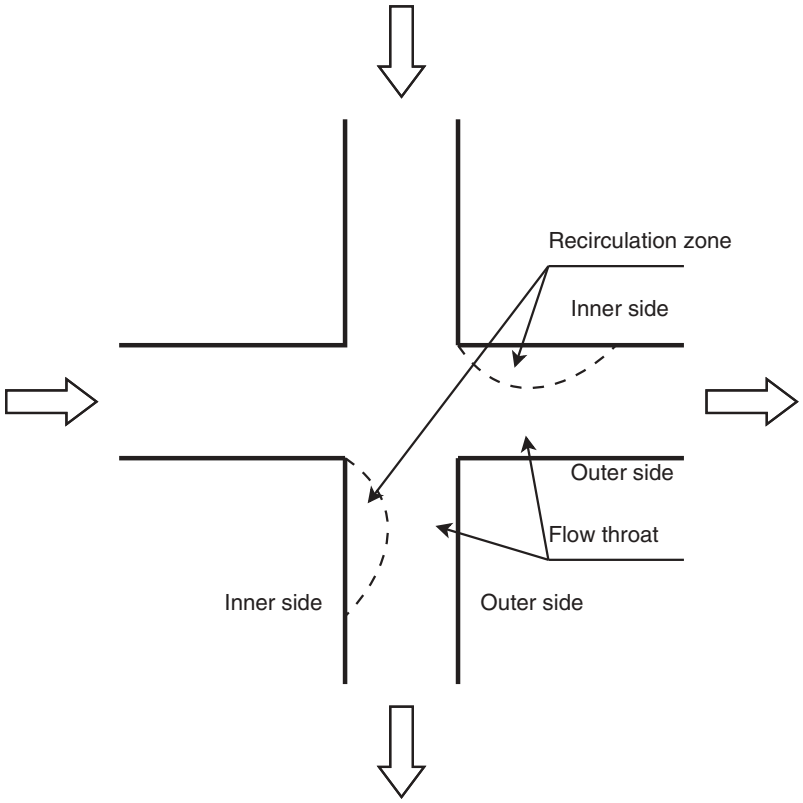

Figure C1. Schematic view of the crossroad hydrodynamic.

Appendix D. Spatial statistics on the hydrodynamic

Table D1. Depth and velocity measurements and statistics.

(a) Water depth gradient analysis; plane approximation of the water depth distribution $\hat{h}(x,y) = \alpha + \beta x + \gamma y$ at the district and subdistrict scales. The water depth gradient at the district scale is not the average of the water depth at the subdistrict scale; the water depth in the larger street is accounted in the district regression but not in the subdistrict one.

	$\beta = \partial_x h$	$\gamma = \partial_y h$	β/γ
District	$8.4e-3$	$3.8e-3$	2.22
AB123	$4.5e-3$	$4.9e-3$	0.93
DE123	$7.8e-3$	$2.7e-3$	2.92
G123	$9.3e-3$	$-10.8e-3$	−0.86
AB567	$3.0e-3$	$8.6e-3$	0.35
DE567	$2.8e-3$	$4.2e-3$	0.68
G567	$3.7e-3$	$1.0e-3$	3.60

(b) Spatial statistics on the hydrodynamic.

	Streets	Min	Mean	Max	Std Dev
Velocity	Large	0.187	0.282	0.380	0.053
$m.s^{-1}$	Narrow	0.077	0.224	0.490	0.061
Discharge	Large	1.828	3.023	4.040	0.516
$L.s^{-1}$	Narrow	0.270	1.073	1.923	0.271
Unit-discharge	Large	0.016	0.025	0.032	0.003
$m^2.s^{-1}$	Narrow	0.005	0.020	0.036	0.005
Froude	Large	0.176	0.302	0.462	0.075
	Narrow	0.094	0.240	0.639	0.154
Reynolds	Large	27000	40158	54350	6917
	Narrow	5730	18136	36166	8662

Appendix E.

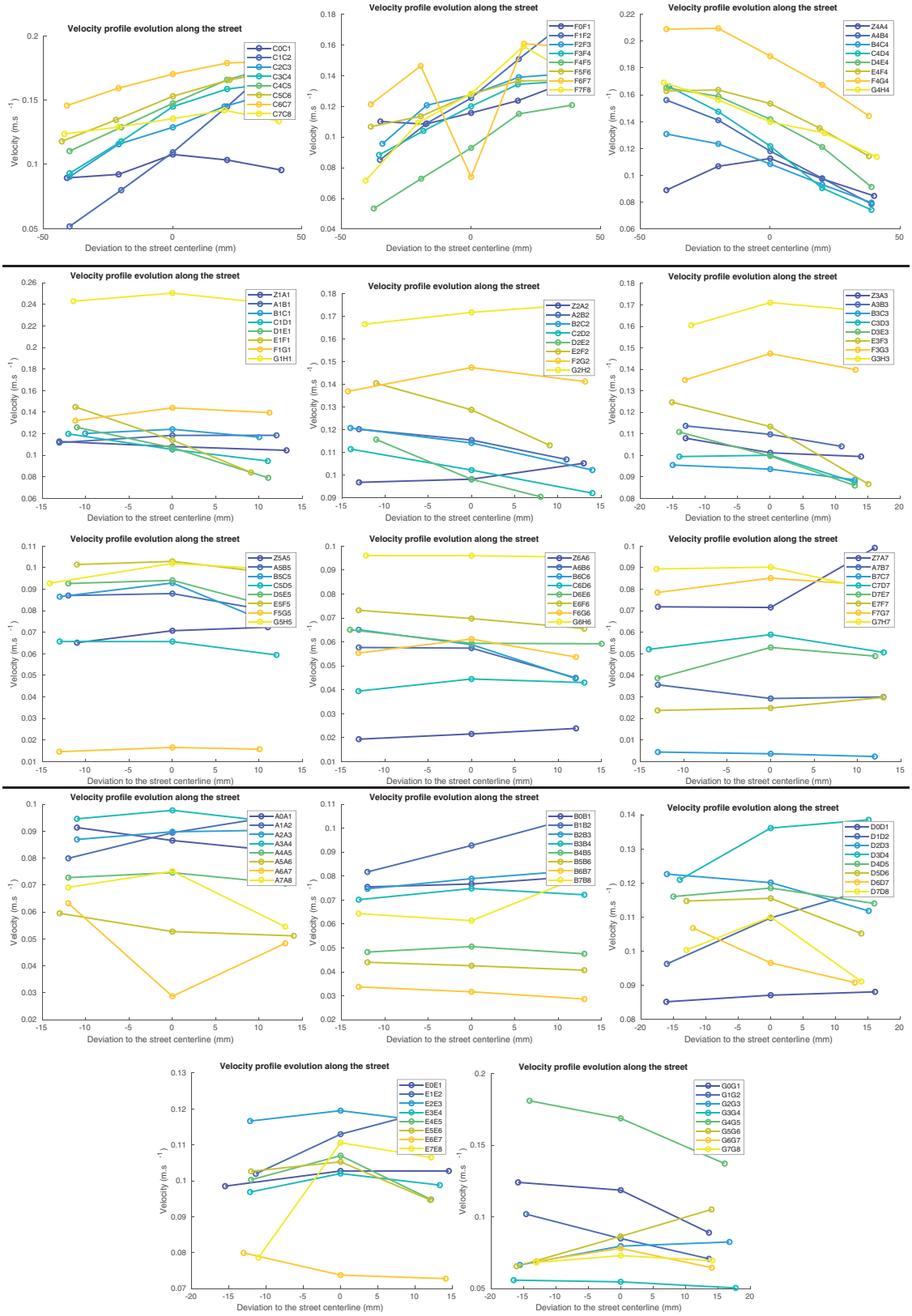

Figure E1. Velocity profiles across street.

Appendix F. Flow repartition at the subdistrict scale

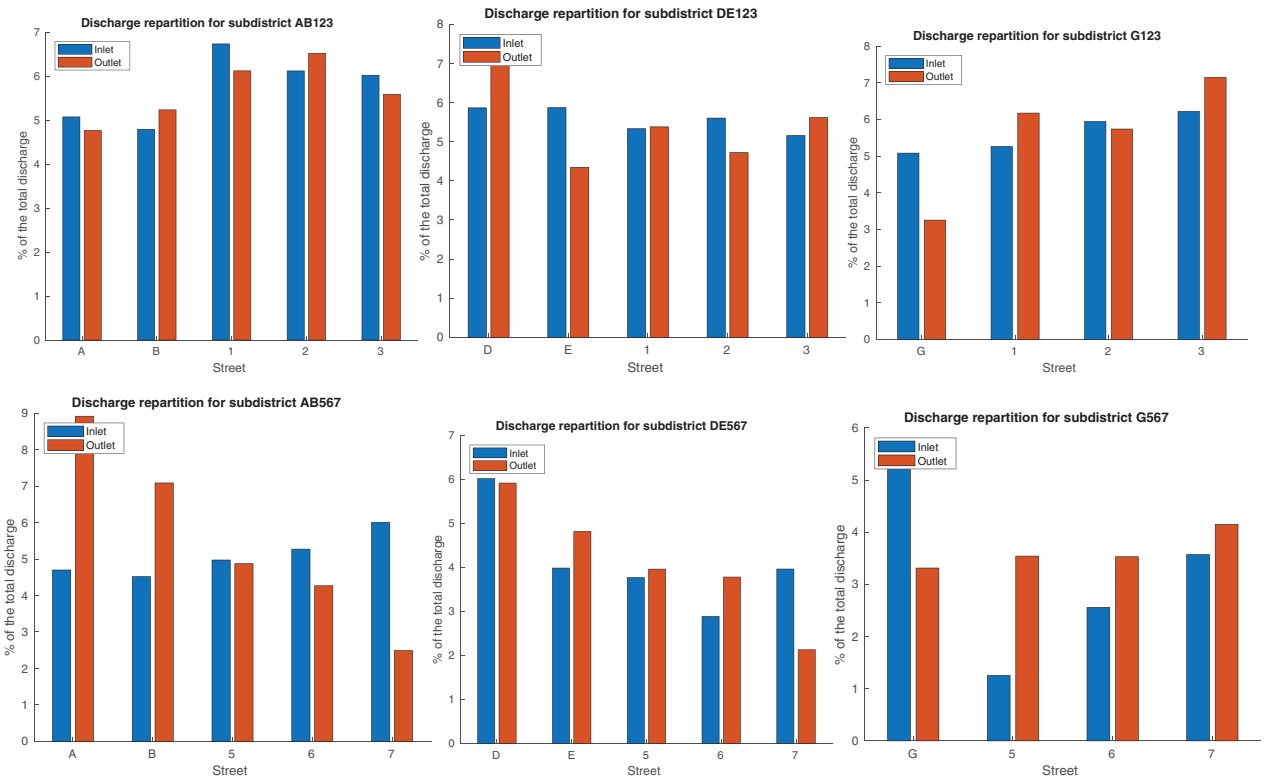

Figure F1. Evolution of the discharge ratios ($Q_{up,k}/Q_{tot}^{dis}$ and $Q_{down,k}/Q_{tot}^{dis}$) between the inlet and the outlet at the subdistrict scale.

Journal Pre-proofs

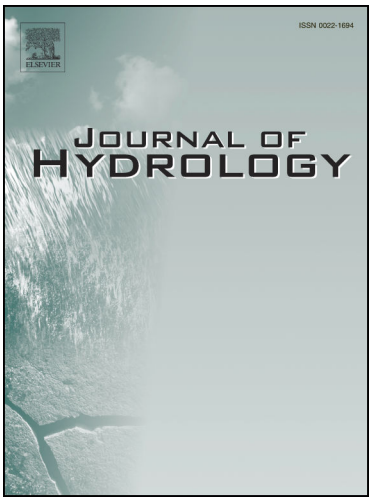

Research papers

Estimation of Multiple Inflows and Effective Channel by Assimilation of Multi-satellite Hydraulic Signatures: The Ungauged Anabranching Negro River

L. Pujol, P-A. Garambois, P. Finaud-Guyot, J. Monnier, K. Larnier, R. Mosé, S. Biancamaria, H. Yesou, D. Moreira, A. Paris, S. Calmant

PII: S0022-1694(20)30791-5
DOI: https://doi.org/10.1016/j.jhydrol.2020.125331
Reference: HYDROL 125331

To appear in: *Journal of Hydrology*

Received Date: 8 April 2020
Accepted Date: 19 July 2020

Please cite this article as: Pujol, L., Garambois, P-A., Finaud-Guyot, P., Monnier, J., Larnier, K., Mosé, R., Biancamaria, S., Yesou, H., Moreira, D., Paris, A., Calmant, S., Estimation of Multiple Inflows and Effective Channel by Assimilation of Multi-satellite Hydraulic Signatures: The Ungauged Anabranching Negro River, *Journal of Hydrology* (2020), doi: https://doi.org/10.1016/j.jhydrol.2020.125331

Estimation of Multiple Inflows and Effective Channel by Assimilation of Multi-satellite Hydraulic Signatures: The Ungauged Anabranching Negro River

L. Pujol(1)*, P-A. Garambois(2)(1)(3), P. Finaud-Guyot(1)(4)(5)(6), J. Monnier (7)(8), K. Larnier(9)(7)(8), R. Mosé (1)(6), S. Biancamaria(10)(11), H. Yesou(14)(1), D. Moreira (12), A. Paris (13), S. Calmant(10)(11)

(1) Laboratoire des Sciences de l'ingenieur, de l'informatique et de l'imagerie (ICUBE), Fluid Mechanics Team, CNRS, Universite de Strasbourg, France

(2) Now at: INRAE (Irstea), Aix Marseille Univ, RECOVER, Aix-en-Provence, France

(3) INSA Strasbourg, Strasbourg, France

(4) Now at: HSM, Univ Montpellier, CNRS, IRD, Montpellier, France

(5) Now at: LEMON, INRIA, Montpellier, France

(6) ENGEES, Strasbourg, France

(7) Institut de Mathematiques de Toulouse (IMT), France

(8) INSA Toulouse, France

(9) CS corporation, Business Unit Espace, Toulouse, France

(10) Laboratoire D'Etudes En Geophysique et Oceanographie Spatiales (LEGOS, UMR 5566 CNES CNRS IRD UPS)

(11) Universite de Toulouse III Paul Sabatier, OMP, Toulouse, France

(12) UFRJ/CPRM, Av. Pasteur 404, 22290-040 Rio de Janeiro, Brazil

(13) Collecte Localisation Satellite (CLS), Toulouse, France

(14) SErvice Régional de Traitement d'Image et de Télédétection (SERTIT), Université de Strasbourg, Pole API, Illkirch, France

Abstract

With the upcoming SWOT satellite mission, which should provide spatially dense river surface elevation, width and slope observations globally, comes the opportunity to assimilate such data into hydrodynamic models, from the reach scale to the hydrographic network scale. Based on the HiVDI (Hierarchical Variational Discharge Inversion) modeling strategy (Larnier et al. [1]), this study tackles the forward and inverse modeling capabilities of distributed channel parameters and multiple inflows (in the 1D Saint-Venant model) from multisatellite observations of river surface. It is shown on synthetic cases that the estimation of both inflows and distributed channel parameters (bathymetry-friction) is achievable with a minimum spatial observability between inflows as long as their hydraulic signature is sampled. Next, a real case is studied: 871 km of the Negro river (Amazon basin) including complex multichannel reaches, 21 tributaries and backwater controls from major confluences. An effective modeling approach is proposed using (i) WS elevations from ENVISAT data and dense in situ GPS flow lines (Moreira [2]), (ii) average river top widths from optical imagery (Pekel et al. [3]), (iii) upstream and lateral flows from the MGB large-scale hydrological model (Paiva et al. [4]). The calibrated effective hydraulic model closely fits satellite altimetry observations and presents real like spatial variabilities; flood wave propagation and water surface observation frequential features are analyzed with identifiability maps following Brisset et al. [5]. Synthetic SWOT observations are generated from the simulated flowlines and allow to infer model parameters (436 effective bathymetry points, 17 friction

patches and 22 upstream and lateral hydrographs) given hydraulically coherent prior parameter values. Inferences of channel parameters carried out on this fine hydraulic model applied at a large scale give satisfying results using noisy SWOT-like data at reach scale. Inferences of spatially distributed temporal parameters (lateral inflows) give satisfying results as well, with even relatively small scale hydrograph variations being inferred accurately on this long reach. This study brings insights in: (i) the hydraulic visibility of multiple inflows hydrographs signature at large scale with SWOT; (ii) the simultaneous identifiability of spatially distributed channel parameters and inflows by assimilation of satellite altimetry data; (iii) the need for prior information; (iv) the need to further tailor and scale network hydrodynamic models and assimilation methods to improve the fusion of multisource information and potential information feedback to hydrological modules in integrated chains.

Keywords: 1D Saint-Venant Model, Hydrology couplings, Variational Assimilation, Satellite Altimetry, SWOT, Hydraulic Visibility, Ungauged River

---

* Corresponding author: l.pujol@unistra.fr

1. Introduction

Hydrographic networks represent major flowpaths for freshwater in the water cycle and an interface with the space of human societies. It is of prior importance in a context of climate change to improve the knowledge and representation of continental water fluxes, including river discharge, defined as an essential physical variable (see Global Climate Observing System [6, 7]). However, modeling flows structure in the different compartments of a catchment remains a hard task (see [8] and references therein) especially at poorly gauged locations. In complement of in situ sensors networks, which are declining in several regions (e.g. [9]), new generations of earth observation satellites and sensors provide increasingly accurate and dense measurements of water surface variabilities.

The Surface Water and Ocean Topography (SWOT) satellite, to be launched in 2021, will bring observations of water surface (WS) with an unprecedented spatio-temporal coverage [10, 11, 12, 13, 14]. This will yield greater hydraulic visibility (see definition in [15, 16, 17]) of hydrological responses through WS signatures from the local scale to the hydrographic network scale, hence an opportunity to better characterize hydrological fluxes and potentially constrain local to integrated hydrodynamic models and inverse problems. However, estimating river discharge Q from "geometric" observables of flow surface (elevation Z, width W and slope S) remains a difficult inverse problem particularly in case of poor knowledge on river bathymetry and friction (see [18, 1] and references therein).

Hydraulic inverse problems with various model complexities, data-unknowns types and amounts are investigated by recent studies in a satellite data context (see [13] for a review). A few studies started to test the benefit of assimilating (synthetic) SWOT WS observations with sequential methods in simplified hydraulic models, for estimating inflow discharge assuming known river friction and bathymetry [19, 20] or inferring bathymetry assuming known friction [21, 22]. Next, methods based on low-complexity models have been proposed for estimating river

discharge from WS observables in case of unknown bathymetry b and friction K, based on the low Froude model [23, 18], hydraulic geometries [24] or empirical algebraic flow models [25]. The intercomparison of low complexity methods in [26] highlights the difficulty of estimating the so-called unknown triplet (Q, K, b) from WS observables as well as the importance of good prior guesses on the sought parameters.

The combined use of dynamic flow models of river systems and optimization methods enables to solve hydraulic inverse problems, as shown for upstream flood hydrograph(s) estimation by [27] from WS width time series and a 1D Saint-Venant model or by [28, 29, 30] using variational assimilation of flow depth time series in a 2D shallow-water model. The variational data assimilation (VDA) approach (see e.g. [31] and references therein) is suitable to address the present hydraulic inverse problem from WS observations (see [32, 5, 33, 34, 1] and references therein - single upstream hydrographs in all studies except multiple "stepwise" offtakes on synthetic and densely observed irrigation-like cases in [32]). It consists in fitting the modeled flow features to observations through the optimization of control parameters in a variational framework. To be solved efficiently, such an ill-posed inverse problem needs to be regularized: see [35] for the theory of regularization of such inverse problems and [32, 1] for the present inverse flow problem.

Crucial aspects of this difficult inverse problem are (i) the spatio-temporal sparsity of altimetric observations regarding flow controls – as analyzed in [5] for inferable hydrographs frequencies with the introduction of the *identifiability maps* and in [34] for inferable channel parameters patterns; (ii) the sensitivity of the triplet inference to good prior guesses on the sought parameters as highlighted in a SWOT context by [18, 36, 1, 37, 34]. The latest is highlighted by recent discharge estimates (in a triplet setup) from synthetic SWOT data on the Pô, Garonne and Sacramento Rivers in [1] (see also [38]), from AirSWOT airborne measurements on the Willamette River in [37] or from ENVISAT altimetric data on an anabranching portion of the Xingu River [34]. Using a biased prior hydrograph results in a biased estimate of inflow hydrograph despite a correct temporal variability at observation times - see [1] for detailed analysis. A hierarchical modeling strategy HiVDI (Hierarchical Variational Discharge Inversion) is proposed in [1] including low complexity flow relations (Low Froude and locally steady-state) for providing robust prior guesses to the VDA process by taking advantage of databases or regional hydrological models.

Most studies mentioned above tackle the estimation of a single upstream inflow discharge hydrograph from WS observations on relatively short river reaches regarding the spatio-temporal sparsity of (satellite) observations sampling and without complex flow zones - confluences, multichannel portions (except [34]), floodplains. Moreover, few recent studies address the effective modeling of (ungauged) river channels using multisatellite data [15, 39, 34, 40].

The present study investigates the challenging inference of multiple inflows and channel parameters patterns from hydraulic signatures in a SWOT context. Particular attention is paid to the difficult inference of hydraulic controls (HC) with correlated effects on WS signatures including overlapping backwater effects. Moreover, we present an effective hydraulic modeling approach based on multi-satellite observations of WS and accounting for hydrological

model inputs. It is applied to a long river reach including confluences with tributaries and strong backwater effects in the Amazon basin. The computational inverse method, based on the full 1D Saint-Venant equations, is that presented in [5, 1] with a spatially distributed friction power law in water depth and a simple piecewise linear channel bathymetry [34]. It is adapted here to account for lateral inflows/offtakes and is weakly coupled to the large scale MGB hydrological model [41, 42, 43]. Numerical investigations of the resulting WS signatures and identifiability tests are presented along with sensitivity analysis to the parameters of both the (forward) hydraulic model and the inverse method. The challenging inference of multiple inflows and channel parameters patterns is investigated with various observations densities including the assimilation of synthetic SWOT ones.

The paper is organized as follows. Section 2 presents the modeling approach with the 1D Saint-Venant flow model and the inverse computational method. Section 3 investigates the capabilities of the inverse method for identifying spatially distributed inflows with and without unknown channel parameters given observation patterns of WS signatures including overlapping backwater effects. Section 4 presents the effective modeling approach from multisatellite data applied to 871 km of the Negro river (Amazon basin) and the analysis of flow propagation features against SWOT observability. Section 5 proposes inference tests for spatially distributed inflows with and without unknown parameters on the Negro case in the presence of strong backwater effects.

2. Modeling Approach

2.1. The flow model

The Saint-Venant equations ([44]) consist in the unidirectional form of the shallow water equations and are commonly used to describe open channel flows (see e.g. [45, 46, 47] for detailed assumptions including the long wave one). In what follows, x denotes the curvilinear abscissae from upstream to downstream along a reach of length $\mathcal{L}$ (usual simplifying hypothesis are used) and $t \in [0, T]$ denotes the time. In this representation, let $A(x,t)$ be the flow cross sectional area $\left[\mathrm{m}^2\right]$ and $Q(x,t)$ the discharge $\left[\mathrm{m}^3.\mathrm{s}^{-1}\right]$ such that $U = Q/A$ represents the longitudinal cross-section averaged velocity $\left[\mathrm{m.s}^{-1}\right]$. The Saint-Venant equations in (A, Q) variables at a flow cross section read as follows:

$$\begin{cases} \partial_t A + \partial_x Q & = k_{lat} q_{lat} \\ \partial_t Q + \partial_x \left(\frac{Q^2}{A}\right) + gA\,\partial_x Z & = -gAS_f + k_{lat} U q_{lat} \end{cases} \tag{1}$$

where $Z(x,t)$ is the WS elevation [m] and $Z = (b + h)$ with $b(x)$ the river bed level [m] and $h(x,t)$ the water depth [m], $R_h(x,t) = {}^{A}/_{P_h}$ the hydraulic radius [m] , $P_h(x,t)$ the wetted perimeter $[m]$, g is the gravity magnitude $\left[\mathrm{m.s}^{-2}\right]$, $q_{lat}(x,t)$ is the lineic lateral discharge $\left[\mathrm{m}^2.\mathrm{s}^{-1}\right]$, and k_{lat} is a lateral discharge coefficient chosen equal to one here since we consider inflows only. In DassFlow, the friction term S_f is classically parameterized with the empirical Manning-Strickler law established for uniform flows:

$$S_f = \frac{|Q|Q}{K^2 S^2 R_h^{4/3}} \tag{2}$$

The Strickler friction coefficient K $\left[\mathrm{m}^{1/3}.\mathrm{s}^{-1}\right]$ is defined as a power law in h:

$$K\left(x, h\left(x,t\right)\right) = \alpha\left(x\right)\ h\left(x,t\right)^{\beta(x)} \tag{3}$$

where α and β are spatially distributed parameters. This spatially distributed friction law enables a variation of friction effects in function of the flow state (see effective modeling of multichannel flows in [34]).

Inflow hydrographs $Q_{in}(t)$ and $q_{lat,l}(t)$ at $l \in [1..L]$ are classically imposed respectively upstream of the river domain and at known injection cells, that is inbetween two computational cross-sections along the river channel. Let us recall the Froude number definition $\mathrm{Fr} = {}^{U}/_{c}$ comparing the average flow velocity U to pressure wave celerity $c = \sqrt{{}^{gA}/_{W}}$ where W is the flow top width $[m]$. Considering subcritical flows ($\mathrm{Fr} < 1$) in a satellite observability context (see [18]), a boundary condition is imposed at the downstream end of the model using the Manning-Strickler equation depending on the unknowns $(A, Q, K)_{out}$. The initial condition is set as the steady state backwater curve profile $Z_0\left(x\right) = Z\left(Q_{in}\left(t_0\right), q_{lat,1..L}\left(t_0\right)\right)$ for hot-start. This 1D Saint-Venant model (eq. (1)) is discretized using the classical implicit Preissmann scheme (see e.g. [48]) on a regular grid of spacing Δx using a double sweep method enabling to deal with flow regimes changes, Δt is precised in numerical cases. This is implemented into the computational software DassFlow [49].

2.2. The computational inverse method

The paper studies the estimation of spatially and temporally distributed flow controls from WS observables using the inverse method presented in [1] (see also [5]) with an augmented composite control vector c; the method is detailed in AppendixA. The principle of the inverse method is to estimate (discrete) flow controls by minimizing the discrepancy between observed and simulated flow lines, Z_{obs} and $Z(c)$ respectively, the latter depending on the unknown parameters vector c through the hydrodynamic model (eq. (1)). This discrepancy is classically evaluated with the observation cost function term $j_{obs}(c) = \frac{1}{2}\left\|(Z(\mathrm{c}) - Z_{obs})\right\|^2_{\mathcal{O}}$ computed on the observation spatial and temporal grids, see details in AppendixA.

The control vector c contains temporally and spatially distributed unknown "input parameters" of the 1D Saint-Venant model: a friction law ([34]) and lateral inflows, unlike in [1], where there is a spatially uniform friction law $K(h)$ without lateral flows. It reads:

$$c = \left(Q^0_{in},\ ...,\ Q^P_{in}\,;\ Q^0_{lat,1},\ ...,\ Q^P_{lat,1},\ Q^0_{lat,2},\ ...,\ Q^P_{lat,L}\,;\ b_1,\ ...,\ b_I\,;\ \alpha_1,\ ...,\ \alpha_N\,;\ \beta_1,\ ...,\ \beta_N\right)^T \tag{4}$$

where Q^p_{in} is the upstream discharge (the superscript $p \in [0..P]$ denotes the observation time), $Q^p_{lat,l}$ is the lateral discharges injected in the inflow cell $l \in [1..L]$ (note that $Q_{lat,l} = q_{lat,l}\Delta x$), b_i the river bed elevation ($i \in [1..I]$

Figure 1: Flowchart of the method using the HiVDI inverse method [1] for variational calibration, adapted from [50, 51, 34].

denotes the computational cross section index in space) and, for each patch $n \in [1..N]$ with $N \leq I$, the spatially distributed parameters α_n and β_n of the friction law (eq. (3)) depending on the flow depth.

The inversion consists in solving the following minimization problem: $c^* = \text{argmin}_c\ \text{j}(c)$ starting from the so-called prior c_{prior} in the parameter space. This minimization problem is solved using a first order gradient-based algorithm, more precisely the classical L-BFGS quasi-Newton algorithm (see AppendixA). Note that the sought parameters have a correlated influence on the modeled flow lines, therefore leading to an ill-posed inverse problem. In order to be solved efficiently, the optimization problem is "regularized" as detailed in AppendixA. The main steps of the method are illustrated in Fig. 1.

3. Inference capabilities from WS signatures: synthetic test cases

In order to calibrate the parameters of a hydraulic model (eq. (1)) from WS observables, one has to identify and understand the influence of these parameters on the observable(s): in our case the WS profile. Fluvial flows are studied here in the context of satellite altimetry (see [18]). Following [52], the influence of the parameters on the modeled flow lines is referred to as their "hydraulic signature" (HC) and a reach is defined inbetween two fluvial HCs. Fluvial HCs can be defined in steady state (see [52]) as *"local maximal deviations of the flow depth from the normal* depth h_n (equilibrium), *imposing the upstream variation of the water depth profile* $h(x)$ *over the so-called control length* [53]". They can stem from a change in either the hydraulic resistance, cross-section shape, bottom slope or total flow variation through lateral exchanges.

This section studies the influence of inflows on hydraulic signatures, the capabilities of the inverse method described above to infer multiple inflows and channel parameters (either spatially constant or not), with a focus on the influence of the spatial observability of those hydraulic signatures.

3.1. Test case design

Three test cases configurations representing typical hydraulic-observations setup of increasing complexities involving lateral inflows are presented (see Fig. 2). Cases $\mathcal{C}h1$ and $\mathcal{C}h2$ are designed to study the effect on the inference of the overlapping signatures triggered by the propagations of, respectively, one or two lateral hydrographs, concommitantly with the one of the upstream inflow hydrograph. Case $\mathcal{C}h3$ is a complexification of $\mathcal{C}h2$ through the introduction of a non-flat bottom and a variable friction pattern $K = \alpha(x)$ as needed in a real river case in the next sections ($\beta = 0$ in eq. (3) - see investigations on spatialized friction laws with multiscale bathymetry controls in [34]).

For all three channels the boundary conditions (fluvial) consist in: (i) a normal depth (equilibrium) imposed downstream and (ii) sinusoidal hydrographs (see Tab. 1) imposed upstream and at lateral injection cells. The

Figure 2: **TOP:** Academic test cases configurations. Rectangular channels of length $\mathcal{L} = 1000\,\mathrm{m}$ and constant cross section width $W = 300\,\mathrm{m}$, constant bottom slope of $10^{-3}\,\mathrm{m/m}$ for $\mathcal{C}h1, 2$ and varying between 10^{-4} *and* $10^{-2}\,\mathrm{m/m}$ for $\mathcal{C}h3$ - the bottom $b\,(x)$ is defined by linear interpolation between the 4 bathymetry points (diamonds, $b = \{2,\ 1.88,\ 1.28,\ 1.12\}$ m) - and friction defined by constant values on 3 patches ($\alpha = \{30,\ 12.5,\ 30\}\ \mathrm{m}^{1/3}.\mathrm{s}^{-1}$). Upstream inflow at $x = 0$; for $\mathcal{C}h1, 2, 3$ respectively lateral injections at abscissae (in m): $x = 300$, $x = \{300, 700\}$, $x = \{350, 700\}$, and observations at $\{x_{S1}, ..., x_{S5}\} = \{150, 500, 850, 450, 550\}$, $\{x_{Sb1}, ..., x_{Sb5}\} = \{150, 325, 450, 600, 800\}$, $\{x_{Sc1}, ..., x_{Sc4}\} = \{0, 300, 600, 1000\}$. **BOTTOM:** Sample waterlines with visible upstream and downstream controls and signatures. For the sake of clarity here, upstream and injected flow are set at $100\,\mathrm{m^3s^{-1}}$ (Fr $\sim 0.12 - 0.3$). Using the identifiability index $I_{ident} = T_{wave}/\Delta t_{obs}$ introduced in [5] with $T_{wave} = \mathcal{L}/c_k$ and the kinematic wave velocity for a rectangular channel $c_k = 5/3U$ ($c_k = 1.16\,\mathrm{m.s^{-1}}$ considering average speed $U = 0.69\,\mathrm{m.s^{-1}}$) and a high observation frequency ($\Delta t_{obs} = 20\,\mathrm{s}$), gives a high identiability index $I_{ident} = 43$ for the present flow observation configuration.

Case	Q_{in}			$Q_{lat,1}$			$Q_{lat,2}$			Froude range
	Q_0	a_Q	T	Q_0	a_Q	T	Q_0	a_Q	T	
$\mathcal{C}h1$	100	0	6300	100	20	6300	-			0.13-0.29
$\mathcal{C}h2a$	100	20	6300	100	20	6300	100	20	6300	0.12-0.3
$\mathcal{C}h2b$				400	80	6300				0.05-0.55
$\mathcal{C}h2c$				100	20	630				0.1-0.33
$\mathcal{C}h2d$				100	20	6300				0.12-0.3
$\mathcal{C}h3$				100	20	6300				0.09-0.53

Table 1: Parameter values for sinusoidal hydrographs $Q(x,t) = Q_0(x) + a_Q(x)\sin\left(\frac{2\pi}{T}t\right)$ used in synthetic channels; resulting modeled Froude ranges. Flows in $\mathrm{m^3s^{-1}}$, time T in s.

simulation time step is set to $\Delta t = 20\,\mathrm{s}$ for all cases. They are set up as twin experiments, where a forward run of the flow model (eq. (1)) is used to generate perfect WS elevation observations which are then used to infer an unknown parameter vector c (eq. (4)) with the inverse method described in section 2.2 and AppendixA. The inferences are started from erroneous prior guesses $c^{(0)}$ that verify Manning-Strickler law for hydraulic consistency, that is unbiased priors (see investigations in [1, 34]); hydrograph priors are constant values equal to the average value of the target hydrographs.

Increasingly challenging inverse problems are considered, with increasing number of unknowns sought simultaneously and various observations densities. Cases $\mathcal{C}h1$ and $\mathcal{C}h2$ are used to infer temporal parameters only, given a channel of constant slope and friction. Case $\mathcal{C}h3$ is the most challenging case with all inflows and non constant channel parameters sought simultaneously.

3.2. Informative content of hydraulic signatures: single/multiple inflows inferences

The fluvial signature from a single lateral inflow is divided in two parts (see $\mathcal{C}h1$ on Fig. 2, bottom): (i) in the reach downstream of the injection point, the cumulative flow ($Q = Q_{in} + Q_{lat,1}$) is uniform with a water depth corresponding to the normal depth imposed downstream, (ii) in the reach upstream of the injection point an M1 backwater curve profile (see [54], [55, 52] in the present "altimetry context") is obtained given the upstream flow Q_{in} and the water depth imposed downstream of this reach as the normal depth corresponding to the cumulative flow. In the case of two distinct lateral injections ($\mathcal{C}h2$), WS signatures overlap in the most upstream reach because of the stronger backwater effect created by two downstream inflows, which represent a more challenging inference problem.

Inference trials in case $\mathcal{C}h1$ with control vector $c_1 = \left(Q^0_{lat,1},\ ...,\ Q^P_{lat,1}\right)^T$, assuming a known constant $Q_{in}\,(x = 0, t)$, show that a single observation point in space with a dense sampling in time, placed either upstream ($S1$, in Fig.

2, top) or downstream ($S2$) from the lateral inflow, is sufficient to infer one lateral inflow hydrograph perfectly - noiseless twin experiments - (not presented). Indeed, the hydraulic signature of a lateral inflow is visible and fully informative either upstream from it because of its downstream control on the upstream flow line or downstream from it, in the signature of the cumulative flow. This means that as long the river is well temporally-observed regarding its response time (see [5] without lateral inflows) and that the temporal variations of the observed system stem from a single control, only one spatial point is needed to infer this parameter.

In the case of two distinct lateral injections ($\mathcal{C}h2$), WS signatures overlap in the most upstream reach because of the stronger backwater effect created downstream by the two inflows, which represents a more challenging inference problem considering the unknown control vector $c_2 = \left(Q^0_{in}, ..., Q^P_{in}\,;\, Q^0_{lat,1}, ..., Q^P_{lat,1}, Q^0_{lat,2}, ..., Q^P_{lat,2}\right)^T$. Several variants of $\mathcal{C}h2$ are considered to study the possible misattibution of flow controls (locations, amplitudes and frequencies) in case of identical inflow hydrographs ($\mathcal{C}h2a$), the backwater influence of inflow hydrographs on Q_{in} downstream signature observed at $S1$ given 4 times larger inflow amplitude ($\mathcal{C}h2b$) or 10 times higher frequency ($\mathcal{C}h2c$), different observations samplings "mixed" inflows signatures (see Fig. 2 and Tab. 1).

3.2.1. Inference of multiple inflows

For all cases, using perfect and dense observations in space (1 every 10 m) and also in time leads to quasi perfect inferences. The influence of a sparser sampling and of the observability patterns of overlapping WS signatures on the identifiability of multiple inflows with the present inverse method is studied here - without a priori weighting of the parameters in the inverse method, that is equal and unadjusted $\sigma_\square$ values (see AppendixA). The inferred hydrographs are summed up in Fig. 3. Scores are given in Tab. 2, including cost function values and iterations number at convergence.

Variant $Ch2a$. Given only one observation station by reach ($S1$, $S2$, $S3$) very satisfying inferences of the 3 inflows are obtained(Fig. 3, red line). Hence sufficient information is provided by those three stations observing distinct signatures in each reach from upstream to downstream: ($S1$) propagation of the inflow $Q_{in}(x = 0, t)$ in presence of the overlapping backwater effects due to $Q_{lat,1}(x = 300, t)$ and $Q_{lat,2}(x = 700, t)$; ($S2$) propagation of $Q_{in}(x = 0, t)+$ $Q_{lat,1}(x = 300, t)$ in presence of the overlapping backwater effect due to $Q_{lat,2}(x = 700, t)$; ($S3$) the propagation of the total discharge without downstream control.

Variant $Ch2b$. Assimilation is more difficult than in $\mathcal{C}h2a$ but inferred hydrographs (Fig. 3, red line) are still accurate (Tab. 2). This testifies to the ability to discriminate multiple sources of various amplitudes given observations of hydraulic signatures at higher frequency and at pertinent locations ($S1$, $S2$ and $S3$).

Interestingly, this case highlights the expected misattribution behaviour between inflow sources as shown by an intermediate iteration (Fig. 3, orange line) and remaining to a lesser extent at convergence (red line): Q_{in} and $Q_{lat,1}$ are respectively over- and underestimated). This may be due to the relatively higher contribution of Q_{in} to the observed signature (it impacts WS elevation at $S1$, $S2$ and $S3$) and consequently its contribution in the cost

Figure 3: Inflows inferences from WS observations for all $Ch2$ variants. Intermediate iteration in the assimilation process are represented for $Ch2b$ and $Ch2c$; they are hand-picked to illustrate "intermediate" behaviours before convergence ("inferred").

Case	Q_{in}		$Q_{lat,1}$		$Q_{lat,2}$		Cost	N_{ite}
	RMSE	rRMSE ($\times 10^{-6}$)	RMSE	rRMSE ($\times 10^{-6}$)	RMSE	rRMSE ($\times 10^{-6}$)		
$\mathcal{C}h2a$	0.08	2.5	0.15	4.7	0.05	1.6	8.0×10^{-6}	54
$\mathcal{C}h2b$	0.72	22.9	1.34	10.6	0.08	2.7	9.4×10^{-6}	261
$\mathcal{C}h2c$	0.06	1.9	0.27	8.7	0.04	1.3	7.7×10^{-6}	78
$\mathcal{C}h2d$	2.21	70.0	3.31	105.0	0.03	0.9	7.9×10^{-6}	24

Table 2: Inferred parameters misfits to the truth for $Ch2$ variants. The RMSE [m^3s^{-1}] and rRMSE represent the misfit of the inferred parameters, while the cost function used in the assimilation process represents the misfit of variables.
$RMSE = \sqrt{\frac{1}{n}\sum_{i=1}^{n}\left(Q^i_{target} - Q^i_{infered}\right)^2}$, $rRMSE = RMSE/\sum_{i=1}^{n} Q^i_{target}$

function (observation part).

Note that the final overestimation of Q_{in} in $\mathcal{C}h2b$ is slightly greater than in $\mathcal{C}h2a$. This is likely due to greater WS elevation variation at $S1$ caused by backwater from $Q_{lat,1}$, which is first attributed to Q_{in} since it has more impact on the cost function. Remember that, with perfect observations of WS signatures, at the end of the optimization process, nearly perfect hydrographs are inferred. However, the small flow misattributions during this optimization shows the difficulty of inferring multiple controls using an observation located in a strong backwater signal.

Variant Ch2c. Perfect inferences are obtained. An intermediate iteration (Fig. 3, orange line) shows that the expected misattribution of frequencies for all 3 inflows is present, though it disappears at convergence (Fig. 3, red line). This testifies to the ability to discriminate multiple sources of various frequencies given observations of hydraulic signatures at higher frequency and at pertinent locations ($S1$, $S2$ and $S3$).

Variant Ch2d. Convergence is achieved but the flow upstream of $S4$ is misattributed between Q_{in} and $Q_{lat,1}$. Signatures of Q_{in} and $Q_{lat,1}$ are only observed mixed, downstream of $Q_{lat,1}$ (at $S4$ and $S5$) and downstream from both $Q_{lat,1}$ and $Q_{lat,2}$ (at $S3$). Given that all stations are located in the downstream infuence of both inflows, the distribution of flow between them makes little difference on the observed WS dynamics. This confirms the need to have at least one observation station between each sought inflow in order to be able to "separate" them.

3.2.2. Synthesis

These first tests showed that for inferring multiple inflows, i.e. spatially distributed temporal controls, a minimal spatial observability of their WS signature is required with one observation point between each inflow here. In case of observation stations affected by backwater influence, the potential difficulty of separating multiple inflows from their

"mixed signature" is highlighted; using a higher spatial density of (simultaneous) observations leads to improved inferences in the present configuration. Moreover, using observations with high temporal density (with regards to the response time in the considered river system) and low spatial density, different frequencies can be correctly attributed to multiple inflows (as highlighted for a single upstream inflow in [5]). Furthermore, note that if a supercritical regime occurs in a reach between inflows, their hydraulic signatures are disconnected (not shown), effectively reducing the assimilation problem to that of case $Ch1$.

3.3. Multiple and composite controls inference

In this section multiple inflows are sought simultaneously with channel parameters on case $\mathcal{C}h3$. Three friction patches are consistently applied to sub-reaches inbetween the 4 sought bathymetry points. The control vector is $c_3 = \left(Q^0_{in},\, ...,\, Q^P_{in}\,;\, Q^0_{lat,1},\, ...,\, Q^P_{lat,1},\, Q^0_{lat,2},\, ...,\, Q^P_{lat,2}\,;\, b_1,\, b_2,\, b_2,\, b_4\,;\, \alpha_1,\, \alpha_2,\, \alpha_3\right)^T$. Searching both inflows and channel parameters creates a configuration (intendedly) prone to equifinality problems on the sought parameters having correlated influence in the water surface signal. Three observation configurations (see Fig. 2) are studied: one with a high station density ($\mathcal{C}h3a$: 100 stations, 1 every 10 m), another with fewer stations ($\mathcal{C}h3b$: 9 stations, $\mathrm{Sb}_{1..5}$ and $\mathrm{Sc}_{1..4}$) and a third one with even fewer stations ($\mathcal{C}h3c$: 4 stations, $\mathrm{Sc}_{1..4}$). Priors for inflows are those defined for case $Ch2$ (subsection 3.2.1), priors for channel parameter are hydraulically consistent with flow priors and initial flow line. For this equifinality prone configuration, the $\sigma_\square$ values used in the inverse problem regularization, related to the sought parameters (see section AppendixA) and denoted as weights, are given in Tab. 3.

Inference results are presented in Fig. 4. In red, the final estimate of c_3 for $Ch3a$ with the "default" weights set (see Tab. 3). In green, final inferences for variant-specific parameter weights adjusted through trial and error. In orange, intermediate inferences with the "default" set of parameter weights. Equal values of 1, corresponding to "no weighting", were also tested: they lead to inaccurate inferences (not shown) and thus the "default" weights producing more interpretable results are preferred. In further iterations, after the ones plotted in orange, behaviours similar to the $Ch3a$ "default" weights inferences (Fig. 4, in red) appear (not shown), i.e. a shift of inferred hydrographs and Strickler coefficients away from the target. Also note that the inferred flow oscillation in the first time step stems from the influence of the initialization scheme (see section 2.1) in the optimization on this quickly responding channel.

Q_{in} is underestimated while the local friction is overestimated, denoting a local tendency to equifinality. This is linked to a strong backwater influence, created by both $Q_{lat,1}$ and the increase in friction at $x = 300$ m. This local inflow error leads to compensation in downstream hydrographs. By adjusting parameter weights through trial and error, accurate inferences are obtained (Fig. 4, in green). This means that dense observations of the WS elevation are not sufficient for inferring all flow controls contained in c_3 and that spatially distributed regularization parameters, acting as weights in the parameter search, are required.

Figure 4: Inflow, bathymetry and friction patch inferences from WS observations for all $\mathcal{C}h3$ variants. In red, final inference with "default" parameter weights (see Tab. 3). In green, final inference with adjusted parameter weights. In orange, intermediate inferences with "default" parameter weights.

Case		$\sigma_{Q_{in}}\left(\mathrm{m^3s^{-1}}\right)$	$\sigma_{Q_{lat,1}}\left(\mathrm{m^3s^{-1}}\right)$	$\sigma_{Q_{lat,2}}\left(\mathrm{m^3s^{-1}}\right)$	$\sigma_{\alpha}\left(\mathrm{m^{1/3}s^{-1}}\right)$	$\sigma_b\,(\mathrm{m})$	Cost	N_{ite}
"Default"	$\mathcal{C}h3a$	50	50	50	600	2	0.54	180
	$\mathcal{C}h3b$						0.54	97
	$\mathcal{C}h3c$						0.63	54
"Adjusted"	$\mathcal{C}h3a$		30	30	400		0.23	156
	$\mathcal{C}h3b$	1	0.9	1.2	300		0.25	108
	$\mathcal{C}h3c$						0.26	100

Table 3: Parameter weight sets in $Ch3$ variants.

297

298 *Variant $\mathcal{C}h3b$ and $\mathcal{C}h3c$.* With sparses observations, the "default" weight set leads to worse inferences. However,
299 the existence of a set of adjusted weights that lead to good inferences (Fig. 4, in green) is enough to show that the
300 minimum observation spatial density of 1 station between each inflow can be sufficient to infer the extended control
301 vector c_3. Note that adjusted weight for $Ch3b$ and $Ch3c$ are different from adjusted weights for $Ch3a$ (see Tab. 3).

302 Using less observation points in space, the influence of spatial parameters decreases without loss of meaningful
303 information and thus the relative influence of inflows increases. This simple test highlights the weighting influence
304 of the $\sigma_{\square}$ parameters in the regularization method in the present flow configuration. The spatial distribution and
305 density of WS observations along with the weights change the hydraulic representativity of spatially distributed
306 parameters in the optimization process.

307 The main difficulty uncovered with these academic cases is the challenge presented by simultaneous inferences
308 of multiple inflows and channel parameters from their potentially overlapping hydraulic signatures. However, in the
309 case of unbiased prior parameters and dense WS observation patterns relatively to those of spatio-temporal controls,
310 satisfiying inferences are obtained with the present inverse method. A real and complex river case is considered
311 hereafter.

312 4. Effective hydraulic model of the Negro river

313 After addressing increasingly challenging hydraulic inverse problems on synthetic test cases in the previous
314 section, a real complex river flow case is now considered. It consists in 871 km of the Negro river, including several
315 confluences with tributaries and anabranching flow zones. The reach is located upstream of the Solimoes-Negro
316 confluence which is responsible for significant backwater effects (see e.g. [52]). This section presents the elaboration

Figure 5: Study zone on the Negro river. ENVISAT Virtual Stations are numbered from 1 to 18 starting from upstream. The boundaries of the studied reach are defined by stations 1 and 18. The 21 tributaries are divided between actual rivers and inflow points from the hydrological model. SWOT swaths give an almost full spatial coverage of the reach. In gray is the average water extent map used to extract width values, from [3].

of effective flow models in view of performing forward and inverse flow modeling from WS observations of varying sparsity in the next section.

The modeling approach consists in (i) a 1D hydraulic model (full Saint-Venant equations, see subsection 2.1) (ii) based on effective cross sections defined from multisatellite and in situ data and (iii) weakly coupled to the large scale hydrological model MGB [41, 42, 43]. The idea is to build an effective river flow model both in coherence with the main hydrological signals (inflows) propagations along with observable flow surface signatures and hydraulic controls (see [52]). As shown in what follows, this 1D approach allows for a fair representation of flow propagation and longitudinal signatures, which are the core focus of this paper.

4.1. Study zone

The study domain corresponds to the main stream of the Negro River, a major "left-bank" Amazon tributary draining the north part of the basin, with an average discharge of $28\,400\,\mathrm{m^3.s^{-1}}$ [56]. The reach covers the 871 km upstream of its confluence with the Solimoes and presents singular channel morphologies such as multichannel flow zones mainly located in two large grabens ([57]). Part of the reach is strongly influenced by the control imposed by the Solimoes river at its confluence (average discharge of $100\,819\,\mathrm{m^3.s^{-1}}$ according to ORE HYBAM gauge data [58], their confluence gives birth to the Amazon river). This hydraulic control is due to higher discharge and a consequently lower slope of the Negro River in its lower reach when compared to the Solimões River near to the confluence [59, 60]. The reach of interest has been crosscut by 18 ENVISAT ground tracks every 35 days from 2003 to 2010 (see [61]), representing 68 to 79 measurements of WS elevations at each of the 18 Virtual Stations (VS). Note that the measurements are not simultaneous for each station.

4.2. Effective models construction

This section presents the elaboration of effective flow models from multisatellite data. First, a $\mathcal{G}1$ "sparse" channel geometry is built from effective bottom elevations at ENVISAT VS resolution. Next, in view to test the additional constraints brought by spatially dense satellite data (synthetic SWOT), a more spatially detailled effective channel geometry $\mathcal{G}2$ is built using a high resolution water mask and an in situ flow line as explained below.

4.2.1. Effective geometry $\mathcal{G}1$ from altimetry and optical data

An effective 1D channel with effective rectangular cross sections is set up from available multisatellite data (altimetry, optical) and a large scale hydrological model following [15, 34]. According to [57], high width to depth ratios make the rectangular channel a pertinent effective modeling approach of the true geometry, even in highly anastomosed reaches - where an error on the actual hydraulic perimeter P_h hence R_h (see subsection 2.1) is expected. This is supported by a qualitative analysis of some additional ADCP measurements of river flow and cross-sectional bathymetry.

- The river centerline from [62], formed by 30×30 m pixels, is used to calculate the river length and to project all spatial objects, such as VS, widths and inflow points, on a single one-dimensional reference.

- A longitudinal profile of cross sectional WS width W is calculated from the average river extent map derived from 31 years (1984-2015) of optic landsat imagery by [3]. A single width value per centerline point is extracted in order to build a 1D rectangular geometry. For multi-channel reaches, the effective width is the sum of the widths of all channels. This underestimates the actual hydraulic perimeter. Specific hand-filtering based on hydraulical expertise was necessary in some anabranching parts of the model where the water extent may include inactive flow zones not accounted for in the present 1D effective model. Note that [63] concurs to the necessity of reach-scale flow zone evaluation in the Amazon river catchment.

- An effective channel bottom elevation b_{env} is obtained at each VS (Fig. 6, in red) from altimetric rating curves (RC) from [64]. Its slopes range from -7.1×10^{-5} to 2.0×10^{-4} m/m with an average of 7.0×10^{-5} m/m. RCs were obtained by adjusting the parameters (γ, δ) of a stage discharge relationship $Q = \gamma\,(Z_{sat} - b)^{\delta}\, S_{sat}^{0.5}$ using WS elevations Z_{sat} and slopes S_{sat} gained by satellite altimetry and discharge Q simulated with the large scale hydrological model MGB ([41, 42, 43]) on the temporal window of interest.

Effective rectangular cross sections geometries are defined at the $R = 18$ VS using the above defined effective bottom elevations $\{b_{env}\}_{r\in[1..R]}$ and river widths $\{W_1\}_{r\in[1..R]}$. The final model geometry ($\mathcal{G}1 = \{b_{env}, W_1\}_{r\in[1..R]}$) is obtained by linear interpolation between those 18 effective cross sections on the model grid with $\Delta x = 200$ m.

4.2.2. Effective geometry $\mathcal{G}2$ at increased spatial resolution

Spatially dense WS elevation data is introduced in the form of an in situ GPS flow line with $G = 579$ spatial points. It was collected by survey ship along the whole studied reach over 7 days during the low-flow period in december 2010 ([2]); it provides local WS elevations Z every 1.4 km on average and WS slopes S for every 25 km reach (ranging between 2.0×10^{-5} and 8.11×10^{-5} m/m, averaging at 3.4×10^{-5} m/m). Under the hypothesis of a wide rectangular cross section and a steady uniform flow, the Manning equation writes:

$$Q = K\,(Wh)^{5/3}\,(W + 2h)^{-2/3}\,\sqrt{S} \tag{5}$$

The water depth writes $h = (Z - b)$ and the bottom elevation is sought using (i) the fixed WS width pattern W_2 from imagery, (ii) the WS elevation Z_{GPS} and slope S_{GPS} given by the GPS profile and (iii) the discharge Q from the hydrological model (see subsection 4.1) on the river domain at the corresponding time t_*. We invert an effective bathymetry b_{GPS} using equation 5 by minimizing the square sum of misfits to b_{env} at ENVISAT stations through the modification of $M = 14$ friction values ($(\alpha_m,\, \beta_m = 0)$, $m \in [1..M]$, friction law eq. (3)). They are

Figure 6: Effective river channel bottom and width for spatially sparse, $\mathcal{G}1 = \{b_{env}, W_1\}_{r\in[1..R]}$, and spatially dense, $\mathcal{G}2 = \{b_{GPS}, W_2\}_{G\in[1..G]}$, model geometries along with a low-flow GPS waterline from [2].

simply spatialized into M "hydraulic" patches consistent with large scale morphological features classified as follows: single channels, multiple channels (from 2 to 3), lightly anastomosed and heavily anastomosed (Fig. 6, in purple). The friction coefficient values are coherent with the physical properties of the classified reaches.

The new bathymetry b_{GPS} is coherent with the best available reference data and its corresponding set of physically distributed Strickler patches. The final model geometry is $\mathcal{G}2 = \{b_{GPS}, W_2\}_{G\in[1..G]}$.

In the following, using either geometry $\mathcal{G}1$ or $\mathcal{G}2$, the hydraulic model is inflowed with time series at a daily time step upstream of the river domain and at 21 tributaries (both river tributaries and runoff inflows) corresponding to the 21 catchment cells feeding into the Negro river cells in the large scale hydrological model MGB ([42, 41]). The largest of these tributaries is the Branco river at 657 km.

4.3. Effective Models calibration against altimetry

The friction of the hydraulic model (eq. (1)) is calibrated against altimetric WS elevation time series following [34], i.e. $\left\{Z^{obs}_{s,p}\right\}^{env}_{S=16,P\in[68..79]}$ at ENVISAT VS, the most downstream VS being used as BC (see subsection 2.1). The friction law is distributed using $N = 17$ "ENVISAT" patches with constant $(\alpha_n,\, \beta_n = 0)$, $n \in [1..N]$ values for each reach between two successive VS. This choice is made to avoid spatial "overparameterization" in the calibration process regarding the spatial sparsity of ENVISAT observations of WS signatures. The aim of parameter calibration is to obtain a "real-like" model as close as possible of the sparse observation set. Three models are considered, to assess the impact of the bathymetry refinement and of the downstream BC on the modeled hydraulic signatures and on inverse problems: a "sparse" model ($M1$) using channel geometry $\mathcal{G}1$ and the WS elevation time series from VS 18 as BC, a refined model ($M2a$) with channel geometry $\mathcal{G}2$ including all the spatial variability from multisource data described above while keeping the same BC and a further changed refined model ($M2b$) where the BC is changed to an altimetric RC which is of interest for "operational-like" applications in other rivers and basins.

The inverse method presented in [1] and described in subsection 2.2 and AppendixA is used here, without regularization terms, for friction calibration. Effective Strickler patches, starting from priors corresponding to average values of the "hydraulic" patches used above (Fig. 6, in purple), are calibrated following [34] who use observations of the same nature. Friction patterns $c^*_{\mathcal{G}1}$, $c^*_{\mathcal{G}2a}$ and $c^*_{\mathcal{G}2b}$ found with the inverse method are shown in Fig. 7. Most differences in calibrated friction from $M1$ (Fig. 7, in red) to $M2a$ (Fig. 7, in blue) correspond to their difference in bathymetry at the virtual station point (Fig. 7, gray line), i.e. a lower slope in $M2a$ leads to a higher inferred Strickler parameter in order to match WS observations (e.g. in patch 2 and 6. Inferred parameters for $M2b$ roughly match those of $M2a$, with some discrepancies in patch 2, 15 and 17. Using a different BC influences WS sensitivity to parameters and the relative contribution to the cost function of local WS misfits, which explains differences in patch 15 and 17 ; the one in patch 2 stems for the high friction values, hence lower WS sensitivity as

Figure 7: Friction patches after calibration against ENVISAT WS elevation observations. Inferred Strickler coefficient values are very close for all configurations for patches 1, 3 to 5 , 9 to 14 and 16. Patches 2, 6 and 15 are especially sensitive to model variations.

analyzed after.

4.3.1. Water levels analysis

The following presents a detailed analysis of the effective hydraulic model for configuration $M1$, along with an analysis of changes obtained for configurations $M2a$ and $M2b$.

The simulated WS elevation are compared to observed WS elevation at each ENVISAT virtual station in Fig. 8 - other time series are available in AppendixB. For the 3 models calibrated above, the modeled WS are fairly close to observed WS given the limited modeling complexity and data uncertainties. More precisely, the fit to the altimetric WS elevation time series is fairly good, as shown for $M1$ in Fig. 8, and nearly unbiased as shown in Fig. 9(left). The WS elevation global RMSE is at 0.936 m for $M1$; similar results are found with $M2a$ (see Tab. 4). Errors are greater in low and high flows, with consistent underestimations of flow amplitude upstream (VS $1-4$) which turns into overestimation downstream (VS $9-13$), before disappearing closer to the BC (VS $14-18$). VS 5 to 8 are particularly accurate. Error metrics are coherent with those from current state of the art models using satellite data (see e.g. [40] on the Congo river).

The analysis of the time series for $M1$ gives insight on the 1D model behaviour regarding the real flow physics sampled with the sparse nadir altimetry data and dense in situ low flow line. Modeling errors can stem from either an (expected) improper representation of the channel and flow complexity or uncertain (ungauged) inflows and data.

Concerning the hydraulics, from downstream to upstream, relative errors are lower in anabranching reaches outside of the backwater influence starting at the Branco tributary ($x = 657$ km up to around $x = 350$ km) and in the backwater influence of the (known "perfect") downstream BC. Overall, relative errors are higher upstream, in single channeled, low water height reaches and in the Branco backwater influences. Note that 2D complex lateral flows in floodplains or retention behaviours from "igarape" rivers may happen in high flow periods (see [65, 66]). These unaccounted phenomenons may decrease flood wave velocities and cause hydrograph skewness ([67, 68, 10]).

The 1D modeling of water levels compared to altimetry observations (Fig. 8) can first be analyzed as follows:

- Stations 14 to 18 are located in reaches with different morphological properties. Stations 14 and 15 are located in a densely anastomosed reach upstream of the Branco river confluence, a major tributary. Stations 16 and 17 are in single channel reaches, upstream from the confluence with the Solimoes river. Station 18 is in a densely anastomosed reach at the location of the BC forcing on WS elevation. Their low relative misfits do not testify to the absence of complex hydraulic behaviours in this area but rather to the dominating influence of the BC.

	Global RMSE (m)	Global Average bias (m)	Upstream RMSE (m)	Upstream Average bias (m)
M1	0.94	−0.02	0.88	−0.08
M2a	0.94	−0.02	0.91	−0.01
M2b	1.72	0.23	0.90	−0.05

Table 4: RMSE and bias over 8 years for the $M1$, $M2a$ and $M2b$ models. Upstream metrics are calculated for stations 1 to 9 only, which are outside of the BC's backwater influence. The high global RMSE for $M2b$ comes from the known dephasing of the Solimoes and Negro peak flow, which is not reproduced by the RC.

- Stations 5 to 13 are located in mostly homogeneous anastomosed reaches, with stations 5 to 8 in a less densely anastomosed region than stations 9 to 13. This spatial division corresponds to two trends in relative misfit, where lower misfit is seen in the less anastomosed reaches. This testifies to the difficulty of modeling potentially 2D hydrodynamics using 1D approach. Indeed, the more channels there are, the further away the simulated wetted perimeter is from the true wetted perimeter (and so the hydraulic radius). Note that parameterizing the Strickler coefficient as described in eq.(3) and including $\beta(x)$ in the control vector during the calibration process, instead of the simpler $\beta(x) = 0$ used here, does not yield a better fit in this complex case modeled with a single rectangular channel.

- Stations 1 to 4 are located on single channel reaches. Although the area seems the most suitable to be modeled in 1D, it still has the highest relative misfit to ENVISAT observations. For stations 1 and 2, this is partly due to effective width estimation errors being more prevalent in the relatively narrow channel (around 2 km in width). Furthermore, note that effective channel bottom elevation for these stations are respectively 37.3 m and 36.3 m while the lowest ENVISAT WS elevation observation are respectively 36.6 m and 35.8 m. This corresponds to low-flow water heights of 0.7 m and 0.5 m which do not fit field measurements. Consequently, relatively high friction coefficients are inferred between station pairs 1-2 and 2-3 to fit low water depth. This misfit might be due to data error, including effective width errors for stations 3 and 4 located in areas of sharp width variations. Note that the higher the friction values, the less sensitivity of the modeled WS elevation, which explains the highest spread of Strickler coefficient (K = 40 to 55 $\mathrm{m^{1/3}s^{-1}}$) in reach 2 found during calibration for the 3 models (Fig. 7).

The introduction of the refined geometry $\mathcal{G}2$ in $M2a$, recall for generating spatially distributed SWOT data and to perform inference tests hereafter, has low impact on WS elevation bias and errors at ENVISAT VS (see Fig. 9), with only stations 1, 2 and 3 showing significant change. Using a rating curve as downstream BC in $M2b$ mostly impacts the downstream part of the model where some misfit to altimetry data appears. Indeed, it is more difficult, using a simple power law depending on the local flow variables, to capture the influence of the confluence with the Solimoes River - not modeled. The latest having strong discharge variations out of phase with the one of the Negro River itself (e.g. [16]).

Figure 8: Modeled and observed WS elevation at ENVISAT VS after friction calibration at all stations for $M1$

Figure 9: Relative misfit between modeled and observed WS elevation at ENVISAT for $M1$ (left, base model) $M2a$ (middle, WS elevation at downstream BC) and $M2b$ (right, rating curve at downstream BC). Crosses are average values, horizontal bars are median values.

4.3.2. Effective model analysis

As a preliminary to hydraulic parameters inference from WS observables, this subsection studies the spatio-temporal features of the simulated hydraulic signatures, their sensitivity to model parameters and their observability given a SWOT sampling. First, an analysis of a flood wave propagation, resulting from multiple inflows, and its hydraulic signature visibility is performed using identifiability maps following [5]. The latter consist in a space-time representation of the WS signal and flow propagation features against the observability pattern. These maps, inspired by the theory of characteristics (see [69, 47]), enable to read how the sought upstream discharge information is sampled in the downstream WS deformations and help to estimate inferable hydrograph frequencies. Next, a numerical sensitivity evaluation of the flow model is carried out.

In the context of regional hydrological modeling including river networks representation, the sensitivity of the present flow model is studied by using erroneous inputs. These inputs are also used in section 5 as erroneous priors for various assimilation setups.

- Inflow: two hydrograph sets (containing lateral inflows and the upstream BC inflow) corresponding respectively to 70% and 130% of the true hydrographs are used as erroneous values for sensitivity trials and are referred to as Q_{FG}^{-30} and Q_{FG}^{+30} respectively.
- Friction: two Strickler repartitions, with coefficient values worth respectively 70% and 130% of the truth are used as erroneous values for sensitivity and are referred to as K_{FG}^{-30} and K_{FG}^{+30} respectively.
- Bathymetry: the inflow sets Q_{FG}^{-30} and Q_{FG}^{+30} and the true Strickler values are used to dig two bathymetries as described in section 4.3. The bathymetry derived from underestimated flows is referred to as b_{FG}^{-30} (it overestimates the true bathymetry), and the other is referred to as b_{FG}^{+30}.

SWOT will provide spatially distributed observations with interesting revisit frequencies at the scales of the current river domain and hydrological signal propagations. Fig. 10 shows the evolution of the simulated WS elevation anomaly during the yearly peak flow (red-blue heatmap) as well as its multiple SWOT observability (in black). Based on the modeled flow, accounting for several inflows, the propagation of an intumescence corresponding to the annual flood wave signature is represented along the river through the maximum WS elevation in time (following [55]) (Fig. 10, top, blue points). This intumescence propagation is visible on the upstream 400 km of the river from day 164 to day 173. It is detected by a SWOT swath at $t = 166$ d and another one at $t = 170$ d. It is more

difficult to detect this signature in the downstream part of the river ($x > 400\,\text{km}$) affected by the strong downstream control imposed by high water depths at the Negro-Solimoes confluence; a downstream control due to the Branco tributary also overlaps from $x = 657\,\text{km}$ to around $x = 400\,\text{km}$. This control can be seen through the tracked WS elevation maximum (Fig. 10, top, in gray), where an early rise in WS elevation originates from $x = 657\,\text{km}$, and through the extreme waterlines (Fig. 10, bottom, in blue), which highlights the change in length of this influence in low and high flows. As a consequence, WS observations on the downstream part may contain combined information due to the upstream hydrographs propagation but also to the expression of downstream controls.

The maximum WS elevation is tracked for simulations with erroneous parameters as defined above (Fig. 10, top, in red, green and cyan). They are not plotted where the flow displays "pool behaviour" (gray points). They highlight the sensitivity of propagation to model parameters which is also an important point when they are varied during an optimization process as featured in section 5. The propagation time from 0 to 400 km can be evaluated to around 10 days, and is estimated as follows for the rest of the river domain.

The conservative part of the Saint-Venant equations (i.e. without source terms) is hyperbolic: some quantities depending on the water depth and velocity (known as the Riemann invariants) are transported by waves at speeds different from the flow speed (see e.g. [69, 47]). The wave celerities are $U+c$ and $U-c$ with $c = \sqrt{gh}$ for rectangular cross sections (see analysis of propagation features in [5]). For the fluvial regime of interest here ($\text{Fr} = U/c < 1$), information propagates both downstream and upstream and the Riemann invariants are modified along the wave due to the source term effects. The wave celerities obtained on the Negro River model are given by reach in Table 5, relatively high wave speeds are obtained hence propagation of information both upstream and downstream, with spatio-temporal variability. The WS signature (and the discharge) thus reflects the nonlinear combination of information coming from both upstream (due to inflows variations) and downstream (due to local hydraulic controls or downstream BC - see the method of characteristic in [47]). This highlights the difficulty of inferring multiple inflows from sparse observations of WS signature, especially given uncertain channel parameters and backwater effects.

Nevertheless interesting frequential information can be gained from the identifiability map as introduced in the case of a single inflow. Using the kinematic wave speed $\frac{5}{3}U$ (Fig. 10, top, dashed blue line) which compares fairly well to the intumescence speed on the upstream part of the reach (Fig. 10, top, $x < 400\,\text{km}$). This gives an approximate propagation time $T_{wave} = 26\,\text{d}$ on the whole domain, greater than the SWOT observation cycle period of 21 days. This brings the reach identifiability index to $I_{ident} = 1.23$ (defined as $I_{ident} = T_{wave}/\Delta t_{obs}$, i.e. the average number of time a wave is observed, see [5]). However, in the present case, the notion defined by [5] accounts for a single upstream inflow, not spatially distributed lateral inflows with potential upstream backwater controls. Actual identifiability indices for reaches in between each lateral inflow would be much lower (estimated identifiabilities in between each inflow pair are given in Tab. 5 considering a fictious $\Delta t_{obs} = 1\,\text{d}$ full domain observability). Furthermore, SWOT swaths observations consist in WS snapshots on different parts of the river

Figure 10: **TOP:** Identifiability maps and flood wave propagation during the yearly peak flow (may-june) in the Negro river model. The WS anomaly (heatmap) is given by $Z_{ano}(x,t) = Z(x,t) - \overline{Z(x)}$, where $\overline{Z(x)}$ is the average local WS elevation from day 160 to 190. Blue points: tracking of maximum WS elevation value $Z_m(x) = \max_{t\in[0,365]} Z(x,t)$, $\forall x \in [0, L]$. Gray points: tracking of maximum WSE in the downstream pool. Dashed blue lines: fictitious trajectory at kinematic speed (sparse dashes) $c_k = 5/3U$ and at $U + c$ (dotted dashes), starting at $x = 0$, at the time of the local WS elevation peak. The speeds are calculated from the simulated flow speed U and water height h and updated every $\Delta x = 200\,\mathrm{m}$, such as $t^{p+1} = t^p + \frac{\Delta x}{c_k^p}$. **BOTTOM:** Extreme flow forcings and flow model variables over a 2 year period. Blue lines: Extreme simulated waterlines. Red lines: corresponding extreme Froude values. Green lines: corresponding cumulative injected flows.
Vertical black dashes are lateral inflow locations. Bold vertical dashes are inflows inferred in subsection 5.2.

x (km)	0	65	121	163	193	216	388	418	465	502	528	598	623	628	657	700	739	754	789	1000
$\frac{5}{3}\bar{u}_{HF}$	2.35	1.42	1.22	1.07	1.02	0.75	0.50	0.52	0.53	0.50	0.48	0.35	0.32	0.41	0.61	0.47	0.44	0.47	0.44	
c_{HF}	8.32	9.23	9.71	10.31	10.36	11.19	12.52	12.61	12.62	13.49	13.95	15.90	16.28	16.82	17.93	17.26	17.56	19.37	19.69	
$u_{HF} + c_{HF}$	9.74	10.08	10.44	10.95	10.97	11.64	12.82	12.92	12.93	13.79	14.23	16.11	16.47	17.06	18.29	17.54	17.82	19.65	19.95	
$u_{HF} - c_{HF}$	-6.92	-8.38	-8.98	-9.67	-9.75	-10.73	-12.22	-12.29	-12.30	-13.19	-13.66	-15.68	-16.09	-16.57	-17.56	-16.99	-17.29	-19.09	-19.42	
$I_{ident,HF}$	0.32	0.46	0.40	0.33	0.26	2.64	0.69	1.04	0.81	0.60	1.69	0.82	0.18	0.82	0.81	0.97	0.39	0.86	2.14	
$\frac{5}{3}\bar{u}_{LF}$	1.40	0.96	0.83	0.70	0.69	0.52	0.34	0.37	0.45	0.40	0.41	0.25	0.22	0.26	0.31	0.26	0.24	0.24	0.23	
c_{LF}	5.54	6.16	6.54	7.13	7.05	7.72	8.70	8.59	7.87	8.71	8.81	11.30	11.83	12.54	14.11	13.37	13.78	16.09	16.59	
$u_{LF} + c_{LF}$	6.38	6.74	7.04	7.54	7.47	8.03	8.91	8.81	8.14	8.94	9.06	11.45	11.96	12.70	14.30	13.52	13.93	16.24	16.72	
$u_{LF} - c_{LF}$	-4.70	-5.58	-6.04	-6.71	-6.64	-7.40	-8.50	-8.37	-7.60	-8.47	-8.56	-11.15	-11.70	-12.39	-13.93	-13.22	-13.64	-15.95	-16.45	
$I_{ident,LF}$	0.54	0.67	0.58	0.50	0.39	3.80	1.03	1.47	0.95	0.76	1.97	1.16	0.26	1.29	1.61	1.76	0.73	1.71	4.21	

Table 5: Identifiability indexes between each pair of inflow at low and high flow (see Fig. 10, bottom). Speeds are given in $\mathrm{m.s}^{-1}$. I_{ident} is given for a reach of length L and an observation time step $\Delta t_{obs} = 1\,\mathrm{d}$ by $I_{ident} = \frac{L}{\frac{5}{3}\bar{u}\Delta t_{obs}}$.

domain at given times, hence containing various and mixed signatures (in the sense introduced in section 3) of both several inflows and channel parameters - the more downstream, the more aggregated is the inflow information. Inferences of multiple inflows and frequential analysis are presented in the next section given known or uncertain channel parameters, spatio-temporally dense or sparse (SWOT) observations.

5. Inferences from satellite observables

This section studies the challenging inference of ungauged channel parameters and multiple inflows on the Negro River case, which represents a real and complex large scale problem. Typical inverse problems in hydrological-hydraulic modeling are studied here considering SWOT WS observations. The inference of channel parameters or/and inflows in the 1D Saint-Venant model is addressed using the inverse method presented in subsection 2.2 (see also section AppendixA). The downstream BC is set as a known altimetric rating curve. Three observation sets are generated: spatially and temporally dense ($\Delta t = 600\,\mathrm{s}$) observations (DenseSet), SWOT observations from the hydraulic model outputs masked by SWOT swaths (SWOTSet) and noisy SWOT observations using the large scale simulator [70] to add realistic measurement noise (SWOTNoiseSet). We first present inferences of inflows only, then of channel parameters, and finally of all those spatio-temporal controls simultaneously.

539

540 *5.1. Multiple hydrographs inferences*

541 Depicting flow structure within a river network and a catchment is a key issue in hydrological modeling, especially
542 in ungauged basins. Seeking to infer, from distributed WS observations, flow controls that are both temporally and
543 spatially distributed can represent a very challenging inverse problem, as previously highlighted on synthetic cases.

544 Inferences of $L = 21$ inflow hydrographs from 2 years of SWOT synthetic observations are studied here.
545 The channel geometry, friction and BCs are assumed to be known, hence the control vector reduced to $c =$
546 $\left(Q^0_{lat,1},\ ...,\ Q^P_{lat,1},\ Q^0_{lat,2},\ ...,Q^P_{lat,L}\right)^T$. The inferences are started from a prior guess $c^{(0)}$ consisting in true hy-
547 drographs affected by uncertainties of $\pm 30\%$, that is Q^{+30}_{FG} and Q^{-30}_{FG} as defined above. Note that the inference is
548 started from a hydraulically consistent initial state using an unbiased prior in the first time steps (see investigations
549 in [1, 34]); the prior values of regularization parameters σ_{Qlat} correspond to inflows magnitudes.

550 The inferred hydrographs from inflow prior Q^{-30}_{FG} are presented in Fig. 11 for DenseSet (green lines) and
551 SWOTNoiseSet observations (orange lines). Results from prior Q^{+30}_{FG} are available in AppendixC. SWOTSet and
552 SWOTNoiseSet give almost identical inferences, therefore only the SWOTNoiseSet inferences are presented. For
553 under- and overestimated priors, the assimilation of dense and SWOT observations enables to infer the true hy-
554 drographs fairly well. RMSE ranges from $8.86\,\mathrm{m^3 s^{-1}}$ at $x = 465\,\mathrm{km}$ up to $578.31\,\mathrm{m^3 s^{-1}}$ for the Branco tributary
555 at $x = 657\,\mathrm{km}$. RMSE for all inferences presented in Fig. 11 can be found in section AppendixC. Some inferences
556 show global under- or overestimations (e.g. $x = 216\,, 388\,, 789\,\mathrm{km}$). These biases are linked to the prior bias. Strong
557 and numerous overlapping backwater signals may also influence flow misattribution, as discussed in the academic
558 cases (section 3) for a small scale model. As tested in numerical experiments (not shown), increasing a scalar value
559 $\sigma_{Q_{lat,l}}$ can give more effective weight to an hydrograph $Q_{lat,l}$ in the inference and it can be found further away from
560 its prior guess, which highlights the role of the covariance matrix used for regularization.

561 Note that temporal oscillations appear on the inferred hydrographs when using SWOTNoiseSet which is "tem-
562 porally sparse" observation patterns compared to flow propagation, which is not the case of DenseSet. These
563 oscillations are especially present in downstream inflows, which may link them to particular hydraulic responses
564 in the BC influence zone, although they can be seen in upstream inflows as well. They tend to be prevalent in
565 declining limbs of hydrographs (e.g. in Fig. 11, at 789 km, from day 120 to 300).

566 Note that, regardless of oscillations, inferences tend to be further from the truth in decreasing hydrographs.
567 These oscillations are not the effect of signal misattribution, as they are present with any number of inferred
568 hydrographs (not shown), nor are they caused by the prior's shape, as filtered priors also lead to oscillations (not
569 shown). Instead, the oscillations seems to stem from the combination of the low observation frequency compared
570 to the spatially distributed inflow hydrographs and the nonlinear hydraulic response. Keep in mind that we track
571 flow information through WS elevation deformations caused by the nonlinear propagation of parameter signatures
572 (see subsection 4.3.2).

Figure 11: Lateral hydrographs inferences from SWOTNoiseSet and DenseSet, using the Q_{FG}^{-30} inflow prior .

Figure 12: Difference between target and inferred WS elevation at $870\,km$, as observed by DenseSet and SWOTSet. The dotted line represents the inferred waterline inferred from SWOTSet (with Q_{FG}^{-30} as inflow prior), but observed by DenseSet. The difference between this waterline and the target waterline is the misfit to target. At SWOT pass times, the misfit is low as expected from an inference from SWOTSet. It only displays WS elevation oscillations at unobserved times.

A sample illustration of those oscillations on the simulated WS elevation is presented in Fig. 12, at 870 km, downstream for three oscillating inferred hydrographs (at $x = 738$, 754 and 789 km). The inferred waterline from SWOTNoiseSet is compared to the truth at all simulated times and at SWOT pass times only. The misfit is logically lowest at SWOT pass times (goal of the optimization), while unobserved periods exhibit a slightly oscillating (unconstrained) misfit. Higher frequency observations, such as DenseSet, prevent this behaviours through a more complete spatio-temporal observability of the WS signatures, hence constrain the spatio-temporal parameters inference further. Some model configurations where temporal parameters are discretized at a greater time step than observation one do no exhibit such behaviours (e.g. results with DenseSet, [34]). As already shown in [5] for the identification of a single hydrograph, the identification is possible only in time windows representing the wave propagation time $T_{wave} \sim 26$ days in the present case, yet with multiple inflows and observation sample (see subsection 4.3.2). As a consequence, outside the "identifiable time windows", the infered values are not necessarily representing reality (see related WS misfit in Fig. 12). They are the optimal solution corresponding to the considered priors of the optimization problem. In practice, this means that introducing an additional regularization term j_{reg}, like $\int_0^t \frac{\partial^2 h}{\partial t^2} dt$ at observation points, would smooth (as following a spline curve) between the identifiable windows instead of the obtained oscillations. This smooth discharge curve would not be more physical than the present oscillations and we made the choice to not hide this well understood phenomena. It is a logical consequence of the disparity between the samplings of observations and parameters and does not impede interpretations of hydraulic signatures and identifiability.

Seeking to infer a control that is both temporally and spatially distributed represents a challenging assimilation problem. In the present case: (i) the observation frequency now plays a role in identifying the hydraulic signature, on top of its spatial density and resulting flow propagation: (ii) varying nonlinear flow propagation, and so WS signatures, can result in different inferences depending whether they are performed from observations of rising/declining hydrographs propagations (local $Q(Z)$ hysteresis) and (iii) indirect contributions to parameter weight in the inverse method appear, as successive hydrographs influence the whole downstream water line (established in subsection 3.2), which gives greater "effective weight" to upstream hydrographs as the cause of the misfit is observed in more stations and thus accounted for multiple times in the cost function. The inferred flow variations may be compensating for errors made at upstream stations with different SWOT pass times, impacting their WS elevation

Figure 13: Bathymetry and friction pattern inferences from SWOTSet

either through backwater control or through the modification of the BC and its own backwater effect.

5.1.1. Spatial parameters inference

The inference of effective channel parameters is studied here considering a control vector composed of all friction coefficient values and bathymetry points. The bathymetry is composed of $I = 436$ free points (1 every 2000 m) between each of which it is obtained by linear interpolation. SWOTSet is used, with a spatial observations sampling (1 point every 200 m), i.e. 10 times greater than the sought bathymetry for observed reaches. Two inferences from hydraulically consistent priors are presented, one with the refined bathymetry b_{FG}^{-30} introduced in subsection 4.3.2 (Fig. 13, in green) and another one with $b_{env}^{+2.6m}$, a shifted bathymetry from the $M1$ model in subsection 4.2.1, in red. The 2.6 m correspond to the spatially averaged shift of b_{FG}^{-30} compared to b_{env}. $b_{env}^{+2.6m}$ does not contain a priori information on target bathymetry shape - such as a coarse DEM prior. The friction prior is K_{FG}^{-30} for both inferences.

Using b_{FG}^{-30} and $b_{env}^{+2.6m}$ as priors, the inference of channel parameters (friction and bathymetry) respectively reach a RMSE of $\left(4.362\,\mathrm{m}^{1/3}\mathrm{s}^{-1},\ 1.231\,\mathrm{m}\right)$ and $\left(4.762\,\mathrm{m}^{1/3}\mathrm{s}^{-1},\ 1.913\,\mathrm{m}\right)$. Upstream ($x = 0 - 110$ km), irregularities appear in both inferred bathymetries and correspond to underestimated Strickler coefficients. The high friction partially hides the hydraulic signature of the bathymetry and enables inference error inconsequential to the cost function. Downstream ($x = 600 - 870$ km), in the strong backwater control of the downstream BC, inferences tend to stay close to their prior values. Furthermore, inferences from the unrefined prior $b_{env}^{+2.6m}$ are smoother than those from the refined prior b_{FG}^{-30}. This testifies to the role of the a priori bathymetry shape knowledge contained in the prior when the WS elevation sensitivity to bathymetry is low. Strong backwater effects make the inference of channel parameters more difficult and parameter compensation appears due to the lessened sensitivity of the simulated WS (e.g. in green, at the last friction patch). The refined bathymetry prior b_{FG}^{-30} leads to inferred bathymetry and friction that are closer to the truth. It will be used in the extended control vector inferences below.

5.2. Inference of channel parameters and inflows

This section investigates the simultaneous inference of both unknown inflows and channel parameters on the large scale Negro River case; it combines all previously mentioned difficulties and corresponds to an ungauged configuration. In the following, the aim is to determine: 1) if SWOT data are sufficient to infer the extended control vector given unbiased prior parameters; 2) how the added spatial complexity from lateral inflows impacts spatial parameter inference. In addition, further investigations on the impact of lateral inflow prior shape, representing for example hydrological modeling uncertainty in a simple manner, are presented. The considered extended control vector is the following:

(a)(b)

Figure 14: Inflow, bathymetry and friction patch inferences from SWOT synthetic data: c^*_{flat}, inferred control vector without a priori hydraulic behaviour.

$$c_{ext} = (Q_{lat,x=65}(t)\,,\, Q_{lat,x=502}(t)\,,\, Q_{lat,x=657}(t)\,,\, Q_{lat,x=754}(t)\;;\, b_1,\, ...,\, b_H\;;\, \alpha_1,\, ...,\, \alpha_N) \tag{6}$$

The inferences are performed from DenseSet and SWOTNoiseSet. The bathymetry and friction priors are b^{-30}_{FG} and K^{-30}_{FG} respectively. Four major lateral inflows located at $x = 65$, 502, 657 and 754 km (Fig. 10, bold dashed bars) are considered. Their reduced number facilitates the analysis of their spatial impacts. The other inflows are set to their target values. Two inflows prior types are used: Q^{flat}_{FG}, that gives no a priori on hydrograph shapes and Q^{filter}_{FG}, hydrographs obtained by applying a 80 days moving average filter to the true hydrographs. Prior flow values in Q^{flat}_{FG} are set to the target flow values from the first time step up to 120 days for the sake of initial hydraulic consistency. Inferences of all parameters for these inflow priors are presented in Fig. 14 and Fig. 15. The inferred control vectors are referred to as c^*_{flat} and c^*_{filter}. Inferred parameter scores can be found in Tab. 6.

Inferred spatial parameters patterns are similar to those obtained previously without unknown inflows in subsection 5.1.1. c^*_{flat} features a fair bathymetry fit downstream ($x = 600 - 870$ km) while c^*_{filter} stays close to the prior value. This may be due to the different range of the simulated hydraulic responses in the first iterations: using Q^{flat}_{FG} leads to an increase in WS elevation sensibility to bathymetry. Upstream ($x = 0 - 110$ km), increased bathymetry irregularities in c^*_{flat} are linked to the erroneous prior Q^{flat}_{FG} leading to bathymetry errors in the first iterations, coupled with lower inferred Strickler coefficients, hence a lessened impact of bathymetry on the water surface and the inability to correct the "initial" errors.

In terms of temporal behaviours, both priors give fair estimates of hydraulic controls for DenseSet. Inferences from SWOTNoiseSet are close to those from DenseSet with the presence of oscillations and the rising part of hydrographs are better fitted than decreasing ones, as observed in subsection 5.1. In both c^*_{filter} and c^*_{flat} and for both observation sets, a correlation between sought inflows at $x = 502$; 657 and 754 km appears. The Branco river flow, at $x = 657$ km, is better inferred and its well fitted peaks are also found in the two smaller rivers (e.g. at 520 days), which are in its upstream and downstream influences zones (see Fig. 10, left). In all inferences, the total flow at the downstream BC closely matches that of the truth, which means that only hydraulic signature is misattributed across the 4 inferred temporal parameters, not on the total flow. In c^*_{filter}, more accurate inferences are obtained, with a smaller influence of the Branco river on other inflows in its influence zone and more accurate inference of small scale behaviours. The filtered prior Q^{filter}_{FG} introduces information on low frequency behaviours of the sought inflows, helping the assimilation process to converge to correct the target inflows. This configuration

(a)(b)

Figure 15: Inflow, bathymetry and friction patch inferences from SWOT synthetic data : c^*_{filter}, inferred control vector with a priori hydraulic behaviour.

Obs set	Prior	$RMSE$ $[m^3 s^{-1}]$ $(rRMSE)$				Nash-Sutcliffe			
		65 km	502 km	657 km	754 km	65 km	502 km	657 km	754 km
DenseSet	Q_{FG}^{flat}	189 (0.12)	329 (0.17)	1472 (0.22)	430 (0.45)	0.84	0.90	0.87	0.10
NoiseSWOTSet		209 (0.14)	360 (0.18)	1719 (0.26)	421 (0.44)	0.81	0.88	0.82	0.10
DenseSet	Q_{FG}^{filter}	101 (0.07)	195 (0.10)	412 (0.06)	158 (0.17)	0.94	0.97	0.99	0.49
NoiseSWOTSet		102 (0.07)	208 (0.11)	503 (0.07)	154 (0.16)	0.94	0.96	0.99	0.51

(a) Hydrograph scores

Obs set	Prior	$RMSE_\alpha$ $[\mathrm{m}^{1/3}\mathrm{s}^{-1}]$	$RMSE_b$ [m]
DenseSet	Q_{FG}^{flat}	5.35	1.89
NoiseSWOTSet		5.12	1.64
DenseSet	Q_{FG}^{filter}	5.30	2.06
NoiseSWOTSet		5.13	1.99

(b) Channel parameters scores

Table 6: Inferred parameter scores for extended control inferences.

allows for a better fit of small scale variation in the controls.

6. Conclusion

This paper investigated the inference of river channel parameters and multiple inflows from water surface signatures in the context of satellite altimetry with the forthcoming SWOT mission and using water extents from optical data as well. The HiVDI inverse method presented in [1], based on the 1D Saint-Venant equations and a variational assimilation scheme adapted to account for lateral inflows (mass and momentum injections). Given hydraulically consistent prior guesses and regularization weights, it is successfully applied to synthetic test cases and a long reach of the anabranching Negro River in the Amazon basin using multisatellite data.

Through low Froude synthetic cases, it is shown that the signature of a lateral inflow is visible downstream from the inflow point through the total flow signature and can be visible upstream in case of downstream control at the injection. Following this analysis and using the HiVDI variational assimilation method (global in time and space), a study of the minimum spatial density of water surface observations necessary to infer lateral inflows from their hydraulic signatures is carried out. Synthetic twin experiments yield the following results: (i) given high observation temporal frequency relative to model hydraulic response, perfect inflows inferences can be obtained; (ii) to correctly attribute signatures between multiple lateral inflows, a minimum of 1 observation point between each injection cell is necessary; (iii) when simultaneously inferring inflows and/or channel parameters, a sensitivity to parameter weights (see section AppendixA) appears; (iv) given a priori parameter weights, accurate inferences of

inflows and channel parameters is achievable even with the minimum spatial observability.

A method for building effective river models in coherence with multisatellite data and including realistic spatial variations is introduced based on multisource data of water surface elevation, width and slopes. This method makes use of (i) multimission altimetric rating curves (see [64]) or equivalently a distributed hydrological model and altimetry data and (ii) water surface width like those from current databases (see [71]); it should be applicable to rivers from the future SWOT database. It is applied here to build a simple effective 1D model of the Negro river upstream from its confluence with the Solimoes river. It fits currently available satellite water surfaces signatures and contains real-like spatial variabilities and flood wave propagation features.

The inference capabilities of spatially distributed channel parameters and inflows from synthetic SWOT observations are highlighted on the Negro River case given hydraulically coherent priors. The inference of temporal parameters in the form of 21 spatially distributed lateral inflow hydrographs leads to accurate estimates and low water surface misfit at observation times. High frequency observations give good inferences, with an expected sensitivity to both prior bias (see [1, 34]) and prior shape.

SWOT-like observations lead to comparable inferences, with slight oscillations due to the frequential disparity between observations temporal controls combined to their spatial distribution and the resulting nonlinear flow propagation on the domain, as analyzed with identifiability maps. Those oscillations related to model-observations time scales could be overcome by introducing additional regularizations - not done here for the sake of hydraulic analysis. Inference of purely spatial parameters (bathymetry/friction) were carried out as well, leading to some complementary remarks: (i) channel parameters equifinality is most present in the downstream part of the model, where the waterline is influenced by the strong backwater effect of the boundary condition (Solimoes River) which diminishes water surface sensitivity to other parameters; (ii) bathymetry prior shape influences the inferred bathymetry. Finally, simultaneous inference of channel parameters and spatially distributed inflows was achieved with satisfying accuracy. We show that, with the present method, large scale temporal parameter variations can be found from synthetic SWOT observations even without a priori knowledge of the shape of the hydrological response, but that small scale variations can be better inferred with a priori hydrograph shape knowledge.

Recall that the estimation of discharges and channel parameters from (SWOT) WS observations is a difficult inverse problem because of the correlated influence of flow controls on the observable water surface signatures - non uniqueness/equifinality issues. It is therefore necessary to use hydraulically consistent priors as investigated in [1, 37, 34] with HiVDI method that contains low complexity flow relations for deriving robust prior guesses from databases and hydrological models, or even in situ depth/discharge data when available (see [1]) - not the scope of this paper. As already discussed in [1], the VDA solution depends on the priors which are the first guess value and the covariances matrixes. Ongoing research efforts in the SWOT community, in view of global discharge estimates, focus on the determination of priors through the construction of a SWOT a-priori database based on [72, 71] and global/regional model outputs (see [26, 1]), constrained with available in situ gauge measurements. Note that

a-priori estimations/databases could be enriched or reprocessed during or after the SWOT mission lifetime and HiVDI would enable to refining discharge estimates (see [1]). Moreover, as shown in [73], priors obtained by deep learning can greatly improve global estimation.

More generally, reaching unbiased estimates of discharge, from downstream to upstream of river networks with varying densities of in situ discharge data hence ungauged river portions/basins, is a crucial challenge in hydrology that could benefit from the fusion of complementary in situ and remotely sensed data in integrated models. The present study brings insight in lateral inflows inference from hydraulic signatures and paves the way for further research on integrated hydrological-hydraulic assimilation chains for river networks and in coherence with multi-satellites observables (of local hydrodynamic signatures) to benefit from them in a regionalization perspective.

Searching for distributed channel parameters and inflows given temporally sparse SWOT data and a global assimilation method brings the issue of signal attribution to the forefront, especially at the scale of a river network. Further research should focus on tributaries that could be amenable to the use of SWOT and multisatellite observations to better constrain estimates of lateral inflows and next distributed fluxes on network models considering hydrological-hydraulic couplings. The introduction of pertinent signatures, scales and constrains in the forward-inverse models (e.g. forward operators, covariance matrices, cost function terms) should help maximizing the use of various information sources and enable smooth discharge estimates and better signal attribution, given uneven and heterogeneous satellite data in combination with other complementary databases/knowledge. This could help leveraging better inferences of hydrological responses and flow structure within a river basin and eventually enable information feedback to rainfall-runoff modules and ultimately regionalization issues.

Author contributions and acknowledgments

This work is a part of the PhD thesis work of LP.

Research plan: LP, PAG, JM, PFG; computational software DassFlow1D and satellite data curation toolbox adapted from their previous versions by LP; Numerical investigations by LP with PAG, PFG, KL, JM for analysis. JM is the principal designer of the inverse computational method and its analysis.

Data : The water surface widths were derived by SB and HY contributed to their analysis using satellite images. The SWOT synthetic observations were generated by KL. The multisatellite dataset was provided by SC and altimetric rating curves and MGB outputs by AP. The GPS flow lines were provided by DM and SC.

Fundings: Most authors have been co-funded by CNES Tosca research project 2014-2019; project supervision: JM, PAG. PhD of LP is co-funded by CNES and ICUBE.

[1] K. Larnier, J. Monnier, P-A. Garambois, and J. Verley. On the estimation of river discharges from altimetry. *Inverse Problems Sc. Eng. (IPSE). Accepted, to appear*, 2020. URL `https://hal.archives-ouvertes.fr/hal-01811683`.

[2] D.M. Moreira. *Apport des données de géodésie spatial pour l'étude du bassin hydrologique amazonien*. PhD thesis, LEGOS - Laboratoire d'Etudes en Géophysique et Océanographie Spatiale, 2016. URL http://www.theses.fr/2016TOU30372.

[3] J-F. Pekel, A. Cottam, and N. Gorelick. High-resolution mapping of global surface water and its long-term changes. *Nature*, 540(418):19, 2016. doi: 10.1038/nature20584. URL https://www.nature.com/articles/nature20584#supplementary-information.

[4] R.C.D. Paiva, D.C. Buarque, W. Collischonn, M-P. Bonnet, F. Frappart, S. Calmant, and E.M. Carlos. Large-scale hydrologic and hydrodynamic modeling of the amazon river basin. *Water Resources Research*, 49(3): 1226–1243, 2013. doi: 10.1002/wrcr.20067. URL https://agupubs.onlinelibrary.wiley.com/doi/abs/10.1002/wrcr.20067.

[5] P. Brisset, J. Monnier, P-A. Garambois, and H. Roux. On the assimilation of altimetric data in 1D Saint-Venant river flow models. *Advances in water resources*, 119:41–59, 2018.

[6] World Meteorological Organization. GCOS/GTOS plan for terrestrial climate-related observations, version 2.0. URL https://library.wmo.int/doc_num.php?explnum_id=3891.

[7] World Meteorological Organization. GCOS systematic observation requirements for satellite-based products for climate 2011 update: Supplemental details to the satellite-based component of the implementation plan for the global observing system for climate in support of the UNFCCC (2010 update)., 2011. URL https://library.wmo.int/doc_num.php?explnum_id=3710.

[8] J. Schuite, N. Flipo, N. Massei, A. Rivière, and F. Baratelli. Improving the spectral analysis of hydrological signals to efficiently constrain watershed properties. *Water Resources Research*, 55(5):4043–4065, 2019. doi: 10.1029/2018WR024579. URL https://agupubs.onlinelibrary.wiley.com/doi/abs/10.1029/2018WR024579.

[9] B.M. Fekete and C.J. Vorosmarty. The current status of global river discharge monitoring and potential new technologies complementing traditional discharge measurements. *IAHS - PUB*, 2002.

[10] D. Alsdorf, P. Bates, J. Melack, M. Wilson, and T. Dunne. Spatial and temporal complexity of the Amazon flood measured from space. *Geophysical Research Letters*, 34(8), 2007. doi: 10.1029/2007GL029447. URL https://agupubs.onlinelibrary.wiley.com/doi/abs/10.1029/2007GL029447.

[11] M. Durand, L. Fu, D.P. Lettenmaier, D.E. Alsdorf, E. Rodríguez, and D. Esteban-Fernandez. The Surface Water and Ocean Topography Mission: Observing Terrestrial Surface Water and Oceanic Submesoscale Eddies. *Proceedings of the IEEE*, 98(5):766–779, May 2010. doi: 10.1109/JPROC.2010.2043031.

[12] E. Rodríguez. SWOT Science requirements document. JPL document, JPL, 2012. URL https://swot.jpl.nasa.gov/system/documents/files/2176_2176_D-61923_SRD_Rev_B_20181113.pdf.

[13] S. Biancamaria, D.P. Lettenmaier, and T.M. Pavelsky. The SWOT mission and its capabilities for land hydrology. *Surveys in Geophysics*, 37(2):307–337, Mar 2016. ISSN 1573-0956. URL http://dx.doi.org/10.1007/s10712-015-9346-y.

[14] E. Rodríguez, Esteban-Fernandez D., E. Peral, C.W. Chen, J-W. Blesser, and B. Williams. Wide-swath altimetry: A review. in D. Stammer A. Cazenave (Eds.). *Satellite Altimetry over Oceans and Land Surfaces (Chapter 2)*, page CRC press, 2018.

[15] P-A. Garambois, S. Calmant, H. Roux, A. Paris, J. Monnier, P. Finaud-Guyot, A.S. Montazem, and J.S. da Silva. Hydraulic visibility: Using satellite altimetry to parameterize a hydraulic model of an ungauged reach of a braided river. *Hydrological Processes*, 31(4):756–767, 2017. ISSN 1099-1085. URL http://dx.doi.org/10.1002/hyp.11033. hyp.11033.

[16] A.S. Montazem, P-A. Garambois, S. Calmant, P. Finaud-Guyot, J. Monnier, D.M. Moreira, J.T. Minear, and S. Biancamaria. Wavelet-based river segmentation using hydraulic control-preserving water surface elevation profile properties. *Geophysical Research Letters*, 46(12):6534–6543, JUN 28 2019. ISSN 0094-8276. doi: 10.1029/2019GL082986.

[17] E. Rodríguez, M. Durand, and R.P. de M. Frasson. Observing rivers with varying spatial scales. *Water Resources Research*, 2020. doi: 10.1029/2019WR026476. URL https://agupubs.onlinelibrary.wiley.com/doi/abs/10.1029/2019WR026476.

[18] P-A. Garambois and J. Monnier. Inference of effective river properties from remotely sensed observations of water surface. *Advances in Water Resources*, 79:103–120, 2015. URL https://www.sciencedirect.com/science/article/abs/pii/S0309170815000330.

[19] K.M. Andreadis, E.A. Clark, D.P. Lettenmaier, and D.E. Alsdorf. Prospects for river discharge and depth estimation through assimilation of swath-altimetry into a raster-based hydrodynamics model. *Geophysical Research Letters*, 34(10), 2007. doi: 10.1029/2007GL029721. URL https://agupubs.onlinelibrary.wiley.com/doi/abs/10.1029/2007GL029721.

[20] S. Biancamaria, M. Durand, K.M. Andreadis, P.D. Bates, A. Boone, N.M. Mognard, E. Rodríguez, D.E. Alsdorf, D.P. Lettenmaier, and E.A. Clark. Assimilation of virtual wide swath altimetry to improve arctic river modeling. *Remote Sensing of Environment*, 115(2):373 – 381, 2011. ISSN 0034-4257. doi: 10.1016/j.rse.2010.09.008. URL http://www.sciencedirect.com/science/article/pii/S0034425710002816.

[21] M. Durand, K.M. Andreadis, D.E. Alsdorf, D.P. Lettenmaier, D. Moller, and M. Wilson. Estimation of bathymetric depth and slope from data assimilation of swath altimetry into a hydrodynamic model. *Geophysical Research Letters*, 35(20), 2008. doi: 10.1029/2008GL034150. URL https://agupubs.onlinelibrary.wiley.com/doi/abs/10.1029/2008GL034150.

[22] Y. Yoon, M. Durand, C.J. Merry, E.A. Clark, K.M. Andreadis, and Alsdorf D.E. Estimating river bathymetry from data assimilation of synthetic SWOT measurements. *Journal of Hydrology*, 464 - 465(0):363 – 375, 2012. ISSN 0022-1694. doi: 10.1016/j.jhydrol.2012.07.028. URL http://www.sciencedirect.com/science/article/pii/S0022169412006294.

[23] M. Durand, J. Neal, E. Rodríguez, K.M. Andreadis, L.C. Smith, and Y. Yoon. Estimating reach-averaged discharge for the river Severn from measurements of river water surface elevation and slope. *Journal of Hydrology*, 511:92–104, 2014. doi: 10.1016/j.jhydrol.2013.12.050.

[24] C.J. Gleason and L.C. Smith. Toward global mapping of river discharge using satellite images and at-many-stations hydraulic geometry. *Proceedings of the National Academy of Sciences*, 111(13):4788–4791, 2014. ISSN 0027-8424. doi: 10.1073/pnas.1317606111. URL http://www.pnas.org/content/111/13/4788.

[25] D.M. Bjerklie, C.M. Birkett, .W. Jones, C. Carabajal, J.A. Rover, J.W. Fulton, and P-A. Garambois. Satellite remote sensing estimation of river discharge: Application to the Yukon river Alaska. *Journal of Hydrology*, 561: 1000 – 1018, 2018. ISSN 0022-1694. doi: 10.1016/j.jhydrol.2018.04.005. URL http://www.sciencedirect.com/science/article/pii/S0022169418302464.

[26] M. Durand, C.J. Gleason, P-A. Garambois, D. Bjerklie, L.C. Smith, H. Roux, E. Rodriguez, P.D. Bates, T.M. Pavelsky, J. Monnier, X. Chen, G. Di Baldassarre, J-M. Fiset, N. Flipo, R.P.d.M. Frasson, J. Fulton, N. Goutal, F. Hossain, E. Humphries, J.T. Minear, M.M. Mukolwe, J.C. Neal, S. Ricci, B.F. Sanders, G. Schumann, J.E. Schubert, and L. Vilmin. An intercomparison of remote sensing river discharge estimation algorithms from measurements of river height, width, and slope. *Water Resources Research*, 52(6):4527–4549, 2016. doi: 10.1002/2015WR018434. URL https://agupubs.onlinelibrary.wiley.com/doi/abs/10.1002/2015WR018434.

[27] H. Roux and D. Dartus. Use of parameter optimization to estimate a flood wave: Potential applications to remote sensing of rivers. *J. of Hydrology*, 328:258–266, 2006.

[28] M. Honnorat, X. Lai, F-X. le Dimet, and J. Monnier. Variational data assimilation for 2D fluvial hydraulics simulation. *CMWR XVI-Computational Methods for Water Ressources. Copenhagen, june 2006.*

[29] R. Hostache, X. Lai, J Monnier, and C. Puech. Assimilation of spatially distributed water levels into a shallow-water flood model. Part II: Use of a remote sensing image of Mosel River. *Journal of Hydrology*, 390:257–268, 2010. URL http://www.sciencedirect.com/science/article/pii/S0022169410004166.

[30] X. Lai and J. Monnier. Assimilation of spatially distributed water levels into a shallow-water flood model. Part I: mathematical method and test case. *Journal of Hydrology*, 377:1–11, 2009. URL http://www.sciencedirect.com/science/article/pii/S0022169409004508. 1-2.

[31] D.G. Cacuci, I.M. Navon, and M. Ionescu-Bugor. *Computational Methods for Data Evaluation and Assimilation*. Taylor and Francis CRC Press: Boca Raton, 2013.

[32] I. Gejadze and P-O. Malaterre. Discharge estimation under uncertainty using variational methods with application to the full Saint-Venant hydraulic network model. *International Journal for Numerical Methods in Fluids*, 83(5):405–430, 2017. ISSN 1097-0363. doi: 10.1002/fld.4273. URL http://dx.doi.org/10.1002/fld.4273. fld.4273.

[33] H. Oubanas, I. Gejadze, P-O. Malaterre, and F. Mercier. River discharge estimation from synthetic SWOT-type observations using variational data assimilation and the full Saint-Venant hydraulic model. *Journal of Hydrology*, 559:638 – 647, 2018. ISSN 0022-1694. doi: 10.1016/j.jhydrol.2018.02.004. URL http://www.sciencedirect.com/science/article/pii/S0022169418300805.

[34] P-A. Garambois, K. Larnier, J. Monnier, P. Finaud-Guyot, J. Verley, A.S. Montazem, and S. Calmant. Variational estimation of effective channel and ungauged anabranching river discharge from multi-satellite water heights of different spatial sparsity. *Journal of Hydrology*, 581:124409, 2020. ISSN 0022-1694. URL https://doi.org/10.1016/j.jhydrol.2019.124409.

[35] B. Kaltenbacher, A. Neubauer, and O. Scherzer. *Iterative regularization methods for nonlinear ill-posed problems*, volume 6. Walter de Gruyter, 2008.

[36] Y. Yoon, P-A. Garambois, R. Paiva, M. Durand, H. Roux, and E. Beighley. Improved error estimates of a discharge algorithm for remotely sensed river measurements: Test cases on Sacramento and Garonne rivers. *Water Resources Research*, 52(1):278–294, 2016.

[37] S. Tuozzolo, G. Lind, B. Overstreet, J. Mangano, M. Fonstad, M. Hagemann, R.P.M. Frasson, K. Larnier, P-A. Garambois, J. Monnier, and M. Durand. Estimating river discharge with swath altimetry: A proof of concept using AirSWOT observations. *Geophysical Research Letters*, 46(3):1459–1466, 2019. doi: 10.1029/2018GL080771. URL https://agupubs.onlinelibrary.wiley.com/doi/abs/10.1029/2018GL080771.

[38] H. Oubanas, I. Gejadze, P-O. Malaterre, M. Durand, R. Wei, R.P.M. Frasson, and A. Domeneghetti. Discharge estimation in ungauged basins through variational data assimilation: The potential of the SWOT mission. *Water Resources Research*, 54(3):2405–2423, 2018. doi: 10.1002/2017WR021735. URL https://agupubs.onlinelibrary.wiley.com/doi/abs/10.1002/2017WR021735.

[39] R. Schneider, P.N. Godiksen, H. Villadsen, H. Madsen, and P. Bauer-Gottwein. Application of CryoSat-2 altimetry data for river analysis and modelling. *Hydrology and Earth System Sciences*, 21(2):751–764, 2017. doi: 10.5194/hess-21-751-2017. URL https://www.hydrol-earth-syst-sci.net/21/751/2017/.

[40] F.E. O'Loughlin, J. Neal, G.J.P. Schumann, E. Beighley, and P.D. Bates. A LISFLOOD-FP hydraulic model of the middle reach of the Congo. *Journal of Hydrology*, page 124203, 2019. ISSN 0022-1694. doi: 10.1016/j.jhydrol.2019.124203. URL http://www.sciencedirect.com/science/article/pii/S0022169419309382.

[41] W. Collischonn, D. Allasia, B.C. Da Silva, and E.C.M. Tucci. The MGB-IPH model for large-scale rainfall-runoff modelling. *Hydrological Sciences Journal*, 52(5):878–895, 2007. URL https://doi.org/10.1623/hysj.52.5.878.

[42] P.R.M. Pontes, F.M. Fan, A.S. Fleischmann, R.C.D. Paiva, D.C. Buarque, V.A. Siqueira, P.F. Jardim, M.V. Sorribas, and W. Collischonn. MGB-IPH model for hydrological and hydraulic simulation of large floodplain river systems coupled with open source GIS. *Environmental Modelling Software*, 94:1 – 20, 2017. ISSN 1364-8152. doi: 10.1016/j.envsoft.2017.03.029. URL http://www.sciencedirect.com/science/article/pii/S136481521630189X.

[43] R.C.D. Paiva, D.C. Buarque, W. Collischonn, M-P. Bonnet, F. Frappart, S. Calmant, and E.M. Carlos. Large-scale hydrologic and hydrodynamic modeling of the amazon river basin. *Water Resources Research*, 49(3):1226–1243, 2013. doi: 10.1002/wrcr.20067. URL https://agupubs.onlinelibrary.wiley.com/doi/abs/10.1002/wrcr.20067.

[44] Adhemar J-C. de Saint-Venant. Théorie du mouvement non-permanent des eaux, avec application aux crues des rivières et à l'introduction des marées dans leur lit. *CR Acad. Sci. Paris*, 73(147-154):5, 1871.

[45] V.T. Chow. Handbook of applied hydrology. *McGraw-Hill Book Co., New-York, 1467 pages*, 1964.

[46] C. Ancey. *Hydraulique à surface libre.* Ecole Polytechnique Fédérale de Lausanne Ecublens, 2018.

[47] V. Guinot. *Wave propagation in fluids: models and numerical techniques, second edition.*, volume 49. 2010.

[48] J. A. Cunge, M. Holly, F., and A. Verwey. *Practical Aspects of Computational River Hydraulics.* Pitam Publishing,, 1980.

[49] Data assimilation for free surface flows. Technical report, Mathematics Institute of Toulouse-INSA group-CS corp.CNES-CNRS, 2019. URL http://www.math.univ-toulouse.fr/DassFlow.

[50] J. Monnier, F. Couderc, D. Dartus, K. Larnier, R. Madec, and J-P. Vila. Inverse algorithms for 2D shallow water equations in presence of wet dry fronts. application to flood plain dynamics. *Advances in Water Resources*, 97:11–24, 2016.

[51] J. Monnier. *Variational data assimilation: from optimal control to large scale data assimilation*. Open Online Course, INSA Toulouse, 2014. URL https://www.math.univ-toulouse.fr/%7Ejmonnie/Enseignement/CourseVDA.pdf.

[52] A. Montazem, P.-A. Garambois, P. Finaud-Guyot, S. Calmant, J. Monnier, and D. Moreira. Physical basis for river segmentation from water surface observables. In *AGU Fall Meeting Abstracts*, volume 2017, pages H44H–06, December 2017. URL https://ui.adsabs.harvard.edu/abs/2017AGUFM.H44H..06S.

[53] P.G. Samuels. Backwater lengths in rivers. *Proceedings of the Institution of Civil Engineers*, 87(4):571–582, 1989. URL https://doi.org/10.1680/iicep.1989.3779.

[54] V.T. Chow. *Open-channel Hydraulics*. Mc Graw-Hill, New-York, USA, 1959.

[55] A. Montazem. *Représentation et segmentation hydraulique effective de rivières pour le calcul de debit par altimetrie SWOT à l'échelle globale*. Thèse de doctorat, Universite de Toulouse III Paul Sabatier, Toulouse, France, 2018.

[56] Agência Nacional de Âguas (ANA). Brasil hydrografia. http://www.portalbrasil.net/brasil_hidrografia.htm. Accessed: 2020-02-06.

[57] E.M. Latrubesse and E. Franzinelli. The late quaternary evolution of the negro river, amazon, brazil: Implications for island and floodplain formation in large anabranching tropical systems. *Geomorphology*, 70(3):372 – 397, 2005. ISSN 0169-555X. doi: 10.1016/j.geomorph.2005.02.014. URL http://www.sciencedirect.com/science/article/pii/S0169555X05000826. Tropical Rivers.

[58] G. Cochonneau, F. Sondag, J-L. Guyot, B. Geraldo, N. Filizola, P. Fraizy, A. Laraque, P. Magat, J-M. Martinez, L. Noriega, E. Oliveira, J. Ordonez, R. Pombosa, Seyler F., J. Sidgwick, and P. Vauchel. *L'Observatoire de Recherche en Environnement, ORE HYBAM sur les grands fleuves amazoniens*. 2006. ISBN 978-1-901502-78-7.

[59] N. Filizola, N. Spínola, W. Arruda, Fr. Seyler, S. Calmant, and J. Silva. The Rio Negro and Rio Solimões confluence point-hydrometric observations during the 2006/2007 cycle. *River, Coastal and Estuarine Morphodynamics-RCEM*, 2009:1003–1006, 2009.

[60] J. Callède, D.M. Moreira, and S. Calmant. Détermination de l'altitude du zéro des stations hydrométriques en Amazonie brésilienne. Application aux lignes d'eau des Rios Negro, Solimões et Amazone. *Journal of Water Science*, 26(2):153–171, 2013. doi: 10.7202/1016065ar.

[61] J.S. Da Silva, F. Seyler, S. Calmant, O.C. Rotunno Filho, E. Roux, A.A.M. Aranjo, and J-L. Guyot. Water level dynamics of amazon wetlands at the watershed scale by satellite altimetry. *International Journal of Remote Sensing*, 33(11):3323–3353, 2012. URL http://dx.doi.org/10.1080/01431161.2010.531914.

[62] G.H. Allen and T.M. Pavelsky. Patterns of river width and surface area revealed by the satellite-derived north american river width data set. *Geophysical Research Letters*, 42(2):395–402, 2015. ISSN 1944-8007. URL http://dx.doi.org/10.1002/2014GL062764.

[63] E. Park and E.M. Latrubesse. The hydro-geomorphologic complexity of the lower amazon river floodplain and hydrological connectivity assessed by remote sensing and field control. *Remote Sensing of Environment*, 198: 321 – 332, 2017. ISSN 0034-4257. doi: 10.1016/j.rse.2017.06.021. URL http://www.sciencedirect.com/science/article/pii/S0034425717302808.

[64] A. Paris, R.C.D. de Paiva, J.S. da Silva, D.M. Moreira, S. Calmant, P-A. Garambois, W. Collischonn, M-P. Bonnet, and F. Seyler. Stage-discharge rating curves based on satellite altimetry and modeled discharge in the amazon basin. *Water Resources Research*, 52(5):3787–3814, 2016. doi: 10.1002/2014WR016618. URL https://agupubs.onlinelibrary.wiley.com/doi/abs/10.1002/2014WR016618.

[65] A.S. Fleischmann, W. Collischonn, R. Paiva, and C.E. Tucci. Modeling the role of reservoirs versus floodplains on large-scale river hydrodynamics. *Natural Hazards*, 99(2):1075–1104, Nov 2019. ISSN 1573-0840. URL https://doi.org/10.1007/s11069-019-03797-9.

[66] A.C. Fassoni-Andrade, R.C.D. de Paiva, and A.S. Fleischmann. Lake topography and active storage from satellite observations of flood frequency. *Water Resources Research*, 56(7), 2020. doi: 10.1029/2019WR026362. URL https://agupubs.onlinelibrary.wiley.com/doi/abs/10.1029/2019WR026362.

[67] A.S. Fleischmann, R.C.D. Paiva, W. Collischonn, M.V. Sorribas, and P.R.M. Pontes. On river-floodplain interaction and hydrograph skewness. *Water Resources Research*, 52(10):7615–7630, 2016. doi: 10.1002/2016WR019233. URL https://agupubs.onlinelibrary.wiley.com/doi/abs/10.1002/2016WR019233.

[68] W. Collischonn, A.S. Fleischmann, R.C.D. Paiva, and A. Mejia. Hydraulic causes for basin hydrograph skewness. *Water Resources Research*, 53(12):10603–10618, 2017. doi: 10.1002/2017WR021543. URL https://agupubs.onlinelibrary.wiley.com/doi/abs/10.1002/2017WR021543.

[69] O. Thual. *Hydrodynamique de l'environnement*. Editions de l'Ecole Polytechnique, 2010.

[70] CNES. SWOT hydrology toolbox. URL https://github.com/CNES/swot-hydrology-toolbox.

[71] G.H. Allen and T.M. Pavelsky. Global extent of rivers and streams. *Science*, 2018. ISSN 0036-8075. doi: 10.1126/science.aat0636. URL http://science.sciencemag.org/content/early/2018/06/27/science.aat0636.

[72] Konstantinos M. Andreadis, Guy J-P. Schumann, and Tamlin Pavelsky. A simple global river bankfull width and depth database. *Water Resources Research*, 49(10):7164–7168, 2013. ISSN 1944-7973. URL http://dx.doi.org/10.1002/wrcr.20440.

[73] K. Larnier and J. Monnier. Hybrid neural network - data assimilation algorithm to infer river features. *submitted*, 2020.

[74] J. C. Gilbert and C. Lemaréchal. Some numerical experiments with variable-storage quasi-newton algorithms. *Mathematical programming*, 45(1-3):407–435, 1989.

[75] L. Hascoët and V. Pascual. The Tapenade Automatic Differentiation tool: Principles, Model, and Specification. *ACM Transactions On Mathematical Software*, 39(3), 2013. URL `http://dx.doi.org/10.1145/2450153.2450158`.

[76] F. Bouttier and P. Courtier. Data assimilation concepts and methods march 1999. *Meteorological training course lecture series. ECMWF*, page 59, 2002. URL `http://msi.ttu.ee/~elken/Assim_concepts.pdf`.

[77] A.C. Lorenc, S.P. Ballard, R.S. Bell, N.B. Ingleby, P.L.F. Andrews, D.M. Barker, J.R. Bray, A.M. Clayton, T. Dalby, D. Li, et al. The met. office global three-dimensional variational data assimilation scheme. *Quarterly Journal of the Royal Meteorological Society*, 126(570):2991–3012, 2000.

[78] A. Weaver and P. Courtier. Correlation modelling on the sphere using a generalized diffusion equation. *Quarterly Journal of the Royal Meteorological Society*, 127(575):1815–1846, 2001.

[79] S.A. Haben, A.S. Lawless, and N.K. Nichols. Conditioning and preconditioning of the variational data assimilation problem. *Computers & Fluids*, 46(1):252–256, 2011.

[80] S.A. Haben, A.S. Lawless, and N.K. Nichols. Conditioning of incremental variational data assimilation, with application to the met office system. *Tellus A*, 63(4):782–792, 2011.

AppendixA. The computational inverse method

The computational inverse method is based on Variational Data Assimilation (VDA) applied to the 1D Saint-Venant model (eq. (1)). The computational inverse method is the one presented in [5, 1] with an augmented composite control vector c (eq. (4)): c contains a spatially distributed friction coefficient enabling to model complex flow zones (while it is an uniform friction law $K(h)$ in [1]). This definition of $K(x, h)$ enables to consider more heterogeneous bathymetry controls. c also contains lateral flow hydrographs $Q_{lat,i}(t)$ to deal with in/offtakes due to tributaries or underground flows. It is important to point out that the imposed downstream BC is an unknown of the inverse problem. It is constrained with the observed water elevations and inferred river bottom slope using a locally uniform flow hypothesis (i.e. Manning equation, see subsection 2.1) - except in the last real case above. The cost function $j(c)$ is defined as:

$$j(c) = j_{obs}\,(c) + \gamma\, j_{reg}\,(c) \tag{A.1}$$

where $\gamma > 0$ is a weighting coefficient of the so-called "regularization term" $j_{reg}(c)$. The term $j_{obs}(c)$ measures the misfit between observed and modeled WS elevations such that:

$$j_{obs}(c) = \frac{1}{2} \left\| \left(Z\left(c\right) - Z_{obs} \right) \right\|_{\mathcal{O}}^2 \tag{A.2}$$

The norm $\|\cdot\|_{\mathcal{O}} = \|\mathcal{O}^{1/2}\cdot\|_2$ is defined from an a priori positive definite covariance matrix $\mathcal{O}$. Assuming uncorrelated observations $\mathcal{O} = diag\left(\sigma_Z\right)$. The modeled WS elevations Z depend on c through the hydrodynamic model (eq. (1)) and the inverse problem reads as

$$c^* = \mathrm{argmin_c}\ \mathrm{j}\left(c\right) \tag{A.3}$$

This optimal control problem is solved using a Quasi-Newton descent algorithm: the L-BFGS algorithm version presented in [74]. The cost gradient $\nabla j(c)$ is computed by solving the adjoint model; the latter is obtained by automatic differentiation using Tapenade software [75]. Detailed know-hows on VDA may be found e.g. in the online courses [76, 51].

To be solved efficiently this optimization problem needs to be "regularized". Indeed the friction and the bathymetry may trigger indiscernible surface signatures therefore leading to an ill-posed inverse problem; we refer e.g. to [35] for the theory of regularization of such inverse problems and to [1] for a discussion focused on the present inverse flow problem.

Following [1], the optimization problem (eq. (A.3)) is regularized as follows. First the regularization term j_{reg} is added to the cost function (eq. (A.1)). We simply set: $j_{reg}(c) = \frac{1}{2}\left\|b"(x)\right\|_2^2$. Therefore this term imposes (as weak constraints) the inferred bathymetry profile $b(x)$ to be an elastic interpolating the values of b at the control points (i.e. a cubic spline).

A specificity of the present context is the large inconsistency between the large observation grid (altimetry points) and the finer model grid. Between the sparse observations points (equivalently the control points), the bathymetry profile $b(x)$ is reconstructed as a piecewise linear function. It is worth to point out that the resulting reconstruction is consistent with the physical analysis presented in [52, 55]. (This study analyses the adequation between the SW model (eq. (1)) behavior and the WS signature).

Next and following [77, 78, 1], the following change of control variable is made:

$$k = B^{-1/2}\left(\mathrm{c} - \mathrm{c}_{prior}\right) \tag{A.4}$$

where c is the original control vector, c_{prior} is a prior value of c and B is a covariance matrix. The choice of B is crucial in the VDA formulation; its expression is detailed below. After this change of variable the new optimization problem reads:

$$\min_{k} \mathrm{J}\,(k) \;\text{ with } \mathrm{J}\,(k) = j\,(c) \tag{A.5}$$

It is easy to show that this leads to the following new optimality condition: $B^{1/2}\nabla j(c) = 0$; somehow a preconditioned optimality condition. For more details and explanations we refer to 79, 80 and [1] in the present inversion context.

Assuming uncorrelated controls the matrix B is defined as block diagonal such that $B = \mathrm{diag}\ (\mathrm{B_Q}, \mathrm{B_{Qlat,1}}, \ldots, \mathrm{B_{Qlat,L}}, \mathrm{B_b}, \mathrm{B}_\alpha,]$ Still following [1], the covariance matrices B_Q, B_{Qlat} and B_b are set as the classical second order auto-regressive correlation matrices:

$$(B_Q)_{i,j} = (\sigma_Q)^2\ \exp\left(-\frac{|t_j - t_i|}{\Delta t_Q}\right),\ \left(B_{Q_{lat,l}}\right)_{i,j} = (\sigma_{Q_{lat}})^2 \exp\left(-\tfrac{|t_j - t_i|}{\Delta t_Q}\right) \text{ and } (B_b)_{i,j} = (\sigma_b)^2\ \exp\left(-\frac{|x_j - x_i|}{L_b}\right) \tag{A.6}$$

The VDA parameters Δt_Q and L_b represent prior hydraulic scales and act as correlation lengths. We refer to [5] for a thorough analysis of the discharge inference in terms of frequencies and wave lengths and [1] in the present river-observation context. In the present study, the friction parameters applied to deca-kilometric patches are assumed to be uncorrelated thus the matrices B_α and B_β are diagonal:

$$(B_\alpha)_{i,i} = (\sigma_\alpha)^2,\ (B_\beta)_{i,i} = (\sigma_\beta)^2 \tag{A.7}$$

The scalar values $\sigma_\square$ may be viewed as variances ; their values are given in the numerical results section.

Finally, in a noised observation context and to avoid overfitting noisy data, we denote by δ the noise level such that $\|Z_{obs} - Z_{true}\|^2 \leq \delta$ with Z_{obs} the observed and Z_{true} the true WS elevation profiles. A common technique to avoid overfitting noisy data, in the context of Tykhonov's regularization of ill-posed problems, is Morozov's discrepancy principle, (see e.g. [35] and references therein): the regularization parameter γ (see eq. (A.1)) is chosen a posteriori such that j does not decrease below the noise level.

AppendixB. Extended friction calibration results

Figure B.16: ENVISAT WS elevation misfit after friction calibration at all stations for $M2a$.

Figure B.17: ENVISAT WS elevation misfit after friction calibration at all stations for $M2b$.

AppendixC. Additional graphs and RMSE for lateral hydrograph inferences on the Negro River with DenseSet and SWOTNoiseSet observation patterns

Figure C.18: Lateral hydrograph inferences from SWOTNoiseSet and DenseSet, using the Q_{FG}^{+30} inflow prior

x (km)	μ (d)	σ (m^3s^{-1})	DenseSet RMSE (m^3s^{-1})	SWOTNoiseSet RMSE (m^3s^{-1})
65		2500	79.62	122.34
121		1500	97.74	134.59
163		1000	64.17	70.44
193		1000	49.06	50.75
216		700	37.04	41.48
234		800	112.76	120.43
247		1000	89.82	105.24
261		800	56.57	45.62
388		1000	98.30	125.94
418		800	60.64	49.12
465	1	600	8.86	12.64
502		2000	116.21	194.86
528		1000	66.85	83.55
598		600	28.69	29.08
623		1000	40.75	44.83
628		1200	119.85	126.13
657		5000	421.26	578.31
700		1500	263.07	264.27
739		2800	127.97	173.35
754		2000	140.89	158.19
789		2400	249.73	283.92

(a) With prior Q_{FG}^{-30}

x (km)	μ (d)	σ (m^3s^{-1})	DenseSet RMSE (m^3s^{-1})	SWOTNoiseSet RMSE (m^3s^{-1})
65		2500	134.66	156.34
121		1500	142.70	138.31
163		1000	69.46	66.83
193		1000	45.66	43.47
216		700	45.31	47.28
234		800	128.18	130.98
247		1000	122.21	125.72
261		800	35.82	33.85
388		1000	146.13	149.39
418		800	33.81	32.22
465	1	600	13.53	15.37
502		2000	212.87	235.58
528		1000	87.67	91.96
598		600	28.62	28.85
623		1000	39.51	43.31
628		1200	123.45	126.71
657		5000	581.03	775.15
700		1500	250.54	256.81
739		2800	157.54	194.14
754		2000	147.88	154.01
789		2400	293.07	297.37

(b) With prior Q_{FG}^{+30}

Table C.7: Inferred lateral inflows parameter weights and RMSE

AppendixD. Technical specifications

Host bridge: Intel Corporation 8th Gen Core Processor Host Bridge/DRAM Registers

PCI bridge: Intel Corporation Xeon E3-1200 v5/E3-1500 v5/6th Gen Core Processor PCIe Controller

Memory: 2x16Gb SODIMM DDR4 Synchronous 2667 MHz (0.4 ns)

Resolution mode: sequential

Resolution method: implicit-explicit preissmann scheme

Sample run: inference of the full triplet on the Negro model (inferred control vector c^*_{filter} in subsection 5.2)

- Control vector components: 4x740 flow points, 436 bathymetry points, 17 friction patches (3413 total sought values)
- Total run time (direct): under 15 min
- Total run time (inverse): 20.8 h
- Number of iterations: 35
- Average iteration time length: 35.8 min

E3S Web of Conferences **40**, 06010 (2018) https://doi.org/10.1051/e3sconf/20184006010
River Flow 2018

1D/2D porosity model for urban flood modeling: case of a dense street networks

Pascal Finaud-Guyot[1,*], *Pierre-André* Garambois[2], *Shangzhi* Chen[2], *Guilhem* Dellinger[1], *Abdellah* Ghenaim[2], and *Abdellali* Terfous[2]

[1]ICube laboratory (UMR 7357), fluid mechanics team, ENGEES, 1 quai Koch, 67000 Strasbourg, France

[2]ICube laboratory (UMR 7357), fluid mechanics team, INSA Strasbourg, 24 boulevard de la victoire, 67084 Strasbourg cedex, France

Abstract. An increasing urbanization of floodplains has led to higher vulnerability of urban areas and building a new generation of robust, accurate and computationally affordable models dedicated to urban floods is highly required for improving prediction systems and mitigation measures. A better understanding of urban floods hydrodynamics may also be required. In view to achieve computationally affordable and reliable simulations a new 1D/2D parsimonious hydraulic model *Flood1D2D* is introduced for flood modeling in complex branched urban networks. It takes advantage of a cut-cell technique and a new effective model able to take into account some essential sub-grid flow features such as flow vein contractions due to recirculations downstream of a crossroad. It is shown that this local phenomenon can be correctly reproduced thanks to this 1D/2D coupled SW model parameterized with roughness and porosity. The ability of the model to reproduce realistic flood discharge distributions at the subdistrict scale is also tested on a part of the branched network of ICUBE experimental rig. Further studies should tackle the issues of calibration and unsteady modeling.

1 Introduction

An increasing urbanization of floodplains has led to higher vulnerability of urban areas with various amounts of damages and human losses depending on flood features. Therefore, building a new generation of robust, accurate and computationally affordable models dedicated to urban floods is highly required for improving prediction systems and mitigation measures.

In the field of urban flood modeling several approaches have been proposed using shallow water (SW) equations either in 1D or 2D parameterized with a classical friction law [1], SWE modified with macro scale porosity [2, 3], or even 3D Navier Stokes equations [4].

Each of these hydrodynamic models are more or less adapted in reproducing local and/or global scale free surface flow variables (water flux, depth or cross sectional area) depending on the real physical complexity of the flow. The most complex models are computationally expensive and require a generally unaffordable amount of data to be constrained. For instance, the flow complexity at a crossroad and downstream is at least 2D in space [5, 6]. Classical

*e-mail: pascal.finaudguyot@engees.unistra.fr

porosity approaches, are able to account the effect of sub-grid building geometry and stagnant waters, reveal to be a good compromise between physical realism of modeled flood flows and computational cost at the district and city scales [3].

In view to achieve computationally affordable and reliable flood simulations in complex branched urban networks, a 1D/2D parsimonious hydraulic model with pororsity *Flood1D2D* is introduced [7]. This modeling paradigm and parameterization takes advantage of empirical findings on the effects of 3D flow structures on local and global flow patterns in urban geometries, but also of a parsimonious and computationally affordable 1D/2D SW coupling between 1D streets and 2D crossroads achieved with a split cell technique. In the streets, a complementary parameterization of the SW equations with a porosity approach is introduced to account for the effects of recirculation areas occurring downstream of each crossroad.

The conceptual and discrete model are presented and validated in the next section. A discussion around a global scale sensitivity analysis is proposed in section 3. Concluding remarks and perspectives are provided in section 4.

2 *Flood1D2D* - An effective model for urban floods

A new hydrodynamic model has been designed for an effective representation of urban flood flows throughout branched networks of streets and crossroads. It takes advantage of a cut-cell technique and introduces a parsimonious effective model able to take into account some essential sub-grid flow features.

2.1 Conceptual model

Urban flood flows may involve complex 3D hydrodynamic structures such as those involved at confluences/defluences [8, 9] or recirculation zones downstream of crossroads [6]. Such local flow structures may have impact on water repartition, hence on larger scale flow patterns [10]. A 2D SW modeling approach is able to simulate realistic global flow patterns as shown by [4] on the ICUBE urban flood configuration.

The proposed effective modeling approach is based on a full 2D SW model at crossroads and a much cheaper 1D effective approach in streets remaining physically coherent as shown in this paper and sufficiently informative for operational purpose. The modeling paradigm, based on SW equations and illustrated in figure [fig:Effective-1D], consists in : 2D cells in the crossroad and effective 1D cells including the full street width but without constrain in the velocity direction.

Recirculation zones often observed downstream of flow junctions are assumed to be only present in effective 1D cells. As highlighted in section 2.3.2, classical SW equations in 1D are unable to account for recirculation effects on flow variables. Therefore an effective approach is introduced based on the idea of an equivalent flow vein narrowed by the recirculation zone downstream of a crossroad.

This study considers steady-state hydrodynamics and a recirculation area is defined as a zone on which there is on average no flux in the street direction. 1D cells are defined on the whole street width (figure 1) and can contain 2 domains representing:

- Ω_u an ineffective flow area located in a recirculation zone for which the modeled velocity vector is considered as nil.
- Ω_v an effective flow vein.

Flow vein contraction is measured with the variable $\phi = L_v/L$ with $L = L_u + L_v$ where L represents the full width of the 1D cell and L_u (resp. L_v) is the width of the recirculation

(resp. flow vein). Notice that such a definition of ϕ, corresponding to the effective flow width with respect to the full cell width, is similar to a porosity as it can be defined in [11].

In both cells, the hydrodynamics is modeled using the full 2D SW equations (1) to make easier the coupling between streets and crossroads [12]:

$$\frac{\partial}{\partial t}\begin{bmatrix} h \\ q \\ r \end{bmatrix} + \frac{\partial}{\partial x}\begin{bmatrix} q \\ \frac{q^2}{h} + \frac{1}{2}gh^2 \\ \frac{qr}{h} \end{bmatrix} + \frac{\partial}{\partial y}\begin{bmatrix} r \\ \frac{qr}{h} \\ \frac{r^2}{h} + \frac{1}{2}gh^2 \end{bmatrix} = \begin{bmatrix} 0 \\ gh\left(S_{0,x} - S_{f,x}\right) \\ gh\left(S_{0,y} - S_{f,y}\right) \end{bmatrix} \tag{1}$$

where t (resp. x and y) is the time (resp. space), g the gravitational acceleration, h represents the water depth, q (resp. r) the unit-discharge in the x (resp. y) direction, $S_{0,x}$ (resp. $S_{0,y}$) the bottom slope in the x (resp. y) direction and $S_{f,x}$ (resp. $S_{f,y}$) the friction slope in the x (resp. y) direction estimated using the classical Strickler formulation:

$$S_{0,x} = -\frac{\partial z_b}{\partial x} \quad S_{0,y} = -\frac{\partial z_b}{\partial y} \quad S_{f,x} = -gh\frac{(u^2+v^2)^{1/2}}{K^2 h^{4/3}}u \quad S_{f,y} = -gh\frac{(u^2+v^2)^{1/2}}{K^2 h^{4/3}}v \tag{2}$$

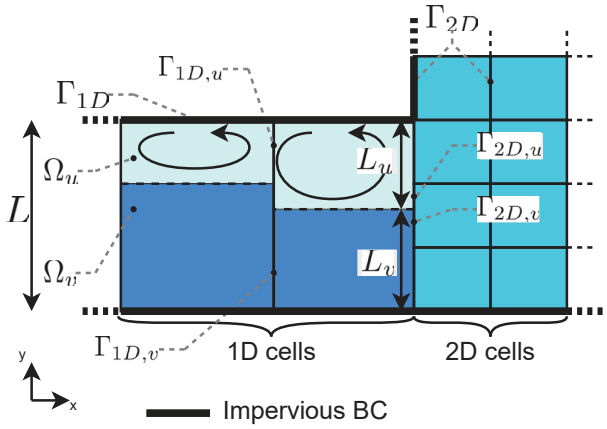

Figure 1. Sketch of a typical mesh configuration describing a 1D/2D "frontal" coupling close to a crossroad/flow junction.

2.2 Finite volume approach

On both 1D or 2D domains, (1) is discretized and solved using a finite volume approach:

$$\mathbf{U}_i^{n+1} = \mathbf{U}_i^n - \Delta t\left[\frac{1}{A_i}\sum_{j\in N(i)} \mathbf{P}_{i,j}L_j\mathbf{F}_j^n + \mathbf{S}(\mathbf{U}_i^n)\right] \tag{3}$$

where $\mathbf{U}_i$ is the vector of the modeled variables $[h \;\; q \;\; r]^T$, $\mathbf{F}_j^n$ stands for the Riemann fluxes through the interface j, $\mathbf{S}(\mathbf{U}_i^n)$ is the source terms vector that applies on cell i, L_j is the length of interface j and $\mathbf{P}_{i,j}$ is the matrix that accounts for the coordinate change from the global coordinate system to the one attached to the interface j of cell i.

The flux $\mathbf{F}_j^n$ is estimated using a Riemann solver [2] and thus depends on the left and right states of each interface.

To take into account the sub-grid flow features (due to recirculation), the sum of the interfaces is subdivided to make appears two elementary fluxes: F_u (resp. F_v) through $L_{u,j}$ (resp. $L_{v,j}$). $L_{u,j}$ is the recirculation width at the interface and is estimated as $L_{u,j} = (L_{u,L} + L_{u,R})/2$ where the subscript $_L$ (resp. $_R$) stands for the cell on the left (resp. right) side of the interface. The definition of ϕ allows writing $L_u = (1 - \phi) \times L_j$ leading to:

$$L_{u,j} = \frac{(L_{u,L} + L_{u,R})}{2} = \left[1 - \frac{\phi_L + \phi_R}{2}\right] \times L_j \qquad L_{v,j} = \frac{\phi_L + \phi_R}{2} \times L_j \tag{4}$$

With such considerations, (3) can be written either for the 1D or the 2D cells as :

$$\mathbf{U}^{n+1}_{\{1D,2D\},i} = \mathbf{U}^{n}_{\{1D,2D\},i} - \Delta t \left[\frac{1}{A_i} \sum_{j \in \Gamma_{\{1D,2D\},v}} \mathbf{P}_{i,j} L_{v,j} \mathbf{F}^n_{v,j} + \sum_{j \in \Gamma_{\{1D,2D\}}} \mathbf{P}_{i,j} L_j \mathbf{F}^n_j + \sum_{j \in \Gamma_{\{1D,2D\},u}} \mathbf{P}_{i,j} L_{u,j} \mathbf{F}^n_{u,j} + \mathbf{S}(\mathbf{U}^n_i) \right] \tag{5}$$

In the numerical tool *Flood1D2D*, the fluxes are computed using the PorAS Riemann solver [2] based on $\mathbf{U}_L$ and $\mathbf{U}_R$, the hydraulic variables in the left-hand and right-hand cells of the interface. $\mathbf{U}$ being computed as $[h \;\; q/\phi \;\; r/\phi]^T$ (resp. $[h \;\; 0 \;\; 0]^T$) when computing through L_v (resp. L_u).

2.3 Validation

The proposed model is validated here on a dambreak experiment in a bend and a four branches crossroad with porosity. A detailed validation of *Flood1D2D* is presented [7], including a comparison to analytical configurations (with and without porosity) and with the classical 2D shallow water model Telemac.

2.3.1 Dambreak in a 90° bend

This first test case aims to highlight that this "frontal" 1D/2D coupling without porosity allows reproducing satisfactorily a highly transient dambreak experiment in open channel with 90° bend [13].

The experimental geometry is composed of a rectangular channel of width $B = 0.495$m with a 90° bend connected to an upstream reservoir and ended with a free outlet. The precise dimensions of the domain are provided in [13]. The channel is initially empty and the initial water level in the reservoir is $z_{ini} = 0.25$m above the bottom of the channel. At $t = 0$s, the water contained in the reservoir is instantaneously released in the channel. The computational domain is meshed using a 1D/2D structured mesh (see figure 2, top left). A simulation is also performed with *Flood1D2D* using only a classical 2D modeling of the domain with a structured mesh and the PorAS Riemann solver. In both case, the discretization step is set to $\Delta x = 0.025$m.

The computed water depth using *Flood1D2D* are plotted and compared to the experimental results at various locations and in time (figure 2). Using both approaches (1D2D or 2D), the water depth map highlights the mobile hydraulic jump generated by the bend and traveling backward to the reservoir; very similar results can be observed in [13]. The computed water depth profiles are fairly close to the experimental ones. The water depth increases abruptly two times: first when the water flows from the reservoir and then when the hydraulic jump moves backward in the upstream part of the channel rand eaches the gauging points G4 to G1. The farther the point form the reservoir the shorter is the interval between those two increases of h. Such evolution do not appears for the last gauging point (G11 - cyan curve) as it is located downstream of the bend. After the second peak, the water depth decreases

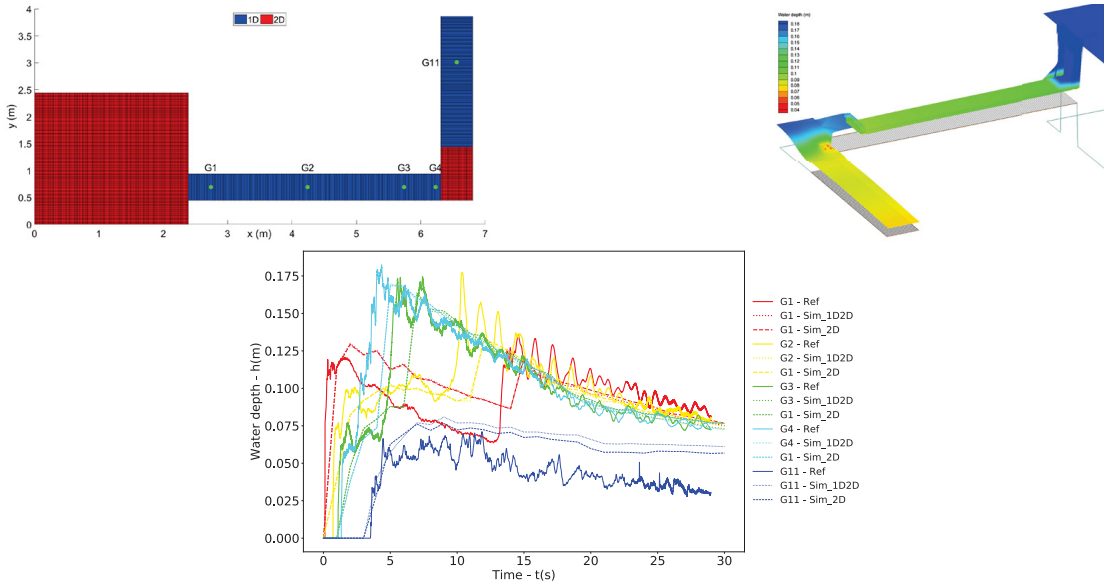

Figure 2. Experimental dambreak in a bend. Top left - 1D/2D mesh; top right - Simulated water surface at $t = 7s$; bottom - comparison of the temporal evolution of the water depth between experiment (plain line) and simulation with 1D2D model (dot line) and classical 2D model (dashed line)

slowly for every gauging point, simulation being in fairly good agreement. Note that water depth in the downstream channel is overestimated by the model (G11 - cyan curve), which can be explained by the boundary condition specified as a free outlet. It is coherent with a free fall for supercritical flow but not for subcritical flow as the water depth at the fall is then the critical depth.

2.3.2 Four branches crossroad

Flood1D2D outputs with and without porosity are compared to Telemac2D ones with a $k-\epsilon$ model chosen as reference on a 4 branches crossroad in this section. The recirculation shape hence the porosity value of each 1D cell of *Flood1D2D* is defined from an empirical equation from [5].

Flood1D2D water depth profiles along the West-East street are presented on figure 3 along with 2D reference water depth plotted on line AB. Water depth profiles in the street upstream of the crossroad are comparable to the reference with a difference on the order of 5mm (for an averaged water depth of 0.11m). Downstream of the crossroad, because of a recirculation the flow vein is contracted, hence flow is accelerated and its free surface presents an inflection for $x \in [3.5; 5]$. This shape is correctly reproduced by *Flood1D2D* parameterized with friction and porosity but not with friction only for which water depth steadily decreases from upstream to downstream.

Even with a distributed friction coefficient such contracted flow profiles cannot be reproduced using a 1D approach as the friction coefficient is embedded in the source term S_f (2) of the SW equation. Indeed this term is of the opposite sign of the velocity which remains monotonous in a prismatic reach as water depth profile.

The proposed model uses an effective 1D approach with a porosity able to account for flow contraction due to a recirculation and simulate a realistic water depth profile. A calibration of the predicted porosity shape and the roughness would help to fit more closely *Flood1D2D* results to the reference.

As a matter of facts, the proposed approach is able to reproduce a realistic contracted flow pattern downstream of a crossroad by introducing a parameterization using a porosity function ϕ. Section 3 discusses the effects of this parameterization at a larger scale.

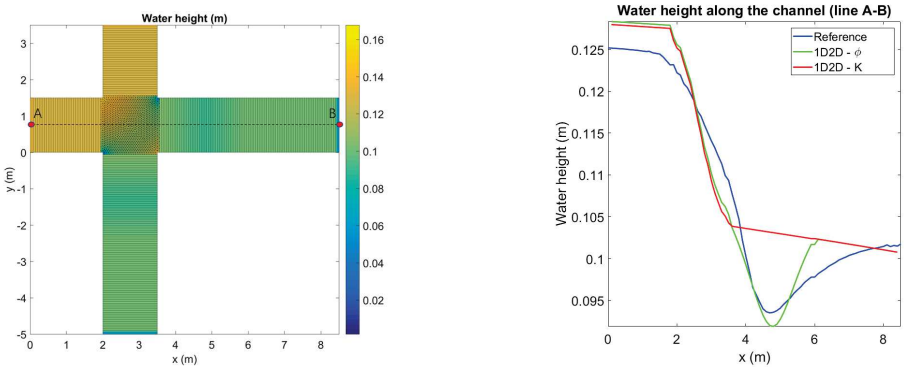

Figure 3. Four branches crossroad modeling. Left: Map of the steady state water depth simulated using the proposed *Flood1D2D* model with K and ϕ; equal inflow discharge $Q = 0.075\text{m}^3.\text{s}^{-1}$ in the north and west streets, rating curve as a the downstream boundary condition on west and south streets. Right: water depth profile using various modeling approaches.

3 Discussion: *Flood1D2D* response surface

As illustrated in section 2.3.2 : adding the new ϕ parameterization allows reproducing, at the local scale, realistic contracted flow profiles whereas K alone not. Does improving locally these simulated flow features improves global scale hydrodynamics forecasts? The sensitivity of *Flood1D2D* is thus compared on a crossroads network (see section 3.1) with two different parameterizations: a first one with no porosity and a spatially varied Strickler coefficient and a second one with a uniform Strickler coefficient and a spatially varied porosity in each street.

3.1 Modeled crossroads network

The sensitivity of *Flood1D2D* is determined on a sub-part of the 'ICUBE Urban flood experimental rig' developped in Strasbourg [10].

The sub-part chosen includes four crossroads with streets of various widths and orientations. A set of experimental data allows knowing the discharge and the water depth patterns in each street.

The network is modeled using a 1D/2D structured mesh with a discretization step $\Delta x = 0.025$m (see figure 4). The boundary conditions are set to upstream discharge in streets E, F, 3 and 4 (corresponding to the experimental values) and rating curves computed for each downstream end. In every configuration, the simulation is run during 1000s to ensure steady state flow over the whole domain.

3.2 4.1 - SW Characterization in K_{street} / K_{cross}

The model is parameterized using two uniform values of the Strickler coefficient: K_{street} in streets and K_{cross} in crossroads. Each parameter is taken in the set of value [25, 50, 75, 100, 125, 150] and all combinations are tested. The street outlet discharge is

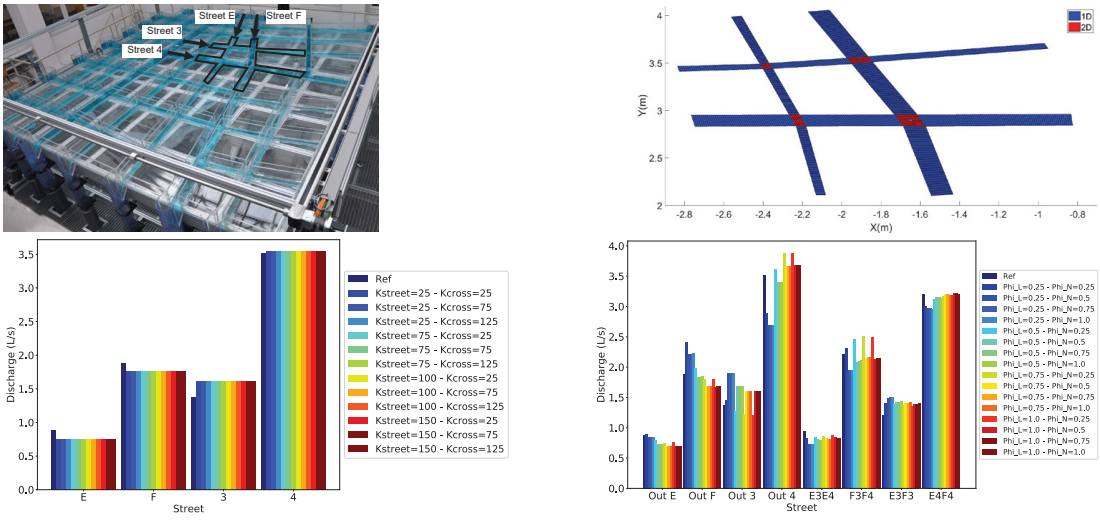

Figure 4. Crossroad network sensitivity analysis. Top left: experimental rig and illustration of the modeled zone; top right: 1D/2D mesh; bottom left: outlet discharge sensitivity to a parameterization with K_{street} and K_{cross}; bottom right: outlet and street discharge sensitivity to a parameterization with $\phi_{r,n}$ and $\phi_{r,l}$. For the sake of clarity, only some simulation results have been plotted.

compared to the experimental value on figure 4. For each street, the first bar corresponds to the experimental value. Whatever the parameterization of the model, each discharge flowing out from streets E and F (resp. 3 and 4) is systematically under- (resp. over-) estimated. Interestingly, K_{street} seems to impose an averaged street discharge value (look for instance the shift in the outlet discharge for street F when K_{street} varies from 25 to 50). K_{cross} has a smaller impact on outflow discharge repartition (with always the same trend around the value imposed by K_{street}).

3.3 SW Parameterization in K_{unif} / ϕ_{large} / ϕ_{narrow}

The model is parameterized using a uniform value of the roughness coefficient $K = 75\text{m}^{1/3}.\text{s}^{-1}$ since few sensitivity to K_{cross} is found in the previous spatialization. A distributed porosity is defined for all streets downstream of crossroads following a parabolic profile:

$$\phi(s) = \begin{cases} as^2 + bs + c \text{ for } 0 \leq s \leq 0.5 \quad \text{with } \phi(0) = \phi(1/2) = 1 \quad \text{and} \quad \phi(1/4) = \phi_r \\ 1 \text{ elsewhere} \end{cases} \tag{6}$$

where s is the adimensional curvilinear abscissa (0 (resp. 1) at the upstream (resp. downstream) end of each street).

The model is parameterized, by adjusting a, b and c, with two values of ϕ_r: ϕ_r, l in large streets (F and 4) and ϕ_r, n in narrow streets (E and 3). In order to sample *Flood1D2D* response surface, all the combinations of values of ϕ_r, l and ϕ_r, n in [0.25, 0.50, 0.75, 1.00] are tested.

The outlet street discharges and those in the four streets between crossroads are compared to the experimental values on figure 4. For each street, the first bar corresponds to the experimental value.

For each street and all parameter sets tested, there are both under and over estimations of street outlet discharge which was not possible with roughness only. Despite the sparse sampling of this wide parameter space, the spread of model response quite centered around

discharge measurements suggests that there may exist parameter sets reproducing those values. It clearly shows the ability of the proposed model and parameterization to model various non monotonous flow patterns and potentially realistic local discharge and global discharge distributions. The issues related to the calibration of spatially distributed K and ϕ parameters should be further studied, especially equifinality problems in the light of their influence on discharge repartition at large scale in branched networks.

4 Conclusion

This study introduced a new 1D/2D SW model dedicated to effective and computationally affordable urban floods modeling, in view for example of operational use. Its structure and parsimonious parameterization is based on empirical observations and aims at reproducing effectively local and global flow physics.

The proposed *Flood1D2D* model is successfully validated on a complex unsteady dambreak case in a channel including a sharp bend and also on a four branch crossroad including porosity. It is shown that a classical 1D/2D SW model parameterized with roughness only fails to account for free surface deformations due to flow vein contraction downstream of a crossroad. The ability of the new model to reproduce realistic discharge distributions at larger scale is also tested on a part of the branched network of ICUBE experimental rig. Further studies should tackle:

- The problem of calibrating spatially distributed K and ϕ parameters along with their influence on simulated flow variables at the (local) street and crossroad scales and on the discharge repartition at the district and city scales
- The benefit of such a parsimonious parameterization in reducing parametric equifinality problems
- Unsteady parameterizations in order to extend model applicability to very transient flooding events.

References

[1] P. Finaud-Guyot, C. Delenne, V. Guinot, C. Llovel, Comptes Rendus Mécanique **339**, 226 (2011)
[2] P. Finaud-Guyot, C. Delenne, J. Lhomme, V. Guinot, C. Llovel, International Journal for Numerical Methods in Fluids **62**, 1299 (2010)
[3] V. Guinot, Advances in Water Resources **37**, 40 (2012)
[4] Q. Araud, phdthesis, Université de Strasbourg (2012)
[5] J.L. Best, I. Reid, Journal of Hydraulic Engineering **110**, 1588 (1984)
[6] E. Mignot, N. Rivière, R.J. Perkins, A. Paquier, Journal of Hydraulic Engineering **134**, 701 (2008)
[7] S. Chen, Ph.D. thesis, Université de Strasbourg (2018)
[8] E.H. Taylor, Transactions of the American Society of Civil Engineers **109**, 893 (1944)
[9] N. Rivière, G. Travin, R.J. Perkins, Water Resour. Res. **47**, W10517 (2011)
[10] P. Finaud-Guyot, P.A. Garambois, Q. Araud, F. Lawniczak, P. François, J. Vazquez, R. Mosé, Urban Water Journal (2018)
[11] J. Lhomme, Ph.D. thesis, Montpellier 2 university (2006)
[12] P. Finaud-Guyot, phdthesis, Université Montpellier II - Sciences et Techniques du Languedoc (2009)
[13] S. Soares-Frazao, Y. Zech, Journal of Hydraulic Engineering **128(11)**, 956 (2002)

INTERNATIONAL JOURNAL FOR NUMERICAL METHODS IN FLUIDS
Int. J. Numer. Meth. Fluids (2010)
Published online in Wiley Online Library (wileyonlinelibrary.com). DOI: 10.1002/fld.2398

Sensitivity of the 1D shallow water equations with source terms: Solution method for discontinuous flows

C. Delenne*, †, P. Finaud-Guyot, V. Guinot and B. Cappelaere

HydroSciences Montpellier, UMR 5569 (UM1, UM2, CNRS, IRD), Université Montpellier 2 CCMSE, Eugène Bataillon, Montpellier 34095, France

SUMMARY

A finite volume-based numerical technique is presented concerning the sensitivity of the solution of the one-dimensional Shallow Water Equations with scalar transport. An approximate Riemann solver is proposed for direct sensitivity calculation even in the presence of discontinuous solutions. The Shallow Water Sensitivity Equations are first derived as well as the expressions of the sensitivity source terms, initial and boundary conditions. The numerical technique is then detailed and application examples are provided to assess the method's efficiency in estimating the sensitivity to different parameters (friction coefficient and initial and boundary conditions). The application of the dam-break problem to a trapezoidal channel is also provided. The comparison with the analytical solution and the classical empirical approach illustrates the usefulness of the direct sensitivity calculation. Copyright © 2010 John Wiley & Sons, Ltd.

Received 26 August 2009; Revised 24 June 2010; Accepted 25 June 2010

KEY WORDS: shallow water equations; sensitivity; finite volume; Riemann solver; source terms; initial and boundary conditions

1. INTRODUCTION

The assessment of the sensitivity of a model output to different parameters is a key step in the optimization of model performance, since it can be used to define the relevant parameters for the calibration procedures. Sensitivity analysis is thus seen by some authors [1] as a prerequisite for model building and exploitation, in any scientific discipline where models are used. In shallow water modelling, sensitivity analysis may be used to determine how the response of the model is affected by changes in topography, boundary or initial conditions, or in any physical parameter such as the friction coefficient [2].

The sensitivity of a model output (called variable hereafter) to a given parameter is usually defined as the partial derivative of this variable with respect to the parameter. This derivative can be computed using either a discrete or a continuous approach. In the discrete approach, the governing equations for the model variables are first solved numerically and the results are then differentiated with respect to the parameter of interest. Typically, the classical empirical (or finite difference) approach consists in performing two simulations with two slightly different values of the parameter of interest and computing the difference between both results, normalized by the parameter variation. An example of another efficient approach, known as complex differentiation, can be found in [3]. These methods are best-suited to the analysis of complex models dealing with complex geometries, or to the analysis of model response, where the transfer function between

*Correspondence to: C. Delenne, HydroSciences Montpellier, UMR 5569 (UM1, UM2, CNRS, IRD), Université Montpellier 2 CCMSE, Eugène Bataillon, Montpellier 34095, France.
†E-mail: delenne@msem.univ-montp2.fr

the model inputs and outputs is not known exactly. Continuous approaches can be used when the governing equations for the model are known. Differentiating these equations with respect to the parameter of interest leads to the sensitivity equations, that can be solved analytically or numerically.

Both the discrete and continuous approaches, however, use the assumption that the solution of the governing equations is continuous and differentiable with respect to the parameter. They meet problems when the model output becomes discontinuous [4]. This is the case, for example, of the solutions of the shallow water equations (SWEs) in the presence of hydraulic jumps or moving bores. The non-differentiable character of the flow solution yields locally infinite sensitivity values across discontinuities. A sensitivity source term, in the form of a Dirac function, can be introduced at shocks locations to avoid this kind of behaviour [5]. This approach was acknowledged for scalar hyperbolic problems using a different reasoning in [6] and applied to design numerical methods for hyperbolic systems of conservation laws (HSCL) [7, 8]. In these papers however, the solutions proposed for the accurate discretization of the Dirac source term in the framework of shock-capturing numerical methods prove not to be entirely satisfactory in a number of cases [8].

The purpose of this paper is to present a finite volume-based numerical technique for the sensitivity analysis of the one-dimensional SWEs with scalar transport in the continuous and discontinuous cases. The difficulties encountered in the previous papers for the treatment of the Dirac source term have been overcome here.

The SWEs and the derivation of the Shallow Water Sensitivity Equations (SWSEs) are presented in Section 2 and the expressions of the sensitivity source term, initial and boundary conditions are derived. Section 3 is devoted to the detailed presentation of the numerical technique for discontinuous solutions, with a focus on source term and boundary condition discretization. Application examples are provided in Section 4 concerning the sensitivity analysis to Manning's friction coefficient, and to initial and boundary conditions in a rectangular channel. An application to a trapezoidal channel is also provided. Section 5 is devoted to concluding remarks.

2. GOVERNING EQUATIONS

2.1. The sensitivity equations

The development of the sensitivity equations is illustrated using the one-dimensional SWEs with passive scalar transport. These equations form a 3×3 HSCL, where the first two equations account for mass and momentum conservation and the third one is a scalar transport equation. They can be written in vector form as

$$\frac{\partial \mathbf{U}}{\partial t}+\frac{\partial \mathbf{F}}{\partial x}=\mathbf{S} \tag{1a}$$

$$\mathbf{U}(x,0)=\mathbf{U}_0(x) \tag{1b}$$

$$\mathbf{U}(x_\mathrm{b},t)=\mathbf{U}_\mathrm{b}(t) \tag{1c}$$

where $\mathbf{U}$ is the vector of the conserved variables, $\mathbf{F}$ the flux vector and $\mathbf{S}$ the source term; the subscript b denotes the domain boundary and the subscript 0 the initial condition. $\mathbf{U}$, $\mathbf{F}$, and $\mathbf{S}$ are defined as

$$\mathbf{U}=\begin{pmatrix} h \\ hu \\ hv \end{pmatrix}=\begin{pmatrix} h \\ q \\ r \end{pmatrix},\quad \mathbf{F}=\begin{pmatrix} q \\ q^2/h+gh^2/2 \\ qv \end{pmatrix},\quad \mathbf{S}=\begin{pmatrix} 0 \\ gh\,(S_0-S_\mathrm{f}) \\ 0 \end{pmatrix} \tag{2}$$

where g is the gravitational acceleration, h the water depth, u the flow velocity ($q=hu$ the unit discharge), $S_0=-\partial z_\mathrm{b}/\partial x$ the bottom slope (with z_b the bottom elevation), S_f the friction slope (defined in Section 2.3) and v can be any variable subjected to passive scalar transport (for example,

DOI: 10.1002/fld

v can be the concentration of a pollutant in $\mathrm{kg\,s^{-1}}$ and $r=hv$, the conserved quantity of pollutant in the flow).

The flux function $\mathbf{F}$ and the source term $\mathbf{S}$ defined in Equation (2) depend on the flow solution $\mathbf{U}$ and on several parameters, such as the gravitational acceleration, the friction coefficient n_{M}, the initial and/or boundary conditions, etc. The notation $\mathbf{F}(\mathbf{U},\psi)$ and $\mathbf{S}(\mathbf{U},\psi)$ is used in the following, where ψ denotes any of the parameters on which $\mathbf{F}$ and $\mathbf{S}$ may depend. A sensitivity analysis with respect to a given parameter ψ consists in studying the influence of a small variation in this parameter on the solution of the flow equations. The governing equations for the sensitivity (called sensitivity equations hereafter) are obtained by differentiating the flow equation (1a) with respect to the parameter ψ.

The parameter ψ is perturbed by a function $\tilde{\psi}(x,t)$ that is non-zero only on a sub-domain of the problem domain and defined as

$$\tilde{\psi}(x,t)=\psi_0\varepsilon(x,t) \tag{3}$$

where $\varepsilon(x,t)$ is the so-called perturbation indicator, with $\varepsilon=0$ in the regions where the parameter remains unchanged and $\varepsilon=1$ in the regions where ψ is modified for the purpose of the sensitivity analysis. Perturbing ψ yields a perturbation $\tilde{\mathbf{U}}$ in the solution $\mathbf{U}$ of (1a):

$$\frac{\partial(\mathbf{U}+\tilde{\mathbf{U}})}{\partial t}+\frac{\partial\mathbf{F}(\mathbf{U}+\tilde{\mathbf{U}},\psi+\tilde{\psi})}{\partial x}=\mathbf{S}(\mathbf{U}+\tilde{\mathbf{U}},\psi+\tilde{\psi}) \tag{4}$$

The sensitivity $\mathbf{s}$ of $\mathbf{U}$ to ψ is defined as the partial derivative of $\mathbf{U}$ with respect to ψ

$$\mathbf{s}\equiv\frac{\partial\mathbf{U}}{\partial\psi}=\lim_{\psi_0\to 0}\frac{\tilde{\mathbf{U}}}{\psi_0} \tag{5}$$

Subtracting Equation (1a) from (4) and using a first-order Taylor series expansion in the limit of small $\tilde{\psi}$ and $\tilde{\mathbf{U}}$ yields

$$\frac{\partial\tilde{\mathbf{U}}}{\partial t}+\frac{\partial}{\partial x}\left(\frac{\partial\mathbf{F}}{\partial\psi}\tilde{\psi}+\frac{\partial\mathbf{F}}{\partial\mathbf{U}}\tilde{\mathbf{U}}\right)=\frac{\partial\mathbf{S}}{\partial\psi}\tilde{\psi}+\frac{\partial\mathbf{S}}{\partial\mathbf{U}}\tilde{\mathbf{U}} \tag{6}$$

Substituting Equations (3) and (5) into (6) and simplifying by ψ_0 leads to the following partial differential equation in $\mathbf{s}$

$$\frac{\partial\mathbf{s}}{\partial t}+\frac{\partial}{\partial x}\left(\frac{\partial\mathbf{F}}{\partial\mathbf{U}}\mathbf{s}\right)=\frac{\partial\mathbf{S}}{\partial\mathbf{U}}\mathbf{s}+\frac{\partial\mathbf{S}}{\partial\psi}\varepsilon-\frac{\partial}{\partial x}\left(\frac{\partial\mathbf{F}}{\partial\psi}\varepsilon\right) \tag{7}$$

Equation (7) is rewritten as

$$\frac{\partial\mathbf{s}}{\partial t}+\frac{\partial\mathbf{G}}{\partial x}=\mathbf{Q} \tag{8a}$$

$$\mathbf{s}=\begin{pmatrix}\eta\\ \theta\\ \rho\end{pmatrix}\equiv\begin{pmatrix}\partial h/\partial\psi\\ \partial q/\partial\psi\\ \partial r/\partial\psi\end{pmatrix} \tag{8b}$$

$$\mathbf{G}=\frac{\partial\mathbf{F}}{\partial\mathbf{U}}\mathbf{s}=\begin{pmatrix}0 & 1 & 0\\ c^2-u^2 & 2u & 0\\ -uv & v & u\end{pmatrix}\mathbf{s}=\begin{pmatrix}\theta\\ (c^2-u^2)\eta+2u\theta\\ -uv\eta+\theta v+u\rho\end{pmatrix} \tag{8c}$$

$$\mathbf{Q}=\frac{\partial\mathbf{S}}{\partial\mathbf{U}}\mathbf{s}+\frac{\partial\mathbf{S}}{\partial\psi}\varepsilon-\frac{\partial}{\partial x}\left(\frac{\partial\mathbf{F}}{\partial\psi}\varepsilon\right) \tag{8d}$$

DOI: 10.1002/fld

where $c=(gh)^{1/2}$ is the propagation speed of the waves in the fluid at rest. Equations (8) are the conservation form of the Shallow Water Sensitivity Equations (SWSEs). The source term $\mathbf{Q}$ defined in Equation (8d) is the only one that depends on the nature of the parameter ψ; its expression is given in Sections 2.3–2.5 (after the treatment of discontinuous solutions).

2.2. Sensitivity equations for discontinuous flow problems

The sensitivity partial derivative equation (8a) is derived using the assumption that the flow solution $\mathbf{U}$ is continuous and differentiable with respect to the parameter ψ over the solution domain. Discontinuous solutions (e.g. shocks such as hydraulic jumps, moving bores, etc.) are not differentiable with respect to the parameter ψ in the general case and the governing equations must be modified so as to account for extra terms in the balance equations (see [5–8]). Indeed, consider a shock moving at a speed c_s with left- and right-hand values $\mathbf{U}_L$ and $\mathbf{U}_R$ for the flow variable $\mathbf{U}$ and left- and right-hand values $\mathbf{s}_L$ and $\mathbf{s}_R$ for the sensitivity $\mathbf{s}$; applying the so-called Rankine–Hugoniot conditions (or jump relationship) to a control volume that contains the shock leads to the following equality for the flow variables:

$$(\mathbf{U}_L-\mathbf{U}_R)c_s=\mathbf{F}_L-\mathbf{F}_R \tag{9}$$

The jump relationship for the sensitivity variables is more complex. As shown in [5] and generalized in [6, 8] for a non-uniform perturbation indicator ε, the perturbation $\tilde{\psi}$ yields variations $\tilde{\mathbf{U}}_L$ and $\tilde{\mathbf{U}}_R$ in the values of $\mathbf{U}_L$ and $\mathbf{U}_R$, respectively. This also causes a variation $\tilde{c}_s$ in the speed c_s of the shock, and consequently, the shock abscissa x_s is subject to a change $\tilde{x}_s$. The perturbed values of $\mathbf{U}$ and $\mathbf{F}$ on the left- and right-hand side of the shock are then given by

$$\mathbf{U}_L^{(P)}=\mathbf{U}_L+\tilde{\mathbf{U}}_L+\tilde{x}_s\frac{\partial \mathbf{U}_L}{\partial x} \tag{10a}$$

$$\mathbf{U}_R^{(P)}=\mathbf{U}_R+\tilde{\mathbf{U}}_R+\tilde{x}_s\frac{\partial \mathbf{U}_R}{\partial x} \tag{10b}$$

$$\mathbf{F}_L^{(P)}=\mathbf{F}_L+\tilde{\mathbf{F}}_L+\tilde{x}_s\frac{\partial \mathbf{F}_L}{\partial x} \tag{10c}$$

$$\mathbf{F}_R^{(P)}=\mathbf{F}_R+\tilde{\mathbf{F}}_R+\tilde{x}_s\frac{\partial \mathbf{F}_R}{\partial x} \tag{10d}$$

where the superscripts (P) and (x), respectively, denote the perturbed value and the derivative with respect to space of the variable of concern. The jump relationship (9) then becomes

$$(\mathbf{U}_L^{(P)}-\mathbf{U}_R^{(P)})(c_s+\tilde{c}_s)=\mathbf{F}_L^{(P)}-\mathbf{F}_R^{(P)} \tag{11}$$

Substituting (10) into (11) yields

$$\begin{aligned}&\left[\mathbf{U}_L+\tilde{\mathbf{U}}_L+\tilde{x}_s\frac{\partial \mathbf{U}_L}{\partial x}-\left(\mathbf{U}_R+\tilde{\mathbf{U}}_R+\tilde{x}_s\frac{\partial \mathbf{U}_R}{\partial x}\right)\right](c_s+\tilde{c}_s)\\ &\quad=\mathbf{F}_L+\tilde{\mathbf{F}}_L+\tilde{x}_s\frac{\partial \mathbf{F}_L}{\partial x}-\left(\mathbf{F}_R+\tilde{\mathbf{F}}_R+\tilde{x}_s\frac{\partial \mathbf{F}_R}{\partial x}\right)\end{aligned} \tag{12}$$

Subtracting (9) from (12) and retaining only the first-order terms (in the limit of small $\tilde{c}_s$, $\tilde{x}_s$ and $\tilde{\mathbf{U}}$) yields

$$(\mathbf{U}_L-\mathbf{U}_R)\tilde{c}_s+(\tilde{\mathbf{U}}_L-\tilde{\mathbf{U}}_R)c_s+\tilde{x}_s\frac{\partial}{\partial x}(\mathbf{U}_L-\mathbf{U}_R)c_s=\tilde{\mathbf{F}}_L-\tilde{\mathbf{F}}_R+\tilde{x}_s\frac{\partial}{\partial x}(\mathbf{F}_L-\mathbf{F}_R) \tag{13}$$

DOI: 10.1002/fld

Noticing that

$$\tilde{\mathbf{U}} = \psi_0 \mathbf{s} \tag{14a}$$

$$\tilde{\mathbf{F}} = \psi_0 \mathbf{G} + (\partial \mathbf{F}/\partial \psi)\varepsilon\psi_0 \tag{14b}$$

$$\tilde{x_s} = (\partial x_s/\partial \psi)\psi_0 \tag{14c}$$

$$\tilde{c_s} = (\partial c_s/\partial \psi)\psi_0 \tag{14d}$$

and simplifying by ψ_0, the complete jump relationship for the sensitivity can be written as:

$$\begin{aligned}(\mathbf{s}_L - \mathbf{s}_R)c_s = \mathbf{G}_L - \mathbf{G}_R - \frac{\partial c_s}{\partial \psi}(\mathbf{U}_L - \mathbf{U}_R) - \frac{\partial x_s}{\partial \psi}\left[\left(\frac{\partial \mathbf{U}}{\partial x}\right)_L - \left(\frac{\partial \mathbf{U}}{\partial x}\right)_R\right]c_s \\ + \left(\frac{\partial \mathbf{F}}{\partial \psi}\varepsilon\right)_L - \left(\frac{\partial \mathbf{F}}{\partial \psi}\varepsilon\right)_R + \frac{\partial x_s}{\partial \psi}\left[\left(\frac{\partial \mathbf{F}}{\partial x}\right)_L - \left(\frac{\partial \mathbf{F}}{\partial x}\right)_R\right]\end{aligned} \tag{15}$$

The following notation is used for the additional term in (15)

$$\begin{aligned}\mathbf{R} = -\frac{\partial c_s}{\partial \psi}(\mathbf{U}_L - \mathbf{U}_R) - \frac{\partial x_s}{\partial \psi}\left[\left(\frac{\partial \mathbf{U}}{\partial x}\right)_L - \left(\frac{\partial \mathbf{U}}{\partial x}\right)_R\right]c_s \\ + \left(\frac{\partial \mathbf{F}}{\partial \psi}\varepsilon\right)_L - \left(\frac{\partial \mathbf{F}}{\partial \psi}\varepsilon\right)_R + \frac{\partial x_s}{\partial \psi}\left[\left(\frac{\partial \mathbf{F}}{\partial x}\right)_L - \left(\frac{\partial \mathbf{F}}{\partial x}\right)_R\right]\end{aligned} \tag{16}$$

Note that this rather complex expression can be simplified in the case of the solution of the Riemann problem (see Section 3.2). This source term being non-zero only at points where $\mathbf{U}$ is discontinuous, Equation (8a) can be rewritten for continuous and discontinuous solutions

$$\frac{\partial \mathbf{s}}{\partial t} + \frac{\partial \mathbf{G}}{\partial x} = \mathbf{Q} + \mathbf{R}\delta_s \tag{17}$$

where δ_s denotes the Dirac distribution located at the shock. The only term in (17) that depends on the nature of the parameter ψ is the source term $\mathbf{Q}$ defined by Equation (8d). In the following subsections, the expression of $\mathbf{Q}$ is provided for the sensitivity to the friction coefficient and to the initial and boundaries conditions.

2.3. Sensitivity to the friction coefficient

In what follows, the friction slope is assumed to obey a classical Manning–Strickler law under the wide channel approximation

$$S_f = q|q|n_M^2 h^{-10/3} \tag{18}$$

where n_M is Manning's friction coefficient. The expression of $\mathbf{Q}$ can be derived for the particular case where the parameter $\psi = n_M$. Since $\mathbf{F}$ is not a function of n_M, $\partial \mathbf{F}/\partial \psi = 0$ and

$$\mathbf{Q} = \frac{\partial \mathbf{S}}{\partial \mathbf{U}}\mathbf{s} + \frac{\partial \mathbf{S}}{\partial \psi}\varepsilon_{n_M} \tag{19}$$

with

$$\frac{\partial \mathbf{S}}{\partial \mathbf{U}}\mathbf{s} = \begin{pmatrix} 0 \\ g(S_0 + 7/3S_f)\eta - 2gn_M^2|q|h^{-7/3}\theta \\ 0 \end{pmatrix} \tag{20}$$

DOI: 10.1002/fld

and

$$\frac{\partial \mathbf{S}}{\partial \psi}\varepsilon_{n_\mathrm{M}} = \begin{pmatrix} 0 \\ -2gh\dfrac{S_\mathrm{f}}{n_\mathrm{M}}\varepsilon_{n_\mathrm{M}} \\ 0 \end{pmatrix} \tag{21}$$

where $\varepsilon_{n_\mathrm{M}} = 0$ in regions where the friction coefficient is unchanged and $\varepsilon_{n_\mathrm{M}} = 1$ in the regions where it is perturbed for the sensitivity analysis.

2.4. Sensitivity to initial conditions

The sensitivity to the initial conditions is studied by defining ψ as one of the flow variables (h, q, or r) at $t = 0$. Considering the sensitivity to the initial conditions yields

$$\varepsilon(x,t) = 0 \quad \forall t > 0 \tag{22}$$

The expression of $\mathbf{Q}$ then reduces to the term $(\partial \mathbf{S}/\partial \mathbf{U})\mathbf{s}$ defined by (20). The initial condition for the SWSEs (8) is given by

$$\mathbf{s}(x,0) = \begin{pmatrix} \varepsilon_h \\ \varepsilon_q \\ \varepsilon_\mathrm{r} \end{pmatrix} \tag{23}$$

where ε_h, ε_q and ε_r are the perturbation indicators, respectively, for $h(x,0)$, $q(x,0)$ and $r(x,0)$. Assume for instance that a dam-break problem [9] is to be solved for the following initial conditions:

$$h(x,0) = \begin{cases} h_\mathrm{L} & \text{for } x < x_0 \\ h_\mathrm{R} & \text{for } x \geqslant x_0 \end{cases} \tag{24a}$$

$$q(x,0) = 0 \quad \forall x \tag{24b}$$

$$r(x,0) = 0 \quad \forall x \tag{24c}$$

where x_0 is the abscissa of the dam. Assume that the purpose of the analysis is to study the sensitivity of the flow solution to the water depth h_L on the left-hand side of the dam. Then the perturbation indicators in (23) must be defined as:

$$\varepsilon_h(x,0) = \begin{cases} 1 & \text{for } x < x_0 \\ 0 & \text{for } x \geqslant x_0 \end{cases} \tag{25a}$$

$$\varepsilon_q(x,0) = 0 \quad \forall x \tag{25b}$$

$$\varepsilon_\mathrm{r}(x,0) = 0 \quad \forall x \tag{25c}$$

2.5. Boundary conditions

Boundary conditions for the flow are relationships in the form

$$f_i(\mathbf{U}, \psi, t) = 0 \tag{26}$$

As shown in [10], as many boundary conditions f_i must be supplied at a given boundary as there are characteristics entering the domain. It stems from Equation (8c) that the Jacobian matrix $\partial \mathbf{G}/\partial \mathbf{s}$ for the sensitivity is identical to the Jacobian matrix $\partial \mathbf{F}/\partial \mathbf{U}$ for the original flow problem. Consequently, the characteristics for the sensitivity problem are identical to the characteristics for

DOI: 10.1002/fld

the flow problem and the sensitivity problem requires as many boundary conditions as the original flow problem. These conditions are obtained by differentiating Equation (26) with respect to ψ

$$\frac{\mathrm{d}f_i}{\mathrm{d}\psi}=\frac{\partial f_i}{\partial h}\eta+\frac{\partial f_i}{\partial q}\theta+\frac{\partial f_i}{\partial r}\rho \tag{27}$$

Two main situations may occur:

1. The sensitivity analysis is carried out with respect to the initial conditions or to a hydrodynamic parameter. In this case, the boundary conditions are not influenced by the value of ψ and Equation (27) becomes

$$\frac{\partial f_i}{\partial h}\eta+\frac{\partial f_i}{\partial q}\theta+\frac{\partial f_i}{\partial r}\rho=0 \tag{28}$$

2. The sensitivity analysis is carried out with respect to the boundary condition. This is the case, for instance, when the numerical value of the boundary condition to be prescribed is not known with certainty, or measured with a certain imprecision. For example, assuming that a known water depth h_b is to be prescribed at a boundary, (26) becomes

$$f=h-h_\mathrm{b}=0 \tag{29}$$

Applying (27) with $\psi=h_\mathrm{b}$ yields the following sensitivity boundary condition:

$$\eta=1 \tag{30}$$

For a prescribed unit discharge q_b, $f=q-q_\mathrm{b}=0$ and the sensitivity boundary condition is

$$\theta=1 \tag{31}$$

and for a prescribed quantity of the transported variable, $f=r-r_\mathrm{b}=0$ and

$$\rho=1 \tag{32}$$

3. NUMERICAL TECHNIQUE

This section deals with the numerical technique developed to solve the SWSEs. The finite volume discretization is briefly recalled in Section 3.1, then the fluxes calculation using the Riemann problem is detailed in Section 3.2. Section 3.3 is devoted to source terms calculation in the continuous case and Section 3.4 to shock detection and to the calculation of the specific source term $\mathbf{R}$. Section 3.5 describes the discretization of boundary conditions.

3.1. Finite volume discretization

The flow and sensitivity equations (Equations (1a) and (17)) are discretized using a finite volume formulation:

$$\mathbf{U}_i^{n+1}=\mathbf{U}_i^n-\frac{\Delta t}{\Delta x_i}(\mathbf{F}_{i-1/2}^{n+1/2}-\mathbf{F}_{i+1/2}^{n+1/2})+\Delta t\mathbf{S}_i^{n+1/2} \tag{33a}$$

$$\mathbf{s}_i^{n+1}=\mathbf{s}_i^n-\frac{\Delta t}{\Delta x_i}(\mathbf{G}_{i-1/2}^{n+1/2}-\mathbf{G}_{i+1/2}^{n+1/2}+\mathbf{R}_{i-1/2}^{n+1/2}+\mathbf{R}_{i+1/2}^{n+1/2})+\Delta t\mathbf{Q}_i^{n+1/2} \tag{33b}$$

where Δt is the computational time step, Δx_i is the width of the cell i, $\mathbf{U}_i^n$ and $\mathbf{s}_i^n$ are, respectively, the average value of $\mathbf{U}$ and $\mathbf{s}$ over the cell i at the time level n, $\mathbf{F}_{i-1/2}^{n+1/2}$ and $\mathbf{G}_{i-1/2}^{n+1/2}$ are the average values of the fluxes $\mathbf{F}$ and $\mathbf{G}$ through the interface $i-1/2$ (between the cells $i-1$ and i) between the time levels n and $n+1$, $\mathbf{S}_i^{n+1/2}$ and $\mathbf{Q}_i^{n+1/2}$ are the average values of $\mathbf{S}$ and $\mathbf{Q}$ over the cell i between the time levels n and $n+1$, $\mathbf{R}_{i-1/2}^{n+1/2}$ (resp $\mathbf{R}_{i+1/2}^{n+1/2}$) is the contribution of the Dirac source terms possibly generated by shocks propagating from the cell $i-1$ into the cell i (resp. i into $i+1$) between time levels n and $n+1$.

DOI: 10.1002/fld

3.2. Fluxes calculation

The fluxes **F** and **G** in Equation (33) can be computed by solving Riemann problems. However, the Riemann problem for the sensitivity cannot be considered independently from the one for the flow variable, because the Jacobian matrix $\partial\mathbf{F}/\partial\mathbf{U}$ (used in the definition of **G**, Equation (8c)) depends on the flow solution **U**. A single Riemann problem is thus defined for the hyperbolic part of the governing equations (1a) and (8a) at a given interface $i+1/2$ (between cells i and $i+1$)

$$\frac{\partial\mathbf{U}}{\partial t}+\frac{\partial\mathbf{F}}{\partial x}=0 \tag{34a}$$

$$\frac{\partial\mathbf{s}}{\partial t}+\frac{\partial\mathbf{G}}{\partial x}=\mathbf{R}\delta_{\mathrm{s}} \tag{34b}$$

$$(\mathbf{U},\mathbf{s})(x,0)=\begin{cases}(\mathbf{U}_{\mathrm{L}},\mathbf{s}_{\mathrm{L}}) & \text{for } x<x_{i+1/2}\\ (\mathbf{U}_{\mathrm{R}},\mathbf{s}_{\mathrm{R}}) & \text{for } x\geqslant x_{i+1/2}\end{cases} \tag{34c}$$

where $x_{i+1/2}$ is the abscissa of the interface. These equations stem from (1) and (17), where **U** and **F** are constant on both sides of the discontinuity and where no source term is considered (i.e. **S** and **Q** are nil). In this case, the x-derivatives vanish in the expression of **R**, Equation (16), as well as the terms in $(\partial\mathbf{F}/\partial\psi)\varepsilon$ (as a consequence of $\mathbf{Q}=0$ in Equation (8d)) leading to the following simplification:

$$\mathbf{R}=-\frac{\partial c_{\mathrm{s}}}{\partial\psi}(\mathbf{U}_{\mathrm{L}}-\mathbf{U}_{\mathrm{R}}) \tag{35}$$

The two corresponding 3×3 HSCLs defined by Equations (1a) and (17) have the same eigenvalues. These three eigenvalues are real and distinct

$$\begin{pmatrix}\lambda^{(1)}\\ \lambda^{(2)}\\ \lambda^{(3)}\end{pmatrix}=\begin{pmatrix}u-c\\ u\\ u+c\end{pmatrix} \tag{36}$$

The general solution of the Riemann problem for the flow solution is known to be made of three waves separating two internal regions of constant state from the left and right states of the Riemann problem. The HLL/HLLC Riemann solver [11, 12] is based on the *a priori* assumption that the first and third waves ($\mathrm{d}x/\mathrm{d}t=\lambda^{(1)}$ and $\mathrm{d}x/\mathrm{d}t=\lambda^{(3)}$) are discontinuities. The exact nature of such discontinuities (shocks or contact discontinuities), as well as whether such waves satisfy the entropy condition, does not need to be known in the solution process. The second wave ($\mathrm{d}x/\mathrm{d}t=\lambda^{(2)}$) is a contact wave. The fluxes are computed using the original HLLC Riemann solver for the flow problem and a modified HLLC solver for the sensitivity problem.

Using an *a priori* approximation λ^{-} (resp. λ^{+}) of $\lambda^{(1)}$ (resp. $\lambda^{(3)}$) allows the Rankine–Hugoniot conditions to be written, for the first two components of (1a), as

$$(\mathbf{U}_{\mathrm{L}}-\mathbf{U}_{*})\lambda^{-}=\mathbf{F}_{\mathrm{L}}-\mathbf{F}_{*} \tag{37a}$$

$$(\mathbf{U}_{\mathrm{R}}-\mathbf{U}_{*})\lambda^{+}=\mathbf{F}_{\mathrm{R}}-\mathbf{F}_{*} \tag{37b}$$

where the subscript $_{*}$ indicates the value of the variable **U** and the flux **F** in the intermediate region of constant state. Solving Equation (37) for $\mathbf{U}_{*}$ and $\mathbf{F}_{*}$ yields

$$\mathbf{U}_{*}=\frac{-\lambda^{-}\mathbf{U}_{\mathrm{L}}+\lambda^{+}\mathbf{U}_{\mathrm{R}}+\mathbf{F}_{\mathrm{L}}-\mathbf{F}_{\mathrm{R}}}{\lambda^{+}-\lambda^{-}} \tag{38}$$

$$\mathbf{F}_{*}=\frac{\lambda^{+}\mathbf{F}_{\mathrm{L}}-\lambda^{-}\mathbf{F}_{\mathrm{R}}-\lambda^{-}\lambda^{+}(\mathbf{U}_{\mathrm{L}}-\mathbf{U}_{\mathrm{R}})}{\lambda^{+}-\lambda^{-}} \tag{39}$$

DOI: 10.1002/fld

Depending on the values of $\lambda^{(1)}$ and $\lambda^{(3)}$, the interface $i+1/2$ may not be located within the intermediate region of constant state, but in the left or right state. The following estimates for $\lambda^{(1)}$ and $\lambda^{(3)}$ allow all possible flow situations (subsonic/sub-critical and supersonic/supercritical) to be handled by a single formula [13]

$$\lambda^- = \min(u_\mathrm{L} - c_\mathrm{L}, u_\mathrm{R} - c_\mathrm{R}, 0) \tag{40a}$$

$$\lambda^+ = \max(u_\mathrm{L} + c_\mathrm{L}, u_\mathrm{R} + c_\mathrm{R}, 0) \tag{40b}$$

The first and second components of the flux $\mathbf{F} = (\mathbf{F_1}, \mathbf{F_2}, \mathbf{F_3})$ can be estimated using Equation (39) between the cells i and $i+1$

$$(\mathbf{F_1})_{i+1/2}^{n+1/2} = \frac{\lambda^+ q_\mathrm{L} - \lambda^- q_\mathrm{R} - \lambda^- \lambda^+ (z_\mathrm{L} - z_\mathrm{R})}{\lambda^+ - \lambda^-} \tag{41a}$$

$$(\mathbf{F_2})_{i+1/2}^{n+1/2} = \frac{\lambda^+ \mathbf{F}_{2,\mathrm{L}} - \lambda^- \mathbf{F}_{2,\mathrm{R}} - \lambda^- \lambda^+ (q_\mathrm{L} - q_\mathrm{R})}{\lambda^+ - \lambda^-} \tag{41b}$$

Note that in the first component of (39), the free surface elevations z_L and z_R are used instead of the original conserved variables h_L and h_R for well-balancing of the flux and topographical source term [14].

From numerical experiments, it has been shown in [15] that applying this procedure to the third component of the flow HSCL (1a) may cause unphysical oscillations, sometimes leading to instability in the solution of the scalar transport equation. An alternative formulation must be used for the contact discontinuity (note that this was also the case in the HLLC Riemann solver [12]). The third component is thus estimated using the following expression:

$$(\mathbf{F_3})_{i+1/2}^{n+1/2} = \begin{cases} (\mathbf{F_1})_{i+1/2}^{n+1/2} v_\mathrm{L} & \text{if } u \geqslant 0 \\ (\mathbf{F_1})_{i+1/2}^{n+1/2} v_\mathrm{R} & \text{if } u < 0 \end{cases} \tag{42}$$

taking into account the characteristic equation in the passive variable v

$$\frac{\mathrm{d}v}{\mathrm{d}t} = 0 \quad \text{for } \frac{\mathrm{d}x}{\mathrm{d}t} = u \tag{43}$$

The two first components of the sensitivity flux $\mathbf{G}_{i+1/2}^{n+1/2}$ are obtained by extending Equation (41) to the sensitivity balance

$$(\mathbf{G_1})_{i+1/2}^{n+1/2} = \frac{\lambda^+ \theta_\mathrm{L} - \lambda^- \theta_\mathrm{R} - \lambda^- \lambda^+ (\eta_\mathrm{L} - \eta_\mathrm{R})}{\lambda^+ - \lambda^-} \tag{44a}$$

$$(\mathbf{G_2})_{i+1/2}^{n+1/2} = \frac{\lambda^+ \mathbf{G}_{2,\mathrm{L}} - \lambda^- \mathbf{G}_{2,\mathrm{R}} - \lambda^- \lambda^+ (\theta_\mathrm{L} - \theta_\mathrm{R})}{\lambda^+ - \lambda^-} \tag{44b}$$

As mentioned in previous subsections, such a transposition is not valid strictly speaking because of the extra source term $\mathbf{R}$ that may appear at the discontinuities λ^- and λ^+. However, it should be kept in mind that the present section deals with the conservation part of the equations only and that the source term $\mathbf{R}$ is to be treated separately. Numerical experiments [15] indicate that incorporating $\mathbf{R}$ into (44a) does not bring any noticeable change to the quality of the numerical solution.

The issue identified for the third component of the flow HSCL (1a) holds for the sensitivity HSCL (8a). The sensitivity contact wave should be discretized so as to preserve the invariance property of the sensitivity Riemann invariant along this wave. The third component of the sensitivity flux $\mathbf{G}_{i+1/2}^{n+1/2}$ is thus obtained by extending the treatment proposed for $(\mathbf{F_3})_{i+1/2}^{n+1/2}$ to the sensitivity [15].

DOI: 10.1002/fld

The derivation of Equation (43) with respect to the parameter ψ leads to the following invariance property:

$$\frac{\mathrm{d}\omega}{\mathrm{d}t}=0 \quad \text{for } \frac{\mathrm{d}x}{\mathrm{d}t}=u \tag{45}$$

where ω is the sensitivity of the passive variable v. This equation can also be written in non-conservation form

$$\frac{\partial\omega}{\partial t}+u\frac{\partial w}{\partial x}=0 \tag{46}$$

Moreover, since $r=hv$

$$\mathbf{s}_3=\rho=h\omega+\eta v \tag{47}$$

and

$$\mathbf{G}_3=\theta v+q\omega \tag{48}$$

Substituting these two equations into the third component of (8a) yields

$$\frac{\partial\eta v}{\partial t}+\frac{\partial h\omega}{\partial t}+\frac{\partial\theta v}{\partial x}+\frac{\partial q\omega}{\partial x}=0 \tag{49}$$

expanding the derivatives of ηv and θv, substituting the first component of Equation (1a) and using (46) yields the following equation:

$$\frac{\partial h\omega}{\partial t}+\frac{\partial q\omega}{\partial x}=0 \tag{50}$$

This equation is discretized in a finite volume framework as

$$(h\omega)_i^{n+1}=(h\omega)_i^n+\frac{\Delta t}{\Delta x}[(q\omega)_{i-1/2}^{n+1/2}-(q\omega)_{i+1/2}^{n+1/2}] \tag{51}$$

where qw is computed using the invariance property (46)

$$(qw)_{i+1/2}^{n+1/2}=\begin{cases} q_{i+1/2}^{n+1/2}\omega_{\mathrm{L}} & \text{if } u\geqslant 0 \\ q_{i+1/2}^{n+1/2}\omega_{\mathrm{R}} & \text{if } u<0 \end{cases} \tag{52}$$

Consequently, the third component of the balance equation (33b) is replaced by:

$$\rho^{n+1}=\rho^n+\frac{\Delta t}{\Delta x}[(q\omega)_{i-1/2}^{n+1/2}-(q\omega)_{i+1/2}^{n+1/2}]+(\eta v)_i^{n+1}-(\eta v)_i^n \tag{53}$$

Note that, since the eigenvalues of the Jacobian matrices $\partial\mathbf{F}/\partial\mathbf{U}$ and $\partial\mathbf{G}/\partial\mathbf{s}$ are identical, the stability constraint is the same for the flow and sensitivity problems. The maximum permissible computational time step $\Delta t_{\max}$ is such that the Courant Friedrich Lax number associated with the fastest of the waves $u-c$ and $u+c$ is smaller than unity. The stability constraint is therefore

$$\Delta t_{\max}=\min_i \frac{\Delta x_i}{|u_i^n|+c_i^n} \tag{54}$$

3.3. Source term calculation in the continuous case

The source term $\mathbf{S}$ in (33a) is computed as

$$\mathbf{S}_i^{n+1/2}=\begin{bmatrix} 0 \\ gh(S_0-S_{\mathrm{f}}) \\ 0 \end{bmatrix}_i^{n+1/2} \tag{55}$$

DOI: 10.1002/fld

and discretized using a classical source term upwinding procedure [16]

$$\mathbf{S}_i^{n+1/2} = \begin{bmatrix} 0 \\ gh(S_0 - S_\mathrm{f}) \\ 0 \end{bmatrix}_{i,\mathrm{L}}^{n+1/2} + \begin{bmatrix} 0 \\ gh(S_0 - S_\mathrm{f}) \\ 0 \end{bmatrix}_{i,\mathrm{R}}^{n+1/2} \tag{56}$$

where the subscripts L and R denote the respective contributions of the left and right interface of the cell i to the total source term. The contributions of the interface $i+1/2$ to the cells i and $i+1$ are given by

$$[gh(S_0 - S_\mathrm{f})]_{i,\mathrm{L}}^{n+1/2} = \frac{-\lambda^-}{\lambda^+ - \lambda^-} gh_{i+1/2}^n \left[-\frac{z_{b_i} - z_{b_{i+1}}}{\Delta x_i} - n_\mathrm{M}^2 h_{i+1/2}^{-10/3} q_{i+1/2} |q_{i+1/2}| \right] \tag{57a}$$

$$[gh(S_0 - S_\mathrm{f})]_{i+1,\mathrm{R}}^{n+1/2} = \frac{\lambda^+}{\lambda^+ - \lambda^-} gh_{i+1/2}^n \left[-\frac{z_{b_i} - z_{b_{i+1}}}{\Delta x_i} - n_\mathrm{M}^2 h_{i+1/2}^{-10/3} q_{i+1/2} |q_{i+1/2}| \right] \tag{57b}$$

where the subscript $i+1/2$ denotes the mean of the variable values in cells i and $i+1$.

The source term $\mathbf{Q}$ for the sensitivity is computed as

$$\mathbf{Q}_i^{n+1/2} = \begin{pmatrix} 0 \\ S_0 g\eta + 7/3 S_\mathrm{f} g\eta - 2gn_\mathrm{M}^2 |q| h^{-7/3} \theta - 2gh \dfrac{S_\mathrm{f}}{n_\mathrm{M}} \varepsilon_{n_\mathrm{M}} \\ 0 \end{pmatrix}_i^{n+1/2} \tag{58}$$

and is discretized using the same procedure as $\mathbf{S}$.

3.4. Shock detection and calculation of R

In [6–8] the following criteria were identified as satisfactory. A shock is detected for the wave λ^- if the following conditions are both satisfied:

$$u_\mathrm{L} - c_\mathrm{L} > u_* - c_* \tag{59a}$$

$$u_\mathrm{L} + c_\mathrm{L} > u_* + c_* \tag{59b}$$

while a shock is detected for the wave λ^+ if

$$u_* - c_* > u_\mathrm{R} - c_\mathrm{R} \tag{60a}$$

$$u_* + c_* > u_\mathrm{R} + c_\mathrm{R} \tag{60b}$$

where u_* and c_* are, respectively, the flow velocity and the propagation speed of the waves in the fluid at rest in the intermediate region of constant state.

Note that in the original theory of HSCL [17], Equations (59a) and (60b) are necessary and sufficient conditions for shock wave detection. However, in [17] the influence of source terms is not considered. Using these equations alone would lead to detecting a shock even when the water is at rest when the bottom slope is nonzero [7, 8], hence the need for the extra conditions (59b) and (60a).

When a shock is detected, the point source term $\mathbf{R}$ is split into two contributions: the contribution $\mathbf{R}^-$ of the wave λ^- and the contribution $\mathbf{R}^+$ of the wave λ^+. Since the wave λ^- separates the left state of the Riemann problem from the intermediate region of constant state and the wave λ^+

DOI: 10.1002/fld

separates the right state of the Riemann problem from the intermediate region of constant state, applying (16) yields

$$\mathbf{R}^- = -\frac{\partial \lambda^-}{\partial \psi}(\mathbf{U}_\mathrm{L} - \mathbf{U}_*) \tag{61a}$$

$$\mathbf{R}^+ = -\frac{\partial \lambda^+}{\partial \psi}(\mathbf{U}_* - \mathbf{U}_\mathrm{R}) \tag{61b}$$

The key idea in the present solver [15] consists in using Equation (38) for the estimate of $\mathbf{U}^*$ and noticing that the wave speeds λ^- and λ^+ depend on $\mathbf{U}_\mathrm{L}$ and $\mathbf{U}_\mathrm{R}$ only in the conservation part of the equations. Consequently, (61a) may be rewritten as:

$$\mathbf{R}^- = -\left(\frac{\partial \lambda^-}{\partial \mathbf{U}_\mathrm{L}}\frac{\partial \mathbf{U}_\mathrm{L}}{\partial \psi} + \frac{\partial \lambda^-}{\partial \mathbf{U}_\mathrm{R}}\frac{\partial \mathbf{U}_\mathrm{R}}{\partial \psi}\right)(\mathbf{U}_\mathrm{L} - \mathbf{U}_*) \tag{62}$$

Noticing that $\partial \mathbf{U}/\partial \psi = \mathbf{s}$, (62) becomes

$$\mathbf{R}^- = -\left(\frac{\partial \lambda^-}{\partial \mathbf{U}_\mathrm{L}}\mathbf{s}_\mathrm{L} + \frac{\partial \lambda^-}{\partial \mathbf{U}_\mathrm{R}}\mathbf{s}_\mathrm{R}\right)(\mathbf{U}_\mathrm{L} - \mathbf{U}_*) \tag{63}$$

Applying a similar reasoning to the wave λ^+ yields

$$\mathbf{R}^+ = -\left(\frac{\partial \lambda^+}{\partial \mathbf{U}_\mathrm{L}}\mathbf{s}_\mathrm{L} + \frac{\partial \lambda^+}{\partial \mathbf{U}_\mathrm{R}}\mathbf{s}_\mathrm{R}\right)(\mathbf{U}_* - \mathbf{U}_\mathrm{R}) \tag{64}$$

It is easy to check that definitions (40) lead to the following expressions for the row matrices $\partial \lambda^\pm / \partial \mathbf{U}$:

$$\frac{\partial \lambda^-}{\partial \mathbf{U}_\mathrm{L}} = \begin{cases} \dfrac{1}{h_\mathrm{L}}\left[-u_\mathrm{L} - \dfrac{c_\mathrm{L}}{2} \quad 1 \quad 0\right] & \text{if } u_\mathrm{L} - c_\mathrm{L} < \min(u_\mathrm{R} - c_\mathrm{R}; 0) \\ [0 \;\; 0 \;\; 0] & \text{otherwise} \end{cases} \tag{65a}$$

$$\frac{\partial \lambda^-}{\partial \mathbf{U}_\mathrm{R}} = \begin{cases} \dfrac{1}{h_\mathrm{R}}\left[-u_\mathrm{R} - \dfrac{c_\mathrm{R}}{2} \quad 1 \quad 0\right] & \text{if } u_\mathrm{R} - c_\mathrm{R} < \min(u_\mathrm{L} - c_\mathrm{L}; 0) \\ [0 \;\; 0 \;\; 0] & \text{otherwise} \end{cases} \tag{65b}$$

$$\frac{\partial \lambda^+}{\partial \mathbf{U}_\mathrm{L}} = \begin{cases} \dfrac{1}{h_\mathrm{L}}\left[-u_\mathrm{L} + \dfrac{c_\mathrm{L}}{2} \quad 1 \quad 0\right] & \text{if } u_\mathrm{L} + c_\mathrm{L} \geqslant \max(u_\mathrm{R} + c_\mathrm{R}; 0) \\ [0 \;\; 0 \;\; 0] & \text{otherwise} \end{cases} \tag{65c}$$

$$\frac{\partial \lambda^+}{\partial \mathbf{U}_\mathrm{R}} = \begin{cases} \dfrac{1}{h_\mathrm{R}}\left[-u_\mathrm{R} + \dfrac{c_\mathrm{R}}{2} \quad 1 \quad 0\right] & \text{if } u_\mathrm{R} + c_\mathrm{R} > \max(u_\mathrm{L} + c_\mathrm{L}; 0) \\ [0 \;\; 0 \;\; 0] & \text{otherwise} \end{cases} \tag{65d}$$

Substituting Equations (65) into (63) and (64) yields

$$\mathbf{R}^- = \begin{cases} \dfrac{1}{h_\mathrm{L}}\left[\left(u_\mathrm{L} + \dfrac{c_\mathrm{L}}{2}\right)\eta_\mathrm{L} - \theta_\mathrm{L}\right](\mathbf{U}_\mathrm{L} - \mathbf{U}_*) & \text{if } u_\mathrm{L} - c_\mathrm{L} < \min(u_\mathrm{R} - c_\mathrm{R}; 0) \\ \dfrac{1}{h_\mathrm{R}}\left[\left(u_\mathrm{R} + \dfrac{c_\mathrm{R}}{2}\right)\eta_\mathrm{R} - \theta_\mathrm{R}\right](\mathbf{U}_\mathrm{L} - \mathbf{U}_*) & \text{if } u_\mathrm{L} - c_\mathrm{L} \geqslant \max(u_\mathrm{R} - c_\mathrm{R}; 0) \end{cases} \tag{66a}$$

$$\mathbf{R}^+ = \begin{cases} \dfrac{1}{h_\mathrm{R}}\left[\left(u_\mathrm{R} - \dfrac{c_\mathrm{R}}{2}\right)\eta_\mathrm{R} - \theta_\mathrm{R}\right](\mathbf{U}_* - \mathbf{U}_\mathrm{R}) & \text{if } u_\mathrm{L} + c_\mathrm{L} < \min(u_\mathrm{R} + c_\mathrm{R}; 0) \\ \dfrac{1}{h_\mathrm{L}}\left[\left(u_\mathrm{L} - \dfrac{c_\mathrm{L}}{2}\right)\eta_\mathrm{L} - \theta_\mathrm{L}\right](\mathbf{U}_* - \mathbf{U}_\mathrm{R}) & \text{if } u_\mathrm{L} + c_\mathrm{L} \geqslant \max(u_\mathrm{R} + c_\mathrm{R}; 0) \end{cases} \tag{66b}$$

DOI: 10.1002/fld

3.5. Discretization of boundary conditions

3.5.1. Shallow water equations. Three types of boundary conditions are considered hereafter for the equations of mass and momentum conservation: prescribed water depth, prescribed discharge and prescribed stage–discharge relationship. For the sake of conciseness, only the left-hand boundary of the domain is considered, the transposition to a right-hand boundary being straightforward. Only subcritical conditions are considered hereafter, the supercritical case being straightforward.

1. *Prescribed water depth.* Assume that the water depth h_b is to be prescribed at the left-hand boundary. Then, the water depth and the sensitivity at the left-hand interface $1/2$ of the computational cell 1 are given by

$$h_{1/2}^{n+1/2} = h_\mathrm{b} \tag{67a}$$

$$\eta_{1/2}^{n+1/2} = \eta_\mathrm{b} \tag{67b}$$

with $\eta_\mathrm{b} = 0$ or 1 depending on the purpose of the sensitivity analysis (see Section 2.5). The values of q and θ at the boundary are computed by considering, as in the HLL formalism (40a)–(40b), that the boundary states are separated from the inside of the computational domain by a wave moving at speed $\lambda^+ = u_1^n + c_1^n$. Then, Equation (37b) is applicable with h_b and q_b

$$q_{1/2}^{n+1/2} = q_1^n + (h_\mathrm{b} - h_i^n)\lambda^+ \tag{68a}$$

$$\theta_{1/2}^{n+1/2} = \theta_1^n + (\eta_\mathrm{b} - \eta_i^n)\lambda^+ \tag{68b}$$

The water depth $h_{1/2}^{n+1/2}$ and the unit discharge $q_{1/2}^{n+1/2}$ as well as their sensitivity, being entirely determined at the interface $\frac{1}{2}$, the calculation of the momentum flux $(F_2)_{1/2}^{n+1/2}$ and the sensitivity flux $(G_2)_{1/2}^{n+1/2}$ are straightforward.

2. *Prescribed unit discharge.* The boundary conditions are

$$q_{1/2}^{n+1/2} = q_\mathrm{b} \tag{69a}$$

$$\theta_{1/2}^{n+1/2} = \theta_\mathrm{b} = 0 \text{ or } 1 \tag{69b}$$

Applying Equation (37b) to the second components of $\mathbf{U}$ and $\mathbf{s}$ yields directly the second component of the fluxes for the flow variable and sensitivity

$$(F_2)_{1/2}^{n+1/2} = (F_2)_1^n + (q_\mathrm{b} - q_i^n)\lambda^+ \tag{70a}$$

$$(G_2)_{1/2}^{n+1/2} = (G_2)_1^n + (\theta_\mathrm{b} - \theta_i^n)\lambda^+ \tag{70b}$$

3. *Prescribed stage-discharge relationship.* In the case of a known, nonlinear relationship between the water depth and the unit discharge, it is more convenient to rewrite (26) in the form of a relationship between the flow velocity u and the wave celerity in still water c

$$f(u, c, \psi) = 0 \tag{71a}$$

$$\frac{\partial f}{\partial u} v + \frac{\partial f}{\partial c} \chi + \frac{\partial f}{\partial \psi} = 0 \tag{71b}$$

DOI: 10.1002/fld

where χ and v are, respectively, the sensitivity of c and u. This set of equations is complemented by the Riemann invariants $u-2c$ and $v-2\chi$ for the flow and sensitivity, respectively,

$$u_{1/2}^{n+1/2}-2c_{1/2}^{n+1/2}=u_1^n-2c_1^n \tag{72a}$$

$$v_{1/2}^{n+1/2}-2\chi_{1/2}^{n+1/2}=v_1^n-2\chi_1^n \tag{72b}$$

The systems (71a), (72a) and (71b), (72b) may be solved using any iterative procedure such as the Newton–Raphson technique.

3.5.2. Transport equation. Concerning the boundary condition for the variable subjected to passive transport, a value r_b must be prescribed at the left-hand boundary if the unit-discharge q is positive

$$r_{1/2}^{n+1/2}=r_\mathrm{b} \tag{73a}$$

$$\rho_{1/2}^{n+1/2}=\rho_\mathrm{b} \tag{73b}$$

with $\rho_\mathrm{b}=0$ or 1 depending on the purpose of the sensitivity analysis.

When the unit discharge is negative, the values of r and ρ inside the domain are conserved

$$r_{1/2}^{n+1/2}=r_1^n \tag{74a}$$

$$\rho_{1/2}^{n+1/2}=\rho_1^n \tag{74b}$$

The calculation of the third components of $\mathbf{F}$ and $\mathbf{G}$ is then straightforward.

4. COMPUTATIONAL EXAMPLES

4.1. Sensitivity to the friction coefficient: steady flow on a sloping bed

The purpose of this test is to assess the efficiency of the method for the sensitivity to Manning's coefficient, in a case where a reference solution can be computed by discretizing the backwater curve equation

$$\frac{\mathrm{d}h}{\mathrm{d}x}=\frac{S_0-S_\mathrm{f}}{1-\mathrm{Fr}^2} \tag{75a}$$

$$S_\mathrm{f}=q^2n_\mathrm{M}^2h^{-10/3} \tag{75b}$$

using the explicit Euler method. The boundary conditions are a prescribed unit-discharge (q_b) upstream and a prescribed water depth (h_b) downstream.

Since the flow is in steady state, the corresponding sensitivity equation is given by

$$\begin{aligned}\frac{\mathrm{d}\eta}{\mathrm{d}x}&=\eta\frac{\partial}{\partial h}\left(\frac{S_0-S_\mathrm{f}}{1-\mathrm{Fr}^2}\right)+\varepsilon_{n_\mathrm{M}}\frac{\partial}{\partial n_\mathrm{M}}\left(\frac{S_0-S_\mathrm{f}}{1-\mathrm{Fr}^2}\right)\\&=\frac{1}{1-\mathrm{Fr}^2}\left[\left(\frac{10}{3}S_\mathrm{f}-3\mathrm{Fr}^2\frac{S_0-S_\mathrm{f}}{1-\mathrm{Fr}^2}\right)\frac{\eta}{h}-2\frac{S_\mathrm{f}}{n_\mathrm{M}}\varepsilon_{n_\mathrm{M}}\right]\end{aligned} \tag{76}$$

with

$$\varepsilon_{n_\mathrm{M}}(x)=1\quad\forall x \tag{77a}$$

$$\eta_\mathrm{b}(L)=0 \tag{77b}$$

$$\theta(x)=0\quad\forall x \tag{77c}$$

and can also be discretized using the explicit Euler method.

DOI: 10.1002/fld

Table I. Steady flow on a sloping bed: problem parameters.

Symbol	Meaning	Value
g	Gravitational acceleration	$9.81\,\mathrm{m\,s^{-2}}$
L	Length of the simulation domain	3000 m
q_b	Unit-discharge prescribed at the upstream boundary	$1\,\mathrm{m^2\,s^{-1}}$
h_b	Water depth prescribed at the downstream boundary	0.8 m
S_0	Bottom slope	1×10^{-3}
h_0	Initial water depth in the domain	1 m
q_0	Initial unit-discharge in the domain	$1\,\mathrm{m^2\,s^{-1}}$
n_M	Manning's friction coefficient	$0.025\,\mathrm{m^{-1/3}\,s}$
$(\Delta x)_\mathrm{r}$	Cells width used for the reference solution	0.001 m
$(\Delta x)_\mathrm{n}$	Cells width used for the numerical solution	1 m
T	Computational time	15 000 s

The parameters of the test case are given in Table I. The computed water depth, unit-discharge and their sensitivities to Manning's friction coefficient are given in Figure 1 for the proposed solver and the Euler approach. The empirical sensitivity profiles also given in Figure 1 are defined by the normalized difference between two simulations obtained using two slightly different values for n_M (in this case: 0.025 and $0.024\,\mathrm{m^{-1/3}\,s}$). The physical interpretation of the sensitivity η of h with respect to n_M (Figure 1(b)) is that a variation of 1 in n_M leads to a variation in h of about 21 upstream. Indeed, the calculation with $n_\mathrm{M}=0.024$ gives $h=0.8892$ whereas the calculation with $n_\mathrm{M}=0.025$ gives $h=0.8685$ (i.e. a difference of 0.021). The sensitivity of h downstream remains nil because the water depth is prescribed at the downstream boundary. Since the flow is permanent and the unit-discharge is prescribed upstream, q should remain constant in the whole domain and θ should be nil. The differences observed for the unit-discharge q and its sensitivity θ near the downstream boundary are due to a difficulty of the proposed solver to assess the momentum values at cells, given boundary conditions at interfaces. The problem stems from the balancing process between the flux calculation at the interface and the values at cells.[‡] Indeed, the values of q and θ at the interfaces, i.e. the first component of the fluxes $\mathbf{F}$ and $\mathbf{G}$, respectively, are correctly estimated and are, respectively, equal to the prescribed value q_b and to 0 in the whole domain (see Figure 2). Moreover, in this case, despite an unsatisfying value of q, its sensitivity θ is better estimated by the direct approach than by the empirical method.

To assess the convergence of the proposed approach, a convergence analysis is performed in the uniform case, for which an analytical solution is known. The uniform flow is obtained by prescribing h_b to be the normal height

$$h_\mathrm{b}=h_N=\left(\frac{qn_\mathrm{M}}{\sqrt{S_0}}\right)^{3/5} \tag{78}$$

In this configuration, Equation (76) is simplified into

$$\frac{\mathrm{d}\eta}{\mathrm{d}x}=\frac{S_\mathrm{f}}{1-\mathrm{Fr}^2}\left[\frac{10}{3}\frac{\eta}{h}-2\frac{\varepsilon_{n_\mathrm{M}}}{n_\mathrm{M}}\right] \tag{79}$$

This first-order differential equation admits the following analytical solution:

$$\eta(x)=\frac{3}{5}\frac{h_N}{n_\mathrm{M}}(1-\mathrm{e}^{-(S_\mathrm{f}/(1-\mathrm{Fr}^2))\cdot(10/3h)L})\mathrm{e}^{(S_\mathrm{f}/(1-\mathrm{Fr}^2))\cdot(10/3h)x} \tag{80}$$

The convergence analysis is performed using the parameters given in Table I, except $h_\mathrm{b}=h_N\approx 0.8685\,\mathrm{m}$, and eight different values of the spatial discretization step: $\Delta x=\{5;3;2;1;0.5;0.25;0.1;0.05\}\,\mathrm{m}$. The corresponding values of Δt_max are automatically computed using Equation (54).

[‡]Note that the isolated points in Figures 1(c) and (d) are not artefacts due to the drawing of only one point every 25.

DOI: 10.1002/fld

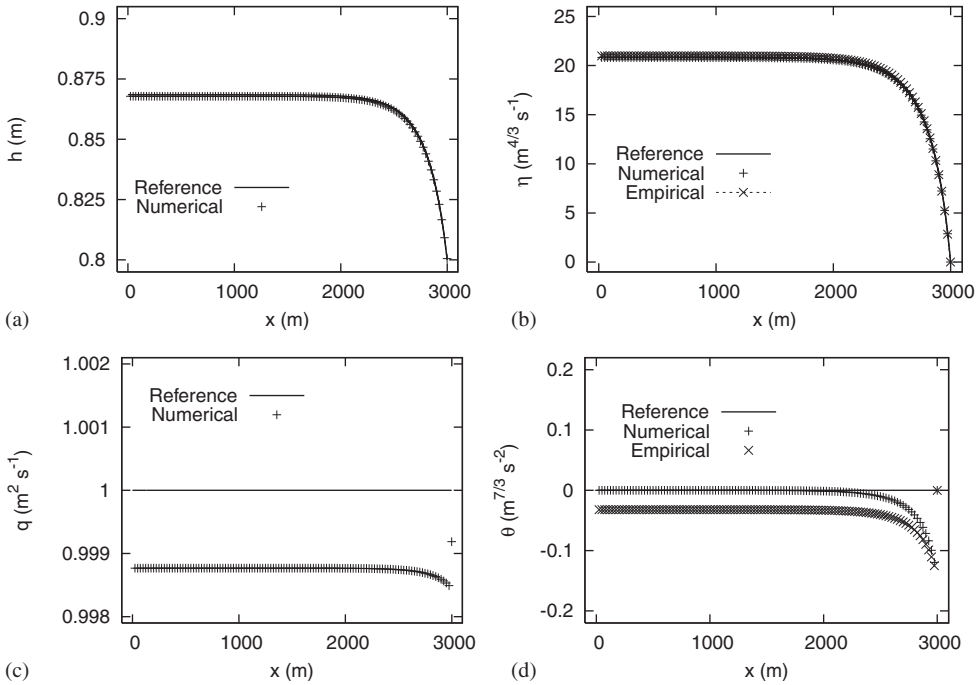

Figure 1. Sensitivity to the Manning coefficient for a steady-state flow on a sloping bed. Comparison between the proposed solver and the explicit Euler method (reference). For the sake of clarity, only one point every 25 is represented.

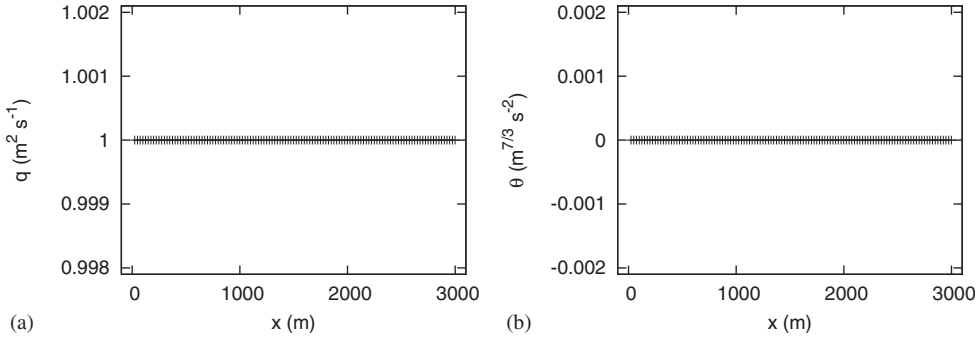

Figure 2. Sensitivity to the Manning coefficient for a steady-state flow on a sloping bed. Values of q and θ computed at the interfaces.

The variations L_1- and L_2-norms of the difference between the analytical and numerical solutions with the cell width Δx are represented in Figure 3 for the variables h, q and their sensitivities. The L_p-norm ($p=1,2$) is defined as

$$L_p = \left\{ \sum_i [Y_i - Y(x_i)]^p \Delta x_i \right\}^{1/p} \tag{81}$$

where Y_i and $Y(x_i)$ represent, respectively, the numerical and analytical solutions with Y being either h, q, η or θ.

Both norms decrease with Δx—the L_2-norm with a slope about twice the one of the L_1-norm—indicating a uniform convergence of the numerical solution to the analytical solution.

DOI: 10.1002/fld

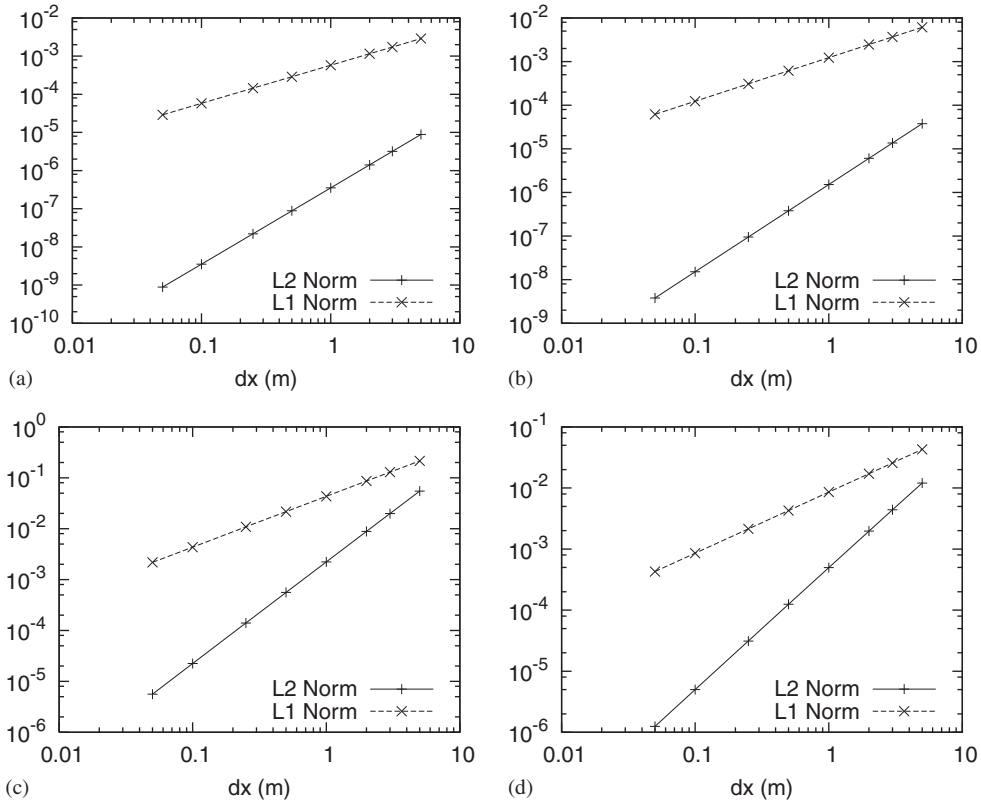

Figure 3. Convergence analysis. L_1 and L_2 norms of the error as functions of cell size (logarithmic scale): (a) h; (b) q; (c) η; and (d) θ.

4.2. *Sensitivity to the initial conditions*: *dam-break on a sloping bed*

The dam-break problem is an initial-value problem in which the water is initially at rest and the water levels are different on both sides of the dam. The variable subjected to passive scalar transport can also have different values on both sides of the dam. This problem is thus a Riemann problem defined as:

$$h(x,0)=\begin{cases} h_{\mathrm{L}} & \text{for } x<x_0 \\ h_{\mathrm{R}} & \text{for } x>x_0 \end{cases} \tag{82a}$$

$$q(x,0)=0 \tag{82b}$$

$$r(x,0)=\begin{cases} r_{\mathrm{L}} & \text{for } x<x_0 \\ r_{\mathrm{R}} & \text{for } x>x_0 \end{cases} \tag{82c}$$

Note that this initial condition does not correspond to equilibrium conditions but gives the advantage that the analytical solution is easy to compute (see [8] for more details).

A sensitivity analysis with respect to the initial water depth h_{L} in the dam is performed. The analytical, empirical and numerical solutions are plotted in Figure 4 for a positive slope and in Figure 5 for a negative slope with the parameters given in Table II. The higher the magnitude of the sensitivity, the more sensitive the variable with respect to the parameter. For example in Figure 4(e), the value of $\theta=\partial q/\partial h_{\mathrm{L}}$ for $x=0$ is 1.96; this means that a variation of 1 for h_{L} leads to a variation of approximatively 1.96 for q (note that this approximation remains valid for small variations). Indeed, the calculation using $h_{\mathrm{L}}=10$ gives $q_{x=0}=19.62$, whereas the calculation using $h_{\mathrm{L}}=11$ gives $q_{x=0}=21.58$ (i.e a difference of 1.96).

DOI: 10.1002/fld

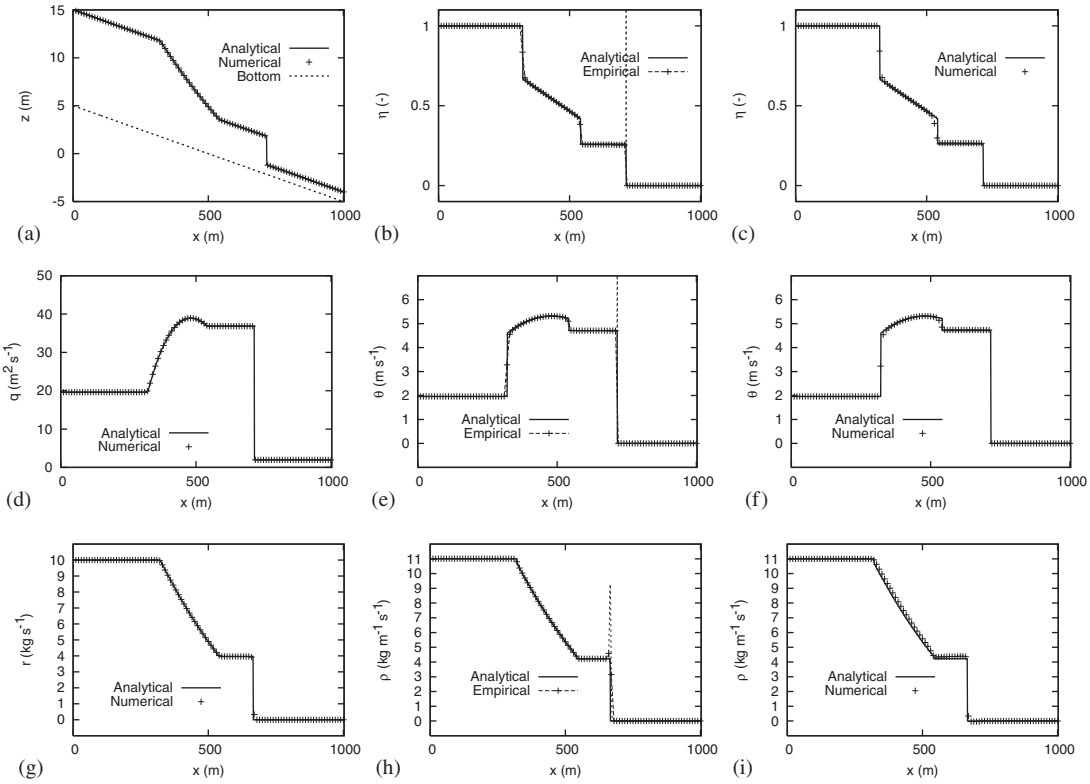

Figure 4. Dam-break problem on a positive slope. Left: flow solution, middle: empirical sensitivity, right: numerical sensitivity. For the sake of clarity, only one point every 100 is represented. The values reached by the peaks in subfigures (b) and (e) are, respectively, about 175 and 2130.

The empirical sensitivity profiles have been obtained using two slightly different values for h_L (i.e. 10 and 10.01 m) and for v_L (i.e. 1 and 1.01, the unit of which depends on the nature of the variable). In Figures 4 and 5 the same scale is used to plot the empirical and numerical sensitivity profiles, but the empirical profiles exhibit artificial peaks in the neighbourhood of the shock that exceed by far the scale range. This is due to the fact that the shock celerity is not exactly the same between both simulations (because it depends on the value of h_L). This behaviour is eliminated with the proposed solver, thanks to the introduction of the Dirac-source term across the shock.

4.3. Sensitivity to the boundary conditions: *Bore propagation into a frictionless channel*

The purpose of this test is to assess the accuracy of the proposed discretization for the sensitivity to boundary conditions in the presence of discontinuous solutions. Consider a horizontal, frictionless channel where the water is initially at rest, with a constant initial depth h_0. At $t=0$, the unit discharge and the value of the variable subjected to passive transport, at the channel upstream ($x=0$), change instantaneously from 0 to constant values: q_b and v_b. A bore appears and propagates into the channel at a constant speed c_s. Writing the jump relationships across the bore leads to

$$q_b = (h_b - h_0)c_s \tag{83a}$$

$$\frac{q_b^2}{h_b} + \frac{g}{2}(h_b^2 - h_0^2) = q_b c_s \tag{83b}$$

where h_b is the water depth at the boundary. Equations (83) are solved uniquely for h_b and c_s using iterative linearization techniques such as Newton–Raphson's method. Since the purpose is to study the sensitivity of the solution to the values of q_b and v_b, the sensitivity boundary condition are

DOI: 10.1002/fld

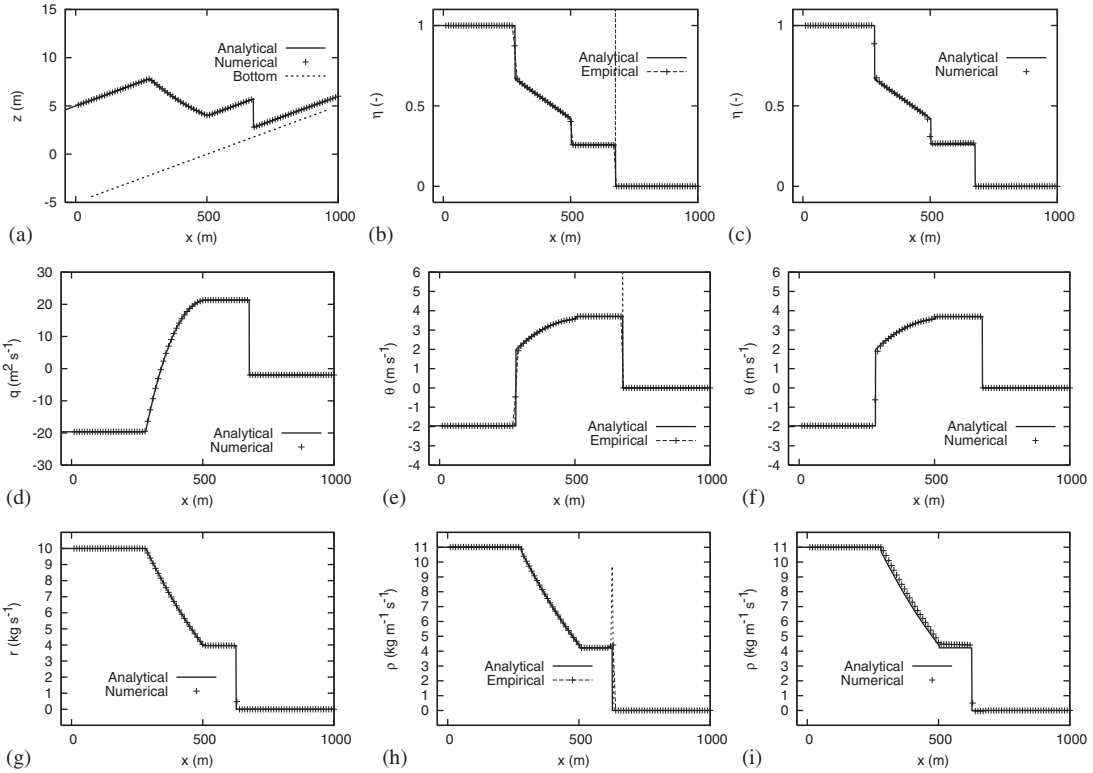

Figure 5. Dam-break problem on a negative slope. Left: flow solution, middle: empirical sensitivity, right: numerical sensitivity. The values reached by the peaks in subfigures (b) and (e) are, respectively, about 170 and 1245.

$\theta_b = 1$ and $\omega_b = 1$. The jump relationships for the sensitivity are obtained by differentiating (83) with respect to q_b, and noticing that the initial water depth sensitivity η_0 in the channel is zero

$$\eta_b c_s + (h_b - h_0)\frac{\partial c_s}{\partial q_b} = 1 \tag{84a}$$

$$2u_b - u_b^2 \eta_b + g h_b \eta_b = c_s + q_b \frac{\partial c_s}{\partial q_b} \tag{84b}$$

Equations (84) can be solved uniquely for η_b and $\partial c_s/\partial q_b$. The bore concerning the variable subjected to passive transport propagates at the constant speed of the contact wave: $\lambda^{(2)} = u = u_b$.

The set of parameters used for this application example is given in Table III. The empirical sensitivity profiles have been obtained using two slightly different values for q_b (i.e. 1 and $1.01\,\mathrm{m^2\,s^{-1}}$) and for v_L (i.e. 1 and 1.01, the unit of which depends on the nature of the variable). The analytical, numerical and empirical sensitivity profiles are given in Figure 6. As shown in the previous test case, the empirical sensitivity profiles also exhibit artificial peaks in the neighbourhood of the shock, that are not present with the proposed solver. In this case, however, diffusion of the numerical solution can be observed near the shock for r and ρ (Figures 6(g) and (h)) that may indicate the need for a higher-order reconstruction.

4.4. Application to a non-rectangular river profile

The direct sensitivity approach can be applied to non-rectangular river profiles. An example is given here for a trapezoidal channel, where the cross-sectional area A is defined by

$$A = (B_0 + h\tan\alpha)h \tag{85}$$

DOI: 10.1002/fld

Table II. Dam-break on a sloping bed: problem parameters.

Symbol	Meaning	Value
g	Gravitational acceleration	$9.81\,\mathrm{m\,s^{-2}}$
L	Length of the simulation domain	1000 m
S_0	Bottom slope	0.01 and −0.01
h_L	Water depth on the left-hand side of the initial discontinuity	10 m
h_R	Water depth on the right-hand side of the initial discontinuity	1 m
q_L and q_R	x unit discharge on the left- and right-hand sides of the initial discontinuity	$0\,\mathrm{m^2\,s}$
v_L	initial value of the variable subjected to passive transport on the left-hand side of the discontinuity	$1\,\mathrm{kg\,s^{-1}}$
v_R	initial value of the variable subjected to passive transport on the right-hand side of the discontinuity	$0\,\mathrm{kg\,s^{-1}}$
x_0	Abscissa of the initial discontinuity	500 m
η_L	Water depth sensitivity on the left-hand side of the initial discontinuity	1 (−)
η_R	Water depth sensitivity on the right-hand side of the initial discontinuity	0 (−)
θ_L and θ_R	Sensitivity of the x unit discharge on the left- and right-hand sides of the initial discontinuity	$0\,\mathrm{m\,s^{-1}}$
ω_L	Sensitivity of the variable subjected to passive transport on the left-hand side of the initial discontinuity	$1\,\mathrm{kg\,m^{-1}\,s^{-1}}$
ω_R	Sensitivity of the variable subjected to passive transport on the right-hand side of the initial discontinuity	$0\,\mathrm{kg\,m^{-1}\,s^{-1}}$
n_M	Manning's friction coefficient	$0\,\mathrm{m^{-1/3}\,s}$
Δx	Cells width	0.1 m
T	Computational time	20 s

Table III. Bore propagation into a frictionless channel: problem parameters. All initial conditions but h_0 are nil.

Symbol	Meaning	Value
g	Gravitational acceleration	$9.81\,\mathrm{m\,s^{-2}}$
L	Length of the simulation domain	100 m
Δx	Cells width	1 m
t	Computational time	15 s
h_0	Initial water depth	1 m
q_b	Unit-discharge prescribed at the upstream boundary	$1\,\mathrm{m^2\,s^{-1}}$
θ_b	Upstream discharge sensitivity	1 (−)
v_b	Value prescribed at the upstream boundary, for the variable subjected to passive transport	$1\,\mathrm{kg\,s^{-1}}$
ω_b	Upstream sensitivity for the variable subjected to passive transport	$1\,\mathrm{kg\,m^{-2}\,s^{-2}}$

where B_0 is the bottom width, h the water depth and α the angle formed by the channel sides to the vertical. The governing equations (1) and (2) can be rewritten as:

$$\frac{\partial \mathbf{U_T}}{\partial t}+\frac{\partial \mathbf{F_T}}{\partial x}=\mathbf{S_T} \tag{86}$$

$$\mathbf{U_T}=\begin{pmatrix}A\\Q\end{pmatrix},\quad \mathbf{F_T}=\begin{pmatrix}Q\\Q^2/A+gh^2B_0/2+gh^3\tan\alpha/3\end{pmatrix},\quad \mathbf{S_T}=\begin{pmatrix}0\\gA(S_0-S_\mathrm{f})\end{pmatrix} \tag{87}$$

DOI: 10.1002/fld

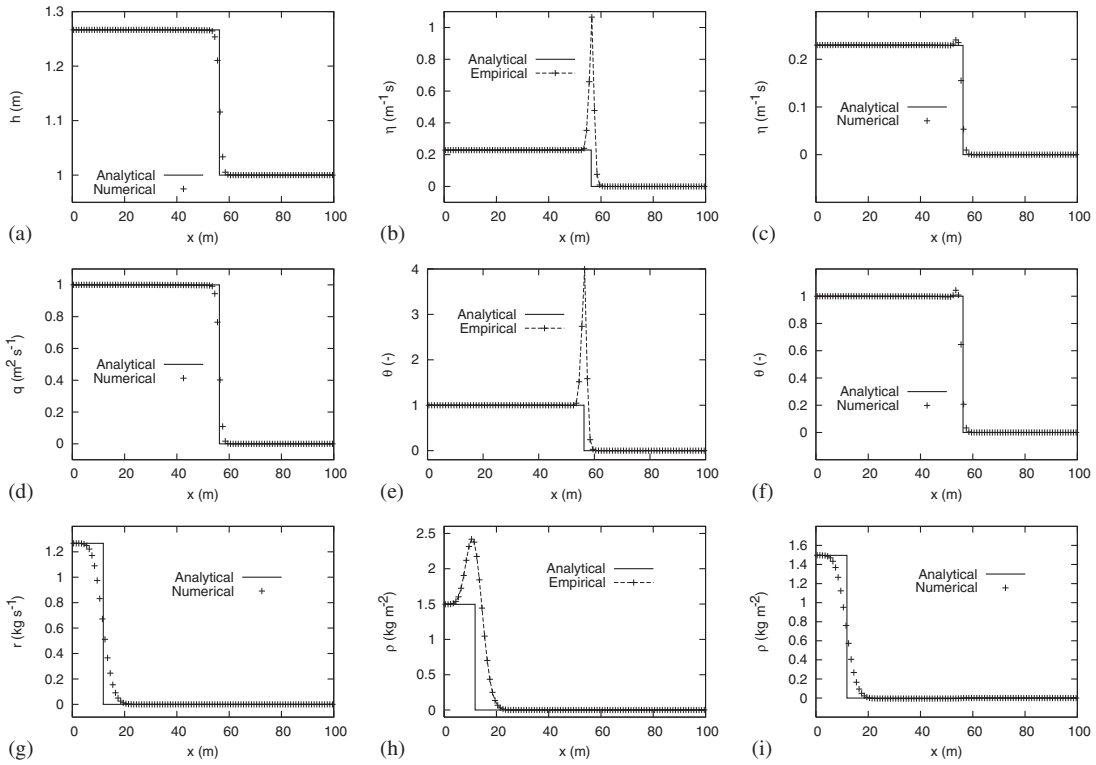

Figure 6. Bore propagation into a frictionless channel and sensitivity with respect to the prescribed unit discharge q_b. Left: flow solution, middle: empirical sensitivity, right: numerical sensitivity.

In this case, the expression of the sensitivity flux becomes

$$\mathbf{G_T} = \begin{pmatrix} \theta \\ gA(B_0^2 + 4A\tan\alpha)^{1/2}\eta - u^2\eta + 2u\theta \end{pmatrix}$$

The flow solution of the dam-break problem applied to a trapezoidal channel is plotted in Figures 7(a) and (c) with the parameters given in Table IV. The sensitivity of A and Q with respect to the initial cross-sectional area in the dam is plotted in Figures 7(b) and (d). In this case again, the direct computation of the sensitivity removes the artefacts of the empirical method.

5. CONCLUSION

The sensitivity equations were derived for the one-dimensional SWEs with scalar transport and source terms. A finite volume-based numerical technique was proposed for both continuous and discontinuous flow solutions. In this latter case, a Dirac-source term, introduced across shocks in the governing sensitivity equations, increases complexity in the solution of the sensitivity problem. However, this approach enables elimination of numerical artefacts present in the empirical method, such as infinite sensitivity values at discontinuities.

Ongoing research focuses on the generalization of the present technique to the solution of the two-dimensional SWEs on unstructured grids. As shown in [15], such a generalization is not trivial because solving the two-dimensional SWEs involves solving a third conservation equation for transverse momentum. In the present work, to preserve the invariance property of the sensitivity Riemann invariant along the contact wave, a part of the third equation has been discretized in non-conservation form. In two dimensions, not discretizing the transverse momentum equation (that can be considered as a passive tracer) in a fully conservative manner can be expected to yield

DOI: 10.1002/fld

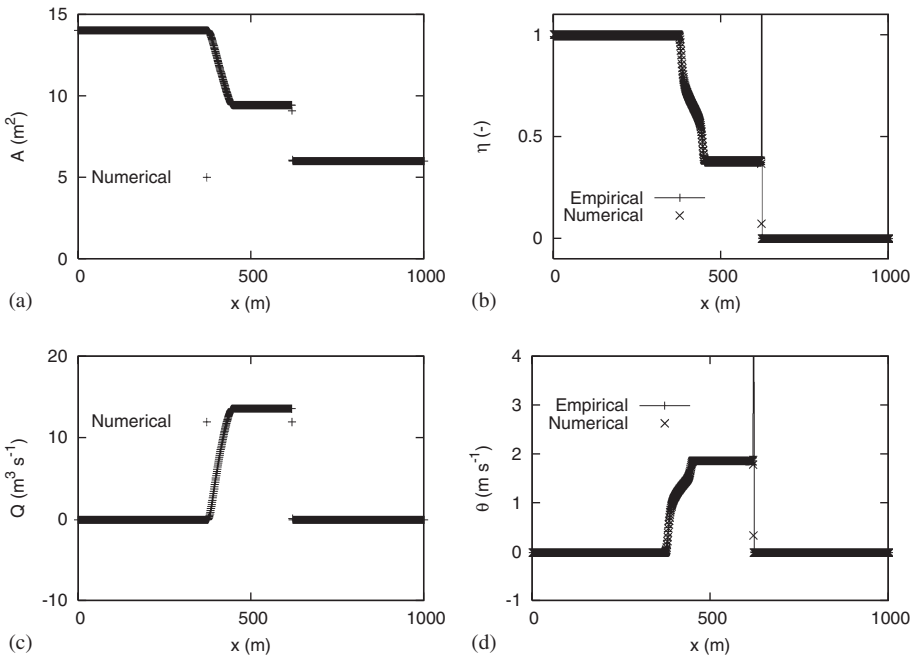

Figure 7. Dambreak problem for a trapezoidal channel. Left: flow solution, right: empirical and numerical sensitivities.

Table IV. Dam-break on a trapezoidal channel: problem parameters.

Symbol	Meaning	Value
g	Gravitational acceleration	$9.81\,\mathrm{m\,s^{-2}}$
L	Length of the simulation domain	1000 m
B_0	Bottom width of the channel	5 m
α	Angle between channel sides and the vertical	$\pi/4$
S_0	Bottom slope	0
h_L	Water depth on the left-hand side of the initial discontinuity	2 m
h_R	Water depth on the right-hand side of the initial discontinuity	1 m
Q_L and Q_R	Discharge on the left- and right-hand sides of the initial discontinuity	$0\,\mathrm{m^2\,s}$
x_0	Abscissa of the initial discontinuity	500 m
η_L	Sensitivity of the water cross-sectional area on the left-hand side of the initial discontinuity	1 (−)
η_R	Sensitivity of the water cross-sectional area on the right-hand side of the initial discontinuity	0 (−)
θ_L and θ_R	Sensitivity of the discharge on the left- and right-hand sides of the initial discontinuity	$0\,\mathrm{m\,s^{-1}}$
n_M	Manning's friction coefficient	$0\,\mathrm{m^{-1/3}\,s}$
Δx	Cells width	0.1 m
T	Computational time	30 s

accuracy and/or stability problems. Moreover, the determination of the exact location of shocks in two dimensions will also increase the complexity of the problem.

The difficulty of the proposed solver in dealing with the imposed boundary conditions in the steady-state configuration with bottom slope and friction (Section 4.1) stems from the HLLC solver itself, in the balancing process between the flux calculation at the interface and the values at cells. The development of sensitivity equations for the approximate state Riemann solver presented in

DOI: 10.1002/fld

[18] is thus under investigation. Since using higher-order schemes for scalar sensitivity equations has been shown to improve the accuracy of sensitivity solutions in a number of cases [6], the applicability of fast, higher-order numerical reconstruction techniques such as the MUSCL-EVR approach [19] is another path for research. The strong diffusion, observed for the variable subjected to passive scalar transport and for its sensitivity in the bore propagation problem, is expected to be limited using these techniques.

ACKNOWLEDGEMENTS

This work was supported by Research Contract ANR-05-PGCU-004, 'RIVES' funded by the French Agence Nationale de la Recherche (ANR)/ National Research Agency. The contribution and support of the following partners are gratefully acknowledged: Cemagref, CETE Méditerranée, CETMEF, LMFA UMR 5509 (CNRS, ECL, INSA Lyon, UCB), INSAVALOR, LCPC, LRPC Bordeaux, LRPC Clermont-Ferrand, Sogreah, URGC (INSA Lyon), UTC.

REFERENCES

1. Saltelli A, Tarantola S, Campolongo F. *Sensitivity Analysis in Practice*: *A Guide to Assessing Scientific Models*. Wiley: New York, 2008.
2. Guinot V, Cappelaere B. Sensitivity equations for the one-dimensional shallow water equations: practical application to model calibration. *Journal of Hydrologic Engineering* 2009; **14**(8):858–861.
3. Lu S, Sagaut P. Direct sensitivity analysis for smooth unsteady compressible flow using complex differentiation. *International Journal for Numerical Methods in Fluids* 2007; **53**(12):1863–1886.
4. Gunzburger MD. Sensitivities, adjoints and flow optimization problems. *International Journal for Numerical Methods in Fluids* 1999; **31**:53–78.
5. Bardos C, Pironneau O. A formalism for the differentiation of conservation laws. *Comptes Rendus de l'Académie des Sciences Paris*, *Series I* 2002; **335**:839–845.
6. Guinot V, Leménager M, Cappelaere B. Sensitivity equations for hyperbolic conservation law-based flow models. *Advances in Water Resources* 2007; **30**:1943–1961.
7. Delenne C, Guinot V, Cappelaere B. Direct sensitivity computation for the Saint-Venant equations with hydraulic jumps. *Comptes Rendus Mécanique* 2008; **336**:766–771.
8. Guinot V, Delenne C, Cappelaere B. An approximate-state Riemann solver for sensitivity equations with discontinuous solutions. *Advances in Water Resources* 2009; **31**(1):61–77.
9. Stoker JJ. *Water Waves*. Wiley-Interscience: New York, 1957.
10. Cunge JA, Holly Jr FM, Verwey A. *Practical Aspects of River Computational Hydraulics*. Pitman Advanced Publishing Program: Boston, 1980.
11. Harten A, Lax P-D, Van-Leer B. On upstream differencing and Godunov-type schemes for hyperbolic conservation laws. *SIAM Review* 1983; **25**:35–61.
12. Toro EF, Spruce M, Speares W. Restoration of the contact surface in the HLL-Riemann solver. *Shock Waves* 1994; **4**:25–34.
13. Davis SF. Simplified second-order Godunov-type methods. *SIAM Journal on Scientific and Statistical Computing* 1988; **9**:455–473.
14. Nujíc M. Efficient implementation of non-oscillatory schemes for the computation of free-surface flows. *Journal of Hydraulic Research* 1995; **33**:101–111.
15. Guinot V. Upwind finite volume solution of sensitivity equations for hyperbolic systems of conservation laws with discontinuous solutions. *Computers and Fluids* 2009; **38**:1697–1709.
16. Vasquez-Cendon ME. Improved treatment of source terms in upwind schemes for the shallow water equations in channels with irregular geometry. *Journal of Computational Physics* 1999; **148**(2):497–526.
17. Lax P-D. Hyperbolic systems of conservation laws. *Communications on Pure and Applied Mathematics* 1957; **10**:537–566.
18. Lhomme J, Guinot V. A general approximate-state Riemann solver for hyperbolic systems of conservation laws with source terms. *International Journal for Numerical Methods in Fluids* 2007; **53**:1509–1540.
19. Soares Frazão S, Guinot V. An eigenvector-based reconstruction scheme for the shallow-water equations on two-dimensional unstructured meshes. *International Journal for Numerical Methods in Fluids* 2007; **53**:23–55.

DOI: 10.1002/fld

INTERNATIONAL JOURNAL FOR NUMERICAL METHODS IN FLUIDS
Int. J. Numer. Meth. Fluids 2010; **62**:1299–1331
Published online 20 May 2009 in Wiley InterScience (www.interscience.wiley.com). DOI: 10.1002/fld.2066

An approximate-state Riemann solver for the two-dimensional shallow water equations with porosity

P. Finaud-Guyot[1,2,*,†], C. Delenne[2], J. Lhomme[2,3], V. Guinot[2] and C. Llovel[1]

[1]*GEI (Ginger Environnement et Infrastructures) société du groupe GINGER, France*
[2]*HydroSciences Université Montpellier 2, France*
[3]*HR Wallingford, U.K.*

SUMMARY

PorAS, a new approximate-state Riemann solver, is proposed for hyperbolic systems of conservation laws with source terms and porosity. The use of porosity enables a simple representation of urban floodplains by taking into account the global reduction in the exchange sections and storage. The introduction of the porosity coefficient induces modified expressions for the fluxes and source terms in the continuity and momentum equations. The solution is considered to be made of rarefaction waves and is determined using the Riemann invariants. To allow a direct computation of the flux through the computational cells interfaces, the Riemann invariants are expressed as functions of the flux vector. The application of the PorAS solver to the shallow water equations is presented and several computational examples are given for a comparison with the HLLC solver. Copyright © 2009 John Wiley & Sons, Ltd.

Received 3 November 2008; Revised 20 March 2009; Accepted 20 March 2009

KEY WORDS: approximate-state Riemann solver; porosity; two-dimensional shallow water; PorAS solver; Godunov-type schemes; source terms

1. INTRODUCTION

The complexity of a two-dimensional flood simulation in urban area has recently led to research on the insertion of porosity in the shallow water models. In that sense, porosity can be used to 'represent the effect that the area subject to flooding is only a fraction of the total surface area' [1]. This approach has also been used to model gas flow across grids [2]. The first known derivation of shallow water flow [3] was very simple in that porosity was not fully taken into account in

*Correspondence to: P. Finaud-Guyot, GEI (Ginger Environnement et Infrastructures) société du groupe GINGER, France.
†E-mail: finaud@msem.univ-montp2.fr

Contract/grant sponsor: GEI (Ginger Environnement et Infrastructures)
Contract/grant sponsor: GINGER Group company
Contract/grant sponsor: Association Nationale de la Recherche et de la Technologie; contract/grant number: 2006/838

the equations. Thus, Hervouet *et al*. [4] have proposed a more detailed set of equations that were neither written nor solved in conservative form. Some solvers have already been proposed for hyperbolic systems of conservation laws (HSCLs) with porosity, such as a Finite Volume Roe solver for two-dimensional Euler equations with porosity [2] and an HLLC-modified Riemann solver for the two-dimensional shallow water equations with porosity [5]. An approximate-state (AS) solver was then proposed [6] for HSCLs with source terms. The present paper aims to propose a new AS solver, named PorAS, to solve HSCLs involving topography- and porosity-driven source terms.

In 1959, Godunov [7] proposed to solve HSCLs by considering finite volumes where the calculated value of each variable is assumed to be the average of the variable over the volume. The fluxes between the volumes can be calculated by solving a Riemann problem at the interface. Theoretically, an exact solution of the Riemann problem can be computed but this is a time-consuming procedure, which is not used effectively even with the development of powerful computers. Therefore, many different approaches have been proposed in the last 50 years to solve the Riemann problem. The different developed solvers can be classified into two categories: those solving a simplified Riemann problem in an exact way and those solving the exact Riemann problem with simplified equations.

Considering simplified Riemann problem solved in an exact way, Roe's solver is based on the assumption that the Jacobian matrix is constant [8]. The matrix is calculated using the consistency and conservation conditions. Since the calculation of the the matrix terms can be difficult, a new algorithm was proposed [9] to solve the Riemann problem without computing the whole Jacobian matrix. A second improvement has been provided to the initial Roe's solver in order to enforce the entropy condition [9–12].

The primitive variable Riemann solver (PVRS) [12] uses the so-called primitive variables (which are most of the time not the conserved variables) to express the Riemann problem to solve. This method is based on the Rankine–Hugoniot relation to compute the flow through the discontinuities and the generalized Riemann invariants for rarefaction waves.

For approximate Riemann solvers—as for many others—being quite inefficient close to strong gradients of the variables, the logical rationale is to combine simple Riemann solvers in regions of smooth flow and more sophisticated ones elsewhere in an 'Adaptive Riemann solver'. One of the first proposed [13] involves the PVRS and the exact Riemann solver. It was first implemented for steady supersonic solutions of the Euler equations [14] and later adapted to an MUSCL scheme [15].

Introduced by Harten *et al*. [16], the HLL solver solves an exact Riemann problem with simplified equations. It is based on the assumption of two waves separating three regions of constant state with an *a priori* determination of the waves' speed. Direct estimation of the flux through the interface can be established by the Rankine–Hugoniot relations through each discontinuity. As noticed by Guinot [17], the HLL solver can be applied to any HSCL, whatever its size. However, contact discontinuities are smoothed for the 3×3 HSCLs. An efficient adaptation of the HLL solver is the HLLC solver [18] that uses three waves separating two intermediate regions of constant state from the left and right states of the Riemann problem. The treatment of the discontinuities has also been improved to reduce the numerical diffusion as much as possible.

Osher [19] splits the Jacobian matrix into two matrices containing, respectively, the positive and the negative eigenvalues, and computes the flux vector as the sum of two vector-valued functions.

Another solver, independent of any physical relation [20], uses the Rankine–Hugoniot relation to establish the flux through the left and the right discontinuities; a heuristic relation being used to establish the missing equation in the system to solve.

DOI: 10.1002/fld

Unlike the previously quoted solvers, AS solvers do not determine the wave configuration to use the appropriate relation through each discontinuity. In [21] is shown that the relations used for the shock waves differ from the ones used for the rarefaction waves only by a third-order term with respect to the conservative variable. The same relations are thus used regardless of the nature of the waves: the Rankine–Hugoniot relation is used when all the waves are assumed to be shocks, whereas the generalized Riemann invariants are used when rarefaction waves are considered. Riemann solvers based on a two-shock assumption have been proposed in [22, 23] for the Euler equations of gas dynamics. The assumption of two rarefaction waves has been used for example to solve the water hammer equations [24], a system of equations describing two-phase flows in pipes [25], shock wave propagation in liquids [26] or the Euler equations of gas dynamics [27].

All the above-mentioned solvers are designed for HSCLs without source terms. Consequently, instability may arise in the presence of source terms induced by the porosity or the bottom slope for the shallow water equation. Different methods have been developed to deal with such issues. The time-splitting method is a multi-step algorithm that first solves the hyperbolic system without source terms (i.e. the conservation part of the equation) and then corrects the computed value by taking into account the source terms. Since the time-splitting method is quite efficient except when the solution is close to a steady state, LeVeque [28] proposes the Quasi-Steady Wave-Propagation Algorithm. This algorithm modifies the Riemann problems at the cell edges by introducing an extra Riemann problem at the centre of the cell. Another splitting method (Source term upwinding) consists of assigning the source terms to both cells across the interface according to the wave celerity in the cells [29]. The topography can also be incorporated as part of the conserved variables vector via a partial differential equation with respect to time [30]. This leads to new Riemann problems that are solved in an exact way [1, 30] or with approximate Riemann solvers [31]. The Quasi-Steady algorithm and the Source term upwinding technique are examples of well-balanced schemes.

The PorAS solver presented in this paper is based on the Riemann invariants through a two rarefaction wave assumption, as proposed by Lhomme and Guinot [6] for shallow water equations without porosity. The developments with porosity were initiated in [32] but did not succeed. To allow a direct computation of the flux through the interface, the Riemann invariants are expressed as functions of the flux vector. The following section describes the governing equations and the solution principle applied to the shallow water equations. Computational examples are given in Section 3 to compare the results obtained using the PorAS and HLLC solvers. Conclusion and discussion are given in Section 4.

2. GOVERNING EQUATIONS

2.1. General framework

The overall goal of the proposed solver is to solve the hyperbolic system of conservation laws for the one-dimensional projection of the two-dimensional shallow water equations with source terms arising from non-uniform porosity and bottom elevation. This system can be written in vector form as

$$\frac{\partial \mathbf{U}}{\partial t} + \frac{\partial \mathbf{F}}{\partial x} = \mathbf{S} \tag{1}$$

DOI: 10.1002/fld

where **U** is the conserved variable, **F** is the flux, **S** the source term and t and x are, respectively, the time and the space coordinates. The shallow water equations with porosity (i.e. the continuity and the momentum equation in each direction) written in the form of (1) leads to define **U**, **F** and **S** as

$$\mathbf{U}=\begin{bmatrix}\phi h\\ \phi hu\\ \phi hv\end{bmatrix},\quad \mathbf{F}=\begin{bmatrix}\phi hu\\ \phi hu^2+\frac{1}{2}g\phi h^2\\ \phi huv\end{bmatrix},\quad \mathbf{S}=\begin{bmatrix}0\\ S_0-S_\mathrm{f}+\frac{1}{2}gh^2\frac{\partial\phi}{\partial x}\\ 0\end{bmatrix} \tag{2}$$

where ϕ is the porosity, g the gravitational acceleration, h the water depth, u and v the velocities in the x and y directions, respectively, S_0 and S_f the source terms corresponding to the bottom slope and to the friction in the x direction, respectively. The detailed calculation has been explained in [5, 32]. The source terms S_0 and S_f are defined as

$$S_0=-gh\phi\frac{\partial z_\mathrm{b}}{\partial x},\quad S_\mathrm{f}=gh\phi\frac{(u^2+v^2)^{1/2}}{K^2h^{4/3}}u \tag{3}$$

where z_b is the bottom elevation and K is the Strickler coefficient. The definition of the friction term S_f accounts only for friction on the river bed. In previous works on the subject [5, 33, 34], the friction term S_f was modified to account also for energy losses due to flow regime variations, multiple reflections waves, etc. As shown in Section 2.2, the PorAS solver do not take the friction term into account because its computation is made in a different step, using the time-splitting algorithm. Therefore, the friction term definition does not matter for the purpose of the present work. It can be proved that the system of conservation laws (1) is hyperbolic, i.e. the Jacobian matrix of the flux **F** with respect to **U** exists and has three real and distinct eigenvalues.

Equation (1) is discretized as follows:

$$\mathbf{U}_i^{n+1}=\mathbf{U}_i^n-\frac{\Delta t}{A_i}\sum_{j\in N(i)}[\mathbf{P}_{i,j}\mathbf{F}_{i,j}^{n+1/2}w_{i,j}+(\mathbf{S}_{i,j}^{n+1/2})_i] \tag{4}$$

where

$$\mathbf{P}_{i,j}=\begin{pmatrix}1 & 0 & 0\\ 0 & n(x) & n(y)\\ 0 & -n(y) & n(x)\end{pmatrix}$$

is the matrix that accounts for the coordinate change from the global (x, y) coordinate system to the local one (ξ, ψ), attached to the interface (see Figure 1), $\mathbf{U}_i^n$ is the average of **U** over the cell i at the time step n, Δt is the computational time step, A_i is the area of the cell i, $N(i)$ is the set of neighbouring cells of i, $\mathbf{F}_{i,j}^{n+1/2}$ is the average of **F** between the time step n and $n+1$ in the normal direction, $w_{i,j}$ is the width of the interface between i and j, $\mathbf{S}_{i,j}^{n+1/2}$ is the contribution of the source terms to the cell i computed from **U** between the cells i and j.

In one dimension, this discretization can be simplified as:

$$\mathbf{U}_i^{n+1}=\mathbf{U}_i^n+\frac{\Delta t}{\Delta x_i}(\mathbf{F}_{i-1/2}^{n+1/2}-\mathbf{F}_{i+1/2}^{n+1/2})+\Delta t(\mathbf{S}_{i-1/2,i}^{n+1/2}+\mathbf{S}_{i+1/2,i}^{n+1/2}) \tag{5}$$

DOI: 10.1002/fld

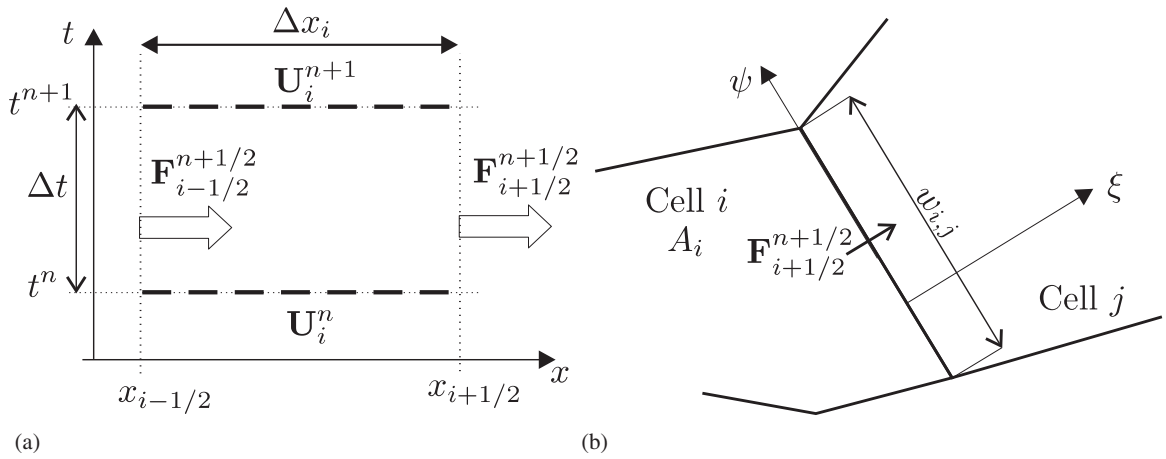

Figure 1. Definition sketch for the finite volume formalism in one dimension (a) and two dimensions (b).

If an explicit method is used to estimate the fluxes (i.e. the fluxes $\mathbf{F}$ are computed using the values of $\mathbf{U}$ at the time step n), the Courant–Friedrichs–Lewy condition must be used to ensure the stability of the numerical solution

$$\frac{\max_p(|\lambda_p|\Delta t)}{\Delta x_i} \leqslant 1 \quad \forall i \tag{6}$$

where λ_p is the pth eigenvalue of the Jacobian matrix $\partial\mathbf{F}/\partial\mathbf{U}$.

It is also possible to generalize (1) to multi-dimensional space problem, but in all cases, the flow variable in a given cell is computed from the balance between the fluxes at the interfaces of the cell and from the contributions of the source terms. As the flux and source terms are frequently computed by solving the one-dimensional equations in the local coordinate system (ξ, ψ), the computation of the one-dimensional equations is a key issue. In [7] is proposed the computation of the flux $\mathbf{F}_{i+1/2}^{n+1/2}$ by solving a Riemann problem at the interface $i+\frac{1}{2}$ between the time step n and $n+1$. The Riemann problem is defined as follows:

$$\begin{aligned} &\frac{\partial\mathbf{U}}{\partial t} + \frac{\partial\mathbf{F}}{\partial x} = \mathbf{S} \\ &\mathbf{U}(x, t^n) = \begin{cases} \mathbf{U}_\mathrm{L} & \text{for } x < x_{i+1/2} \\ \mathbf{U}_\mathrm{R} & \text{for } x > x_{i+1/2} \end{cases} \end{aligned} \tag{7}$$

$\mathbf{U}_\mathrm{L}$ and $\mathbf{U}_\mathrm{R}$ are, respectively, called the left and right state of the Riemann problem.

In most cases, the Riemann solvers do not take the source terms into account in the conservation part of the equation. In such solvers, equilibrium conditions may not be verified. This is the case for instance for water at rest over a non-horizontal bottom. The water depth is not the same on each side of the interface. In the Riemann problem for the shallow water equations, the flux vector computation leads to non-zero discharge and impulse (i.e. the two first components of the flux vector are not nil) [6]. The first component of the source term vector being nil by definition, the non-zero discharge cannot be compensated by the source term discretization. In the second equation, the non-zero impulse can be compensated by a correct discretization of the second component of

DOI: 10.1002/fld

the source term vector (for instance, by using source term upwinding [29, 35]), but this is not the case in the continuity equation. Since equilibrium conditions are not verified, spurious oscillation may arise. In [36] it is proposed to avoid this problem by considering water surface elevation instead of water depth in the shallow water equations. Problems still remain if the variation of the channel width is taken into account in the source terms. For the PorAS solver, equilibrium conditions are satisfied by taking the source terms into account in the Riemann solver. The nature of the waves in the Riemann problem is determined *a priori*. Since characteristic relationships across the rarefaction waves can be approximated by the jump relationships [21, 23], the jump relationships or the Riemann invariants may be used indifferently to provide an approximation of the intermediate states in the solution. The PorAS solver assumes that all waves are rarefaction waves, which simplifies the source terms treatment. This assumption is used to write the Riemann invariant relationships across the waves. Such relationships are generally used to compute the value of **U** and then to estimate **F**. Problems may arise since such a rationale requires the estimation of **S** at the interface; **S** being not necessarily constant on both sides of the interface. Examples with the shallow water equations show that **S** depends on the value of **U** on both sides of the interface. This burden is eliminated in the proposed approach by computing **F** directly at the interface.

2.2. *Flux and source term computation*

This subsection presents the developments for the proposed solver. The solution **U** and the flux **F** are supposed to be differentiable. Equation (1) is multiplied on the left-hand side by the Jacobian matrix **A**. This leads to

$$\mathbf{A}\frac{\partial \mathbf{U}}{\partial t}+\mathbf{A}\frac{\partial \mathbf{F}}{\partial x}=\mathbf{AS} \tag{8}$$

where **A** is given by

$$\mathbf{A}=\begin{pmatrix} 0 & 1 & 0 \\ c^2-u^2 & 2u & 0 \\ -uv & v & u \end{pmatrix} \tag{9}$$

which can also be written as

$$\frac{\partial \mathbf{F}}{\partial t}+\mathbf{A}\frac{\partial \mathbf{F}}{\partial x}=\mathbf{AS} \tag{10}$$

where c is the propagation speed of the pressure waves defined as:

$$c=\left[\frac{\mathrm{d}}{\mathrm{d}h}\left(\frac{gh^2}{2}\right)\right]^{1/2}=(gh)^{1/2} \tag{11}$$

The matrix $\mathbf{\Lambda}$ of the eigenvalues of **A**, the matrix **K** of the eigenvectors of **A** and the inverse matrix of **K** are given by:

$$\mathbf{\Lambda}=\begin{pmatrix} u-c & 0 & 0 \\ 0 & u & 0 \\ 0 & 0 & u+c \end{pmatrix},\quad \mathbf{K}=\begin{pmatrix} 1 & 0 & 1 \\ u-c & 0 & u+c \\ v & 1 & v \end{pmatrix},\quad \mathbf{K}^{-1}=\frac{1}{2c}\begin{pmatrix} u+c & -1 & 0 \\ -2cv & 0 & 2c \\ -(u-c) & 1 & 0 \end{pmatrix} \tag{12}$$

DOI: 10.1002/fld

The wave celerities are therefore given by:

$$\begin{aligned}\lambda_1 &= u-c\\ \lambda_2 &= u\\ \lambda_3 &= u+c\end{aligned} \tag{13}$$

Equation (10) is left multiplied by $\mathbf{K}^{-1}$

$$\mathbf{K}^{-1}\frac{\partial \mathbf{F}}{\partial t}+\mathbf{K}^{-1}\mathbf{A}\frac{\partial \mathbf{F}}{\partial x}=\mathbf{K}^{-1}\mathbf{A}\mathbf{S} \tag{14}$$

Introducing the term $\mathbf{\Lambda}=\mathbf{K}^{-1}\mathbf{A}\mathbf{K}$ leads to:

$$\mathbf{K}^{-1}\frac{\partial \mathbf{F}}{\partial t}+\mathbf{\Lambda}\mathbf{K}^{-1}\frac{\partial \mathbf{F}}{\partial x}=\mathbf{\Lambda}\mathbf{K}^{-1}\mathbf{S} \tag{15}$$

Introducing the definition $\mathrm{d}\mathbf{W}=\mathbf{K}^{-1}\mathrm{d}\mathbf{F}$, Equation (15) can be rewritten as

$$\frac{\partial \mathbf{W}}{\partial t}+\mathbf{\Lambda}\frac{\partial \mathbf{W}}{\partial x}=\mathbf{\Lambda}\mathbf{S}' \tag{16}$$

where the source term $\mathbf{S}'$ is defined by:

$$\mathbf{S}'=\mathbf{K}^{-1}\mathbf{S} \tag{17}$$

From (2) and (12), vectors $\mathrm{d}\mathbf{W}$ and $\mathbf{S}'$ are therefore given by:

$$\mathrm{d}\mathbf{W}=\frac{1}{2c}\begin{bmatrix}\lambda_3\,\mathrm{d}F_1-\mathrm{d}F_2\\ -2cv\,\mathrm{d}F_1+2c\,\mathrm{d}F_3\\ -\lambda_1\,\mathrm{d}F_1+\mathrm{d}F_2\end{bmatrix},\quad \mathbf{S}'=\frac{1}{2c}\begin{bmatrix}S_\mathrm{f}-S_0-\frac{1}{2}gh^2\frac{\partial\phi}{\partial x}\\ 0\\ S_0-S_\mathrm{f}+\frac{1}{2}gh^2\frac{\partial\phi}{\partial x}\end{bmatrix} \tag{18}$$

The overall algorithm used to solve the shallow water equations with porosity (1) and (2) is the same as in [5]. Therefore, the present Riemann solver computes only the flux and the part of the source term that arises from the bottom slope and the porosity gradient. The above-mentioned friction term is computed separately in a different step of the overall algorithm. Therefore, the friction terms are not taken into account in the formulation of the Riemann solver; i.e. S_f is zero in (18). Equation (16) is equivalent to the following set of differential relationships:

$$\frac{\mathrm{d}W_k}{\mathrm{d}t}=\lambda_k S'_k \quad \text{along} \quad \frac{\mathrm{d}x}{\mathrm{d}t}=\lambda_k,\quad k=1,\ldots,m \tag{19}$$

where the subscript k corresponds to the kth component of the vector in (16) and where

$$\mathrm{d}W_k=\sum_{l=1}^{3}K^{-1}_{l,k}\,\mathrm{d}F_l \tag{20}$$

where $K^{-1}_{l,k}$ is the value on the lth column and the kth row of the matrix $\mathbf{K}^{-1}$ and F_l is the lth component of the flux vector $\mathbf{F}$. The Riemann invariants of the system are the W_k if the vector

DOI: 10.1002/fld

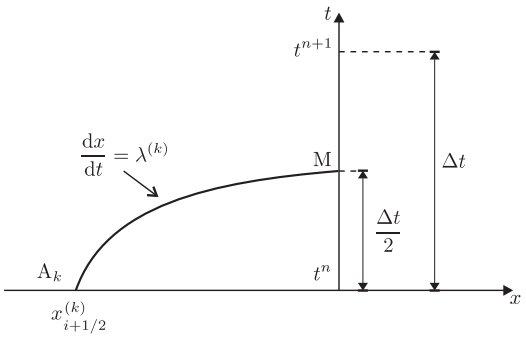

Figure 2. Definition sketch for the integration path along the characteristic.

d**W** can be integrated. It was shown in [37] that it is not possible to integrate d**W** to provide independent Riemann invariants except in particular cases (e.g. for the 2×2 system of conservation laws). The method presented hereafter is thus based on the general formulation (19).

To estimate the flux $\mathbf{F}^{n+1/2}_{i+1/2}$, (19) must be integrated between the points $\mathbf{M}(x_{i+1/2}, t_{n+1/2})$ and the foot A_k of the kth characteristic leading to M: $dx/dt = \lambda_k$ (see Figure 2). Assuming that λ_k is constant along the characteristic, the integration of (19) leads to

$$\int_{A_k}^{M} dW_k = \int_{t^n}^{t^{n+1/2}} \lambda_k S'_k \, dt \approx \frac{\Delta t}{2} \lambda_k \overline{S'_k}, \quad k = 1, 2, 3 \tag{21}$$

where $\overline{S'_k}$ is the average of S'_k along the integration path. Substituting (20) into (21) leads to:

$$\int_{A_k}^{M} \sum_{l=1}^{3} K^{-1}_{l,k} \, dF_l = \frac{\Delta t}{2} \lambda_k \overline{S'_k}, \quad k = 1, 2, 3 \tag{22}$$

The coefficients of the matrix $\mathbf{K}^{-1}$ are assumed to be constant along the characteristics [6]. The coefficients in the kth row of the matrix are thus taken equal to the coefficients on the side of the interface to which the foot A_k of the kth characteristic belongs:

$$K^{-1}_{l,k} = \begin{cases} K^{-1}_{l,k}(\mathbf{U}_L) & \text{if } \lambda_k > 0 \\ K^{-1}_{l,k}(\mathbf{U}_R) & \text{if } \lambda_k < 0 \end{cases} \tag{23}$$

Since the coefficients of the matrix $\mathbf{K}^{-1}$ and λ_k are assumed to be constant along the integration path, (22) can be written as

$$\int_{A_k}^{M} \sum_{l=1}^{3} K^{-1}_{l,k} \, dF_l \approx \sum_{l=1}^{3} K^{-1}_{l,k} \int_{A_k}^{M} dF_l = \frac{\Delta t}{2} \lambda_k \overline{S'_k}, \quad k = 1, 2, 3 \tag{24}$$

and therefore

$$\sum_{l=1}^{3} K^{-1}_{l,k} (F_{l,M} - F_{l,A_k}) = \frac{\Delta t}{2} \lambda_k \overline{S'_k}, \quad k = 1, 2, 3 \tag{25}$$

DOI: 10.1002/fld

where $F_{l,M}$ and F_{l,A_k} represent the lth component of the vector $\mathbf{F}$, respectively, in M and A_k. A_k is located on the left-hand side of the interface when λ_k is positive and on the right-hand side when λ_k is negative. Therefore,

$$F_{l,A_k} = \begin{cases} F_{l,\mathrm{L}} & \text{if } \lambda_k > 0 \\ F_{l,\mathrm{R}} & \text{if } \lambda_k < 0 \end{cases} \tag{26}$$

The value of $\mathbf{F}$ at $M(x_{i+1/2}, t_{n+1/2})$ is computed by solving the 3×3 system of equations (25). This value is assumed to be equal to the average value $\mathbf{F}_{i+1/2}^{n+1/2}$ over the time step $n,\ n+1$. Prior to resolution, the average source term $\overline{S'_k}$ is estimated by

$$\overline{S'_k} = S'_k\left(\mathbf{U}_{\mathrm{LR}}, \left(\frac{\partial z_\mathrm{b}}{\partial x}\right)_{\mathrm{LR}}, \left(\frac{\partial \phi}{\partial x}\right)_{\mathrm{LR}}\right) \tag{27}$$

where

$$\left(\frac{\partial z_\mathrm{b}}{\partial x}\right)_{\mathrm{LR}} \approx \frac{z_{\mathrm{b_R}} - z_{\mathrm{b_L}}}{(\lambda_3 - \lambda_1)\dfrac{\Delta t}{2}} \tag{28a}$$

$$\left(\frac{\partial \phi}{\partial x}\right)_{\mathrm{LR}} \approx \frac{\phi_\mathrm{R} - \phi_\mathrm{L}}{(\lambda_3 - \lambda_1)\dfrac{\Delta t}{2}} \tag{28b}$$

correspond to the average slope over the domain of dependence of the solution. Combining (28) with (2) and (3) leads to

$$S = -g(\phi h)_{\mathrm{LR}} \frac{z_{\mathrm{b_R}} - z_{\mathrm{b_L}}}{(\lambda_3 - \lambda_1)\dfrac{\Delta t}{2}} + \frac{1}{2} g (h_{\mathrm{LR}})^2 \frac{\phi_\mathrm{R} - \phi_\mathrm{L}}{(\lambda_3 - \lambda_1)\dfrac{\Delta t}{2}} \tag{29}$$

where $(\phi h)_{\mathrm{LR}}$ is estimated at the interface between the left and right cells and h_{LR} is the depth at the interface. These variables may depend on the considered characteristic.

The eigenvalues of $\mathbf{A}$ are assumed to be constant. Substituting (12) and (18) in (25) leads to:

$$\lambda_3(F_1 - F_{1,\mathrm{R}}) - (F_2 - F_{2,\mathrm{R}}) = -\frac{\Delta t}{2}\lambda_1 S \quad \text{for } \frac{\mathrm{d}x}{\mathrm{d}t} = \lambda_1 \tag{30a}$$

$$-v(F_1 - F_{1,A}) + (F_3 - F_{3,A}) = 0 \quad \text{for } \frac{\mathrm{d}x}{\mathrm{d}t} = \lambda_2 \tag{30b}$$

$$-\lambda_1(F_1 - F_{1,\mathrm{L}}) + (F_2 - F_{2,\mathrm{L}}) = \frac{\Delta t}{2}\lambda_3 S \quad \text{for } \frac{\mathrm{d}x}{\mathrm{d}t} = \lambda_3 \tag{30c}$$

with

$$F_{l,A} = \begin{cases} F_{l,\mathrm{L}} & \text{if } \lambda_2 > 0 \\ F_{l,\mathrm{R}} & \text{if } \lambda_2 < 0 \end{cases} \tag{31}$$

Since (30a) and (30c) are written for two different waves, the expressions $(\phi h)_{\mathrm{LR}}$ and (h_{LR}) used in (29) for the definition of S may be different. In the following, the variables at the interface are so written with the superscripts $^{(1)}$, $^{(2)}$ and $^{(S)}$; corresponding, respectively, to the variables at the

DOI: 10.1002/fld

interface for the first and second component of the flux vector and for the source term. The next subsection is devoted to their evaluation. Combining (29) with (30) leads to the following system of equations that is valid for the flux vector in the intermediate region of constant state (marked by the star superscript):

$$F_1^* = \frac{1}{\lambda_3-\lambda_1}(F_{2,\mathrm{L}} - F_{2,\mathrm{R}} - \lambda_1 F_{1,\mathrm{L}} + \lambda_3 F_{1,\mathrm{R}}) + \frac{1}{\lambda_3-\lambda_1}\left[\frac{1}{2}g(h_{\mathrm{LR}}^{(1)})^2(\phi_{\mathrm{R}}-\phi_{\mathrm{L}}) - g(\phi h)_{\mathrm{LR}}^{(1)}(z_{\mathrm{b_R}} - z_{\mathrm{b_L}})\right] \tag{32a}$$

$$F_2^* = \frac{1}{\lambda_3-\lambda_1}(\lambda_3 F_{2,\mathrm{L}} - \lambda_1 F_{2,\mathrm{R}} - \lambda_1\lambda_3(F_{1,\mathrm{L}} - F_{1,\mathrm{R}})) + \frac{\lambda_3+\lambda_1}{\lambda_3-\lambda_1}\left[\frac{1}{2}g(h_{\mathrm{LR}}^{(2)})^2(\phi_{\mathrm{R}}-\phi_{\mathrm{L}}) - g(\phi h)_{\mathrm{LR}}^{(2)}(z_{\mathrm{b_R}} - z_{\mathrm{b_L}})\right] \tag{32b}$$

$$F_3^* = v(F_1^* - F_{1,A}) + F_{3,A} \tag{32c}$$

2.3. Estimation of the variables at the interface

The estimation of the different variables at the interface is made by using physical cases. One should notice that porosity can be considered as the effective width of the computing cell available for the flow. In a one-dimensional problem, involving a spatial variation of the porosity or the width leads to the same set of equations.

2.3.1. Estimation of $(\phi h)_{\mathrm{LR}}^{(1)}$ *and* $h_{\mathrm{LR}}^{(1)}$. These values are determined using the continuity and momentum equations. The continuity equation can be written as:

$$(\phi hu)_{\mathrm{L}} = (\phi hu)_{\mathrm{R}} = (\phi hu)^* = q \tag{33}$$

Combining (33) with the expression of the flux F_1^* in (32a) leads to:

$$F_1^* = \frac{1}{\lambda_3-\lambda_1}\left[q(u_{\mathrm{L}}-u_{\mathrm{R}}) + \frac{1}{2}g((\phi h^2)_{\mathrm{L}} - (\phi h^2)_{\mathrm{R}})\right] + \frac{1}{\lambda_3-\lambda_1}\left[\frac{1}{2}g(h_{\mathrm{LR}}^{(1)})^2(\phi_{\mathrm{R}}-\phi_{\mathrm{L}}) - g(\phi h)_{\mathrm{LR}}^{(1)}(z_{\mathrm{b_R}} - z_{\mathrm{b_L}})\right] + q \tag{34}$$

In a steady-state case, F_1^* is equal to the flow q across the interface and hence:

$$q(u_{\mathrm{L}}-u_{\mathrm{R}}) + \tfrac{1}{2}g[(\phi h^2)_{\mathrm{L}} - (\phi h^2)_{\mathrm{R}}] + \tfrac{1}{2}g(h_{\mathrm{LR}}^{(1)})^2(\phi_{\mathrm{R}}-\phi_{\mathrm{L}}) - g(\phi h)_{\mathrm{LR}}^{(1)}(z_{\mathrm{b_R}} - z_{\mathrm{b_L}}) = 0 \tag{35}$$

The first relation linking the three variables has been established; the momentum equation is used to estimate q. The balance is carried out on two cells on both sides of a porosity and bottom elevation discontinuity. To establish the balance, the forces applied to the fluid have to be estimated along the horizontal axis. Hereafter, the flow is assumed to be directed from left to right. The different sketches used to derive the momentum balance are illustrated in Figure 3.

DOI: 10.1002/fld

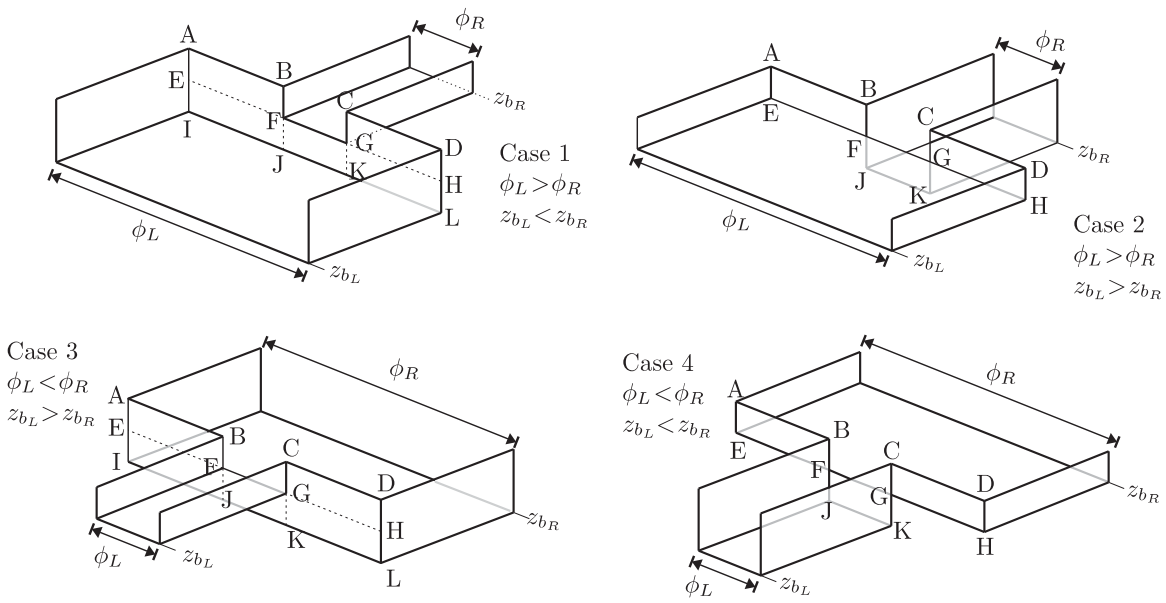

Figure 3. Considered sketches to establish the momentum equation.

The force calculation is detailed for case 1 corresponding to $z_{b_L} < z_{b_R}$ and $\phi_L > \phi_R$.
Force exerted by areas ABFE and CDHG:

$$F_a = -g \int_{\phi_R}^{\phi_L} \left[\int_{z_{b_R}}^{z_L} (z_L - z)\, dz \right] d\phi = -\frac{1}{2} g (\phi_L - \phi_R)(z_L - z_{b_R})^2 \tag{36}$$

Force exerted by area FGKJ:

$$F_b = -g\phi_R \int_{z_{b_L}}^{z_{b_R}} (z_L - z)\, dz = -g\phi_R (z_{b_R} - z_{b_L}) \left(z_L - \frac{z_{b_R} + z_{b_L}}{2} \right) \tag{37}$$

Force exerted by areas EFJI and GHLK:

$$F_c = -g \int_{\phi_R}^{\phi_L} \left[\int_{z_{b_L}}^{z_{b_R}} (z_L - z)\, dz \right] d\phi = -g(\phi_L - \phi_R)(z_{b_R} - z_{b_L}) \left(z_L - \frac{z_{b_R} + z_{b_L}}{2} \right) \tag{38}$$

Total force exerted onto the fluid:

$$F_a + F_b + F_c = -\frac{1}{2} g (\phi_L - \phi_R) h_L^2 - g\phi_R (z_{b_R} - z_{b_L}) \left(z_L - \frac{z_{b_R} + z_{b_L}}{2} \right) \tag{39}$$

The momentum balance should be written for a steady-state regime to ensure static balance:

$$(\phi h u^2 + \tfrac{1}{2} g \phi h^2)_R - (\phi h u^2 + \tfrac{1}{2} g \phi h^2)_L = F_a + F_b + F_c \tag{40}$$

Combining Equations (39) and (40) leads to:

$$q(u_R - u_L) = \frac{1}{2} g [(\phi h^2)_L - (\phi h^2)_R] - \frac{1}{2} g (\phi_L - \phi_R) h_L^2 - g\phi_R (z_{b_R} - z_{b_L}) \left(z_L - \frac{z_{b_R} + z_{b_L}}{2} \right) \tag{41}$$

DOI: 10.1002/fld

Using the same reasoning for cases 2 to 4 leads to the following general expression:

$$q(u_{\mathrm{L}}-u_{\mathrm{R}})=-\frac{1}{2}g[(\phi h^2)_{\mathrm{L}}-(\phi h^2)_{\mathrm{R}}]+\frac{1}{2}g(\phi_{\mathrm{L}}-\phi_{\mathrm{R}})(h_{\mathrm{LR}}^{(0)})^2 +g\phi_{\mathrm{LR}}^{(0)}(z_{\mathrm{b_R}}-z_{\mathrm{b_L}})\left(z_{\mathrm{LR}}^{(0)}-\frac{z_{\mathrm{b_R}}+z_{\mathrm{b_L}}}{2}\right) \tag{42}$$

where

$$\phi_{\mathrm{LR}}^{(0)}=\min(\phi_{\mathrm{L}};\phi_{\mathrm{R}}) \tag{43a}$$

$$z_{\mathrm{LR}}^{(0)}=\begin{cases} z_{\mathrm{L}} & \text{if } z_{\mathrm{b_L}}<z_{\mathrm{b_R}} \\ z_{\mathrm{R}} & \text{if } z_{\mathrm{b_L}}>z_{\mathrm{b_R}} \end{cases} \tag{43b}$$

$$h_{\mathrm{LR}}^{(0)}=\begin{cases} h_{\mathrm{L}} & \text{if } \phi_{\mathrm{L}}>\phi_{\mathrm{R}} \\ h_{\mathrm{R}} & \text{if } \phi_{\mathrm{L}}<\phi_{\mathrm{R}} \end{cases} \tag{43c}$$

Combining (35) and (42) yields the following equation:

$$\frac{1}{2}g(\phi_{\mathrm{L}}-\phi_{\mathrm{R}})[(h_{\mathrm{LR}}^{(0)})^2-(h_{\mathrm{LR}}^{(1)})^2]+g(z_{\mathrm{b_L}}-z_{\mathrm{b_R}})\left[(\phi h)_{\mathrm{LR}}^{(1)}-\phi_{\mathrm{LR}}^{(0)}\left(z_{\mathrm{LR}}^{(0)}-\frac{z_{\mathrm{b_R}}+z_{\mathrm{b_L}}}{2}\right)\right]=0 \tag{44}$$

Equation (44) involves the unknown variables $(\phi h)_{\mathrm{LR}}^{(1)}$ and $h_{\mathrm{LR}}^{(1)}$. However, the equation is valid whatever the values of $\phi_{\mathrm{R}}, \phi_{\mathrm{L}}, z_{\mathrm{b_L}}$ and $z_{\mathrm{b_R}}$ may be. Considering the particular case $\phi_{\mathrm{L}}=\phi_{\mathrm{R}}$ in (44) leads to

$$(\phi h)_{\mathrm{LR}}^{(1)}=\phi_{\mathrm{LR}}^{(0)}\left(z_{\mathrm{LR}}^{(0)}-\frac{z_{\mathrm{b_R}}+z_{\mathrm{b_L}}}{2}\right) \tag{45}$$

whereas the case $z_{\mathrm{b_R}}=z_{\mathrm{b_L}}$ implies $(h_{\mathrm{LR}}^{(1)})^2=(h_{\mathrm{LR}}^{(0)})^2$. Since $h_{\mathrm{LR}}^{(1)}$ corresponds to the water depth at the interface, this value should be positive and thus:

$$h_{\mathrm{LR}}^{(1)}=h_{\mathrm{LR}}^{(0)} \tag{46}$$

2.3.2. Estimation of $(\phi h)_{\mathrm{LR}}^{(S)}$ *and* $h_{\mathrm{LR}}^{(S)}$. A momentum balance on two cells on both sides of a porosity and bottom elevation discontinuity is used. The integral form of the source term can be written as

$$(\Delta S_0)_{\mathrm{LR}}^{n+1/2}=-g(\phi h)_{\mathrm{LR}}^{(S)}(z_{\mathrm{b_R}}-z_{\mathrm{b_L}})+\tfrac{1}{2}g(h_{\mathrm{LR}}^{(S)})^2(\phi_{\mathrm{R}}-\phi_{\mathrm{L}}) \tag{47}$$

and the momentum balance can be written as:

$$(\phi hu^2+\tfrac{1}{2}g\phi h^2)_{\mathrm{L}}^{n+1/2}-(\phi hu^2+\tfrac{1}{2}g\phi h^2)_{\mathrm{R}}^{n+1/2}+(\Delta S_0)_{\mathrm{LR}}^{n+1/2}=0 \tag{48}$$

Combining (47) with (48) leads to:

$$q(u_{\mathrm{L}}-u_{\mathrm{R}})+\tfrac{1}{2}g[(\phi h^2)_{\mathrm{L}}-(\phi h^2)_{\mathrm{R}}]+g(\phi h)_{\mathrm{LR}}^{(S)}(z_{\mathrm{b_L}}-z_{\mathrm{b_R}})-\tfrac{1}{2}g(h_{\mathrm{LR}}^{(S)})^2(\phi_{\mathrm{L}}-\phi_{\mathrm{R}})=0 \tag{49}$$

DOI: 10.1002/fld

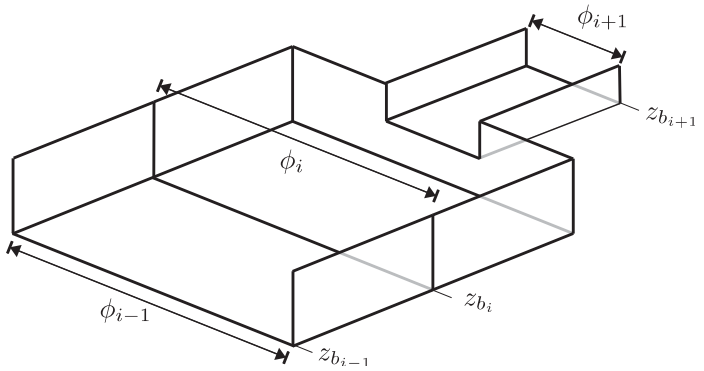

Figure 4. Considered sketch to establish the momentum equation for the estimation of $(\phi h)^{(2)}_{\mathrm{LR}}$ and $h^{(2)}_{\mathrm{LR}}$.

Substituting $q(u_{\mathrm{L}}-u_{\mathrm{R}})$ in (49) by the expression (42) yields:

$$g(z_{\mathrm{b_L}}-z_{\mathrm{b_R}})\left[(\phi h)^{(S)}_{\mathrm{LR}}-\phi^{(0)}_{\mathrm{LR}}\left(z^{(0)}_{\mathrm{LR}}-\frac{z_{\mathrm{b_R}}+z_{\mathrm{b_L}}}{2}\right)\right]+\frac{1}{2}g(\phi_{\mathrm{L}}-\phi_{\mathrm{R}})[(h^{(0)}_{\mathrm{LR}})^2-(h^{(S)}_{\mathrm{LR}})^2]=0 \tag{50}$$

As (50) is equivalent to (44), it is possible to conclude that:

$$(\phi h)^{(S)}_{\mathrm{LR}}=(\phi h)^{(1)}_{\mathrm{LR}} \tag{51}$$

$$(h^{(S)}_{\mathrm{LR}})^2=(h^{(1)}_{\mathrm{LR}})^2\Rightarrow h^{(S)}_{\mathrm{LR}}=h^{(1)}_{\mathrm{LR}} \tag{52}$$

2.3.3. Estimation of $(\phi h)^{(2)}_{\mathrm{LR}}$ *and* $h^{(2)}_{\mathrm{LR}}$. A steady-state momentum balance is carried out on three cells ($i-1$, i and $i+1$) with a porosity and bottom elevation discontinuity between the cells i and $i+1$ (see the sketch on Figure 4).

The momentum balance over the cell i can be written as:

$$(\phi hu)^{n+1}_i-(\phi hu)^n_{i+1}=\frac{\Delta t}{\Delta x_i}\left(F^*_2+\frac{\lambda_3}{\lambda_3-\lambda_1}\Delta S_0\right)^{n+1/2}_{i-1/2}-\frac{\Delta t}{\Delta x_i}\left(F^*_2+\frac{\lambda_1}{\lambda_3-\lambda_1}\Delta S_0\right)^{n+1/2}_{i+1/2}=0 \tag{53}$$

Combining (32b) with (53) leads, for the interface between the cells $i-1$ and i, to:

$$\begin{aligned}
&\left(F^*_2+\frac{\lambda_3}{\lambda_3-\lambda_1}\Delta S_0\right)^{n+1/2}_{i-1/2}\\
&\quad=\frac{1}{\lambda_3-\lambda_1}\left[\lambda_3\left(\phi hu^2+\frac{1}{2}g\phi h^2\right)_{i-1}-\lambda_1\left(\phi hu^2+\frac{1}{2}g\phi h^2\right)_i-\lambda_3\lambda_1((\phi hu)_{i-1}-(\phi hu)_i)\right]\\
&\qquad+\frac{\lambda_3+\lambda_1}{\lambda_3-\lambda_1}\left[\frac{1}{2}g(h^{(2)}_{i-1/2})^2(\phi_{i-1}-\phi_i)+g(z_{\mathrm{b}_{i-1}}-z_{\mathrm{b}_i})(\phi h)^{(2)}_{i-1/2}\right]\\
&\qquad+\frac{\lambda_3}{\lambda_3-\lambda_1}\left[g\phi^{(0)}_{\mathrm{LR}}(z_{\mathrm{b}_{i-1}}-z_{\mathrm{b}_i})\left(z^{(0)}_{\mathrm{LR}}-\frac{z_{\mathrm{b}_{i-1}}+z_{\mathrm{b}_i}}{2}\right)-\frac{1}{2}g(\phi_{i-1}-\phi_i)(h^{(0)}_{\mathrm{LR}})^2\right]
\end{aligned} \tag{54}$$

DOI: 10.1002/fld

Since there is no discontinuity between cells $i-1$ and i:

$$\begin{aligned}(\phi hu^2+\tfrac{1}{2}g\phi h^2)_{i-1} &= (\phi hu^2+\tfrac{1}{2}g\phi h^2)_i \neq (\phi hu^2+\tfrac{1}{2}g\phi h^2)_{i+1}\\ (\phi hu)_{i-1} &= (\phi hu)_i = (\phi hu)_{i+1} = q\\ \phi_{i-1} &= \phi_i \neq \phi_{i+1}\\ z_{\mathrm{b}_{i-1}} &= z_{\mathrm{b}_i} \neq z_{\mathrm{b}_{i+1}}\end{aligned} \tag{55}$$

Introducing (55) into (54) leads to:

$$\begin{aligned}\left(F_2^*+\frac{\lambda_1}{\lambda_3-\lambda_1}\Delta S_0\right)_{i-1/2}^{n+1/2} &= \frac{1}{\lambda_3-\lambda_1}\left[\lambda_3\left(\phi hu^2+\frac{1}{2}g\phi h^2\right)_i-\lambda_1\left(\phi hu^2+\frac{1}{2}g\phi h^2\right)_i\right]\\ &= \left(\phi hu^2+\frac{1}{2}g\phi h^2\right)_i\end{aligned} \tag{56}$$

At the interface between the cells i and $i+1$, the momentum flux can therefore be written as:

$$\begin{aligned}&\left(F_2^*+\frac{\lambda_1}{\lambda_3-\lambda_1}\Delta S_0\right)_{i+1/2}^{n+1/2}\\ &=\frac{1}{\lambda_3-\lambda_1}\left[\lambda_3\left(\phi hu^2+\frac{1}{2}g\phi h^2\right)_i-\lambda_1\left(\phi hu^2+\frac{1}{2}g\phi h^2\right)_{i+1}-\lambda_3\lambda_1[(\phi hu)_i-(\phi hu)_{i+1}]\right]\\ &\quad+\frac{\lambda_3+\lambda_1}{\lambda_3-\lambda_1}\left[\frac{1}{2}g(h^{(2)}_{i+1/2})^2(\phi_i-\phi_{i+1})+g(z_{\mathrm{b}_i}-z_{\mathrm{b}_{i+1}})(\phi h)^{(2)}_{i+1/2}\right]\\ &\quad+\frac{\lambda_1}{\lambda_3-\lambda_1}\left[g\phi^{(0)}_{\mathrm{LR}}(z_{\mathrm{b}_i}-z_{\mathrm{b}_{i+1}})\left(z^{(0)}_{\mathrm{LR}}-\frac{z_{\mathrm{b}_i}+z_{\mathrm{b}_{i+1}}}{2}\right)-\frac{1}{2}g(\phi_i-\phi_{i+1})(h^{(0)}_{\mathrm{LR}})^2\right]\end{aligned} \tag{57}$$

Applying the continuity equation in (57) leads to:

$$\begin{aligned}&\left(F_2^*+\frac{\lambda_1}{\lambda_3-\lambda_1}\Delta S_0\right)_{i+1/2}^{n+1/2}\\ &=\frac{1}{\lambda_3-\lambda_1}\left[\lambda_3\left(\phi hu^2+\frac{1}{2}g\phi h^2\right)_i-\lambda_1\left(\phi hu^2+\frac{1}{2}g\phi h^2\right)_{i+1}\right]\\ &\quad+\frac{\lambda_3+\lambda_1}{\lambda_3-\lambda_1}\left[\frac{1}{2}g(h^{(2)}_{i+1/2})^2(\phi_i-\phi_{i+1})+g(z_{\mathrm{b}_i}-z_{\mathrm{b}_{i+1}})(\phi h)^{(2)}_{i+1/2}\right]\\ &\quad+\frac{\lambda_1}{\lambda_3-\lambda_1}\left[g\phi^{(0)}_{\mathrm{LR}}(z_{\mathrm{b}_i}-z_{\mathrm{b}_{i+1}})\left(z^{(0)}_{\mathrm{LR}}-\frac{z_{\mathrm{b}_i}+z_{\mathrm{b}_{i+1}}}{2}\right)-\frac{1}{2}g(\phi_i-\phi_{i+1})(h^{(0)}_{\mathrm{LR}})^2\right]\end{aligned} \tag{58}$$

The steady-state assumption implies that

$$(\phi hu)_i^{n+1}-(\phi hu)_i^n=0 \tag{59}$$

DOI: 10.1002/fld

and hence

$$\left(F_2^* + \frac{\lambda_3}{\lambda_3 - \lambda_1}\Delta S_0\right)_{i-1/2}^{n+1/2} = \left(F_2^* + \frac{\lambda_1}{\lambda_3 - \lambda_1}\Delta S_0\right)_{i+1/2}^{n+1/2} \tag{60}$$

Combining (60), (58) and (56) yields:

$$\begin{aligned}
&\lambda_1 \left\{ q(u_i - u_{i+1}) + \frac{1}{2} g[(\phi h^2)_i - (\phi h^2)_{i+1}] \right\} \\
&+ (\lambda_3 - \lambda_1) \left[\frac{1}{2} g (h_{i+1/2}^{(2)})^2 (\phi_i - \phi_{i+1}) + g(z_{\mathrm{b}_i} - z_{\mathrm{b}_{i+1}})(\phi h)_{i+1/2}^{(2)} \right] \\
&+ \lambda_1 \left[g \phi_{\mathrm{LR}}^{(0)} (z_{\mathrm{b}_i} - z_{\mathrm{b}_{i+1}}) \left(z_{\mathrm{LR}}^{(0)} - \frac{z_{\mathrm{b}_i} - z_{\mathrm{b}_{i+1}}}{2} \right) - \frac{1}{2} g(\phi_i - \phi_{i+1})(h_{\mathrm{LR}}^{(0)})^2 \right] = 0
\end{aligned} \tag{61}$$

Substituting $q(u_i - u_{i+1})$ in (61) by the expression (42) leads to:

$$\tfrac{1}{2} g (h_{i+1/2}^{(2)})^2 (\phi_i - \phi_{i+1}) + g(z_{\mathrm{b}_i} - z_{\mathrm{b}_{i+1}})(\phi h)_{i+1/2}^{(2)} = 0 \tag{62}$$

As (62) is valid for all existing cases depending on the respective values of ϕ_{i+1}, ϕ_i, z_{b_i} and $z_{\mathrm{b}_{i+1}}$, it is possible to conclude that $h_{i+1/2}^{(2)} = 0$ and $(\phi h)_{i+1/2}^{(2)} = 0$.

Substituting $(\phi h)_{\mathrm{LR}}^{(1)}$, $(\phi h)_{\mathrm{LR}}^{(2)}$, $(\phi h)_{\mathrm{LR}}^{(S)}$, $h_{\mathrm{LR}}^{(1)}$, $h_{\mathrm{LR}}^{(2)}$ and $h_{\mathrm{LR}}^{(S)}$ in the system of equations (32) yields the following expression for the flux through the interface:

$$\begin{aligned}
F_1^* = &\frac{1}{\lambda_3 - \lambda_1} [F_{2,\mathrm{L}} - F_{2,\mathrm{R}} - \lambda_1 F_{1,\mathrm{L}} + \lambda_3 F_{1,\mathrm{R}}] \\
&+ \frac{1}{\lambda_3 - \lambda_1} \left[\frac{1}{2} g(\phi_{\mathrm{R}} - \phi_{\mathrm{L}})(h_{\mathrm{LR}}^{(0)})^2 - g \phi_{\mathrm{LR}}^{(0)} (z_{\mathrm{b_R}} - z_{\mathrm{b_L}}) \left(z_{\mathrm{LR}}^{(0)} - \frac{z_{\mathrm{b_R}} + z_{\mathrm{b_L}}}{2} \right) \right]
\end{aligned} \tag{63a}$$

$$F_2^* = \frac{1}{\lambda_3 - \lambda_1} [\lambda_3 F_{2,\mathrm{L}} - \lambda_1 F_{2,\mathrm{R}} - \lambda_1 \lambda_3 (F_{1,\mathrm{L}} - F_{1,\mathrm{R}})] \tag{63b}$$

$$F_3^* = v(F_1^* - F_{1,A}) + F_{3,A} \tag{63c}$$

where $\phi_{\mathrm{LR}}^{(0)}$, $z_{\mathrm{LR}}^{(0)}$ and $h_{\mathrm{LR}}^{(0)}$ are defined by (43).

2.4. Practical implementation

The values computed for the flux using the system of equations (63) are only valid for the flux in the intermediate constant zone. For the purpose of the solver, it is necessary to determine the flux at the interface between the cells, i.e. the initial discontinuity of the Riemann problem. Five different cases can be defined depending on the wave configuration and the respective location of the intermediate zone and the interface (see Figure 5 for more detail).

It is recalled that configurations C1 and C5 correspond to a supercritical regime, configurations C2 and C4 correspond to a critical regime and configuration C3 corresponds to the subcritical regime. It is necessary to estimate the celerities λ_1^* and λ_3^* in the constant intermediate zone. Along

DOI: 10.1002/fld

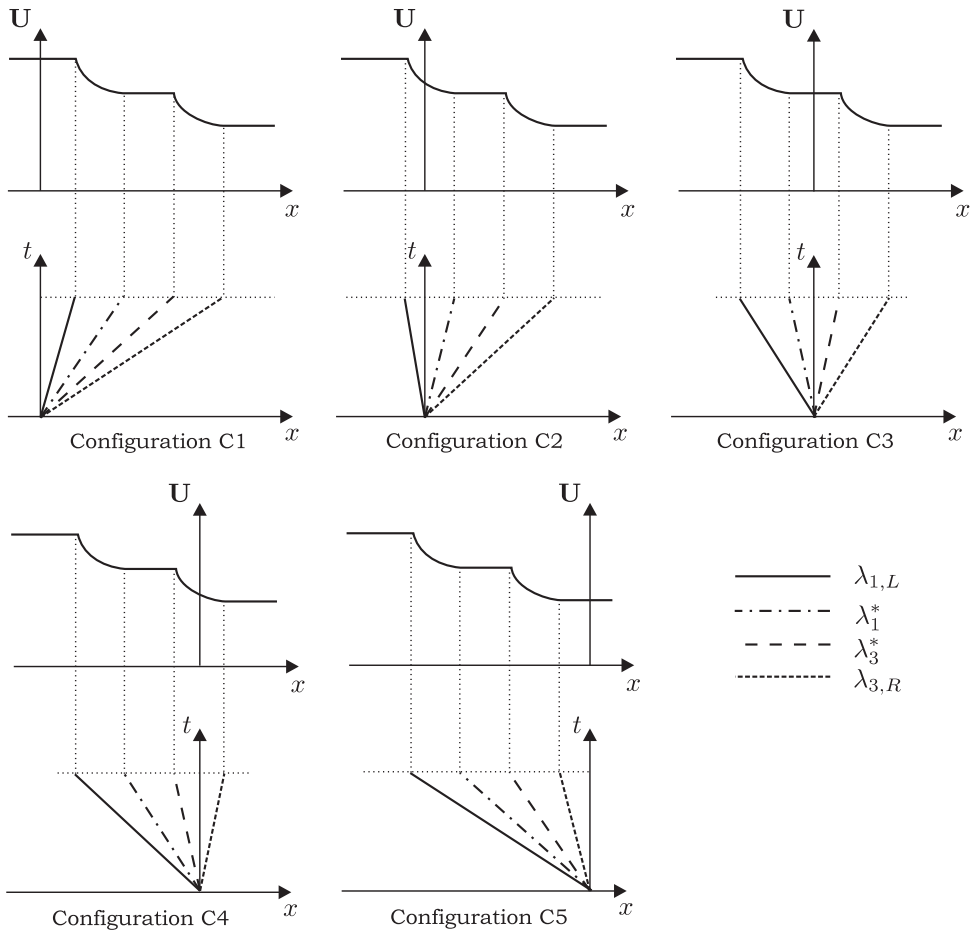

Figure 5. Relative position of the intermediate region to the interface.

each characteristic, the Riemann invariants are used to compute u^* and c^*:

$$\begin{aligned} u^* + 2c^* &= u_\mathrm{L} + 2c_\mathrm{L} \\ u^* - 2c^* &= u_\mathrm{R} - 2c_\mathrm{R} \end{aligned} \tag{64}$$

The source terms have to be taken into account in (64) but the experiment shows that they can be neglected at this stage. Solving the system of equations (64) leads to:

$$\begin{aligned} u^* &= \frac{u_\mathrm{L} + u_\mathrm{R}}{2} + c_\mathrm{L} - c_\mathrm{R} \\ c^* &= \frac{u_\mathrm{L} - u_\mathrm{R}}{4} + \frac{c_\mathrm{L} + c_\mathrm{R}}{2} \end{aligned} \tag{65}$$

The celerities λ_1^* and λ_3^* are computed as follows:

$$\begin{aligned} \lambda_1^* &= u^* - c^* \\ \lambda_3^* &= u^* + c^* \end{aligned} \tag{66}$$

DOI: 10.1002/fld

The comparison of λ_1^*, λ_3^*, $\lambda_{1,\mathrm{L}}$ and $\lambda_{3,\mathrm{R}}$ enables to determine the wave configuration and thus the value of the flux vector component at the initial discontinuity. For the critical regime, the fluxes are computed using the classical HLLC formulae:

$$
\begin{array}{ll}
\lambda_{1,\mathrm{L}}>0 & \begin{cases} F_1 = F_{1,\mathrm{L}} \\ F_2 = F_{2,\mathrm{L}} \end{cases} \quad \text{C1} \\
\lambda_{1,\mathrm{L}}<0 \ \& \ \lambda_1^*>0 & \begin{cases} F_1 = \dfrac{1}{\lambda_3-\lambda_1}[\lambda_3 F_{1,\mathrm{L}} - \lambda_1 F_{1,\mathrm{R}} - \lambda_1\lambda_3(z_\mathrm{L}-z_\mathrm{R})] \\ F_2 = \dfrac{1}{\lambda_3-\lambda_1}[\lambda_3 F_{2,\mathrm{L}} - \lambda_1 F_{2,\mathrm{R}} - \lambda_1\lambda_3(F_{1,\mathrm{L}}-F_{1,\mathrm{R}})] \end{cases} \quad \text{C2} \\
\lambda_1^*<0 \ \& \ \lambda_3^*>0 & \begin{cases} F_1 = F_1^* \\ F_2 = F_2^* \end{cases} \quad \text{C3} \\
\lambda_3^*<0 \ \& \ \lambda_{3,\mathrm{R}}>0 & \begin{cases} F_1 = \dfrac{1}{\lambda_3-\lambda_1}[\lambda_3 F_{1,\mathrm{L}} - \lambda_1 F_{1,\mathrm{R}} - \lambda_1\lambda_3(z_\mathrm{L}-z_\mathrm{R})] \\ F_2 = \dfrac{1}{\lambda_3-\lambda_1}[\lambda_3 F_{2,\mathrm{L}} - \lambda_1 F_{2,\mathrm{R}} - \lambda_1\lambda_3(F_{1,\mathrm{L}}-F_{1,\mathrm{R}})] \end{cases} \quad \text{C4} \\
\lambda_{3,\mathrm{R}}<0 & \begin{cases} F_1 = F_{1,\mathrm{R}} \\ F_2 = F_{2,\mathrm{R}} \end{cases} \quad \text{C5}
\end{array}
\tag{67}
$$

For any waves configuration, the fluxes at the interface can be computed and the values of the conserved variables can therefore be calculated at each time.

3. COMPUTATIONAL EXAMPLES

Eight different geometries have been used to determine the efficiency of the PorAS solver under different flow conditions (subcritical, supercritical, transcritical and hydraulic jump) leading to 13 tests cases (named $T_{i,(\mathrm{sub,\,sup,\,trans,\,jump})}$). The results are compared with the analytical (or semi-analytical) solution and with results calculated using the classical HLLC solver presented in [5]. Each geometry is described in the corresponding sub part. Geometry 1 has been developed to evaluate the PorAS solver performance under steady flow condition ($T_{1,(\mathrm{sub,\,sup,\,trans,\,jump})}$). Further comparisons have also been conducted on the test cases proposed in [6]: $T_{2,(\mathrm{sub,\,trans})}$ and in [5]: T_3, T_4 and T_5. A convergence study is performed both for the PorAS and the HLLC solver: $T_{6,(1,2,3)}$. The efficiency of the PorAS solver is also assessed by comparing the model results with experimental data: T_7. For all the following figures, the reader may have some difficulties to identify the different curves that are merged most of the time.

3.1. One-dimensional flow in case of variable porosity ($T_{1,(\mathrm{sub,\,sup,\,trans,\,jump})}$)

The first geometry consists of permanent flow in a channel with nil bottom slope and variable porosity. The four-associated test cases highlight theperformance of the proposed solver in the

DOI: 10.1002/fld

presence of a spatially varying porosity. A parabolic profile has been chosen for the porosity

$$\phi(x)=\begin{cases} ax^2+bx+c & \text{for } x\in[X_\mathrm{m}-L_0;\, X_\mathrm{m}+L_0] \\ \phi_0 & \text{elsewhere} \end{cases}$$
$$a=\frac{\phi_0-\phi_\mathrm{m}}{L_0^2},\quad b=-2aX_\mathrm{m},\quad c=\phi_0+a(X_\mathrm{m}^2-L_0^2) \tag{68}$$

where $2L_0$ is the length of the porosity variation, X_m is the position of the middle of the porosity variation, ϕ_0 is the porosity outside of the porosity variation area and ϕ_m is the porosity in the middle of the porosity variation. The computational parameters are given in Table I. In steady flow, the momentum equation can be written as:

$$\frac{\mathrm{d}}{\mathrm{d}x}\left(\frac{q^2}{\phi h}+\frac{1}{2}g\phi h^2\right)=\frac{1}{2}gh^2\frac{\mathrm{d}\phi}{\mathrm{d}x} \tag{69}$$

Combining the continuity equation in steady flow with the momentum Equation (69) leads to

$$\phi\frac{\mathrm{d}h}{\mathrm{d}x}(1-Fr^2)=hFr^2\frac{\mathrm{d}\phi}{\mathrm{d}x} \tag{70}$$

where Fr represents the Froude number. Depending on the flow regime, the discretization has to be done from upstream to downstream (supercritical flow):

$$h_\mathrm{d}=h_\mathrm{u}-h_\mathrm{u}\frac{u_\mathrm{u}^2}{\phi(gh_\mathrm{u}-u_\mathrm{u}^2)}(\phi_\mathrm{u}-\phi_\mathrm{d}) \tag{71}$$

The reference for the test case $T_{1,\mathrm{sup}}$ is established by prescribing the upstream boundary condition $h=0.2\,\mathrm{m}$ with a unit discharge $q=1\,\mathrm{m^2\,s^{-1}}$. For the test case $T_{1,\mathrm{sub}}$, the unit discharge is also $q=1\,\mathrm{m^2\,s^{-1}}$ and the downstream boundary condition is $h=1.1\,\mathrm{m}$. For the transcritical test case $T_{1,\mathrm{trans}}$, it is easy to show that the critical point where $Fr=1$ is necessarily obtained for a nil

Table I. Parameters for the first geometry: steady flow test cases (one-dimensional flow in narrowing channel—$T_{1,(\mathrm{sub,\,sup,\,trans,\,jump})}$).

Symbol	Meaning	Value
g	Gravitational acceleration	$9.81\,\mathrm{m\,s^{-2}}$
ϕ_0	Porosity outside of the porosity variation	1
	Minimum of the porosity:	
ϕ_m	for test cases $T_{1,\mathrm{sup}}$ and $T_{1,\mathrm{jump}}$	0.6
	for test cases $T_{1,\mathrm{sub}}$ and $T_{1,\mathrm{trans}}$	0.5
L_0	Length of the porosity variation	25 m
x_m	Position of the minimal porosity ϕ_m in the domain	50 m
L	Domain length	$100\,\mathrm{m}\times 1\,\mathrm{m}$
Δx	Cell size	$0.1\,\mathrm{m}\times 1\,\mathrm{m}$
q	Prescribed unit discharge at the upstream boundary	$1\,\mathrm{m^2\,s^{-1}}$
	Prescribed water depth at the downstream boundary:	
h_{av}	for test case $T_{1,\mathrm{sup}}$	0.2 m
	for test case $T_{1,\mathrm{sub}}$	1.1 m

DOI: 10.1002/fld

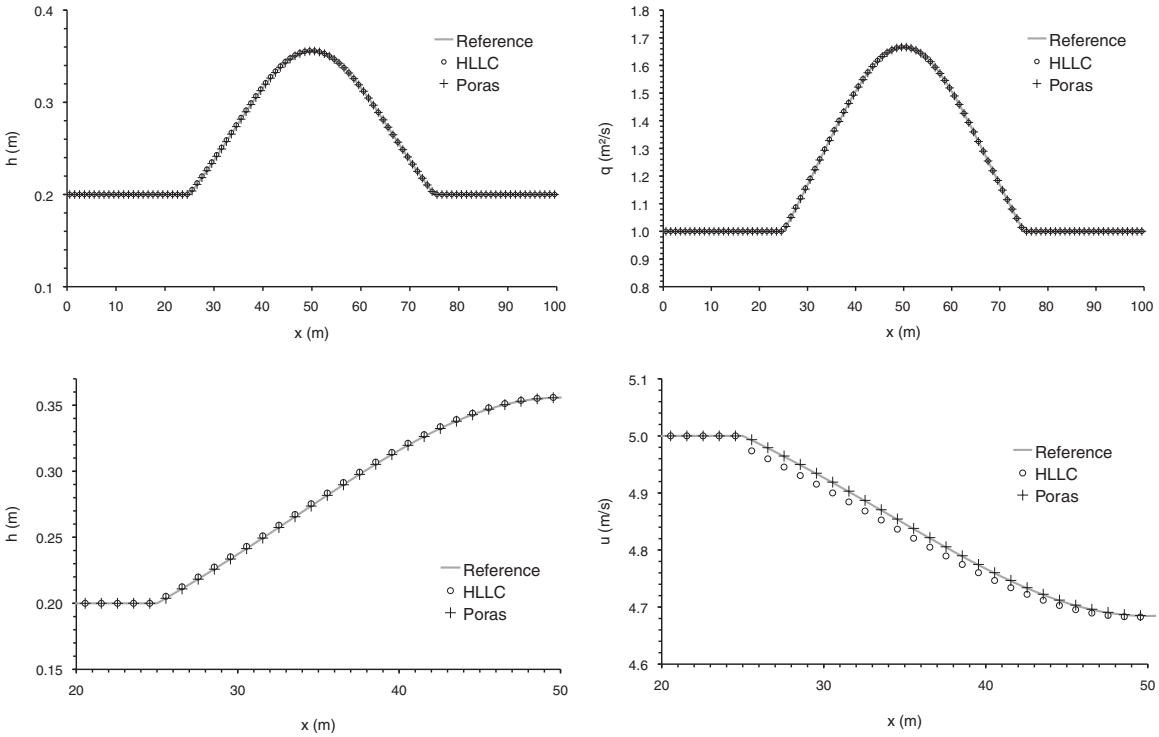

Figure 6. Supercritical one-dimensional flow in narrowing channel ($T_{1,\mathrm{sup}}$). Reference, HLLC and PorAS solutions; Top left, simulated depth; Top right, simulated unit discharge; Bottom left, detail of the water depth profile in the narrowing part; Bottom right, simulated velocity in the narrowing part.

porosity gradient. It is therefore possible to compute the water level, using Equation (70) upstream to the nil porosity gradient and Equation (71) downstream. For the test case with a hydraulic jump, the water profile upstream to the nil porosity gradient has been computed in a same way than for the transcritical test case. At the downstream end of the domain, a subcritical depth is prescribed $h=0.811\,\mathrm{m}$. The position of the hydraulic jump is determined by computing the water profile both from the nil porosity gradient to the downstream end and from the downstream end to the nil porosity gradient; the discretization being used in accordance to the flow regime. The impulse corresponding to both profiles is also computed; the hydraulic jump leading at the point where both impulses are equals. For all the test cases, the spatial discretization step for the reference solution is $\Delta x=0.1\,\mathrm{m}$. The position of the hydraulic jump being very sensitive to the downstream water depth, a second porosity variation has been used downstream to the first one for the numerical test case to ensure that the hydraulic jump stay at the correct location. The middle of the second porosity variation is located at $x=150\,\mathrm{m}$, the porosity in the middle is $\phi_{\mathrm{m}}=0.7$ and the total length is 50 m. The imposed downstream water depth for the reference corresponds exactly to the water depth upstream to the second porosity variation in the numerical simulation.

Simulations are carried out from arbitrary initial conditions over a grid of uniform cell width $\Delta x=0.1\,\mathrm{m}$. The simulation is carried out until steady flow conditions are reached over the computational domain. Figures 6–9 present the profiles obtained for both the HLLC and the PorAS solver. For the sake of clarity, only every 10th cell is represented in the Figures 6–10. In the subcritical, the supercritical and the hydraulic jump test cases, both the water depth and the unit discharge are

DOI: 10.1002/fld

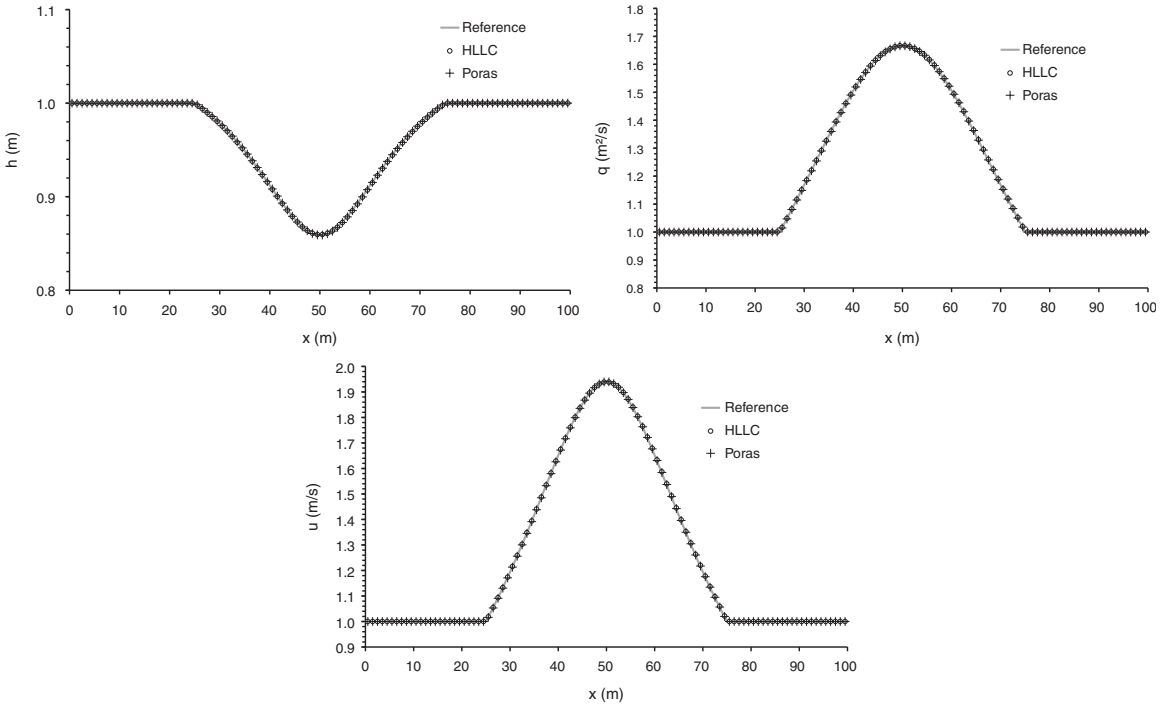

Figure 7. Subcritical one-dimensional flow in narrowing channel ($T_{1,\mathrm{sub}}$). Reference, HLLC and PorAS solutions; Top left, simulated depth; Top right, simulated unit discharge; Bottom, simulated velocity.

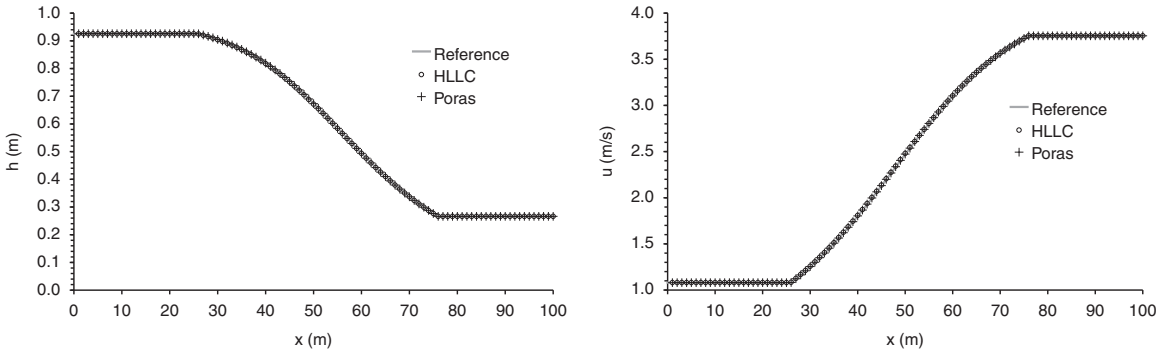

Figure 8. Transcritical one-dimensional flow in narrowing channel ($T_{1,\mathrm{trans}}$). Reference, HLLC and PorAS solutions; Left, simulated depth; Right, simulated velocity.

correctly computed by the two solvers. Nevertheless, the water depth in the narrowing part is better estimated using the PorAS solver in supercritical flow (Figure 6, bottom left). The HLLC solver underestimates the velocity in this region. For the transcritical test case, both water depth and velocity profiles are well computed by the HLLC and the PorAS solvers. Figure 10 presents the discharge computed with the HLLC and the PorAS solver. Since the test cases $T_{1,(\mathrm{sub,\,sup,\,trans,\,jump})}$ are steady-state simulations, the discharge has to be the same over the computational domain. For these simulations, the HLLC solver overestimates the discharge, whereas the PorAS solver keeps

DOI: 10.1002/fld

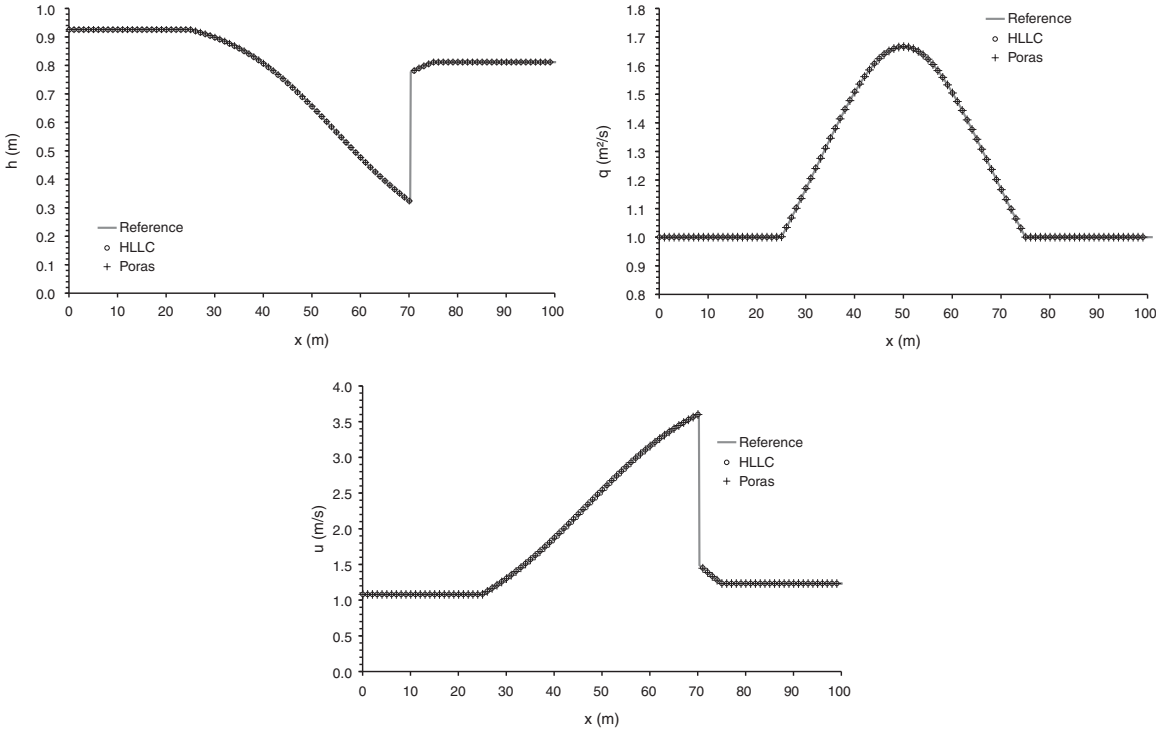

Figure 9. Hydraulic jump in narrowing channel ($T_{1,\text{jump}}$). Reference, HLLC and PorAS solutions; Top left, simulated depth; Top right, simulated unit discharge; Bottom, simulated velocity.

it constant. This phenomena may explain the velocity underestimation for the supercritical test case in the narrowing region. The inefficiency of the HLLC solver for such test cases has been investigated in [6], and as the authors suggested, it is impossible for the HLLC solver to compute correct steady-state conditions.

3.2. *One-dimensional flow over a bump* ($T_{2,(\text{sub, trans})}$)

The previous test cases have highlighted the performance of the proposed solver in the presence of a spatially varying porosity (computed in the source term). The following test cases aim to test the PorAS solver when the varying parameter is the bottom slope. The specifications proposed in [6] have been reused (Tables II and III).

Figure 11 compares the water depth and the unit discharge computed using both solvers with the semi-analytical solution obtained by solving the momentum conservation equation. Both solvers compute correctly the water level but the HLLC solver introduces an unexpected variation of the unit discharge. The same reason as for the previous test cases can be invoked. Further analysis of this problem can be found in [6].

3.3. *Dambreak problem*

To evaluate the performance of the PorAS solver in transient configuration, three dambreak problems have been used.

DOI: 10.1002/fld

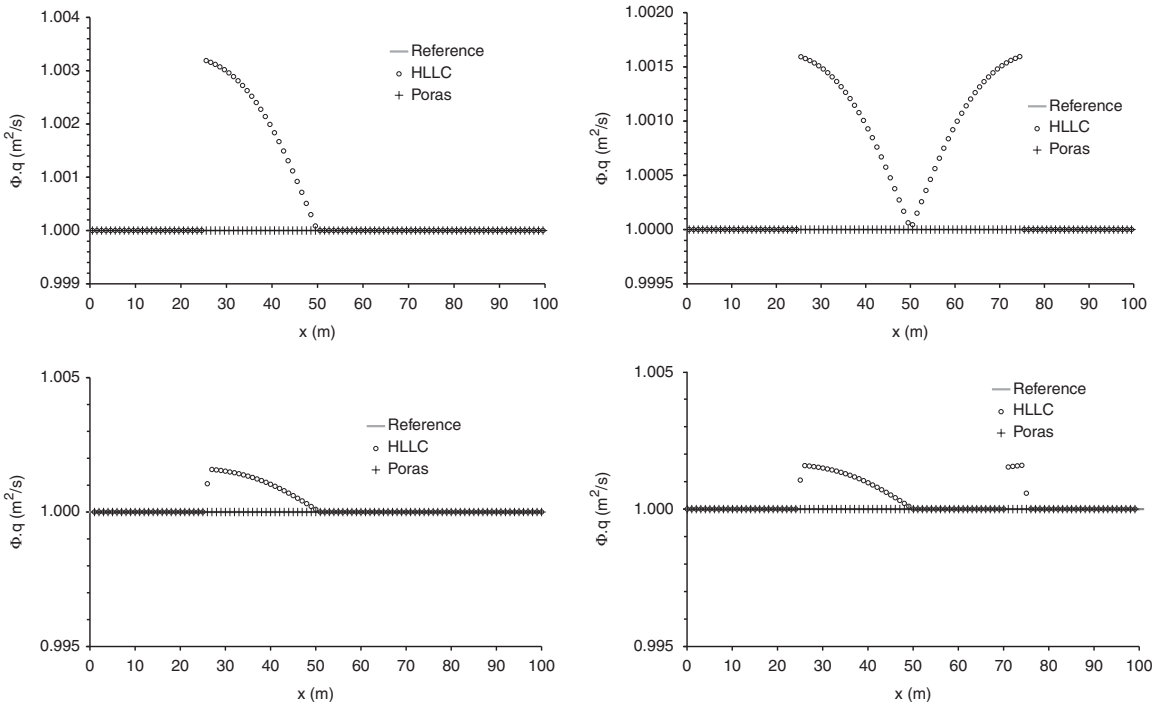

Figure 10. One-dimensional flow in narrowing channel ($T_{1,(\mathrm{sub,\,sup,\,trans,\,jump})}$). Reference, HLLC and PorAS solutions; Top left, simulated discharge for supercritical test case; Top right, simulated discharge for subcritical test case; Bottom left, simulated discharge for transcritical test case; Bottom right, simulated discharge for the hydraulic jump test case.

Table II. Parameters for the second geometry—one-dimensional subcritical flow over a bump ($T_{2,\mathrm{sub}}$).

Symbol	Meaning	Value
g	Gravitational acceleration	$9.81\,\mathrm{m\,s^{-2}}$
h_0	Bump height	0.2 m
L_0	Bump length	4 m
q	Prescribed unit discharge at the upstream boundary	$4.42\,\mathrm{m^2\,s^{-1}}$
z_d	Prescribed water depth at the downstream boundary	2 m
z_0	Initial water level	2 m
Δx	Cell size	1 m

3.3.1. One-dimensional dambreak with variable porosity (T_3). The first transient test case (T_3) consists of a dambreak over a flat bottom with a porosity varying linearly from 0 to 1. Computational parameters are given in Table IV. As explained in [5], this one-dimensional dambreak with variable porosity is equivalent to a classical circular dambreak with uniform porosity. The water level and the unit discharge for the reference are calculated by computing the classical dambreak over a grid with uniform cells width $\Delta x = 10^{-4}$ m. Figure 12 compares the results obtained using the HLLC and the PorAS solver with the reference. With both solvers, the water depth and the unit discharge are correctly estimated. The proposed solver introduces progressively two small peaks on both

DOI: 10.1002/fld

Table III. Parameters for the second geometry—one-dimensional transcritical flow over a bump ($T_{2,\text{trans}}$).

Symbol	Meaning	Value
g	Gravitational acceleration	$9.81\,\text{m}\,\text{s}^{-2}$
h_0	Bump height	0.2 m
L_0	Bump length	4 m
q	Prescribed unit discharge at the upstream boundary	$1.53\,\text{m}^2\,\text{s}^{-1}$
z_0	Initial water level	0.1 m
Δx	Cell size	1 m

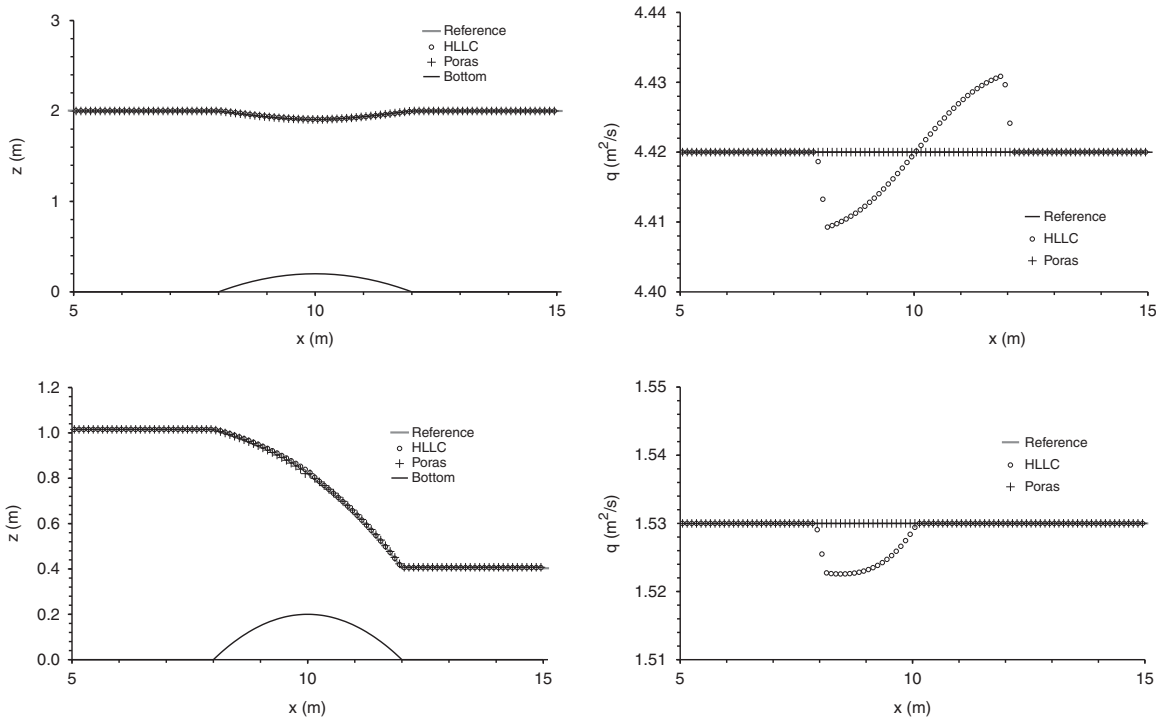

Figure 11. One-dimensional flow over a bump ($T_{2,(\text{sub, trans})}$). Reference, HLLC and PorAS solutions; Left, simulated water level; Right, simulated unit discharge; Top, subcritical test case; Bottom, transcritical test case.

sides of the cell containing the initial discontinuity, corresponding to the critical point. Since the peaks only appear on the water depth profile, it is possible to state that the momentum transfer is correctly estimated whereas the mass transfer is not. Another difference can be observed for $x = 0$ m. The water depth profile is better estimated using the HLLC solver, whereas the PorAS solver better estimates the unit discharge profile. The water depth and the unit discharge profiles at the shock computed by the PorAS solver are also steeper.

3.3.2. One-dimensional dambreak with porosity discontinuity (T_4). The second transient test case is a one-dimensional dambreak through a porosity discontinuity, which is located at the same place

DOI: 10.1002/fld

Table IV. Parameters for the one-dimensional dambreak with variable porosity (T_3).

Symbol	Meaning	Value
g	Gravitational acceleration	$9.81\,\mathrm{m\,s^{-2}}$
$h_{0,L}$	Initial water depth on the left-hand side of the dam	10 m
$h_{0,R}$	Initial water depth on the right-hand side of the dam	1 m
L	Domain length	100 m
x_0	Dam location	50 m
Δx	Cell size	1 m
$\frac{\partial \phi}{\partial x}$	Derivative of the porosity	$0.01\,\mathrm{m^{-1}}$

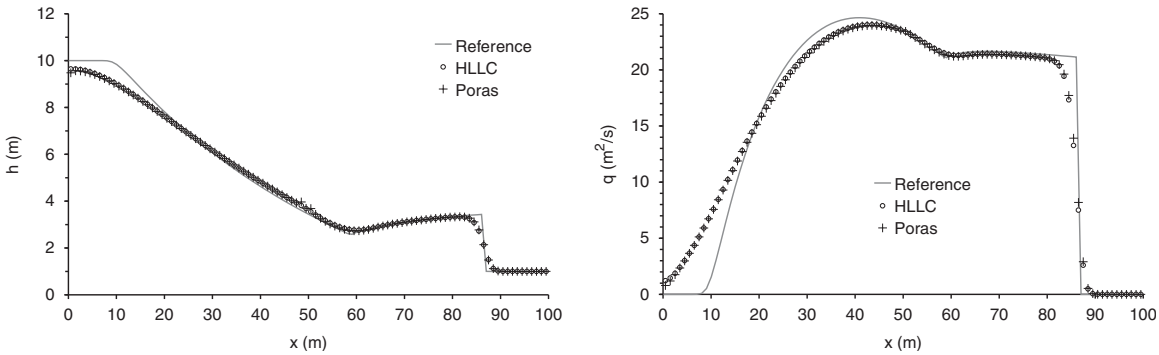

Figure 12. One-dimensional dambreak with variable porosity (T_3). Reference, HLLC and PorAS solutions; left, simulated depth, right simulated unit discharge.

Table V. Parameters for the one-dimensional dambreak with porosity discontinuity (T_4).

Symbol	Meaning	Value
g	Gravitational acceleration	$9.81\,\mathrm{m\,s^{-2}}$
$h_{0,\mathrm{L}}$	Initial water depth on the left-hand side of the dam	10 m
ϕ_{L}	Porosity on the left-hand side of the dam	1
$h_{0,\mathrm{R}}$	Initial water depth on the right-hand side of the dam	1 m
ϕ_{R}	Porosity on the right-hand side of the dam	0.1
L	Domain length	100 m
x_0	Dam location	50 m
Δx	Cell size	1 m

that the initial water discontinuity. Computational parameters are given in Table V. The method used to determine the reference profile is detailed in [5]. Figure 13 compares the profiles obtained with both solvers to the expected ones.

Both solvers compute correctly the water depth and the unit discharge. Nevertheless, they introduce diffusion through the rarefaction waves and the PorAS solver is, in that case, the most diffusive one. With the HLLC solver, the position of the shock is better estimated: at $t=4\,\mathrm{s}$, the shock should theoretically be at the position $x=94.08\,\mathrm{m}$; the position found by the HLLC solver

DOI: 10.1002/fld

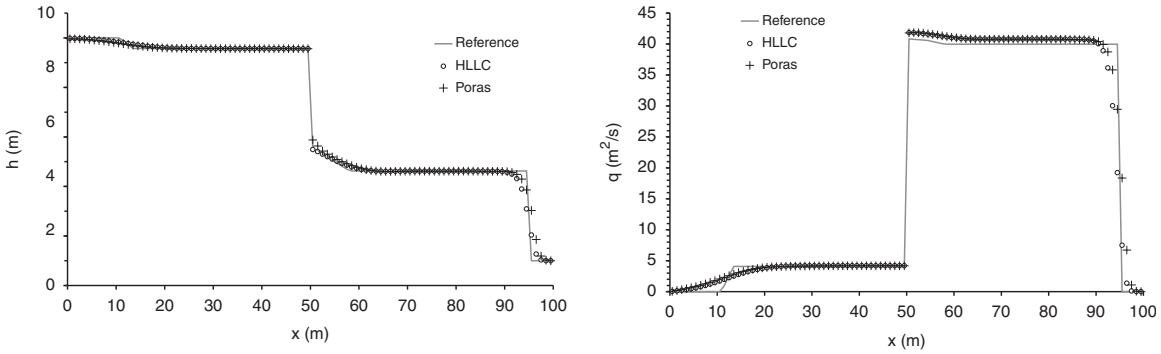

Figure 13. One-dimensional dambreak with porosity discontinuity (T_4). Reference, HLLC and PorAS solutions; left, simulated depth, right simulated unit discharge.

Table VI. Parameters for the two-dimensional dambreak with variable porosity (T_5).

Symbol	Meaning	Value
g	Gravitational acceleration	$9.81\,\mathrm{m\,s^{-2}}$
$h_{0,\mathrm{L}}$	Initial water depth on the left-hand side of the dam	10 m
$h_{0,\mathrm{R}}$	Initial water depth on the right-hand side of the dam	1 m
L	Domain length	$200\,\mathrm{m} \times 200\,\mathrm{m}$
r_0	Radius of the dam	50 m
Δx	Cell size	1 m

is $x = 95$ m and $x = 96$ m for the PorAS solver. It can be noticed that the shock remains steeper with the proposed solver.

3.3.3. Two-dimensional dambreak with variable porosity (T_5). The third transient test case (T_5) is a two-dimensional dambreak of a circular dam over a variable porosity. As shown in [5], the circular dambreak problem with a porosity proportional to the inverse of the distance to the centre of the dam has the same analytical solution as a classical one-dimensional dambreak with a constant porosity. Specifications for this test case are given in Table VI.

The calculated profiles and the analytical solution are compared in Figure 14. Both HLLC and PorAS solvers compute correct water depth and unit discharge profiles. Some differences can be observed depending on the considered direction of the profile. The differences are significant only for the proposed solver: at the critical point, the PorAS solver underestimates the water depth in the x and y directions. Nevertheless, there is always less diffusion and the water depth upstream to the shock is better estimated using the PorAS solver.

3.4. Convergence study (T_6)

The convergence of the numerical solution has been carried out on grids with decreasing spacing and time step. The test case is a steady flow in a culvert with variable porosity and bottom

DOI: 10.1002/fld

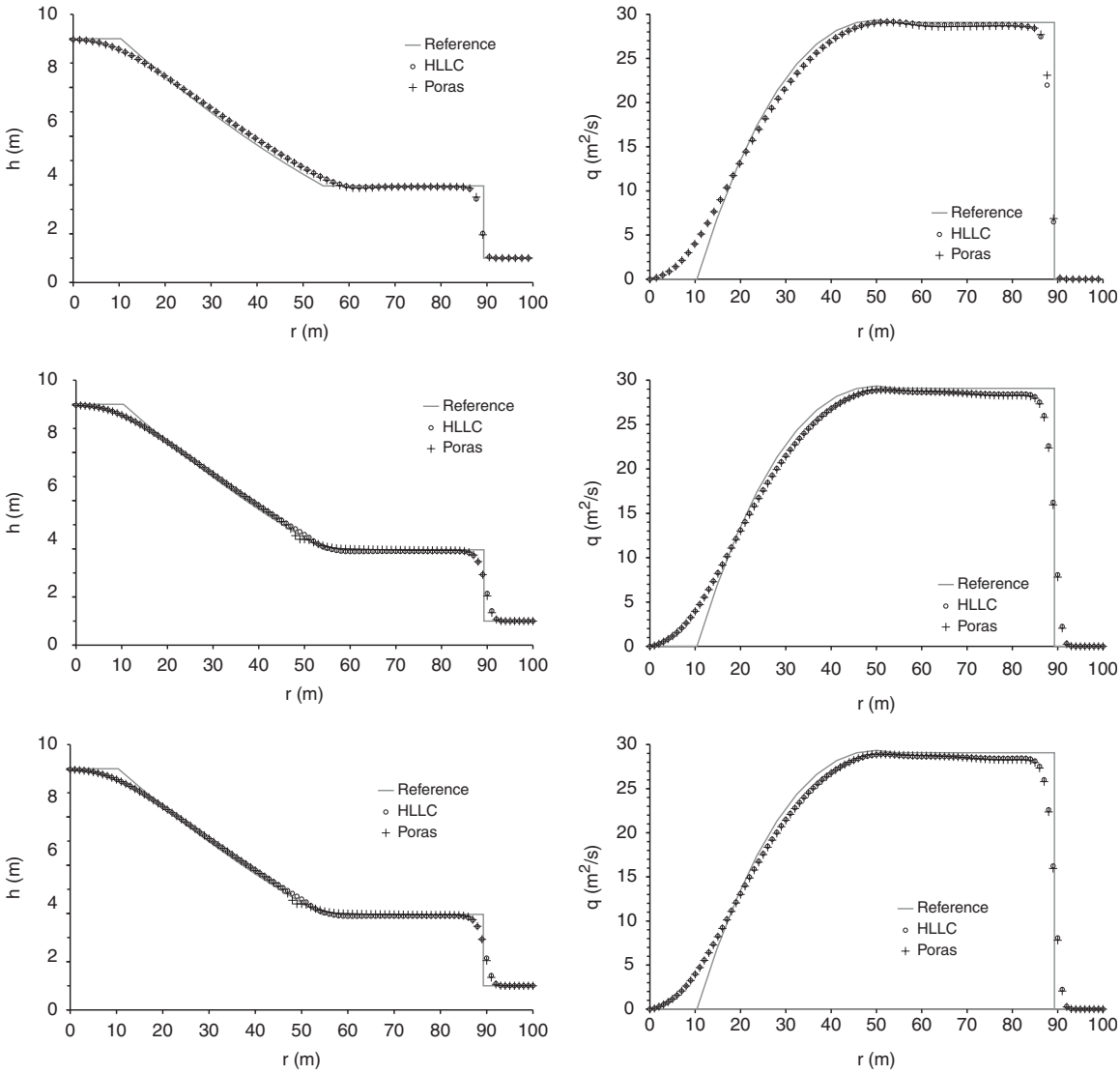

Figure 14. Two-dimensional dambreak with variable porosity (T_5). Reference, HLLC and PorAS solutions; Top: Left, simulated depth along the first bisector; Right, simulated unit discharge along the first bisector; Middle: Left, simulated depth along the X-axis; Right, simulated unit discharge along the X-axis; Bottom: Left, simulated depth along the Y-axis; Right, simulated unit discharge along the Y-axis.

elevation. The evolutions of both porosity and bottom elevation along the culvert are shown in Figure 15.

The semi-analytical solution has been calculated by discretizing the momentum equation. Combining the momentum and continuity equations leads to:

$$\phi(1-Fr^2)\frac{\mathrm{d}h}{\mathrm{d}x} = hFr^2\frac{\mathrm{d}\phi}{\mathrm{d}x} - \phi\frac{\mathrm{d}z_\mathrm{b}}{\mathrm{d}x} \tag{72}$$

DOI: 10.1002/fld

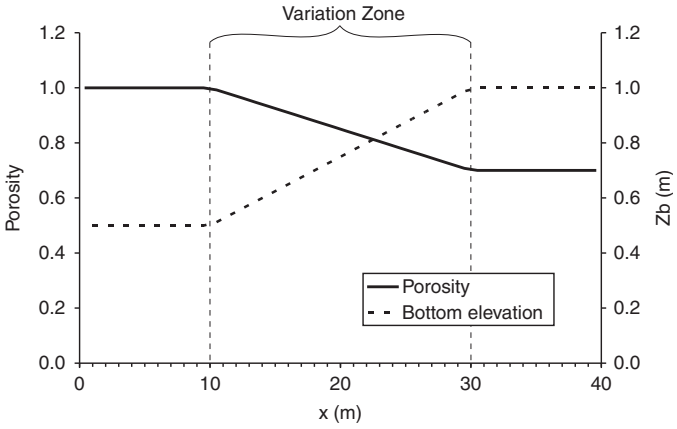

Figure 15. Longitudinal evolution of the porosity and the bottom elevation for the convergence test case.

Since the flow regime has been chosen to be subcritical, Equation (72) should be discretized from downstream to upstream:

$$h_{\mathrm{u}} = h_{\mathrm{d}} + \frac{1}{\phi_{\mathrm{d}}(1 - Fr_{\mathrm{d}}^2)}[h_{\mathrm{d}} Fr_{\mathrm{d}}^2(\phi_{\mathrm{u}} - \phi_{\mathrm{d}}) - \phi_{\mathrm{d}}(z_{\mathrm{b_u}} - z_{\mathrm{b_d}})] \tag{73}$$

To test convergence, computational time step and spatial step should be decreased in the same way. As the equations are explicitly solved, the Courant–Lax–Friedrich conditions has to be insured:

$$Cr = \frac{\lambda \Delta t}{\Delta x} \leqslant \frac{1}{2} \tag{74}$$

The time step is directly computed by the model ensuring that the Courant stability constraint is verified. The time step is therefore automatically reduced in a same proportion that the spatial step. Computational parameters are presented in Table VII. A first coarse grid ($\Delta x = 1\,\mathrm{m}$) is used to calculate the numerical solution using both the HLLC and the PorAS solvers ($T_{6,1}$). The convergence is checked by decreasing the cell width by 10 for the second convergence test case ($T_{6,2}$) and by 100 for the third convergence test case ($T_{6,3}$). For the sake of clarity, only one point every 10 cells (respectively, 100 cells) are represented in the Figure 17 (respectively, 18). The calculated profiles and the analytical solution are compared in Figures 16–18. Both HLLC and PorAS solvers compute correct water depth and unit discharge profiles for all the test cases. For the coarse grid (Figure 16), the free surface is overestimated by the PorAS solver and underestimated by the HLLC solver; both solvers overestimate the unit discharge. The computed discharge is correctly estimated by the PorAS solver and overestimated by the HLLC solver in the variation zone. As the spatial step decreases, the numerical solutions for the water elevation and the unit discharge computed with both the HLLC and the PorAS solvers get closer from the analytical solution. The difference between the discharge computed by the HLLC solver and the reference solution decreases proportionally to the spatial step decreases. The computational effort required to simulate 1000 s for each test case of the convergence study using both solvers is presented in Table VIII. For all the simulations, the PorAS solver saves 4.5% of the computational duration.

DOI: 10.1002/fld

Table VII. Parameters for the convergence test cases ($T_{6,1}$, $T_{6,2}$ and $T_{6,3}$).

Symbol	Meaning	Value
g	Gravitational acceleration	$9.81\,\mathrm{m\,s^{-2}}$
	Porosity upstream to the variation zone	0.7
	Porosity downstream to the variation zone	1
	Bottom elevation upstream to the variation zone	0.5 m
	Bottom elevation downstream to the variation zone	1.0 m
l_0	Length of the variation zone	20 m
X_0	Position of the beginning of the variation zone	10 m
L	Domain length	$100\,\mathrm{m} \times 1\,\mathrm{m}$
	Cell size	
Δx	for test case $T_{6,1}$	$1\,\mathrm{m} \times 1\,\mathrm{m}$
	for test case $T_{6,2}$	$0.1\,\mathrm{m} \times 1\,\mathrm{m}$
	for test case $T_{6,3}$	$0.01\,\mathrm{m} \times 1\,\mathrm{m}$
q	Prescribed unit discharge at the upstream boundary	$1\,\mathrm{m^2\,s^{-1}}$
z_d	Prescribed water level at the downstream boundary	2 m
z_i	Initial water depth over the domain	1 m

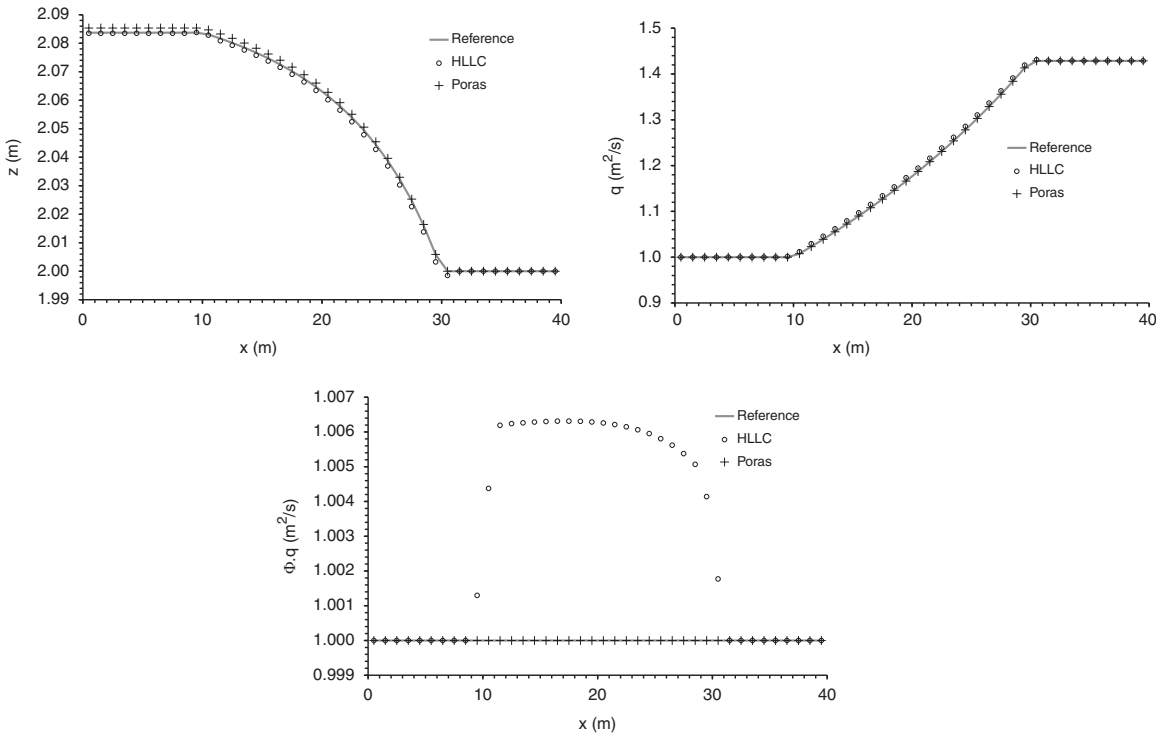

Figure 16. First convergence test case ($T_{6,1}$). Reference, HLLC and PorAS solutions; Top left, simulated water elevation; Top right, simulated unit discharge; Bottom, simulated discharge.

DOI: 10.1002/fld

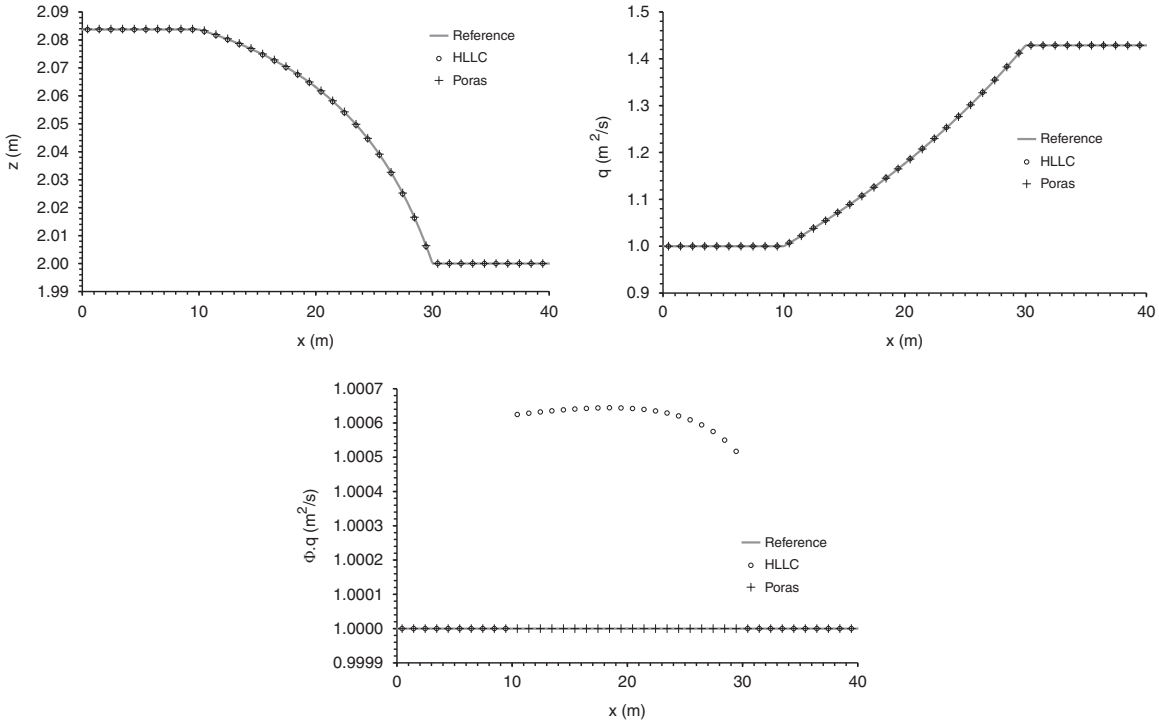

Figure 17. Second convergence test case ($T_{6,2}$). Reference, HLLC and PorAS solutions; Top left, simulated water elevation; Top right, simulated unit discharge; Bottom, simulated discharge.

3.5. *Experimental test case* (T_7)

The usefulness and the validity of the porosity approach for large scale modelling of floods in the presence of urbanized areas have been demonstrated in [5]. In the previous section, the validity of the PorAS solver is demonstrated using (semi-) analytical test cases. In order to check the validity of the PorAS solver under real configuration, comparisons of the model results for both HLLC and PorAS solvers are made with experimental data. The experiments were performed using a scale model of the Italian Toce valley at CESI (Italy) during the IMPACT European project. Square blocks are implemented in a 7 m long and 3.5–5 m wide model to represent urban area (Figure 19).

The measured hydrograph is used as upstream boundary conditions. The computed water surface elevations using both the PorAS and the HLLC solvers at $t = 20$ s are compared with the measured values (Figure 20). There is no significant differences between the computed profiles using the PorAS and the HLLC solver. Moreover, the computed water levels match the measurements; the explanations for the differences presented in [5] remain valid.

4. CONCLUSIONS

An approximate-state Riemann solver has been developed for the classical shallow water equations with source terms arising from non-uniform porosity and bottom elevation. Using the flux components instead of the conserved variable in the expression of the Riemann invariants allows

DOI: 10.1002/fld

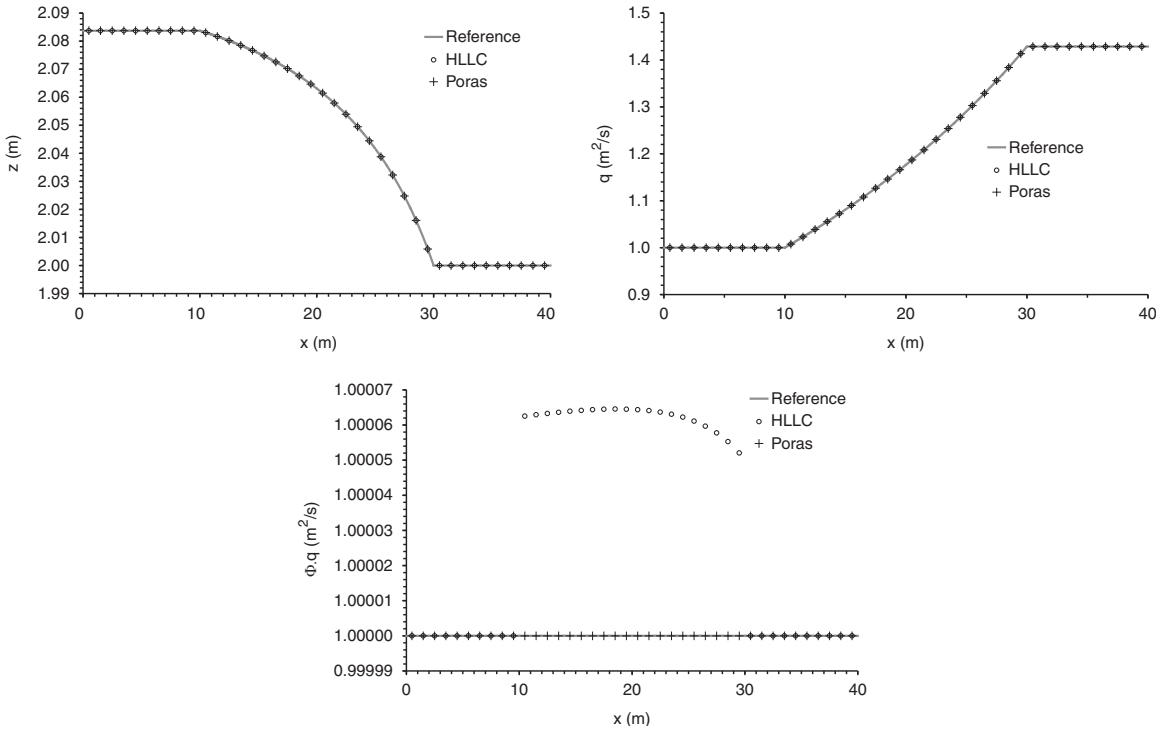

Figure 18. Third convergence test case ($T_{6,3}$). Reference, HLLC and PorAS solutions; Top left, simulated water elevation; Top right, simulated unit discharge; Bottom, simulated discharge.

Table VIII. Computational effort for the convergence test cases ($T_{6,(1,2,3)}$).

	PorAS solver	HLLC solver
$T_{6,1}$	1.50 s	1.52 s
$T_{6,2}$	1 min 6 s	1 min 9 s
$T_{6,3}$	1 h 38 min 53 s	1 h 43 min 20 s

the direct calculation of the fluxes at the interfaces, while accounting for the influence of the source terms in the characteristic equations. This results in improved solution of the continuity and momentum equations, in particular near steady-state configurations. The different computational examples have highlighted both advantages and defaults of the proposed solver. For the transient applications, the efficiency of the proposed solver is the same as that the efficiency of the HLLC solver. On the dambreak simulations with porosity, the over (or under) estimated water depth close to the critical point computed by the proposed solver is balanced by steeper fronts and smaller numerical diffusion. Clear improvements have been obtained with the proposed solver on steady-state simulation with varying parameters (porosity and/or bottom slope). The PorAS solver can therefore be used for both transient and steady-state simulation, substantial improvements being observed on highly variable geometry parameters. The proposed solver is used with a classical Godunov scheme and can easily be extended to higher-order scheme since no modifications to the

DOI: 10.1002/fld

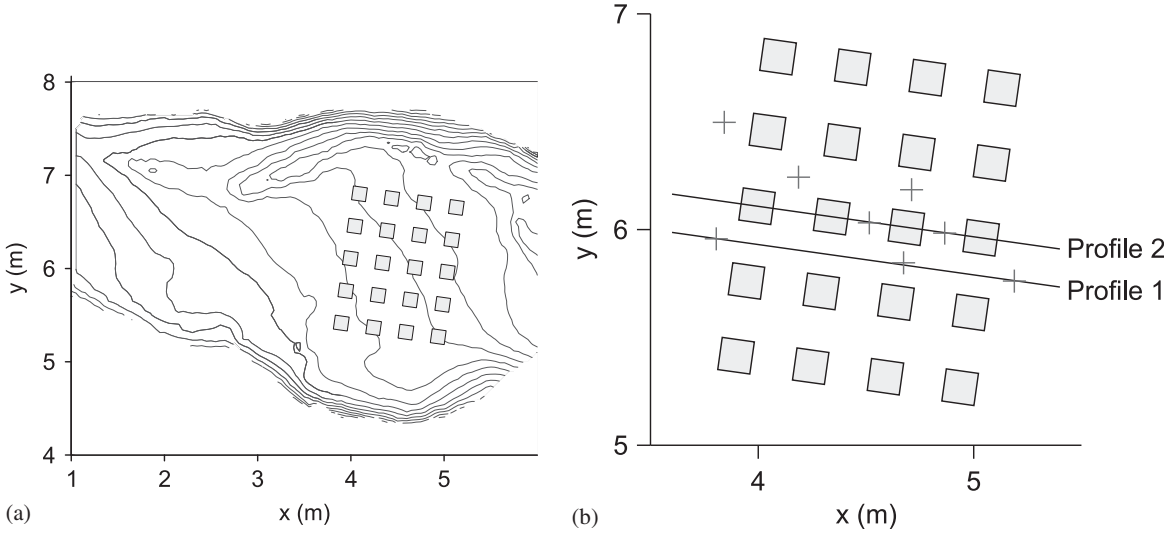

Figure 19. Topography of the valley for the Toce test case, contour line spacing 0.01 m (a). Sketch of the longitudinal profiles and measurement points (b).

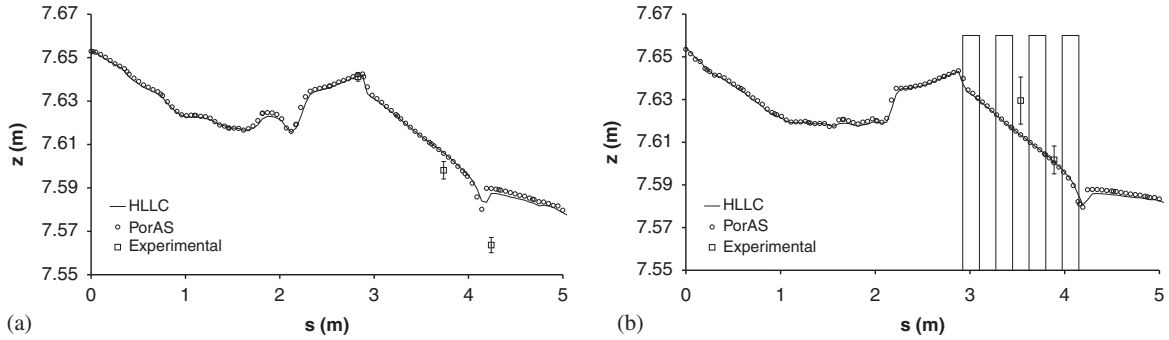

Figure 20. Water surface elevation at $t = 20$ s along profile 1 (a) and profile 2 (b).

Riemann solver are required. Further developments, especially the treatment of critical points, are under investigation.

ACKNOWLEDGEMENTS

This research has been partly carried out during a Ph.D. Thesis funded by GEI (Ginger Environnement et Infrastructures), a GINGER Group company and by the ANRT (Association Nationale de la Recherche et de la Technologie), contract no. 2006/838.

REFERENCES

1. Alcrudo F, Benkhaldoun F. Exact solutions to the Riemann problem of the shallow water equations with a bottom step. *Computers and Fluids* 2001; **30**:643–671.
2. Rochette D, Clain S. Two-dimensional computation of gas flow in a porous bed characterized by a porosity jump. *Journal of Computational Physics* 2006; **219**:104–119.

DOI: 10.1002/fld

3. Defina A, D'Alpaos L, Mattichio B. A new set of equations for very shallow water and partially dry areas suitable to 2D numerical domains. *Proceedings Specialty Conference* '*Modelling of Flood Propagation over Initially Dry Areas*', Milano, Italy, 29 June–1 July 1994.
4. Hervouet JM, Samie H, Moreau B. Modelling urban areas in dam-break flood-wave numerical simulations. *Proceedings of the International Seminar and Workshop on Rescue Actions Based on Dambreak Flow Analysis*, Seinâjoki, Finland, 1–6 October 2000.
5. Guinot V, Soares-Frazão S. Flux and source term discretization in two-dimensional shallow water models with porosity on unstructured grids. *International Journal for Numerical Methods in Fluids* 2006; **50**:309–345.
6. Lhomme J, Guinot V. A general approximate-state Riemann solver for hyperbolic systems of conservation laws with source terms. *International Journal for Numerical Methods in Fluids* 2007; **53**:1509–1540.
7. Godunov SK. A difference method for numerical calculation of discontinuous equations of hydrodynamic equations. *Matematicheskii Sbornik* 1959; **47**:271–300 (in Russian).
8. Roe PL. Approximate Riemann solvers, parameter vectors and difference scheme. *Journal of Computational Physics* 1981; **43**:357–372.
9. Roe PL, Pike J. Efficient construction and utilisation of approximate Riemann solutions. *Computing Methods in Applied Science and Engineering*. North-Holland: Amsterdam, 1984.
10. Harten A, Hyman P. Self-adjusting grid methods for one-dimensional hyperbolic conservation laws. *Journal of Computational Physics* 1983; **50**:235.
11. Roe PL. Sonic flux formulae. *SIAM Journal on Scientific and Statistical Computing* 1992; **13**(2):611–630.
12. Toro EF. *Riemann Solvers and Numerical Methods for Fluid Dynamics*. Springer: Berlin, 1997.
13. Toro EF. A linearised Riemann solver for the time-dependent Euler equations of the gas dynamics. *Proceedings of the Royal Society of London*, *Series A* 1991; **434**:683–693.
14. Toro EF, Chou CC. A linearised Riemann solver for the steady supersonic Euler equations. *International Journal for Numerical Methods in Fluids* 1993; **16**:173–186.
15. Quirk JJ. An alternative to unstructured grids for computing gas dynamic flows around arbitrarily complex two dimensional bodies. *Computers and Fluids* 1994; **23**(1):125–142.
16. Harten A, Lax P-D, Van-Leer B. On upstream differencing and Godunov-type schemes for hyperbolic conservation laws. *SIAM Review* 1983; **25**:35–61.
17. Guinot V. *Wave Propagation in Fluids*: *Models and Numerical Techniques*. ISTE Ltd., John Wiley & Sons Inc.: London, Hoboken, 2008.
18. Toro EF, Spruce M, Speares W. Restoration of the contact surface in the HLL-Riemann solver. *Shock Waves* 1994; **4**:25–34.
19. Osher S, Solomon F. Upwind difference schemes for hyperbolic conservation laws. *Mathematics of Computation* 1982; **38**:339–374.
20. Linde T. A practical, general-purpose, two-state HLL Riemann solver for hyperbolic conservation laws. *International Journal for Numerical Methods in Fluids* 2002; **40**:391–402.
21. Lax P-D. Hyperbolic systems of conservation laws. *Communications on Pure and Applied Mathematics* 1957; **10**:537–566.
22. Colella P. Glimm's method for gas dynamics. *SIAM Journal on Scientific and Statistical Computing* 1982; **3**:76–110.
23. Dukowicz JK. A general, non iterative Riemann solver for Godunov's method. *Journal of Computational Physics* 1985; **61**:119–137.
24. Guinot V. Riemann solvers for water hammer simulations by Godunov method. *International Journal for Numerical Methods in Engineering* 2000; **49**:851–870.
25. Guinot V. Numerical simulation of two-phase flow in pipes using Godunov method. *International Journal for Numerical Methods in Fluids* 2001; **50**:1169–1189.
26. Ivings MJ, Causon DM, Toro EF. On Riemann solvers for compressible fluids. *International Journal for Numerical Methods in Fluids* 1998; **28**:395–418.
27. Toro EF. Direct Riemann solvers for the time-dependent Euler equation. *Shock Waves* 1995; **5**:75–80.
28. LeVeque RJ. Balancing source terms and flux gradients in high-resolution Godunov methods: the quasi-steady wave-propagation algorithm. *Journal of Computational Physics* 1998; **146**:346–365.
29. Bermudez A, Vazquez ME. Upwind methods for hyperbolic conservation laws with source terms. *Computers and Fluids* 1994; **8**:1049–1071.
30. Greenberg JM, Le Roux AY. A well balanced scheme for the numerical processing of the source terms in hyperbolic equation. *SIAM Journal on Numerical Analysis* 1996; **33**:1–16.

DOI: 10.1002/fld

31. Gallouët T, Hérard JM, Seguin N. Some approximate Godunov schemes to compute shallow-water equations with topography. *Computers and Fluids* 2003; **32**:479–513.
32. Lhomme J. One-dimensional, two-dimensional and macroscopic approaches to urban flood modelling. *Ph.D. Thesis*, Montpellier 2 university, 2006 (in French).
33. Sanders BF, Schubert JE, Gallegos HA. Integral formulation of shallow-water equations with anisotropic porosity for urban flood modelling. *Journal of Hydrology* 2008; **362**:19–38.
34. Soares-Frazo S, Lhomme J, Guinot V, Zech Y. Two-dimensional shallow water model with porosity for urban flood modelling. *Journal of Hydraulic Research* 2008; **46**(1):45–64.
35. Garcia-Navarro P, Vazquez-Cendon ME. On numerical treatment of the source terms in the shallow water equations. *Computers and Fluids* 2000; **29**:951–979.
36. Nujíc M. Efficient implementation of non-oscillatory schemes for the computation of free-surface flows. *Journal of Hydraulic Research* 1995; **33**:101–111.
37. Jeffrey A, Tanuiti T. *Nonlinear Wave Propagation*. Academic press: New York, 1964.

DOI: 10.1002/fld